UNIVERSITAT DE BARCELONA

# Toroidal nematics: Point defects, disclination lines and walls

Javier Rojo-González

Aquesta tesi doctoral està subjecta a la llicència ***Reconeixement 4.0. Espanya de Creative Commons***.

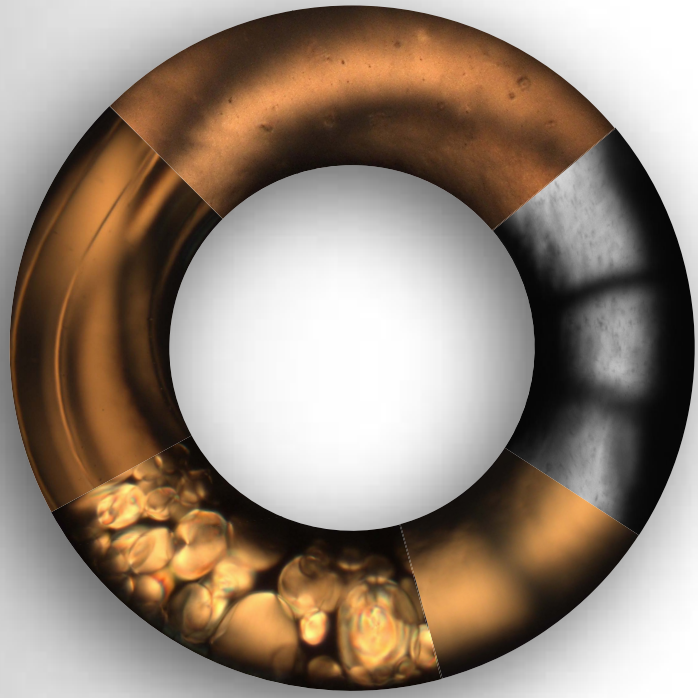
Esta tesis doctoral está sujeta a la licencia ***Reconocimiento 4.0. España de Creative Commons***.

This doctoral thesis is licensed under the ***Creative Commons Attribution 4.0. Spain License***.

PhD thesis

# TOROIDAL NEMATICS:

## Point defects, disclination lines and walls



JAVIER ROJO GONZÁLEZ

UNIVERSITAT DE BARCELONA

Programa de Doctorado en Física

# Toroidal nematics: Point defects, disclination lines and walls

Javier Rojo-González

Director:
Dr. Alberto Fernández-Nieves

Tutor:
Dr. Giancarlo Franzese

Marzo 2025



Universitat de Barcelona

The work described in this thesis has been financially supported by the Ministry of Universities of the Spanish Government through the FPU20/03682 Ph.D. Fellowship.

# Abstract

Confining partially order fluids can lead to frustration if the locally preferred state can not be achieved everywhere simultaneously. When this happens, the configuration of the material can not be given by the local minimum, and a plethora of compatible frustrated configurations become possible. In this case, the ground state configuration results from the minimization of the total energy. This is specially exemplified by nematic liquid crystals where the anisotropic building blocks reduce their free energy by aligning parallel to each other. Perfect parallel alignment can become impossible everywhere when the nematic is confined within different shapes while fixing the orientation at the boundaries. How this frustration is resolved and which configuration the liquid crystal acquires depends on the geometry and topology of the boundary and might require the presence of regions with no defined alignment, called defects.

In this thesis we mainly focus on experimentally studying the configurations acquired by a nematic liquid crystal confined to a stable toroidal droplet with different boundary conditions. We first study the case with tangential alignment at the surface. In this case, we find stable defect populated configurations when the torus is heated to the isotropic phase and cooled back to the nematic phase. They consist mainly on defect pairs whose number and location is random and that turn out to be metastable with an energetic barrier that is high enough for them to not spontaneously annihilate. We also report the appearance of a configuration not fully elucidated that we call "X" pattern and that can have a solitonic character. Note that all these features are observed even when there is no topological requirement for the torus to have defects.

We then study the effect of applying magnetic fields on planar nematic tori with and without defect pairs and find that stable inversion walls form. In the defect free case, two splay-bend walls form, while when a defect pair is present, either one of the walls does not appear or an extra wall is formed depending on the initial location of the defect pair. Interestingly, we find that the mobility of the defects allows for the defect pair wall to reorganize into different types of walls, becoming a wall of the twist type to reduce energy. We also show how, by heating and cooling our nematic droplets in an external magnetic field, the number of defect pairs generated can be controlled.

We finish our work on nematic tori by studying the case with perpendicular anchoring at the surface. We recover previous experimental results and find

that the anchoring strength plays a significant role in the appearance of a configuration characterized by four dark brushes forming a spiral. Moreover, for certain conditions, stable configurations filled with disclination lines are found and experimentally studied using epifluorescence microscopy.

Aside from our experimental work, from a theoretical perspective, we use the decomposition of a director field distortion into four normal modes to derive the compatibility conditions for a 2D and 3D nematic. For that, we use a simple approach based on imposing that the director field variation has to be the same when going through two different paths up to second order. This approach gives an intuitive interpretation of the different equations and provides a simple way to relate them to their counterpart in curved space through the concept of holonomy.

Finally, we also discuss some side projects collaterally related to the main thesis work. We first discuss our studies on water evaporation of chitosan hydrogels. We describe the constructed setup to generate the gels and our experiments that track the mass evolution of the gels in time. Our results suggest that the evaporation rate for our hydrogels is slower than pure water due to an increase in the energy barrier for the water molecules to escape the gel, thus bringing about a kinetic character to the process. We also show the design, construction and first tests on an upscaled prototype for the production of these chitosan hydrogels. We end by briefly describing our work with thermorresponsive hydrogels that present a constant volume phase transition leading to phase coexistence between a swollen and shrunken phases when the temperature is increased rapidly. We mainly show how cylindrical gels suddenly bend due to a spontaneous polarization of the region that shrinks, which is in accordance with the current theory for this process.

**Key works:** Nematic liquid crystals, confinement, torus, boojum, topological defects, inversion walls, disclination lines, hydrogels, evaporation, extreme thermodynamics, biaxial-splay.

# Resum


## Nemàtics toroidals: Defectes puntuals, línies de disclinació i murs

Confinar fluids parcialment ordenats pot resultar en frustració si no es pot assolir l'estat localment preferit a tot arreu simultàniament. Quan això passa, la configuració del material no ve donada pel mínim local, i una gran varietat de configuracions frustrades compatibles són possibles. En aquest cas, l'estat fonamental ve determinat per la minimització de l'energia. Això s'exemplifica especialment amb els cristalls líquids nemàtics, on els seus constituents anisotròpics tendeixen a alinear-se paral·lelament entre ells. Aquest alineament pot no ser possible quan es confina el material i es fixa l'orientació a la superfície. La manera com es resol aquesta frustració i quina configuració adquireix el cristall líquid depèn de la geometria i la topologia de la forma, i pot requerir la presència de regions sense alineament definit, anomenades defectes.

En aquesta tesi estudiem les configuracions que adquireix un cristall líquid nemàtic confinat en una gota toroidal estable amb diferents condicions de contorn. Primer, estudiem el cas amb alineament tangent a la superfície. Trobem configuracions metaestables amb defectes quan el tor s'escalfa fins a la fase isòtropa i es refreda novament fins a la fase nemàtica. Aquestes configuracions consisteixen principalment en parelles de defectes, el nombre i la ubicació dels quals són aleatoris, i que resulten ser metaestables amb una barrera energètica prou gran per evitar la seva annihilació espontània. També informem de l'aparició d'una configuració no del tot dilucidada que anomenem patró "X" i que pot tenir un caràcter solitònic. Noteu que totes aquestes característiques s'observen fins i tot quan no hi ha cap requisit topològic perquè el tor tingui defectes.

A continuació, estudiem l'efecte d'aplicar camps magnètics en tors nemàtics planars amb i sense parelles de defectes, i descobrim que es formen murs d'inversió. En el cas sense defectes, es formen murs de flexió-divergència, mentre que, quan hi ha una parella de defectes present, o bé un dels murs no apareix, o bé es forma un mur addicional, segons la ubicació inicial de la parella de defectes. Curiosament, hem observat que la mobilitat dels defectes permet que el mur associat a la parella es reorganitzi en diferents tipus, convertint-se en un mur de torsió per reduir l'energia. També mostrem com, mitjançant el procés d'escalfament i

refredament de les gotes toroidals nemàtiques en un camp magnètic extern, es pot controlar el nombre de parelles de defectes generats.

Acabem el nostre treball sobre torus nemàtics estudiant el cas amb alineament perpendicular. Recuperem resultats experimentals previs i trobem que la força d'ancoratge té un paper significatiu en l'aparició d'una configuració caracteritzada per quatre bandes fosques amb forma espiral. A més, sota certes condicions, s'identifiquen configuracions estables plenes de línies de disclinació, que estudiem experimentalment utilitzant microscòpia d'epifluorescència.

A part de l'estudi experimental, utilitzem el nou enfocament per descompondre la distorsió del camp director en quatre modes normals per derivar les condicions de compatibilitat per a un nemàtic 2D i 3D. Per a això, fem servir un mètode basat en imposar que la variació del camp director ha de ser la mateixa en recórrer dos camins diferents fins a segon ordre. Aquest enfocament ofereix una interpretació intuïtiva de les diferents equacions i proporciona una manera senzilla de relacionar-les amb els seus equivalents en espais corbats mitjançant el concepte d'holonomia.

Finalment, també discutim el nostre treball en projectes paral·lels col·laterals relacionats amb el treball principal de la tesis. Exposem el nostre treball sobre l'evaporació d'aigua en hidrogels de quitosà. Descrivim el muntatge construït per generar els gels i els nostres experiments mesurant el canvi de massa dels gels amb el temps. Aquests estudis suggereixen que la velocitat d'evaporació dels nostres hidrogels és més lenta que la de l'aigua pura a causa de l'augment de la barrera energètica que les molècules d'aigua han de superar per escapar del gel, i per tant, es un efecte cinètic. També mostrem el disseny, construcció i primeres proves d'un prototip a gran escala per a la producció d'aquests hidrogels de quitosà. Acabem descrivint breument el nostre treball amb hidrogels termo-responsius que mostren una transició de fase a volum constant, que dona lloc a la coexistència de dues fases, una inflada i una contreta, quan la temperatura augmenta ràpidament. Mostrem com els gels cilíndrics es dobleguen sobtadament a causa d'una polarització espontània de la regió que es contreu, un fenomen predit teòricament.

**Paraules clau:** Cristalls líquids nemàtics, confinament, tor, boojum, defectes topològics, murs d'inversió, línies de disclinació, hidrogels, evaporació, termodinàmica extrema, biaxial-splay.

# Acknowledgements

Una tesis doctoral no es solo un trabajo de investigación de varios años sino que supone, a su vez, un proceso psicológico importante para el que la realiza desde su comienzo hasta su fin. Por ello, estar rodeado de las personas adecuadas que te den la fuerza para seguir es fundamental, y afortunadamente, ese ha sido mi caso. Esta sección es el espacio en esta tesis para daros las gracias a todos vosotros.

A mis padres, Benita y Tomás y mi hermana María, gracias por vuestro apoyo incondicional estando tan lejos de casa. A ti, Alberto, gracias por todo aquello que a nivel científico me has aportado dirigendo la tesis y tu comprensión y humanidad en aquellos temas ajenos al trabajo. Gracias a Victor, Ares, Ignasi F., María, Yu y Joshua por las conversaciones, inicialmente durante la comida, y luego en cualquier ámbito, que han derivado en una bonita amistad. Gracias a Ignasi V. Berta, Joel y Ramón Santiago (Ramoncín) del grupo SOC&SAM, por haber convertido una relación laboral en amistad, por las conversaciones interesantes sobre trabajo y por todo el apoyo tanto en las buenas como en las malas. Especialmente te doy las gracias a ti, Ramoncín, por haberte convertido, en estos 6 años que nos conocemos desde el máster, en un gran amigo con el que me alegro profundamente de haber compartido este viaje de doctorado. También al murcianico, Jaime, por tantas conversaciones a horas intempestivas en el departamento, y tantos cafés.

A los compañeros de trabajo y doctorado del SCML, Adrián, Jyo, Caleb, Guillaume, Adrià, Ramón, Anna y Jose. Gracias por ser todos y cada uno de vostros, dentro de las peculiaridades y rarezas de cada uno, unas personas maravillosas y haber creado un ambiente de trabajo ameno y agradable. Gracias Jose por ser tan bueno y empático y por las conversaciones con el café de primera hora de la mañana. Gracias también de todo corazón a Alec, Perpi, Macarena, Dani, Bernat y Eric por vuestra amistad externa al ámbito académico durante todos estos años. Espero que siga así durante muchos más. Por mantener el contacto en las comidas los viernes a mediodía, gracias Moni. Como sé que me dejo a algunas personas de todas las que han pasado por mi vida durante estos cuatro años, gracias a todos vosotros por formar parte de esta tesis.

Por último, y no menos importante, gracias a ti, Mari. Por estar a mi lado estos dos últimos años y en el final de la tesis, donde no todo ha sido fácil. Por escucharme y entenderme y por querer lo mejor para mi y para nosotros. Espero

que este sea el fin de una etapa que dé comienzo a una mejor.

# Contents

**Publications** ix

**List of Figures** ix

**List of Tables** xiii

**1 Introduction** 1
- 1.1 Soft matter: Definition and types . . . 1
- 1.2 Geometrical frustration and confinement . . . 3
- 1.3 Outline of the thesis . . . 5

**2 Fundamentals of nematic liquid crystals and topological defects** 7
- 2.1 Introduction . . . 7
- 2.2 Nematic liquid crystals . . . 9
  - 2.2.1 Continuum description . . . 9
  - 2.2.2 Elastic free energy . . . 11
  - 2.2.3 External fields . . . 14
  - 2.2.4 Anchoring . . . 17
  - 2.2.5 Free energy minimization . . . 19
  - 2.2.6 Competing effects of anchoring alignment and magnetic fields . . . 21
    - 2.2.6.1 Infinite anchoring strength: Transition layer thickness . . . 22
    - 2.2.6.2 Elastic and anchoring competition: Extrapolation length . . . 23
    - 2.2.6.3 Anchoring breakdown: Critical field . . . 24
- 2.3 Topological defects . . . 25
  - 2.3.1 Point defects and boojums . . . 26
    - 2.3.1.1 Point defects in 2D . . . 26
    - 2.3.1.2 Point defects in 3D . . . 28
  - 2.3.2 Line defects . . . 30
  - 2.3.3 Alignment inversion walls . . . 31

2.4 Confinement . . . 35
2.4.1 Poincaré-Hopf Index Theorem . . . 36
2.4.2 Cylindrical confinement . . . 39
2.5 Why nematic tori? . . . 41

**3 Making and stabilizing toroidal droplets and a bit of polymer physics, hydrogels, their behavior and an upscale method for their production 43**
3.1 Introduction . . . 43
3.2 Making toroidal droplets . . . 44
3.2.1 Fundamentals . . . 44
3.2.2 Experimental setup . . . 45
3.2.3 Stability . . . 46
3.3 Polymer physics and hydrogels . . . 47
3.3.1 Free energy of hydrogels . . . 47
3.3.1.1 Mixing free energy . . . 48
3.3.1.2 Elastic free energy . . . 50
3.3.2 Shrinking and swelling . . . 52
3.3.3 Out of equilibrium phenomena in hydrogels . . . 55
3.4 Water evaporation of spherical hydrogels . . . 56
3.4.1 Fabrication of chitosan spherical gels . . . 57
3.4.1.1 Photopolymerizable solution . . . 57
3.4.1.2 Spherical hydrogel fabrication . . . 59
3.4.2 Single gel drying . . . 61
3.4.2.1 Experiments . . . 61
3.4.2.2 Maxwell's evaporation model . . . 63
3.4.3 Effects of gel proximity on drying: Local saturation . . . 66
3.5 Upscaled prototype for the continuous production of spherical hydrogels . . . 69
3.5.1 Prototype: Principle of operation and design . . . 70
3.5.2 Injection tests . . . 72
3.5.3 Crosslinking tests . . . 74
3.5.4 Overview and further work . . . 76
3.6 Stabilization of non-spherical droplets in yield stress materials . . . 76
3.6.1 Yield stress materials . . . 77
3.6.2 Toroidal droplet generation in yield stress materials . . . 79
3.6.3 Sample preservation: Cuvette sealing . . . 80
3.6.4 Generation of nematic cylinders . . . 81
3.7 Study of thermoresponsive cylindrical hydrogels: Extreme thermodynamics . . . 81
3.7.1 Previous work . . . 81

3.7.2 Hydrogel preparation . . . 84
3.7.3 Temperature control setup . . . 86
3.7.4 Cylindrical gels . . . 88
3.7.4.1 Bending and bubbling . . . 88
3.7.4.2 Homogeneity test . . . 92
3.7.4.3 Temperature and size effects on instability . . . 92
3.7.5 Other shapes . . . 94
3.8 Conclusions . . . 95

**4 Planar nematic solid tori** **97**
4.1 Introduction . . . 97
4.2 Polarized optical microscopy . . . 98
4.2.1 Fundamentals . . . 98
4.2.2 Microscope setup . . . 102
4.2.3 Two dimensional flat samples . . . 104
4.2.4 Thick samples with curved boundaries . . . 107
4.2.5 Temperature control . . . 110
4.3 Defect-free planar tori . . . 110
4.3.1 Double-twisted configuration . . . 111
4.3.2 Generating stable defect configurations by heating and cooling cycles . . . 116
4.4 Defect pairs . . . 119
4.4.1 Observations . . . 119
4.4.2 Proposed model . . . 121
4.4.2.1 Analytical ansatz derivation . . . 122
4.4.2.2 Jones Matrix simulations . . . 126
4.4.2.3 Further confirmation: Lattice-Boltzmann simulations . . . 127
4.4.3 Role of curvature . . . 129
4.4.4 Stability of defect pairs . . . 131
4.4.5 Statistics of defect pair generation . . . 134
4.4.5.1 Defect pair number . . . 135
4.4.5.2 Defect pair position . . . 138
4.4.5.3 Defect pair orientation in nematic cylinders . . . 139
4.4.6 Non-canonical defect pairs . . . 141
4.4.6.1 Types . . . 141
4.4.6.2 Statistics: Number and location . . . 143
4.5 An unknown pattern . . . 144
4.5.1 Observations . . . 144
4.5.2 Discussion . . . 148
4.6 Conclusions . . . 150

**5 $K_{24}$ as a bulk deformation mode: Compatibility conditions 153**
5.1 The traditional view: $K_{24}$ as a surface term . . . 153
5.2 Decomposing nematic deformations into normal modes . . . 156
5.2.1 Normal deformations as 2D elastic deformations . . . 159
5.2.2 The free energy of the normal modes . . . 161
5.3 Compatibility conditions for nematic liquid crystals . . . 163
5.3.1 Equality of mixed partial derivatives . . . 164
5.3.2 Compatibility conditions for a 2D nematic . . . 166
5.3.3 Compatibility conditions for a 3D nematic . . . 170
5.3.4 3D compatibility equations: Cases of study . . . 178
5.4 Conclusions . . . 184

**6 Magnetic field effects in planar nematic solid tori 185**
6.1 Experimental setup . . . 185
6.2 Defect-free tori . . . 188
6.2.1 Wall formation . . . 188
6.2.2 Boundary conditions . . . 191
6.2.3 The role of the double twist . . . 192
6.2.4 Wall thickness as a function of magnetic field . . . 193
6.3 Tori with defect pairs . . . 196
6.3.1 Interpreting defect pairs as splay-bend walls . . . 196
6.3.2 Defect pairs close to wall generating regions . . . 198
6.3.3 Defect pairs far from wall generating regions . . . 200
6.3.4 Inversion wall simulations . . . 204
6.3.4.1 Assumptions and simplifications . . . 204
6.3.4.2 Inversion wall types . . . 205
6.3.4.3 Numerical simulations of walls . . . 209
6.3.4.4 Motion and stability of the walls . . . 214
6.4 Heating and cooling under magnetic fields . . . 216
6.4.1 Large magnetic fields . . . 216
6.4.2 Small magnetic fields . . . 218
6.5 Conclusions . . . 218

**7 Homeotropic nematic solid tori 221**
7.1 Previous work in the group . . . 221
7.2 Spiral and concentrated configurations . . . 225
7.2.1 Spiral configuration as a transient state . . . 225
7.2.2 Yield stress material without ethanol: Concentrated-Spiral-Planar transition . . . 228
7.3 Escaped radial configuration with finite anchoring strength . . . 230
7.3.1 One elastic constant model . . . 230

7.3.1.1 Including saddle-splay: $K_{24}$ as an effective anchoring strength . . . 234
7.3.1.2 Homeotropic-Planar transition at finite anchoring strength . . . 235
7.3.1.3 Jones Matrix simulations: Comparison with experiments . . . 236
7.3.2 Role of twist and different elastic constants . . . 238
7.4 Configurations with disclination lines . . . 241
7.4.1 Preliminary discussion . . . 242
7.4.2 Identifying disclination lines with epifluorescence microscopy 245
7.4.3 Loop characterization . . . 249
7.5 Heating and cooling homeotropic tori . . . 252
7.6 Droplet nucleation in homeotropic nematic tori . . . 254
7.7 Conclusions . . . 256

**8 Conclusions and further work 259**
8.1 Nematic liquid crystals confined to toroidal droplets . . . 259
8.2 Hydrogels . . . 263

**References 265**

**Appendices 278**

**A Toroidal droplet generation setup 279**
A.1 Rotating stage . . . 279
A.2 Injection setup . . . 281

**B Upscaled gel generation setup: Drawings 285**

**C Stable toroidal droplet generation: Troubleshooting 291**

**D Extreme thermodynamics: Preliminary studies 297**
D.1 Diffusion coefficient of spherical pNIPAM gels . . . 297
D.2 Quasistatic heating of spherical pNIPAM gels . . . 299
D.3 Quasistatic heating of toroidal pNIPAM gel . . . 301

**E Extreme thermodynamics: Additional data 303**

**F Compatibility equations for a 3D nematic 307**

**G Continuous director evolution in magnetic fields: Ansatzes 313**
G.1 Defect free case . . . 313
G.2 Defect pair located at $\varphi = 0$ . . . 314

# List of Figures


2.1 Schematic of phases with different symmetries . . . . . 8
2.2 Elastic deformation modes for a nematic liquid crystal . . . . . 12
2.3 5CB magnetic susceptibility . . . . . 16
2.4 Competing effects in nematics: System schematic . . . . . 21
2.5 Nematic 2D point defects . . . . . 27
2.6 Nematic 3D point defects . . . . . 29
2.7 Schematic of disclination loop with strength 1/2 . . . . . 30
2.8 Alignment inversion walls schematics . . . . . 32
2.9 Boundaryless surfaces with different number of handles . . . . . 37
2.10 Nematic confined to spherical shapes: Experiments . . . . . 38
2.11 Schematic of the configurations of a nematic liquid crystal confined to a cylinder . . . . . 40

3.1 Toroidal droplets generation setups . . . . . 46
3.2 Hydrogel schematics . . . . . 49
3.3 Isobar plots for continuous and discontinuous transition . . . . . 53
3.4 Schematics of chitosan methacrylation and crosslinking reaction . 58
3.5 Spherical gels fabrication setup . . . . . 60
3.6 Chitosan gels . . . . . 61
3.7 Single gel mass evolution . . . . . 62
3.8 Chitosan gel layer evaporation . . . . . 66
3.9 Chitosan gel lattice evaporation . . . . . 68
3.10 Equilibrium relative humidity of chitosan gels . . . . . 69
3.11 Chitosan gel layer evaporation . . . . . 70
3.12 Upscaled prototype: Injection tests . . . . . 73
3.13 Upscaled prototype: Crosslinking tests . . . . . 75
3.14 Nematic-isotropic transition of a torus and different yield stress materials . . . . . 78
3.15 Cuvette sealing and cylindrical droplets generation . . . . . 81
3.16 Extreme thermodynamics phase coexistence schematics . . . . . 82
3.17 Quasistatic heating and quenching of toroidal hydrogel . . . . . 83

3.18 pNIPAM gels fabrication . . . 85
3.19 Hydrogel heating setups . . . 87
3.20 Bending and bubbling of cylindrical gels . . . 89
3.21 Quenching of cylindrical gels . . . 90
3.22 Quasistatic heating of pNIPAM cylinder . . . 92
3.23 Quenching at different temperatures of cylindrical gels with different sizes . . . 93
3.24 Different shaped gels deformation . . . 95

4.1 Polarized light basics . . . 100
4.2 Inverted microscope for polarized optical microscopy . . . 103
4.3 Flat samples under crossed polarizers . . . 105
4.4 Michel-Lévy chart . . . 107
4.5 Refraction in crossed interfaces . . . 109
4.6 Defect free configuration experimental images . . . 111
4.7 Double twist schematics . . . 113
4.8 Twist angle analysis . . . 114
4.9 Twist angle as a function of aspect ratio . . . 115
4.10 Isotropic-nematic transition of a nematic toroidal droplet at slow cooling rate . . . 116
4.11 Isotropic-nematic transition of a nematic toroidal droplet at fast cooling rate . . . 117
4.12 Double-twisted vs defect pair configuration . . . 118
4.13 Defect pair observations . . . 120
4.14 Defect pair separation . . . 121
4.15 Defect pair ansatz . . . 123
4.16 Defect pair texture schematics . . . 127
4.17 Lattice Boltzmann . . . 128
4.18 Curvature effect on defect pair generation . . . 130
4.19 Defect pair stability energy profile . . . 133
4.20 Two defect pairs annihilation in a nematic cylinder . . . 134
4.21 Defect pair number histogram for the thick and slender torus and the cylinder . . . 135
4.22 Defect pair number statistics and Gaussian fit . . . 137
4.23 Defect pair spatial distribution . . . 139
4.24 Axial symmetry for defect pairs in nematic cylinders . . . 140
4.25 Non-canonical defect pairs . . . 142
4.26 Non-canonical defect pairs distribution . . . 144
4.27 X pattern observations . . . 145
4.28 Crossed-polarizer images of disclination lines . . . 146
4.29 X pattern annihilation events . . . 147

4.30 Chromonic liquid crystal bright field patter . . . . . 149

5.1 Normal deformation modes: Schematics . . . . . 160
5.2 Infinitesimal path construction . . . . . 165
5.3 Compatibility equations in 3D: Schematics . . . . . 171

6.1 Magnetic field experimental setup . . . . . 187
6.2 Defect free planar tori in magnetic field . . . . . 189
6.3 Wall asymmetry in defect free tori . . . . . 192
6.4 Wall width as a function of magnetic field . . . . . 194
6.5 Defect pairs as splay-bend walls . . . . . 197
6.6 Magnetic field effect on defect pairs located in wall generating regions . . . . . 199
6.7 Magnetic field effect on defect pairs located far from wall generating regions . . . . . 201
6.8 Wall annihilation . . . . . 203
6.9 Schematic of coordinates and order parameter space for walls . . 204
6.10 Inversion wall types . . . . . 207
6.11 Wall simulation validation . . . . . 213
6.12 Wall simulation energy results . . . . . 215
6.13 Heating and cooling tori in magnetic fields . . . . . 217

7.1 Homeotropic tori previous phase diagram: SDS concentration - Aspect ratio . . . . . 223
7.2 Homeotropic tori reproduced phase diagram: SDS concentration - Aspect ratio . . . . . 224
7.3 Relative peak width measurements of tori in yield stress material with ethanol and 8mM SDS . . . . . 226
7.4 Spiral concentrated transition . . . . . 227
7.5 Homeotropic tori in yield stress material without ethanol . . . . 228
7.6 Concentrated - Spiral - Planar transition . . . . . 229
7.7 Escaped radial schematics . . . . . 231
7.8 Twist and non equal elastic constant Jones matrix simulations . 239
7.9 Comparison between the one constant approximation and solution for different elastic constants of the escaped radial configuration 241
7.10 Configuration with disclination lines . . . . . 242
7.11 Loops on toroidal surfaces . . . . . 244
7.12 Epifluorescence microscopy for disclination line observation . . . 246
7.13 Epifluorescence image of disclination lines in homeotropic nematic toroidal droplets . . . . . 248
7.14 (1-0) Disclination loop . . . . . 249
7.15 (0-0) Disclination loop . . . . . 250

7.16 Homeotropic tori in the planar polar configuration . . . . . 251
7.17 Heating and cooling homeotropic tori . . . . . 253
7.18 Homeotropic to planar transition of the escaped radial with point defects configuration . . . . . 254
7.19 Droplets aggregates in homeotropic tori . . . . . 255

8.1 Cholesteric and chromonic tori . . . . . 262

A.1 Torus generating setup: Rotating stage . . . . . 280
A.2 Torus generating setup: Injector setup . . . . . 282

B.1 Upscaled setup: I.2 piece . . . . . 290

D.1 Deswelling kinetic of spherical pNIPAM gels . . . . . 298
D.2 Heating rate effect on spherical pNIPAM gels shrinking . . . . . 300
D.3 Quasistatic heating of a toroidal pNIPAM gel . . . . . 301

E.1 Extreme thermodynamics: Mold cylinder 1 . . . . . 303
E.2 Extreme thermodynamics: Mold cylinder 2 . . . . . 304
E.3 Extreme thermodynamics: 3D printed cylinder . . . . . 305
E.4 Extreme thermodynamics: 3D printed arc . . . . . 306

G.1 Coordinate schematics . . . . . 314

# List of Tables


4.1 Special types of polarized light . . . . . 99
4.2 Jones calculus operators for common optical elements . . . . . 102
4.3 Mean defect pair number per heating and cooling cycle. The discrepancy tells us whether the means can be considered equal or not . . . . . 136
4.4 Percentage of defect structures of different types experimentally observed for different aspect rations and cooling rates . . . . . 143

6.1 Slopes obtained from the analysis of wall width for different torus 195

Chapter 1

# Introduction

## 1.1 Soft matter: Definition and types

The term soft matter was coined by Pierre-Gilles de Gennes in his Nobel Prize inaugural speech in 1991 [1] and comprises a large variety of systems within condensed matter that, in colloquial terms, are "easy to deform". Although the exact definition of soft matter can vary between authors, it generally refers to systems with small elastic moduli compared to those in hard condensed matter. Since the elastic moduli is in essence an energy density, being soft typically requires large internal length scales compared to the atom size. For soft materials with atomic relevant length scales, like thermotropic liquid crystals, the softness comes from partially broken symmetries. Having small elastic moduli implies that stresses or external fields with an energy on the order of room temperature, $k_B T$, can significantly affect these materials. This further implies that entropy is very important, making soft matter inherently different from traditional hard condensed matter, where energy is the essential quantity.

The way how thermal fluctuations affect the behavior of soft matter can vary between systems. In this sense, we can classify the different soft matter system according to their nature in:

- **Colloidal systems**: Colloids are small particles larger than the atomic scale that, when suspended in a liquid, move around due to the collision of solvent particles on it. This movement, called Brownian motion is a result of the thermal movement of the solvent molecules and depends on temperature. This allows using colloids as a proxy for atoms where the concentration of colloids drives the transition from liquid to crystal or glass phases [2]. Typically, Brownian motion is observed for particles ranging from tens of nanometers to tens of micrometers.

- **Polymers**: Polymers are large molecules consisting on linked sub-units,

called monomers, that form a chain. Their small size together with the large number of possible states makes the entropy of the chain a very important parameter to describe their behavior in solution. The configuration entropy also plays a significant role for materials made of a collection of polymers.

- **Polymer gels**: Gels are covalently or physically cross-linked polymer chains such that they form a 3D polymer network inside a solvent. Although very dilute, gels are elastic solids. When the solvent is water they are called hydrogels. Compared to hard materials where their elastic properties are dominated by energy, the behavior of gels is dominated by the entropy of the constituent chains and the mixing entropy of the solvent molecules and the polymers. As a result of this and their large internal length scales, they posses low elastic moduli, typically on the order of kPa, which is significantly lower to the GPa order of magnitude for conventional hard matter.

- **Liquid crystals**: Liquid crystals are a group of phases of matter in between conventional solids and liquids that are able to flow but present at least some orientational ordering of their anisotropic building blocks. Therefore, they are partially ordered fluids with some broken symmetries. The simplest phase, called the nematic phase, corresponds to the case where the anisotropic building blocks have no positional order but align along a common direction. From a thermodynamic point of view, as shown by Onsager, this phase can become the stable one just for entropic reasons without the need of an alignment energetic interaction. This is the case since for anisotropic building blocks, the entropy increases when there is alignment since in that case the accessible volume per building block increases. This results in an ordering interaction of the order of $k_BT$. Fluctuations are, thus, important, and moreover, small external fields or surface interactions can be used to manipulate the system state and induce frustration.

- **Emulsions and foams**: In the realm of soft matter, foams and emulsions are liquids saturated with gas bubbles or immiscible droplets respectively separated by fluid membranes. Although comprised of fluids, these materials are solids. They are however soft and flow at high stresses.

- **Biological membranes**: Biological membranes consists of surfactant molecules that self-assemble into membranes. The small size of the membrane makes thermal fluctuations relevant for describing this system.

This list does not intend to be rigorous but just to give a flavor of the different systems studied within soft matter. Indeed, it is usual to have materials

falling simultaneously in different categories such as liquid crystal gels, where the orientational properties of the liquid crystal can couple with the elastic properties of the resulting gel [3], or colloidal hydrogels where the softness of the particles can affect crystallization and overall their phase behavior. [4].

Soft matter has also been defined according to other characteristics like their relaxation times, which are large compared to the atomic time scale and become similar to the human time scale in the order of milliseconds up to months. This, for example, allows using colloidal systems to study crystallization dynamics in real time, which would be very challenging in molecular systems.

## 1.2 Geometrical frustration and confinement

In condensed matter, geometrical frustration refers to the inability of a material to fill space while achieving the locally preferred configuration. The most paradigmatic example of frustration is that of an antiferromagnet in a triangular lattice [5]. In this case, the local energy minimum for each spin is achieved when all the surrounding spins have opposite sign. Nonetheless, if we take three spins in a triangle of the lattice, they can not be arranged such that all of them are surrounded by opposite signed spins simultaneously. In this case, the lattice arrangement of spins frustrates the local preferred configuration such that not all spins can fall into their local energy minimum. This frustration results in interesting and unexpected configurations of the system that can not be predicted from locally minimizing the free energy of the system [6].

This notion of geometrical frustration also appears frequently in soft condensed matter. One example is the packing of colloids on a spherical surface [7]. In this case, the densest packing is obtained for the triangular lattice. For any colloidal arrangement we can mathematically construct a lattice consisting of points corresponding to the colloids' position and then consider the lines joining the closest neighbors to tessellate space. We define the Euler characteristic of the tessellation as $\chi = V - E + F$, where $V$, $E$ and $F$ are its number of vertices, edges and faces. When the colloids decorate the surface of a sphere, the lattice forms a convex polyhedron which must have $\chi = 2$ [8]. Nonetheless, each particle with hexagonal packing contributes 0 to the Euler characteristic and at least 12 particles with 5 neighbors are required to fill the sphere[1] such that the densest configuration can not be achieved everywhere on the spherical surface.

Another paradigmatic example is the case of confined nematic liquid crystals. In this case, the anisotropic building blocks, called nematogens, prefer to align along the same direction everywhere in space. The average orientation of

[1] This is the same case as a traditional soccer ball which is covered by hexagonal and 12 pentagonal panels.

the nematogens defines the director. Importantly, since interactions with the confining surface can be strong relative to the interparticle interactions, well defined orientations of the nematogens at the surface can be established. This allows confining nematic liquid crystals to certain volumes with different boundary conditions at the confining surface. Fulfilling the boundary conditions can be incompatible with a uniform alignment and the system becomes frustrated. Multiple possibilities for solving this frustration can appear, leading to different possible states. In that case, the distortion free energy of the material with respect the uniform state dictates which is the ground state.

If the confining surface is the sphere and the nematogens are forced to lie tangent to the surface, the Poincaré-Hopf index theorem tells us that a smooth director field on the surface is not possible and that we must have singularities in the director field. These regions are called topological defects. How these defects arrange, depend again on the energetics of the system. The need for singularities is a result of the topology of a sphere; hence, the same is true for any confinement shape which can be obtained by a continuous deformation of the sphere. If the topology of the confinement is changed to that of a torus with tangent boundary conditions, a smooth director field can exist, leading to a defect-free state of the liquid crystal whose final configuration will depend on the free energy of the nematic. Indeed, the spontaneous appearance of chiral configurations for achiral nematic liquid crystals is observed under toroidal confinement with parallel anchoring conditions [9, 10]. Moreover, for the toroidal confinement, the curvature of the surface, which is measured by the curvature along the two principal directions ($\kappa_1$,$\kappa_2$), is different at each point and can play a role in determining the preferred configuration of the material. This, for example, affects topological defects which become attracted to regions with either positive or negative Gaussian curvature, $K = \kappa_1\kappa_2$, depending on their nature [11].

This same argument can be extended to other phases of liquid crystals with a different local ground state, like cholesteric liquid crystals or smectics, where the frustration can be resolved in different ways depending on the peculiarities of their free energy [12].

A final example of frustration is that of a gel that shrinks expelling the solvent when the temperature is increased but whose volume is fixed. In that case, phase separation occurs and one part of the material shrinks minimizing its energy at the expense of another region that expands. This internal deformation can couple with the initial geometry producing large deformations of the gel.

In conclusion, frustration prevents the material from reaching the locally preferred minimum free energy configuration everywhere such that it organizes itself to minimize its overall free energy. This results in a configuration that can not be predicted from the local free energy and where the whole sample has to be taken into account. This, in turn, can result in unexpected and

surprising configurations where the confinement geometry, topology or other external factors can play a significant role.

## 1.3 Outline of the thesis

In this thesis, we mainly focus on the experimental study of the different configurations attained by a nematic liquid crystal when confined to a toroidal droplet with different boundary conditions and external fields. We also briefly describe our experiments with hydrogels. The thesis is organized as follows:

- We start by introducing the continuum description of nematic liquid crystals in Chapter 2. We describe their phenomenological free energy which can be divided into a bulk, elastic distortion, surface and external field contributions and briefly discuss the competition between all of them. We end the chapter discussing topological defects of different dimensionality and the effect of confinement through the Poincaré-Hopf index theorem.

- In Chapter 3 we introduce the technique necessary to produce toroidal droplets. In order to stabilize them, a yield stress material which is made of granular-sized hydrogels is used. We then introduce the basics of polymer physics and hydrogels and discuss the results on water evaporation from chitosan hydrogels. The experimental setup used to produce hydrogels in a lab scale and an upscale prototype for industrial production is also discussed. These side projects spark from collaborations with the company Agrobio S.L. We then talk about the stabilization of toroidal droplets in yield stress materials and finish the chapter talking about our results on extreme thermodynamics of thermoresponsive poly(N-isopropylacrylamide) hydrogels where a thermodynamic instability produces large shape changes of the gels.

- Being able to make toroidal droplets, in Chapter 4 we study nematic toroidal droplets with planar boundary conditions. We first introduce polarized optical microscopy which will be used to study our nematic toroidal droplets. We then discuss the defect free double-twisted configuration that has been previously studied and is observed after the toroidal droplets are generated. After heating the toroidal droplet to the isotropic phase and cooling it back to the nematic phase we find new defect populated configurations. These defect populated configurations consist mainly on defect pairs. We describe them and study in detail their statistics when repeatedly heating and cooling the same toroidal droplet. We end the chapter with a brief discussion on an unknown configuration we refer to as "X" pattern.

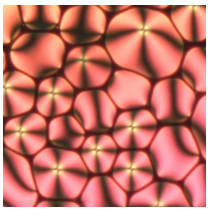
- In Chapter 5 we take a little detour and talk about the bulk interpretation of the saddle-splay distortion energy term through a normal mode decomposition of the elastic distortion. This description allows understanding the spontaneous double-twisted configuration of the defect free planar tori in terms of pure bulk deformations without the need to resort on a surface interpretation of the term. We also use this description together with an infinitesimal path construction to derive the compatibility conditions of a nematic in 2D and 3D in an intuitive way and discuss how curvature enters the equations.

- In Chapter 6 we study the change in configuration of the nematic toroidal droplets described in Chapter 4 when an external magnetic field is applied both in the defect-free and defect populated case and rationalize the results in terms of alignment inversion walls. We end the chapter by studying the effect of heating and cooling the torus in the presence of an external magnetic field.

- To finish our experimental work, in Chapter 7 we study nematic toroidal droplets with perpendicular boundary conditions. We observe different configurations in terms of the interaction with the boundary and the presence or not of ethanol in the outer yield stress material. The defect free configurations are rationalized using a weak anchoring approach and confirmed through Jones Matrix simulations. Moreover, for certain conditions, configurations filled with disclination lines are observed which do not correspond to the ground state for such large tori.

- Finally, in Chapter 8 we summarize the main conclusions of the thesis and briefly discuss the main perspectives and future work that can stem from our experiments and results.

Chapter 2



# Fundamentals of nematic liquid crystals and topological defects

## 2.1 Introduction

Liquid crystals, also called mesophases, are states of matter which lie in between liquids and solids. From a physical point of view, isotropic liquids differ from crystalline solids in their symmetries. A material is said to have a symmetry when, in average, there is no microscopic difference in the material before and after the symmetry operation is performed. From all the possible symmetries, the most relevant in the liquid-solid phase transition are the translational and rotational symmetries. Isotropic liquids have continuous translational and rotational symmetries since there is no preferred location or orientation of their constituents (see Figure 2.1). This is also reflected in the diffusivity of the constituents, which explore all accessible spatial and orientational configurations. When the liquid becomes a crystalline solid, its constituents arrange with an underlying lattice that breaks both the continuous translational and rotational symmetries in all 3 dimensions. As shown in Figure 2.1, in this case, the position of the constituents is fixed by the underlying lattice and does not change in time. This breaks both the continuous translational and rotational symmetries of the isotropic liquid phase.

By contrast to isotropic liquids and crystals, liquid crystals are made of

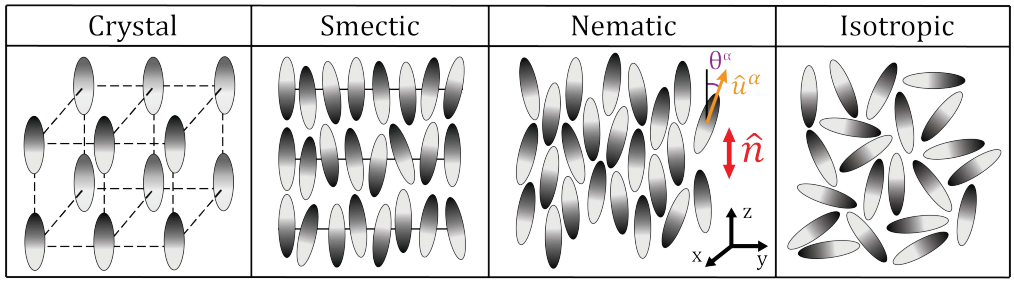



**Figure 2.1:** From left to right: Crystalline solid, smectic and nematic phase. Lines indicate positional ordered, in a lattice for the case of the crystal and in rows for the smectic phase. The director orientation of the nematic phase schematic is shown as a double red arrow.

anisotropic building blocks called mesogens and break some but not all of the symmetries. These phases can be classified by the particular symmetries they break. From these phases, nematic liquid crystals constitute the simplest one of them. They preserve the translational continuous symmetry of the isotropic liquid providing the ability to flow, while the anisotropic building blocks align along the same direction, breaking the continuous rotational symmetry (Figure 2.1). Furthermore, while the molecules align parallel to each other, they do not have a preferential sense, adding an "up-down" symmetry. Other typical liquid crystals phases are smectics (Figure 2.1), where the mesogens are aligned in layers breaking the same symmetries of the nematic phase plus the continuous translational symmetry in the direction perpendicular to the layers and columnar phases where the mesogens arrange in columns breaking the continuous translational symmetry in the two dimensions perpendicular to the columns. It is important to note that liquid crystals do not usually exhibit all the possible liquid crystal phases, but only some of them.

Moreover, liquid crystals can be also classified according to the relevant parameter that predominantly controls the phase transition into thermotropic and lyotropic liquid crystals. In thermotropic liquid crystals the phase of the material depends on temperature, while in lyotropic liquid crystals the mesogens are suspended in a solvent and the phase is controlled by both concentration and temperature. Thermotropic liquid crystals present the isotropic phase at high temperatures, the solid phase at low temperatures with liquid crystal phases occurring at temperatures in between. In this work, we focus on the study of a thermotropic nematic liquid crystal confined to toroidal droplets.

## 2.2 Nematic liquid crystals

### 2.2.1 Continuum description

From a microscopic point of view, the anisotropic constituents of nematic liquid crystals are subjected to thermal fluctuations which result in translational motions of the molecules, as in isotropic liquids, and jiggling in the orientation around the average alignment direction. From a continuum approach, we can characterize the state of the nematic liquid crystal at each point by two quantities: an apolar unit vector called the director $\hat{\mathbf{n}}$, providing the average alignment direction, and a scalar order parameter $S$ that indicates how well the liquid crystal mesogens are aligned. These values are obtained from ensemble averages over volumes around each point that are large compared to the mesogen size but very small compared to the sample size. In this case, the continuum approach is valid.

If we set the director to point in the z direction at a certain point in space, we can define the direction of the $i$-th molecule in the averaging volume by the unit vector $\hat{\mathbf{u}}^\alpha$, which forms an angle $\theta^\alpha$ with the z axis and an angle $\phi^\alpha$ with the x axis (see Figure 2.1). To define the order parameter $S$ we could initially think of using the ensemble average of the component of the mesogen in the z direction $\langle\cos(\theta^\alpha)\rangle_\alpha$. Nevertheless, due to the up-down symmetry, the number of molecules pointing in the $\theta^\alpha$ direction is the same as the ones pointing in the $\pi - \theta^\alpha$ and thus the average is zero. To account for this symmetry, we average over the square of the projection[1]. In 3D, the scalar order parameter is then given by:

$$S = \frac{3}{2}\left(\langle\cos^2(\theta^\alpha)\rangle_\alpha - \frac{1}{3}\right) \tag{2.1}$$

where the 1/3 has been subtracted from the average to make the order parameter 0 in the isotropic limit, when the orientation distribution function is uniform. The scaling factor 3/2 is added such that $S = 1$ for perfect alignment.

To mathematically describe the director, as we have defined it, we need to use a unit vector, which can be characterized by a polar ($\theta$) and an azimuthal angle ($\psi$) in spherical coordinates. This can cause mathematical problems since $\psi$ is degenerate for $\vartheta = 0$ such that the direction of the director is the same independently of the value of $\psi$; and the azimuthal angle is multi-valued since

[1] The scalar order parameter is a scalar derived from the angular distribution function of the mesogens. Higher moments of the distribution can be defined for a more complete description of the distribution function. Nevertheless, using only $S$ is enough to develop a consistent theory of liquid crystals.

$\psi = 0$ is equivalent to $\psi = 2\pi$. Moreover, the director can not be defined at topological defects, which are regions where the order parameter is equal to 0.

To solve these problems, the director and scalar order parameter can be combined into a symmetric traceless rank 2 tensor order parameter ($\bar{\bar{\mathbf{Q}}}$), such that the largest eigenvalue is $2S/3$ and corresponds to the eigenvector pointing in the director direction. The other two eigenvectors point in perpendicular directions due to the symmetry of the tensor and have an eigenvalue of $-S/3$ such that the tensor is traceless. This tensor can be expressed both in terms of an ensemble average of the mesogens orientation or, equivalently, as a function of the director and scalar order parameter as[1]:

$$\bar{\bar{\mathbf{Q}}} = \left\langle \hat{\mathbf{u}}_\mathbf{i} \otimes \ \hat{\mathbf{u}}_\mathbf{i} - \frac{1}{3}\mathbb{I} \right\rangle_i = S\left( \hat{\mathbf{n}} \otimes \ \hat{\mathbf{n}} - \frac{1}{3}\mathbb{I} \right) \tag{2.2}$$

where $\otimes$ represents the tensor product and $\mathbb{I}$ the identity rank-2 tensor. This order parameter solves the issues of the vectorial representation of the director previously discussed since the eigenvectors represent only directions without imposing a polarity and the tensor goes to zero when the sample is isotropic or at topological defects where $S = 0$, removing the singularity.

Using this tensor order parameter, DeGennes defined a phenomenological Landau free energy density to describe the isotropic-nematic phase transition as a function of temperature. This free energy is valid for temperatures close to the transition temperature. It consists on an expansion in the invariant terms of $\bar{\bar{\mathbf{Q}}}$ retaining the symmetry of the nematic liquid crystal. The result turns out to be a function of the scalar order parameter $S$:

$$\begin{aligned} f_{LdG} &= \frac{1}{2}A(T)Tr(\bar{\bar{\mathbf{Q}}}^2) + \frac{1}{3}B(T)Tr(\bar{\bar{\mathbf{Q}}}^3) + \frac{1}{4}C(T)(Tr\bar{\bar{\mathbf{Q}}}^2))^2 + O(\bar{\bar{\mathbf{Q}}}^5) \\ &= \frac{3}{4}AS^2 + \frac{1}{4}BS^3 + \frac{9}{16}CS^4 + O(S^5) \end{aligned} \tag{2.3}$$

where A, B and C are functions of the temperature that depend on the microscopic details of the material. Minimizing this expression for the proper functions A, B and C results in a first order transition in the scalar order parameter, such that $S = 0$ in the isotropic phase and $S > 0$ in the nematic phase. Deep in the nematic phase the typical value experimentally found of the order parameter is $S \sim 0.4 - 0.6$ [13] and does not change significantly with temperature.

In this work we will focus on the configurations of a nematic liquid crystal deep in the nematic phase, so we can consider that the order parameter is

[1] Alternatively, this tensor order parameter can be defined from any physical properties of the mesogens that presents the same anisotropy as the orientation.

constant and describe the configuration of our material in terms of the director field $\hat{\mathbf{n}}$ only, treating the topological defects as singularities of the field.

### 2.2.2 Elastic free energy

The nematic phase is defined by the alignment of the mesogens around the same direction in order to minimize the free energy. This, in turn, implies that the ground state of a sample, in the absence of external fields and boundary effects, corresponds to the aligned state with the director pointing in the same direction everywhere. This implies that any spatial variation of the director field $\hat{\mathbf{n}}(\vec{r})$ needs to have a free energy cost. The free energy will then depend on the director field gradients. Since the director field is unitary, the gradient vector in any direction has to be perpendicular to the director field:

$$n_i n_i = 1 \Rightarrow (\partial_j n_i) n_i = 0 \Rightarrow \hat{\mathbf{n}} \cdot \nabla \hat{\mathbf{n}} = 0 \Rightarrow \hat{\mathbf{n}} \cdot (\nabla \hat{\mathbf{n}} \cdot \hat{\mathbf{v}}) = 0 \tag{2.4}$$

where $n_i$ corresponds to the i-th component of the director, $\hat{\mathbf{v}}$ is a unitary vector, $\nabla \hat{\mathbf{n}}$ is the Jacobian matrix or gradient tensor of the director field and we have adopted Einstein summation convention. From this formula we can see that the gradient vector of the director field in any direction $\hat{\mathbf{v}}$ is perpendicular to the director. This set of 3 equations imposes 3 constrains that reduce the number of degrees of freedom of the gradient tensor from 9 to 6. If we set the director field to point in the z direction, $\hat{\mathbf{n}} = \hat{\mathbf{z}}$, equation 2.4 reduces to $\partial_i n_z = 0$ and we have the following independent gradient components:

$$\begin{cases} a_1 = \dfrac{\partial n_x}{\partial x} & a_4 = \dfrac{\partial n_y}{\partial y} \\ a_2 = -\dfrac{\partial n_y}{\partial x} & a_5 = \dfrac{\partial n_x}{\partial y} \\ a_3 = \dfrac{\partial n_x}{\partial z} & a_6 = \dfrac{\partial n_y}{\partial z} \end{cases} \tag{2.5}$$

From these gradients we can construct a free energy density expansion up to second order which is called the elastic free energy [14]:

$$f_{el} = \sum_{i=1}^{6} K_i a_i + \frac{1}{2} \sum_{i,j=1}^{6} K_{ij} a_i a_j \tag{2.6}$$

where $K$ represent the elastic constants. If we impose that the above energy must be invariant under the symmetry operations of the nematic phase, which include rotations around the director direction, reversal of the director field, and mirror reflections on a plane that contains the director direction, we end up with four independent elastic constants:

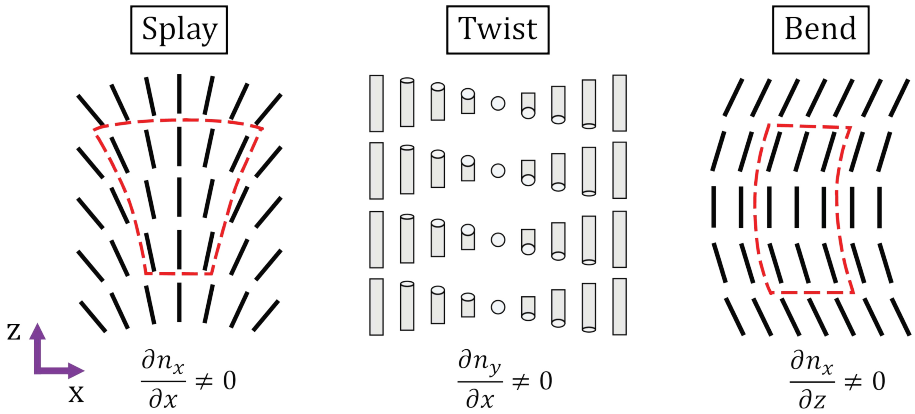



**Figure 2.2:** Schematic of the director field deformations corresponding to single splay (left), single twist (center) and bend. Below each schematic the non-zero partial derivative for each deformation where the director is pointing in the z direction. The red dashed box has its sides parallel and perpendicular to the streamlines. This shows the similarity of bending with the bending of typical beams.

$$f_{el} = \frac{1}{2}K_1(a_1 + a_4)^2 + \frac{1}{2}K_2(a_2 + a_5)^2 + \frac{1}{2}K_3(b_1^2 + b_2^2) - K_{24}(a_1a_4 + a_2a_5) \quad (2.7)$$

This can be rewritten in vector notation as:

$$\begin{aligned} f_{el} =& \frac{1}{2}K_1(\nabla \cdot \hat{\mathbf{n}})^2 + \frac{1}{2}K_2(\hat{\mathbf{n}} \cdot (\nabla \times \hat{\mathbf{n}}))^2 + \frac{1}{2}K_3|\hat{\mathbf{n}} \times (\nabla \times \hat{\mathbf{n}})|^2 \\ & - K_{24}\nabla \cdot [\hat{\mathbf{n}}\nabla \cdot \hat{\mathbf{n}} + \hat{\mathbf{n}} \times \nabla \times \hat{\mathbf{n}}] \end{aligned} \quad (2.8)$$

We have four different types of deformation associated to each independent elastic constant. The $K_1$ term is called *splay* and accounts for the divergence term, or in other words, for the deformation occurring when the gradient in a direction perpendicular to the director tilts the director in that same direction (Figure 2.2 left). The $K_2$ term is called *twist* and accounts for the rotation of the director field around a direction perpendicular to it as we move in that direction (Figure 2.2 center). The $K_3$ term is called *bend* and accounts for the gradients of the director field in the direction parallel to the director field, resulting in a configuration that reminds of the bend of beams (Figure 2.2 right). Finally, the term $K_{24}$ is called*saddle-splay* and can be expressed as a total divergence. This means that, as long as there are no singularities in the interior of the integrating volume, the total saddle-splay energy, computed as the volume integral of the

density, can be expressed as a surface integral by Gauss divergence theorem. In the presence of singularities, the integral can also be converted to a surface integral, by taking a volume that excludes the singular region of the defects. The surface integral after applying the theorem integrates over the outer boundaries and the boundaries surrounding the singularities[1].

This last term is often disregarded as a surface contribution when studying the bulk properties. Indeed, in some cases, like when the director at the surface is forced to point in a direction, it does not play any role in the equilibrium configuration. Nevertheless, it can play an important role in some systems determining the equilibrium configuration, like in toroidal droplets and cylindrical confinement [9, 10, 15, 16, 17].

Sometimes, a controversial surface term with an energy density $K_{13}\nabla \cdot [\hat{\mathbf{n}}(\nabla \cdot \hat{\mathbf{n}})]$ is added to the free energy. This term can be reduced to second derivatives and results in an unbounded free energy from below, leading to the Oldano-Barbero paradox [18]. The simplest approach to solve this paradox is to set $K_{13} = 0$, which is supported by careful experiments showing that the term is negligible [19]. We will stick to the expansion of the free energy in first derivatives of the director field and disregard higher order derivatives, since these terms do not have a significant impact on the director field configurations.

The form of the elastic free-energy becomes particularly simple when all the elastic constants have the same value $K$. This is called the one-constant approximation, since in typical nematics the elastic constants have different values but within the same order of magnitude. In this approximation, the free energy density can be expressed as:

$$f_{el} = \frac{1}{2}K\left[(\nabla \cdot \hat{\mathbf{n}})^2 + |\nabla \times \hat{\mathbf{n}}|^2\right] \tag{2.9}$$

Up to here, we have expressed the elastic free energy in terms of the director field. This form of the elastic free energy is called the Frank-Oseen elastic free energy [14, 20]. For completeness, we can also use the spatial derivatives of the tensor order parameter $\bar{\bar{\mathbf{Q}}}$ to obtain the elastic free-energy expansion. After keeping only the terms that respect the nematic symmetries we end up with the expression [21, 22, 23]:

$$f_{el} = \frac{1}{2}\left[L_1\frac{\partial Q_{ij}}{\partial x_k}\frac{\partial Q_{ij}}{\partial x_k} + L_2\frac{\partial Q_{ij}}{\partial x_j}\frac{\partial Q_{ik}}{\partial x_k} + L_3\frac{\partial Q_{ij}}{\partial x_k}\frac{\partial Q_{kj}}{\partial x_i} + L_6 Q_{ij}\frac{\partial Q_{kl}}{\partial x_i}\frac{\partial Q_{kl}}{\partial x_j}\right] \tag{2.10}$$

[1] This is the same as is typically done in electrostatics when applying Gauss theorem to charges.

where $x_k$ is the $k$-th coordinate and $L_i$ correspond to the elastic constants in this approach. By plugging equation 2.2 into the last expression we can obtain the relationship between the elastic coefficients $K_i$ and $L_i$:

$$\begin{cases} K_1 = (2L_1 + L_2 + L_3)S^2 - \frac{2}{3}L_4S^3 \\ K_2 = 2L_1S^2 - \frac{2}{3}L_4S^3 \\ K_3 = (2L_1 + L_2 + L_3)S^2 + \frac{4}{3}L_4S^3 \\ K_{24} = (2L_1 + L_3)S^2 - \frac{2}{3}L_4S^3 \end{cases} \tag{2.11}$$

Note that the $L_i$ are independent of temperature since they only depend on the molecular interactions, so the temperature dependence of the $K_i$ constants comes from the temperature dependence of the scalar order parameter $S$.

### 2.2.3 External fields

The main feature that made liquid crystals so interesting for technological applications is their ability to change their configuration when applying low magnetic or electric fields, further causing drastic changes in their optical appearance. One of the most known applications of this is liquid crystal displays, where applying an electric field on a flat sample between crossed polarizers changes the transmission of the cell. This allows the cell, in the simplest case, to switch from transparent to opaque [24, 25] making them suitable as pixels for screens.

The interaction of liquid crystals with externals field is a result of the anisotropy of the building blocks. In the case of an external magnetic field, most liquid crystals are diamagnetic materials, which means that they try to reduce the flux of magnetic field through them by generating a magnetic field in the opposite direction. Moreover, the magnetic susceptibility of the molecules, that is, their capacity to counteract the applied field, is different depending on their orientation with respect to the external magnetic field. This anisotropy can be easily understood in liquid crystals made of molecules with aromatic rings, like the nCB series. In this case, if the magnetic field is perpendicular to the aromatic ring, and thus to the molecules' orientation, the delocalized electrons of the ring generate a current around it that generates a small magnetic field opposing the external one (Figure 2.3a). If the magnetic field is parallel to the molecule orientation, the electrons do not have the mobility to generate an opposing field as large as in the previous case (Figure 2.3b).

If we now look at the bulk material, the molecules at a point of the sample are quite aligned with the director. When an external magnetic field is applied parallel/perpendicular to the director field, the molecules will on average form a small angle with the director field and their response to the external field will

be comparable to the response of a single molecule parallel/perpendicular to the field scaled by the number of molecules per unit volume. Mathematically, the effect of an external magnetic field in a material is computed by means of the magnetization $\vec{\mathbf{M}}$, which is a vector field indicating the density of induced magnetic dipoles, like the ones generated by the currents of electrons around the aromatic rings. Since the strength of the induced magnetic dipoles depends on whether the director is parallel or perpendicular to the magnetic H-field $\vec{\mathbf{H}}$, each case has a different magnetic susceptibility:

$$\begin{cases} \vec{\mathbf{M}} = \chi_{\parallel}\vec{\mathbf{H}} & \text{If } \vec{\mathbf{H}} \text{ is parallel to } \hat{\mathbf{n}} \\ \vec{\mathbf{M}} = \chi_{\perp}\vec{\mathbf{H}} & \text{If } \vec{\mathbf{H}} \text{ is perpendicular to } \hat{\mathbf{n}} \end{cases} \tag{2.12}$$

where $\chi_{\parallel}$ and $\chi_{\perp}$ are the magnetic susceptibilities in the parallel and perpendicular directions respectively. They are negative for the diamagnetic case. The magnetic field $\vec{\mathbf{B}}$ can be obtained from the magnetization and H-field via $\vec{\mathbf{B}} = \mu_0(\vec{\mathbf{H}}+\vec{\mathbf{M}})$ with $\mu_0$ the vacuum permeability. For the general case that the external magnetic field is neither parallel or perpendicular to the director, we can use a decomposition into parallel and perpendicular components to obtain the magnetization as the sum of the magnetization for both components:

$$\vec{\mathbf{M}} = \chi_{\parallel}\vec{\mathbf{H}} + (\chi_{\parallel} - \chi_{\perp})(\vec{\mathbf{H}} \cdot \hat{\mathbf{n}})\hat{\mathbf{n}} \equiv \chi_{\parallel}\vec{\mathbf{H}} + \chi_a(\vec{\mathbf{H}} \cdot \hat{\mathbf{n}})\hat{\mathbf{n}} \tag{2.13}$$

where $\chi_a$ is defined as the difference in the principal magnetic susceptibilities. Since the magnetization depends on the angle formed between the magnetic field and the director field, its energy, in general, also depends on the sample orientation. The energy per unit volume of a magnetized sample can be computed using classical electromagnetism as [26]:

$$f_m = \int_0^B \vec{\mathbf{H}} \cdot d\vec{\mathbf{B}} = \frac{1}{2\mu_0}B^2 - \int_0^B \vec{\mathbf{M}} \cdot d\vec{\mathbf{B}} \tag{2.14}$$

The usual magnetic susceptibilities for liquid crystals are very small, of the order of $\chi \sim 10^{-6}$ [1]. The magnetization is thus very small compared to the external magnetic field and the approximation $\vec{\mathbf{B}} \approx \mu_0\vec{\mathbf{H}}$ is valid. This means that the magnetic field inside the sample can be approximated by the external field applied, since the material contribution to distorting the field is very small. In this approximation, for a given magnetic field, the first term of equation 2.14 is constant and only the second depends on the orientation. The magnetic free energy can be expressed as [27]:

[1] Note we are using the magnetic anisotropy per unit volume, which is dimensionless in SI units.

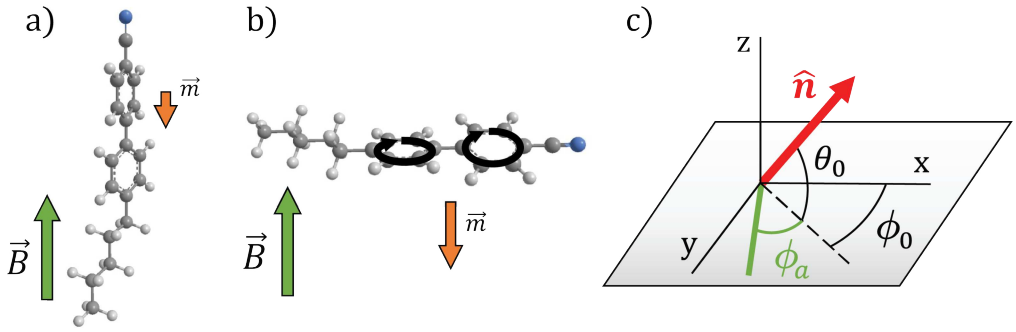



**Figure 2.3:** a) and b) Schematic of the molecular magnetic dipole ($\vec{\mathbf{m}}$) induced by a magnetic field parallel or perpendicular to the liquid crystal molecule 4-Cyano-4'-pentylbiphenyl (5CB). Dark loops show the induced electron currents responsible for a higher magnetic moment. c) Schematic of the polar coordinates and angles characterizing the director at a surface. The green line indicates the preferred in-plane orientation.

$$f_m = -\int_0^B \vec{\mathbf{M}} \cdot d\vec{\mathbf{B}} \approx -\mu_0 \int_0^H \vec{\mathbf{M}} \cdot d\vec{\mathbf{H}} = -\frac{\mu_0}{2}\chi_\perp H^2 - \frac{\mu_0}{2}\chi_a(\hat{\mathbf{n}} \cdot \vec{\mathbf{H}})^2 \quad (2.15)$$

The first term in the right hand side of the previous equation can be dropped out since is constant for a given external field, while the second depends on the relative orientation of the director and the magnetic fields through the square of the dot-product. The final magnetic free energy per unit volume can be expressed as:

$$f_m = -\frac{\mu_0}{2}\chi_a(\hat{\mathbf{n}} \cdot \vec{\mathbf{H}})^2 = -\frac{\chi_a}{2\mu_0}(\hat{\mathbf{n}} \cdot \vec{\mathbf{B}})^2 \quad (2.16)$$

From this expression we see that if $\chi_a > 0$, the minimum is obtained when $\hat{\mathbf{n}} \parallel \vec{\mathbf{B}}$ and the director will prefer to align with the external field. In this case, since $0 > \chi_\parallel > \chi_\perp$, the induced magnetization that opposes the external field is larger when the molecules are perpendicular to the external field, which increases the energy. For diamagnetic materials with negative susceptibility the orientation that minimizes the induced magnetization is, thus, preferred. If, on the other hand $\chi_a < 0$, the minimum is obtained when $\hat{\mathbf{n}} \perp \vec{\mathbf{B}}$ and the director prefers to align perpendicular to the external field. In this work, we use a liquid crystal with $\chi_a > 0$ so it will tend to align along the external magnetic field.

If instead of a magnetic field we study the case of applying an external electric field, all the above treatment remains identical but using the polarizability rather that the magnetic susceptibility. The form of the energy density is the same

with the identifications $\chi_a/\mu_0 \Leftrightarrow \epsilon_0\epsilon_a$ and $\vec{\mathbf{B}} \Leftrightarrow \vec{\mathbf{E}}$, where $\epsilon_0$ is the vacuum permittivity and $\epsilon_a$ the dielectric anisotropy. Nonetheless, in the case of electric fields, more complex phenomena can appear due to the presence of ions in the material, whose anisotropic mobility in the liquid crystal can induce flows. Electrohydrodynamic instabilities can indeed appear when applying high enough voltage in DC mode or low frequency AC mode for different reasons depending on the frequency. Increasing the frequency increases the voltage threshold for the onset of the instability, so the dielectric behavior can be recovered using a high enough frequency [28, 29]

### 2.2.4 Anchoring

All our previous discussion has been focused on the bulk free energy of nematic liquid crystals without taking into consideration the boundaries. At the boundaries, the nematogens come into contact with a different material and interact with it. This interaction indeed depends on the molecular details of the two materials and the minimization of the free energy can induce a preferred alignment of the liquid crystal at the interface. This phenomenon receives the name of anchoring. Depending on whether the preferred alignment corresponds to a single orientation, a finite set of discrete orientations or a continuous set of orientations, the anchoring is said to be monostable, multistable or degenerate [30]. Between these cases, the most common ones are monostable, like homeotropic anchoring where the nematogens prefer to align perpendicular to the surface, and degenerate, like planar degenerate anchoring where molecules prefer to align tangential to the interface with no preferred orientation inside the tangent plane.

The effect of the interface is not limited only to the orientation of the nematogens but can also affect their positional order. In fact, it has been shown that nematic liquid crystals tend to form layers of molecules at the interface, forming a smectic phase at the surface [31, 32]. As one moves inside the bulk a couple layer distances, the layering order is lost and the bulk nematic is recovered. For the purpose of our macroscopic approach, these details can be integrated into an anchoring free energy with minima for the preferred orientation of the nematic at the surface. For the monostable case, a simple quadratic form of the anchoring free energy was proposed by Rapini and Papoular [33, 34]:

$$f_a = -\frac{1}{2} W_a (\hat{\mathbf{n}} \cdot \hat{\mathbf{n}}_0)^2 \tag{2.17}$$

where $W_a$ is a constant called the anchoring strength and $\hat{\mathbf{n}}_0$ is the preferred orientation at the surface. This expression gives good results when the anchoring angle does not deviate very much from the preferred orientation. In the

homeotropic case, where the preferred direction is perpendicular to the surface, this expression reduces to:

$$f_a = -\frac{1}{2}W_a \cos^2\left(\frac{\pi}{2} - \theta_0\right) = -\frac{1}{2}W_a \sin^2(\theta_0) \tag{2.18}$$

where $\theta_0$ is the angle the director forms with the tangent plane. Expansions in higher order terms and more complete expressions for the anchoring free energy taking into account the symmetry of the substrate have been proposed. Zhao et al have proposed a two constant free energy form by an expansion on spherical harmonics of the substrate symmetry [35]:

$$f_a = W_\xi(\hat{\mathbf{n}} \cdot \hat{\xi})^2 + W_\eta(\hat{\mathbf{n}} \cdot \hat{\eta})^2 \tag{2.19}$$

where $\hat{\mathbf{n}}_0$, $\hat{\xi}$ and $\hat{\eta}$ form an orthonormal triad. For the case of unidirectional planar anchoring, using the polar coordinates shown in Figure 2.3c, this expression reduces to:

$$f_a = W_\theta \sin^2(\theta_0) + W_\phi \cos^2(\theta_0)\cos^2(\phi_0 - \phi_a) \tag{2.20}$$

where $W_\theta$ and $W_\phi$ are the polar and azimuthal anchoring strengths respectively, $\theta_0$ and $\phi_0$ are the polar and azimuthal angles of the director at the surface and $\phi_a$ is the preferred azimuthal orientation. In the case of degenerate planar anchoring, $W_\phi = 0$ and we only need the polar anchoring strength. By taking out constant terms and redefining the anchoring constants, we can get an expression similar to the Rapini-Papoular one for homeotropic alignment (Equation 2.18):

$$f_a = -\frac{1}{2}W_a \cos^2(\theta_0) \tag{2.21}$$

We will use equations 2.18 and 2.21 to describe the anchoring free energy for the homeotropic and planar degenerate case.

To impose the desired boundary conditions different strategies have been developed. In the case of an interface with a solid surface, like the glass used in liquid crystal cells, one of the more common ways to impose the anchoring is to either physically rub or modify the substrate topology, deposit a thin layer of polymer on the glass (with the option of rubbing it to favor an orientation) or covalently bond molecules at the surface [36, 37, 38]. In this way, planar anchoring (degenerate or uniaxial) and homeotropic anchoring can easily be imposed. Nevertheless, the anchoring strength is typically fixed and changing it is not straightforward. When the liquid crystal forms an interface with an immiscible fluid, like water for liquid crystals based on organic molecules, the anchoring conditions can be tuned by the presence of suitable surfactants that adsorb on the surface [39, 40]. In this way, both types of anchoring, planar and homeotropic, can be obtained by using different surfactants, and the anchoring

strength can be tuned by means of the concentration of surfactant, even allowing for the transition between different types of anchoring [41, 42].

### 2.2.5 Free energy minimization

We can now express the total free energy of the nematic liquid crystal as the sum of the elastic, magnetic and anchoring contributions. Although for a more general treatment the Landau-de Gennes free energy should be taken into account, since we are far from the phase transition, we can safely assume that the order parameter $S$ is constant and thus the Frank-Oseen description suffices. The total free energy can be obtained by integrating the total free energy density over the sample. This results in a sum of volume and surface integrals:

$$F = \iiint_V f_b\left(n_i, \frac{\partial n_i}{\partial x_j}\right) dV + \iint_S f_s\left(n_i, \frac{\partial n_i}{\partial x_j}\right) dS \tag{2.22}$$

where $f_b$ and $f_s$ are the bulk contributions that depend on the director field and its first derivatives:

$$\begin{cases} f_b = \frac{1}{2}K_1(\nabla \cdot \hat{\mathbf{n}})^2 + \frac{1}{2}K_2(\hat{\mathbf{n}} \cdot (\nabla \times \hat{\mathbf{n}}))^2 + \frac{1}{2}K_3|\hat{\mathbf{n}} \times (\nabla \times \hat{\mathbf{n}})|^2 + f_m \\ f_s = f_a - K_{24}\hat{\mathbf{v}} \cdot (\hat{\mathbf{n}}\nabla \cdot \hat{\mathbf{n}} + \hat{\mathbf{n}} \times \nabla \times \hat{\mathbf{n}}) \end{cases} \tag{2.23}$$

The bulk part $f_b$ corresponds to the splay, bend and twist contributions of the elastic free energy plus the magnetic free energy. The surface part $f_s$ corresponds to the anchoring energy and the saddle-splay term of the elastic free energy where Gauss-theorem has been applied assuming there are no singularities in the volume and $\hat{\mathbf{v}}$ is a normal vector to the surface pointing outwards.

The ground equilibrium configuration of the director can be obtained by minimizing the total free energy in equation 2.22. Since we have a bulk and a surface term, this can be done by minimizing first the bulk term to obtain a family of functions that are local minima [43]. The volume integral has to be minimized under the constraint that the director field is unitary: $n_i n_i = 1$. We can define the Lagrangian as the integrand of the volume integrand plus a Lagrange multiplier to ensure the normalization condition:

$$\mathcal{L}\left(n_i, \frac{\partial n_i}{\partial x_j}, \lambda\right) = f_b\left(n_i, \frac{\partial n_i}{\partial x_j}\right) + \lambda(n_i n_i - 1) \tag{2.24}$$

Since the Lagrangian only depends on the functions $n_i$, their first derivatives $\partial n_i/\partial x_j$ and $\lambda$, the director field that minimizes the integral is obtained from the Euler-Lagrange equations for a Lagrangian of several functions of several variables with single derivatives [27, 44]:

$$\begin{cases} \dfrac{\partial \mathcal{L}}{\partial n_i} - \displaystyle\sum_{j=1}^{3} \frac{\partial}{\partial x_j}\left(\frac{\partial \mathcal{L}}{\partial n_{i,j}}\right) = 0 \\ n_i n_i = 1 \end{cases} \tag{2.25}$$

where $n_{i,j} \equiv \partial n_i / \partial x_j$. This results in a set of four partial differential equations whose solutions correspond to local minima of the director field with different boundary conditions.

If instead of using the Cartesian components of the director, we describe the director orientation in spherical coordinates in terms of polar $\theta$ and azimuthal $\phi$ angles, the normalization conditions is automatically fulfilled, so the Lagrange multiplier is not needed and the Euler-Lagrange equations become:

$$\begin{cases} \dfrac{\partial \mathcal{L}}{\partial \theta} - \displaystyle\sum_{j=1}^{3} \frac{\partial}{\partial x_j}\left(\frac{\partial \mathcal{L}}{\partial \theta_{i,j}}\right) = 0 \\ \dfrac{\partial \mathcal{L}}{\partial \phi} - \displaystyle\sum_{j=1}^{3} \frac{\partial}{\partial x_j}\left(\frac{\partial \mathcal{L}}{\partial \phi_{i,j}}\right) = 0 \end{cases} \tag{2.26}$$

In this case, we get two partial differential equations that might be easier to solve. Nevertheless, problems with the description of the director field in terms of two angles can lead to problems in the solution of the equation for some cases [43].

With the family of solutions of the partial differential equations, the actual solution that minimizes the energy depends on the boundary conditions. If the anchoring conditions are fixed (infinite anchoring strength) the minimum is obtained by choosing the function that fulfills the boundary conditions. In the case of finite anchoring, the solution is obtained by computing the sum of the bulk and surface energy of the family of solutions and minimize this energy to obtain the final solution.

As a simple example, we take the case of a 2D director field in the one constant approximation and with no external field applied. We describe the director field by the angle $\theta(x, z)$ it makes with the vertical direction $\hat{z}$. The director field is expressed as:

$$\hat{\mathbf{n}} = (\sin\theta, 0, \cos\theta) \tag{2.27}$$

The bulk energy becomes:

$$F_b = \frac{1}{2} K \iiint_V \left[ \left(\frac{\partial \theta}{\partial x}\right)^2 + \left(\frac{\partial \theta}{\partial z}\right)^2 \right] dV' \tag{2.28}$$

Since the normalization condition is fulfilled, the Lagrangian corresponds to the integrand:

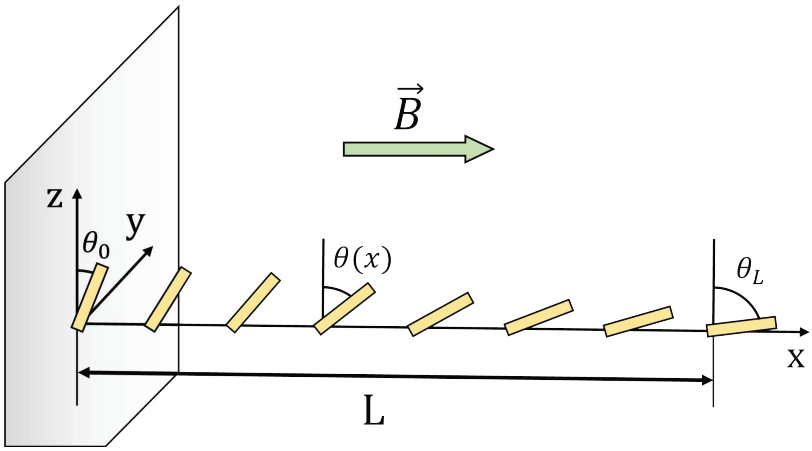



**Figure 2.4:** Schematic of the nematic liquid crystal model system to theoretically study competition between energy terms. $\theta(x)$ is the angle between the director at position x and the vertical position z.

$$\mathcal{L} = \left(\frac{\partial\theta}{\partial x}\right)^2 + \left(\frac{\partial\theta}{\partial z}\right)^2 \tag{2.29}$$

Plugging the Lagrangian into equation 2.26, we get the differential equation:

$$\frac{\partial^2\theta}{\partial x^2} + \frac{\partial^2\theta}{\partial z^2} \equiv \Delta\theta = 0 \tag{2.30}$$

The minimization problem shows that any possible solution $\theta(x, z)$ needs to fulfill Laplace's equation. The exact solution for each problem is set by the boundary conditions.

### 2.2.6 Competing effects of anchoring alignment and magnetic fields

As we have seen, there are three sources of free energy for a nematic liquid crystal. The elastic part, that tends to make it align everywhere, the magnetic part, which for the case of $\chi_a > 0$ tends to align the director field with the magnetic field, and the anchoring part which tries to impose a preferred alignment at the boundaries. The preferred alignment for each component of the free-energy can be different, leading to a competition between effects.

Studying this competition can give us more physical insight into the director field configuration. Following [27] we will imagine a simple system, where we assume that the liquid crystal fills half the space, with a flat boundary at $x = 0$

that imposes a planar alignment. The director field is 2D and points in a direction within the $x$-$z$ plane characterized by the angle it makes with the surface $\theta(x)$ which, by symmetry, only depends on the distance to the boundary. We will also use the one constant approximation for the elastic free energy and assume a uniform magnetic field $\vec{\mathbf{B}} = \mathrm{B}\hat{\mathbf{x}}$. A schematic of the system is shown in Figure 2.4.

In this case, the total free energy per unit area of the system becomes:

$$\frac{F_t}{A} = \int_0^\infty \left[\frac{1}{2}K\left(\frac{\partial\theta}{\partial x}\right)^2 - \frac{\chi_a}{2\mu_0}B^2\sin^2\theta\right]dx - \frac{1}{2}W_a\cos^2(\theta(0)) \tag{2.31}$$

The Euler-Lagrange minimization of the bulk part results in the differential equation:

$$K\frac{\partial^2\theta}{\partial x^2} + \frac{\chi_a}{\mu_0}B^2\sin\theta\cos\theta = 0 \tag{2.32}$$

#### 2.2.6.1 Infinite anchoring strength: Transition layer thickness

When we apply a constant external magnetic field in a nematic liquid crystal with positive $\chi_a$, the director will reduce its energy by aligning with the external field. If the boundaries do not impose any alignment the minimum energy configuration corresponds to the director aligned with the external field. In the absence of a magnetic field, if the liquid crystal has a flat surface that favors a given alignment, the minimum energy of the system corresponds to the system aligned in the direction preferred by the boundary.

Since both the magnetic field and anchoring want to align the director field in a certain direction, when both directions differ there will be a competition effect between the two. This is the case presented in Figure 2.4 where the magnetic field points perpendicular to the surface while the anchoring favors the planar orientation.

If we assume an infinite anchoring strength, the boundary condition is fixed to $\theta(0) = 0$. Far from the surface we can assume that the anchoring does not have a significant effect and assume the director can align with the external magnetic field giving the second boundary condition $\theta(\infty) = \pi/2$. The equilibrium configuration is obtained by solving equation 2.32 and applying both boundary conditions[1]:

$$\theta(x) = \frac{\pi}{2} - 2\arctan\left(e^{-\frac{x}{\xi_m}}\right) \tag{2.33}$$

[1]If the equation is multiplied by $\partial\theta/\partial x$, it becomes a total derivative and it can be solved by integrating twice and imposing the boundary conditions.

where $\xi_m \equiv \frac{\sqrt{\mu_0 K/\chi_a}}{B}$ is called the transition layer thickness and has units of length. We can see that for $x \gg \xi_m$ the angle becomes $\theta(x) \approx \pi/2$ so the director field becomes aligned with the external magnetic field. For $x \lesssim \xi_m$, the angle transitions from aligned with the wall to aligned with the magnetic field. The transition layer thickness $\xi_m$ can be understood as the thickness of the layer where the anchoring conditions affects the director field configuration. For larger distances from the surface, the surface does not play a role and the director field aligns with the external magnetic field.

#### 2.2.6.2 Elastic and anchoring competition: Extrapolation length

If instead of assuming infinite anchoring strength the anchoring is finite, the director field at the interface $\theta(0)$ can deviate significantly from the preferred orientation under suitable conditions, like a high elastic torque that can be obtained by fixing the director field angle at a distance L from the surface to the value $\theta(L) = \theta_L \neq 0$.

In this case, there is no external magnetic field so the Euler-Lagrange equation becomes:

$$\frac{\partial^2 \theta}{\partial x^2} = 0 \tag{2.34}$$

which results in a linear profile of the angle $\theta$:

$$\theta(x) = C_1 x + C_2 = \frac{\partial \theta}{\partial x} x + C_2 \tag{2.35}$$

By imposing the boundary condition $\theta(L) = \theta_L$ the solution, as a function of the angle at the surface $\theta(0)$, becomes:

$$\theta(x) = \frac{\theta_L - \theta(0)}{L} x + \theta(0) \tag{2.36}$$

To determine the angle at the boundary of the equilibrium configuration $\theta(0)$, we compute the total free energy including the anchoring term:

$$\frac{F_t}{A} = \frac{K}{2L} \left( \frac{\theta_L - \theta(0)}{L} \right)^2 - \frac{1}{2} W_a \cos^2(\theta(0)) \tag{2.37}$$

We can obtain $\theta(0)$ by minimizing the previous energy as a function of this angle. Imposing that the derivative of the free energy with respect $\theta(0)$ is zero results in the equation:

$$\frac{K}{W_a} \frac{\theta_L - \theta(0)}{L} - \frac{1}{2} \sin(2\theta(0)) \approx b \frac{\partial \theta}{\partial x} - \theta(0) = 0 \tag{2.38}$$

Where in the last approximation we have assumed that the director deviation at the surface is small $\theta(0) \ll 1$ and we have defined $b \equiv K/W_a$. In this approximation the angle at the surface becomes:

$$\theta(0) = b\frac{\partial\theta}{\partial x} \tag{2.39}$$

The angle at the surface depends on the gradient of the director. The larger the gradient, the larger the elastic torque to recover the uniform alignment $\theta = \theta_L$ and the more the director deviates at the surface from the preferred orientation. The proportionality constant $b$ has units of length and is called the extrapolation length. In the strong anchoring limit, $W_a \to \infty$ and $b \to 0$ so that the anchoring is able to keep the director orientation at the boundary fixed to $\theta(0) = 0$. By contrast, in the limit of infinite elastic constant, $K \to \infty$ and thus $b \to \infty$; any small gradient in the director field is able to significantly change the director orientation at the boundary.

The meaning of $b$ can be further understood by finding the conditions for the angle at the surface given by equation 2.39 to be significantly different from the preferred direction. Setting $\theta(0) \sim 1$, we then find:

$$b \sim \frac{1}{\frac{\partial\theta}{\partial x}} \sim \frac{\Delta x}{\Delta\theta} \tag{2.40}$$

where the $\Delta$ in the right term indicates finite difference. From this equation, the extrapolation length can be defined as the length where a unit change in the angle of the director produces a high enough torque to significantly deviate the director at the surface $\theta(0) \sim 1$. Alternatively, it can be seen as the inverse of the gradient in the director that is able to overcome the anchoring strength and deviate the director from the preferred orientation.

#### 2.2.6.3 Anchoring breakdown: Critical field

We have just seen that elastic torques produced by director gradients can break the anchoring preferred alignment. Nevertheless, fixing the director direction at a position is hard to realize experimentally. A simpler approach consists on to applying a magnetic field that tends to align the sample everywhere. For small magnetic fields, the anchoring strength will be able to keep the director field aligned at the boundary, while a high enough magnetic field should be able to break the anchoring conditions.

To compute this critical magnetic field that makes the director deviate significantly from the preferred alignment, we have seen in equation 2.40 that the necessary director field gradient at the surface to break the anchoring conditions

is $1/b$. In the case of infinite anchoring strength, we can compute the director gradient at the surface from equation 2.33 resulting in $1/\xi_m$.

When the anchoring conditions are finite, the value of the critical magnetic field $B_c$ that gives a high enough elastic torque at the surface to break the anchoring conditions is obtained from equating both torques:

$$\begin{aligned} \frac{1}{b} &\approx \frac{1}{\xi_m} \\ B_c &\approx W_a \sqrt{\frac{\mu_0}{\chi_a K}} \end{aligned} \tag{2.41}$$

This means that, if the anchoring is finite, magnetic fields equal or larger to $B_c$, are able to break the anchoring conditions such that the whole sample aligns with the external field.

The computation of the transition layer thickness, extrapolation length and critical magnetic field allows understanding the relevant parameters determining the director field configuration. Although the one constant approximation is used, these expressions can still be used using the relevant elastic constant associated to the configuration of the material.

## 2.3 Topological defects

In general, nematic liquid crystals reduce their free energy by aligning into the same direction in a homogeneous configuration. If we take our material and start with a random configuration of the director field, we could expect it will continuously relax towards the homogeneous ground state to minimize its free energy. Nevertheless, this is not always possible, and some initial configurations can not continuously transform into the homogeneous state. This forces a configuration with a higher elastic free energy that can not relax into the uniform state. More interestingly, two different configurations that can not continuously transform into the uniform configuration might not be able to continuously transform into each other, allowing us to classify all the possible configurations into disjoint groups of configurations that can be transformed into each other.

These configurations, in general, revolve around the so called topological defects and can be singular or non singular depending on whether the director field has mathematical singularities or not. In this case, the term topological refers to the fact that these singularities can not be continuously removed. We will focus mainly in the case where the director field has singularities. Continuous transformations of the director field can move the singularities around but these cannot be taken out of the sample. As we will see, annihilation of individual defects can not happen, but annihilation between two defects can occur.

When dealing with singularities in a director field, we can classify them according to the dimensionality of their singular core into: point defects (0D), line defects (1D) and walls (2D).

### 2.3.1 Point defects and boojums

Point defects in nematic liquid crystals have been well-known and identified long ago. Nevertheless, the nature of the defects is very different depending on whether we have a 2D system or consider 3D space, where the first case is significantly simpler and easier to visualize.

#### 2.3.1.1 Point defects in 2D

In the 2D case, the orientation of the director field can be defined by a single angle $\theta(x, y)$ and the order parameter space of the director, this is, the space of all possible different orientations, is the projective space $\mathbb{SP}^1$ [45], corresponding to the unit circle with antipodal points identified. The antipodal points of the circle of possible orientations are identified due to the inversion symmetry of the director.

The different topological defects can be classified according to their winding number, which is defined as the number of whole revolutions that the director makes as we go around a loop surrounding only the singularity of interest. Since the director field as we go around the loop has to return to the same orientation, by continuity, the winding number is a half-integer[1] with the sign determined by the rotation sense. If the director rotates in the same/opposite sense of the rotation around the circuit we use to compute the winding number, the defect is defined as positive/negative. Mathematically it can be expressed as [45]:

$$s = \frac{1}{2\pi} \oint_l (\nabla\theta) \cdot d\vec{\mathbf{l}} \tag{2.42}$$

where $d\vec{\mathbf{l}}$ is the differential tangent vector of the loop circuit. The winding number topologically classifies point defects into classes so any two point defects with the same winding number can be continuously transformed into each other, while point defects with different winding numbers can not. The winding number is also called the topological charge of the defect, since it is preserved under continuous deformations. Minimizing the elastic free energy for a point defect of charge $s$ located at the origin $\vec{\mathbf{r}} = 0$ in the one constant approximation results in the director field given by the angle function [27]:

[1] We will use the term half-integers to designate the group formed by dividing all the integers by 2, which include integers and fractions with a denominator of 2.

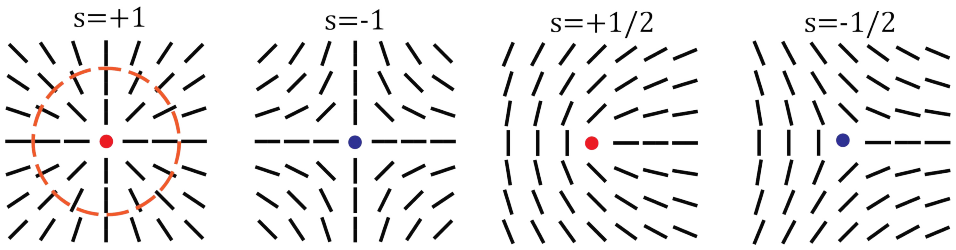



**Figure 2.5:** Examples of director field configuration of 2D point defects with different topological charge $s$. The dashed orange circle represents a contour around the defect that can be used to compute the winding number.

$$\theta(\vec{\mathbf{r}}) = s\phi(\vec{\mathbf{r}}) + C \tag{2.43}$$

where $\phi$ is the position angle in polar coordinates and $C$ is a constant. Since $\phi(0)$ is not defined, the director field presents a discontinuity at the origin. An example of the director field for point defects with $s = -1/2, +1/2, -1$ and $+1$ is shown in Figure 2.5. We can now compute the elastic energy corresponding to a point defect of charge $s$ in a sample of size $R$:

$$F_e = \frac{1}{2}K \iint_S |\nabla\theta|^2 dS = \pi K \int_a^R \frac{s^2}{\rho^2} d\rho = \pi K s^2 \ln\left(\frac{R}{a}\right) \tag{2.44}$$

where $a$ is a cutoff length to avoid the divergence of the integral, physically corresponding to the core size where the liquid crystal is not nematic anymore. To compute the total energy of the configuration, another term accounting for the free energy of the core region should be added. Nevertheless, for large enough samples, this term becomes negligible compared to the elastic free energy. The free energy of the defect then goes as $s^2$ so that if the topological charge is doubled, the total energy increases four times. This means that low topological charge defects will be energetically preferred.

When having several topological defects in the same sample, the general procedure for establishing the topological charge of each of them is making loops around the defect cores that pass through the same point, in a sort of bouquet of loops, and compute the winding number over those loops [46]. This is the so called common point construction for consistently computing topological charges. Nevertheless, in the 2D case, it can be shown that the topological charge of the individual defects remains the same and is well defined by using loops surrounding the individual defects, without the need of the common point. Moreover, if we make a loop surrounding several defects, the total topological charge of the configuration inside the loop is the sum of the charges of the individual defects. This means that the configuration of several point defects can be

continuously transformed into a configuration with only one defect with charge equal to the sum of the charges. This implies that defects of opposite charge can annihilate resulting in the uniform configuration and that point defects of large charge can break into several defects with smaller charges. Indeed, this is energetically preferred since a $+1$ defect that breaks into two $+1/2$ reduces its energy in half.

The great conceptual advantages of the 2D case is that we can understand a system of point defects like a system of particles with a topologically invariant charge that can move around and interact elastically which each other. Indeed, the interaction between point defects is identical to the one of a Coulomb gas and defects with opposite charges attract each other potentially annihilating, while defects with sign-like charges repel. Furthermore, defects with large topological charge can split into defects with smaller charges.

#### 2.3.1.2 Point defects in 3D

In the 3D case, the director can point in any direction of space. The parameter order space is the projective space $\mathbb{RP}^2$ corresponding the unit sphere with antipodal points identified. In a similar way to the 2D case, we can compute the topological charge of the director field by taking a spherical surface that surrounds the defect and evaluate how many times the sphere in the order parameter space is covered [45, 47]:

$$s = \frac{1}{4\pi} \oiint_S \hat{\mathbf{n}} \cdot \left( \frac{\partial \hat{\mathbf{n}}}{\partial u} \times \frac{\partial \hat{\mathbf{n}}}{\partial v} \right) \mathrm{dudv} \tag{2.45}$$

where $(u, v)$ are local coordinates of the surface. While in two dimensions, the classification was simple, in the case 3D case there are some subtleties. The possible values of the topological charge in this case are the integers $\mathbb{Z}$. Nevertheless, we can see that the previous integral is odd in $\hat{\mathbf{n}}$, so that the integral changes sign under the inversion $\hat{\mathbf{n}} \to -\hat{\mathbf{n}}$ that represents the same system. The previous definition thus has a sign ambiguity, since the same defect can have both charges depending on the vectorial definition chosen of the director field $\hat{\mathbf{n}}$. Point defects with opposite charge can be converted continuously into one another[1] and are therefore topologically equivalent.

In general, point defects in 3D are characterized by positive integers, without any sign consideration. This ambiguity of the sign is also a consequence of the fact that the combination of two defects with charge $n$ and $m$ is not equivalent to a defect $n + m$ but, depending on how the defects are brought together, can result in an $n + m$ or $|n - m|$ point defect [46]. In a system of several

[1] This can be demonstrated by moving a defect around a disclination line or rotating the director field around a given axis by $\pi$.

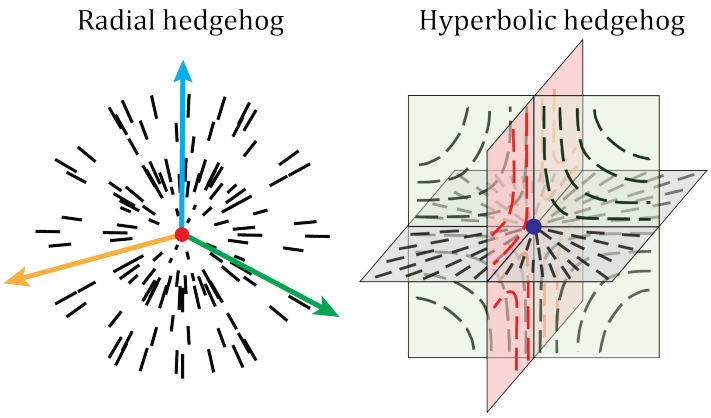



**Figure 2.6:** Radial and hyperbolic hedgehogs configurations. Both configurations have rotational symmetry around the vertical axis. For the hyperbolic hedgehog, the director field in three perpendicular planes is shown. The gray plane has the configuration of a two dimensional +1 defect, while the perpendicular planes (green and red) have the configuration of a two dimensional −1 defect.

point defects without defect lines, the relative sign of the charge between point defects can be defined by using the common point construction such that every ball surrounding each point defect goes through a common point forming a "bouquet" of balls.

Point defects with a topological charge of 1 have been traditionally classified into two basic configurations: Radial hedgehogs where the director points in the radial direction (Figure 2.6 left) and hyperbolic hedgehogs that have a plane with the director in the radial configuration of a +1 two dimensional defect, and all the perpendicular planes to that one have a director field with the hyperbolic configuration of a −1 two dimensional defect (Figure 2.6 right). When having a system with a radial and an hyperbolic hedgehog, the common point construction shows that they have opposite topological charge so, traditionally, the $+1/-1$ charge is assigned to the radial/hyperbolic hedgehog respectively.

As for 2D nematics, the higher the topological charge, the higher the elastic distortion around them and the higher the total free energy cost, which grows as $s^2$. We can then expect to observe mainly point defects with the lowest possible charge of 1. Moreover, when a surface is present, the defect can reduce its energy by moving to the surface. In this way, there is only half of the configuration of the defect in the liquid crystal and its energy cost is reduced by half. Point defects located on the surface of a liquid crystal samples are called boojums.

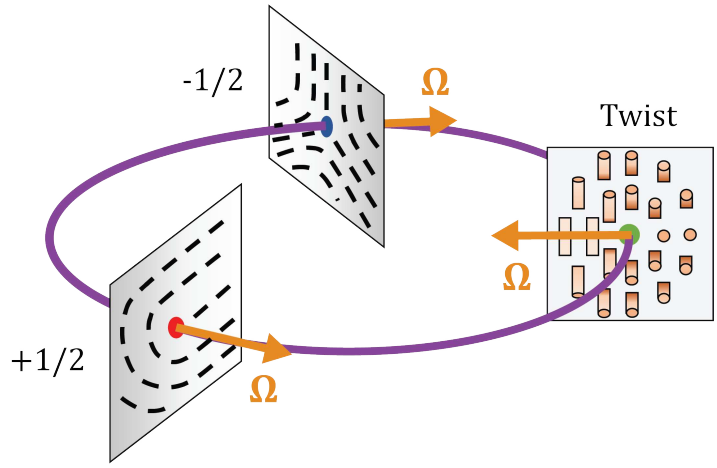



**Figure 2.7:** Schematic of a disclination loop showing the director field in three cross-sections. The two cross-sections on the left part show the configuration of $+1/2$ and $-1/2$ wedge disclinations where the director field lies in the cross-section plane. The right cross-section shows the configuration of a twist disclination. These three configurations are homotopic to each other and can be continuously transformed into each other, making it possible for the three of them to appear in the same loop. Orange arrows indicate the rotation axis $\mathbf{\Omega}$ at each cross-section.

### 2.3.2 Line defects

If instead of having a singularity in a single point in space, the singular core spans a line, we have a disclination line. When characterizing the director field around a line it is natural to study what happens to the cross-sections at different points of the line. If the director field lies tangent to the cross-section plane, the case reduces to 2D point defects where topological defects can be classified by their winding number.

In 3D space, however, the director field can point in any direction of space and point out of the cross-section. We can still classify the lines by taking a circuit that surrounds the disclination and measure the winding number of the director field. We can still define the winding number as the number of full rotations the director makes when going once around the disclination which, by continuity, must be a half-integer. The sign of the winding number, though, does not have a physical meaning anymore, since the director can rotate around any axis perpendicular to it. Thus, to describe the disclination configuration around a point of the disclination line we can use the winding number, also called strength of the disclination, and the rotation axis $\mathbf{\Omega}$ [27].

Another interesting result of characterizing the 3D director field around a loop surrounding the disclination is that all of the configurations with the same

strength are topologically equivalent, meaning that they can be continuously transformed into each other. This means, that as we move along the disclination line, the rotation axis $\mathbf{\Omega}$ can continuously change, as shown in Figure 2.7. The absolute value of the winding number, in contrast, must be preserved by continuity within nearby cross-sections[1]. This implies that a configuration corresponding to a $+1/2$ 2D defect at a point of the disclination can be converted to a $-1/2$ at a different point.

In the case of integer strength disclinations, it can be shown that the singularity can be continuously removed by escaping in the third dimension. This is specially illustrated in the case of a $+1$ radial defect where the singularity can be removed at the center by taking the director out of the plane as we get closer to the singularity making it point perpendicular to the plane right at the center. This way, integer strength disclination lines can always be removed[2]. Moreover, for this same reason, any higher non-integer winding number is topologically equivalent and can be continuously converted into a configuration with a $1/2$ winding number. As a result, there are only two topologically different types of disclinations, necessarily singular ones with a $1/2$ strength and non-singular or singular ones but removable with 0 strength.

Finally, $1/2$ disclination lines can not have an endpoint inside the liquid crystal, they either have their ends at the boundary as 2D defects, or form closed loops. This is a consequence of the continuity of the director field between nearby cross-sections, such that the strength is preserved and thus a singularity must exist.

### 2.3.3 Alignment inversion walls

If the singular core region spans a surface, we have a singular wall. In this case there is a discontinuity of the director field across in a plane, as schematically shown in Figure 2.8a. As pointed out by DeGennes [27] singular walls are not stable, since they can split into disclination lines reducing the energy or continuously remove the singularity. The singularity indeed can be removed by making the director point in the vertical direction at the wall[3] as shown in Figure 2.8b. In this case, we get an alignment inversion wall, where, as we go across the wall, the director rotates by $\pi$. When there are no singularities, we can define the wall center location as the set of points where the director field

[1] This can be seen in an easier way if we interpret the loop cross-sections as a time evolution of the director field with the time been represented by the exact position on the disclination.

[2] This is indeed a consequence of the fact that you can not "lasso a ball". this is, any close circuit in the order parameter space can shrink to a point. The non-removable disclination lines start and end in antipodal points.

[3] Alternatively the singularity can be removed by making the director field point horizontal at the wall resulting directly in the uniform configuration.

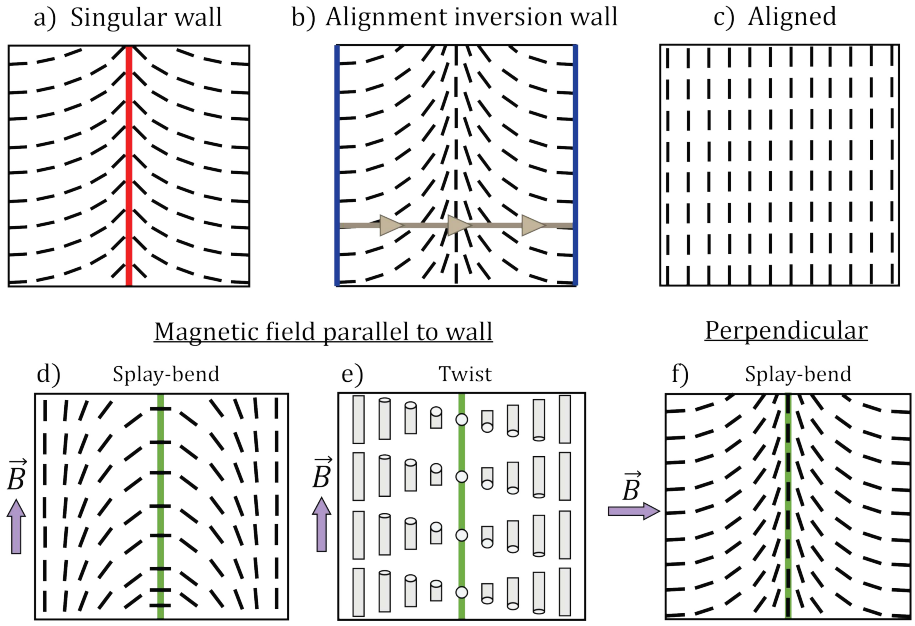



**Figure 2.8:** a) Schematic of a cross-section of a singular wall. Red line indicates the singular region b) Previous wall with the singularity removed by the alignment of the director in the vertical direction at the wall position. Blue lines indicate the boundaries at each side of the wall and the gray arrow corresponds to a path going from one boundary to the other through the wall. c) Uniform configuration obtained from a vertical alignment of the inversion wall in b). d)-f) Different types of alignment inversion walls described by Helfrich. Green line indicates the wall position where the director is perpendicular to the orientation far from the wall. d) and e) Inversion walls types with magnetic field parallel to the wall: Splay-Bend and twist walls respectively. f) Splay-bend wall with magnetic field perpendicular to the wall.

is perpendicular to the boundary condition.

These alignment inversion walls can deform continuously into the uniform configuration, as can be seen by aligning vertically the director field in the previous case (Figure 2.8c). It is worth noting that the transition to the uniform configuration requires the rotation of the director field far from the wall. Hence, if the boundary conditions are fixed at both sides of the alignment inversion wall, as shown in Figure 2.8b, the inversion wall is topologically protected and can not be unwinded by continuous deformations while keeping the boundary conditions fixed. For our nematic liquid crystals this effect can be achieved by applying a uniform external magnetic field parallel to the director at the boundaries. If the field is high enough, this will effectively fix the orientation of

the director at the boundaries and any alignment inversion wall of the sample can not be removed.

To understand why the alignment inversion wall can not be removed, we can take the configuration on a line going from one boundary to the other crossing the wall as shown in Figure 2.8b. The director field at each boundary points in the same direction, so we have a 3D director field in a line with periodic boundary conditions which is equivalent to a loop around a disclination. This has further consequences in the sense that all the possible configurations are either topologically equivalent to the uniform configuration (integer number of turns when going from one boundary to the other) or to an alignment inversion wall with $\pi$ rotation (equivalent to the 1/2 disclination case).

In the simplest case where the inversion wall forms a flat plane and the director field only varies along the perpendicular direction to this wall, a simple classification was given by Helfrich [48]. He distinguished between three types of walls depending on the main type of elastic deformations involved and whether the magnetic field direction, corresponding to the director field direction at the boundaries, is parallel or perpendicular to the wall plane. When the magnetic field is parallel to the wall, he defined two walls depending on the main elastic deformation. The splay-bend wall (Figure 2.8d) where the director field lies in the plane formed by the magnetic field and the normal to the wall, and the twist wall (Figure 2.8e) where the director field rotates around the normal to the wall. When the magnetic field is perpendicular to the wall, there is only one type, the splay-bend wall (Figure 2.8f). The differences in the splay-bend walls when the magnetic field is parallel and perpendicular to the wall is that in the first case, the relevant deformation is splay far from the wall and bend at the wall position, while in the second case, bend is important far from the wall and splay near the wall.

These alignment walls are localized in the sense that the distortion of the director field is concentrated in a region of space. Indeed, the external magnetic field wants to align the director parallel to it, which is not possible everywhere due to the $\pi$ rotation of the wall. The magnetic field will try to make the region where the director rotates as small as possible, while the elastic deformation will prefer to expand it. The balance between the elastic and magnetic effects results in a finite wall width ($\eta$) that depends on the magnitude of the magnetic field $B$. The width of the wall can be defined, for example, as the distance between the points that form a 45° angle with the magnetic field [48]. We can show, without the need to explicitely minimize the energy, that $\eta \propto 1/B$.

Let's imagine that, for a given magnetic field $B$, we know the solution $\hat{\mathbf{n}}(x)$ that minimizes the free energy. The total free energy can be computed as:

$$F = \int_{-\infty}^{\infty} \left[ f_{el} + B^2 f_{1m} \right] dx \tag{2.46}$$

where $f_{el}$ is the elastic energy with different elastic constants and we have defined $f_{1m}$ as the magnetic free energy density resulting from an external field of $B = 1T$, where we assume SI units, so that $B^2 f_{1m}$ is the magnetic free energy density. Now we study what happens if we "expand" the wall by a factor $\alpha$. In this case the new director field is defined by $\hat{\mathbf{n}}'(x) = \hat{\mathbf{n}}(x/\alpha)$ and the new wall width is $\eta' = \alpha\eta$. If we want to compute the new elastic energy, we have to take into account that the elastic energy in general is a quadratic form of the first derivatives as shown in equation 2.7. The first derivative of the expanded wall is related the first derivative of the original wall as:

$$\frac{\partial \hat{\mathbf{n}}'(x)}{\partial x} = \frac{\partial \hat{\mathbf{n}}(x/\alpha)}{\partial x} = \frac{1}{\alpha}\frac{\partial \hat{\mathbf{n}}(y)}{\partial y} \tag{2.47}$$

where $y = x/\alpha$. The elastic free energy density of the new configuration can be expressed as a function of the original elastic free energy as: $f'_{el} = f_{el}/\alpha^2$, where the $\alpha^2$ term appears from the multiplication of pairs of derivatives from the quadratic form. Since the magnetic free energy does not depend on the derivatives, the magnetic free energy of the new configuration can be expressed as $B'^2 f_{1m}$. The total energy of the expanded wall becomes:

$$F = \int_{-\infty}^{\infty} \left[\frac{1}{\alpha^2} f_{el} + B'^2 f_{1m}\right] dx \propto \int_{-\infty}^{\infty} \left[f_{el} + \alpha^2 B'^2 f_{1m}\right] dy \tag{2.48}$$

where in the last step we have used the change of variables $y = x/\alpha$, and taken out of the integral the multiplicative factor $1/\alpha$ that does not affect the equilibrium configuration. The free energy of the expanded wall is expressed as a function of the original solution of the director field $\hat{\mathbf{n}}(y)$ and its first derivatives. The integrand of the free energy is very similar to the one the original director field minimizes 2.46. Comparing both integrands, the previous integral is minimized by the original solution when $\alpha^2 B'^2 = B^2$. This in turns means that the expanded wall with width $\eta' = \alpha\eta$ corresponds to the equilibrium solution for a magnetic field $B' = B/\alpha$. Multiplying both equations we can compute the dependence of the wall width with the magnetic field:

$$\begin{aligned} B'\eta' &= B\eta = ct \\ \eta &\propto \frac{1}{B} \end{aligned} \tag{2.49}$$

Due to the assumptions used, this dependence is valid for an infinite system in the direction perpendicular to the wall. For a finite system, it becomes a very good approximation when the wall width is much smaller than the system size.

This dependence can also be checked by finding the solution for an infinite twist wall with the magnetic field parallel to the wall, where there is only twist deformation. The director field lies in the wall plane and can be described by the angle it forms with the magnetic field $\hat{\mathbf{n}} = (0, \sin\theta(x), \cos\theta(x))$. The wall is perpendicular to the x direction and the magnetic field points in the z direction. The free energy is:

$$F = \int_{-\infty}^{\infty} \left[ \frac{1}{2} K_2 \left( \frac{\partial \theta}{\partial x} \right)^2 - \frac{\chi_a}{2\mu_0} B^2 \cos^2\theta \right] dx \tag{2.50}$$

The Euler-Lagrange equation is:

$$K_2 \frac{\partial^2 \theta}{\partial x^2} + \frac{\chi_a}{\mu_0} B^2 \cos\theta \sin\theta = 0 \tag{2.51}$$

This equation is indeed very similar to the one solved before for computing the transition layer thickness (Section 2.2.6.1). The solution is obtained through similar methods imposing that $\theta(-\infty) = 0$ and $\theta(\infty) = \pi$:

$$\theta(x) = 2 \arctan\left( e^{\frac{x}{\xi_m}} \right) \tag{2.52}$$

where $\xi_m$ is the layer transition thickness for an elastic constant $K_2$. The wall width is then given by the layer transition thickness, and is inversely proportional to the magnetic field:

$$\eta = \frac{1}{B} \sqrt{\frac{K_2 \cdot \mu_0}{\chi_a}} \tag{2.53}$$

The width of the inversion wall can be controlled by the magnitude of the magnetic field. Increasing the magnetic field localizes more the elastic distortion reducing the width of the wall.

## 2.4 Confinement

The boundary conditions at the interface of the nematic liquid crystal volume can play a significant role in the final configuration of the director field. On top of that, the geometry and topology of the confinement surface can also affect the final configuration of the liquid crystal. While the geometry plays a role in the particular equilibrium director field configuration, the topology of the confinement, together with appropriate boundary conditions, imposes global constraints that have to be met by any possible director field configuration. This relation between the topology of the confinement and the global constraints

of the director field is mathematically formulated in the Poincaré-Hopf index theorem [8, 49, 50].

### 2.4.1 Poincaré-Hopf Index Theorem

The Poincaré-Hopf index theorem[1] particularized for director fields states [51]:

**Theorem:** *Let $M$ be a compact differentiable manifold. Let $\hat{\mathbf{n}}$ be a director field on $M$ with isolated point defects with topological charge $s_i$. If $M$ has a boundary, $\hat{\mathbf{n}}$ points in the normal direction to it. Then, the sum of the topological charge of the point defects is equal to the Euler characteristic of the manifold $\chi(M)$:*

$$\sum_i s_i = \chi(M). \tag{2.54}$$

The Euler characteristic is a topological invariant so it is preserved under continuous transformations of the manifold. This implies that, for a director field on the manifold without disclination lines, the sum of the topological charges of its point defects is fixed. This is a global constraint and does not give any information on the exact configuration preferred by the director field, although it does enforce the presence of defects when the Euler characteristic is different from zero. The preferred configuration is dictated by the physics of the system through the minimization of the free energy.

The first case discussed by the theorem is when the compact differentiable manifold is boundaryless. For our liquid crystals, this is the case. The requisite for the theorem to apply is that, at the surface, the director field belongs to the surface manifold, or, in other words, that the director field is tangential to the surface so we have planar anchoring. Although we may have nematic liquid crystal in the interior of the boundaries, the theorem only applies to the total topological charge at the surface.

In this case, the Euler characteristic can be related to the topology of the manifold through the genus $g$ of the surface, which is defined as the number of handles of the surface. In this sense, a spherical surface (Figure 2.9a) has no handles, and thus, $g = 0$; a torus (Figure 2.9b) has one handle and $g = 1$; a double torus (Figure 2.9c) has two handles and $g = 2$ and so on. Surfaces with the same genus can be continuously deformed into each other, while for transforming a surface into one with a different genus it is necessary to "pierce and glue" the surface. The Euler characteristic as a function of the genus can be written as [50]:

[1] This theorem is also colloquially known as the hairy-ball theorem.

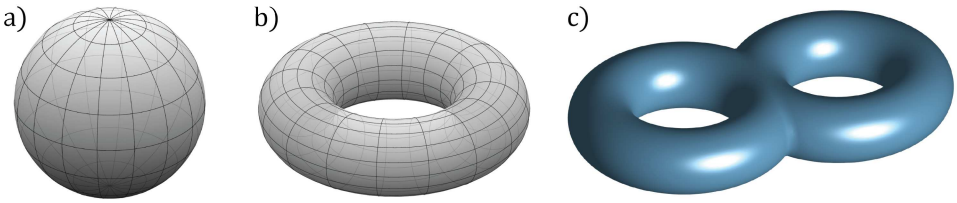



**Figure 2.9:** Boundaryless surfaces with different topologies. a) Spherical surface: $g = 0$. b) Torus: $g = 1$. c) Double torus: $g = 2$

$$\chi(g) = 2(1 - g) \tag{2.55}$$

A nematic on a sphere ($g = 0$), must have a total topological charge on the surface of +2, so the presence of defects is mathematically required[1]. For a torus ($g = 1$), the total topological has to be zero. This does not imply that the final configuration has to be defect free, but that the sum of topological charges is 0. The total topological charge of higher genus surfaces decreases by -2 per extra handle, so a double torus has a total topological charge of -2, a triple torus of -4 and so on. This implies, that the only surface topology that can be defect free is, indeed, the toroidal one.

The second case of the theorem is when we have a manifold with boundaries. This is the case when the 3D manifold is the volume occupied by the nematic. In this case, for the theorem to apply, the boundary conditions need to be homeotropic. For volumes delimited by the previously described compact boundaryless boundaries, the total Euler characteristic is half the Euler characteristic of the surface such that $\chi(M) = (1 - g)$ [52, 53]. This implies that the total topological charge of a ball with homeotropic boundary conditions is +1, a solid torus with homeotropic boundary conditions has a total charge of 0, and so on. From these manifolds, it is again the solid torus the only one that can be defect free.

### Spherical confinement

One of the simple ways to confine a nematic liquid crystal is by making a dispersion of droplets in an immiscible fluid. The anchoring at the surface can be controlled by the surfactants on the outer fluid and can be parallel or homeotropic. Another possibility is to make thin double emulsions using microfluidics such that the nematic liquid crystal forms a spherical shell [54, 55]. If we impose planar anchoring conditions in this last case, the system becomes very similar to a 2D nematic on a spherical surface with the director

[1] You can not comb a hairy ball without any defects.

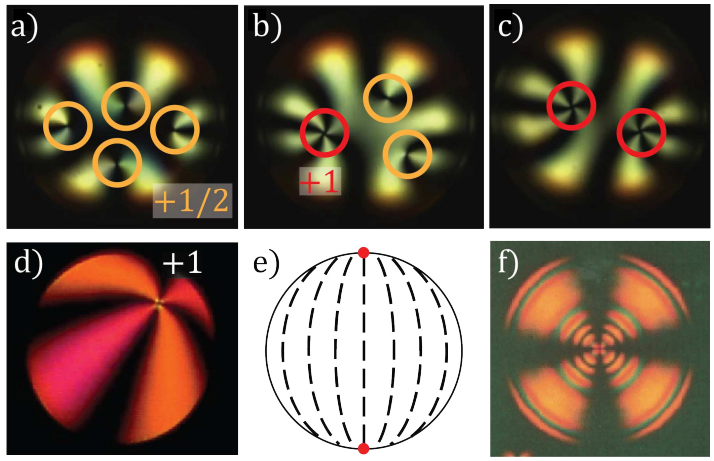



**Figure 2.10:** a)-c) Crossed polarizer images of the tetravalent, trivalent and bivalent configurations of a nematic liquid crystal confined to a spherical shell with parallel anchoring conditions. The point defects are marked by a circle whose color indicates the charge. Orange circle correspond to +1/2 defects and red circles to +1 defects. Images has been adapted from [56]. d) Crossed polarizer image of a bipolar droplet under crossed-polarizers. One of the two defects are shown. Image adapted from [39]. e) Schematic of the director field of the bipolar configuration. f) Crossed polarizer image of a homeotropic nematic droplet in the radial configuration. Image adapted from [58].

tangential to it. In this case, the total topological charge is +2. This has indeed been realized experimentally and different arrangements of defects have been found [56, 57], like the tetravalent configuration with four +1/2 defects (Figure 2.10a), the trivalent configuration with two +1/2 defects and a +1 (Figure 2.10b) and the bipolar one with two +1 defects (Figure 2.10c). Although the exact configuration observed depends on the details and geometry of the system, in all cases the constraint of a +2 total topological charge is fulfilled.

If instead of having a shell, we have a spherical droplet with parallel boundary conditions, the Poincaré-Hopf constraint still applies on the surface, such that surface point defects are required. The typical configuration observed is the bipolar configuration [39] where two +1 boojums appear at antipodal regions (Figure 2.10d). The total surface topological charge is again +2. Since now we have 3D point defects, their topological charge has to be an integer number so the bipolar configuration is the one with defects of lowest possible topological charge. The director field of the bipolar configuration resembles the meridians going from one defect to the other, as shown schematically in Figure 2.10e.

Finally, we can also have nematic droplets with homeotropic boundary conditions. In this case, the total topological charge according to the Poincaré-Hopf

index theorem has to be +1. The typical configuration experimentally observed is the radial one with a +1 radial hedgehog at the center (Figure 2.10f) [40, 59].

#### Higher genus droplets

While surface tension favors spherical droplets, making droplets with higher genus is more challenging and there has been less experimental work on this system. Experimentally, it has been observed that solid-tori with planar boundary conditions form a defect-free double-twisted configuration satisfying the Poincaré-Hopf index theorem [9, 60]. In the case of homeotropic toroidal droplets, a defect free twisted escaped radial configuration is observed [52, 61], again fulfilling the zero total topological charge constraint. Lastly, nematic droplets with planar boundary conditions and a larger number of handles have also been produced. These droplets present boojums to fulfill the total surface charge constraint [9, 60].

### 2.4.2 Cylindrical confinement

Another typical confinement geometry for liquid crystals is the cylindrical one. Experimentally it can be easily realized by pumping the liquid crystal into a glass capillary. The anchoring conditions can be modified by treating the surface of the glass capillary.

If we initially neglect the edges of the capillary, for planar anchoring conditions, it is easy to picture a defect free configuration where the director field is aligned in the cylinder axis direction (Figure 2.11a). This configuration, which completely minimizes the free energy of a nematic liquid crystal without external fields, is called axial [62]. As we can see, there are no defects in it. Indeed, a cylinder with periodic boundary conditions, as for the axial configuration, is topologically equivalent to a torus so the Poincaré-Hopf index theorem imposes a total topological charge of 0.

While the planar case is simple and straightforward, imposing homeotropic anchoring conditions leads to a richer panorama in terms of possible configurations. First of all, for simplicity, we will assume translational invariance, such that the configuration is described solely by the configuration on a cross-section. In this case, we again have periodic boundary conditions and the total topological charge has to be zero. A defect-free configuration can be easily visualized: the escaped radial configuration (Figure 2.11b). In this configuration the director changes from being perpendicular to the surface to becoming parallel to the cylinder axis as we go from the surface to the center of the cross section, becoming axial right at the center and avoiding the singularity [62, 63]. There are other variations of this configuration like the twisted escaped radial where

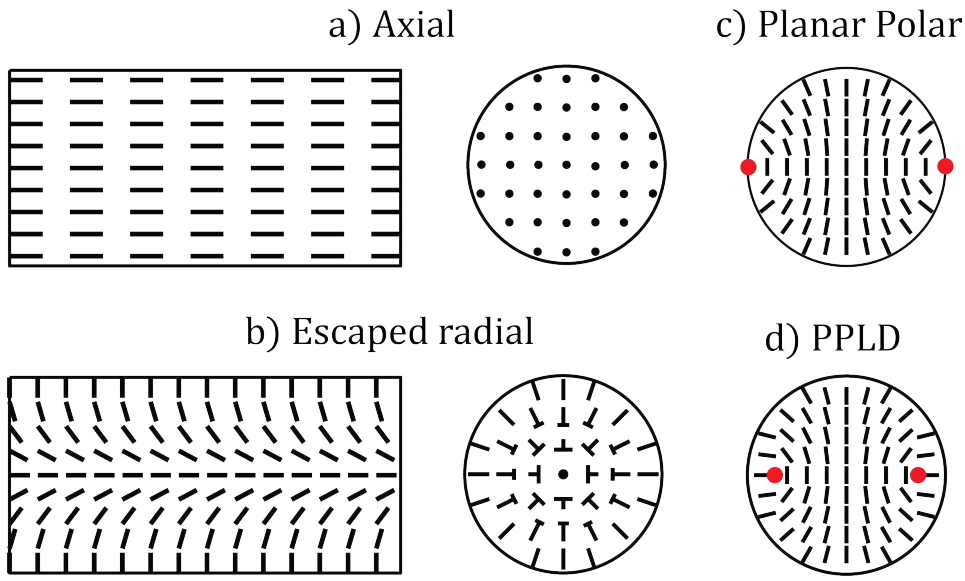



**Figure 2.11:** a) Schematic of axial configuration for planar boundary conditions. b) Escaped radial configuration schematic. The nails in the cross-section view indicate the out of plane tilt of the director. c) Schematic of the cross-section director field for the planar polar configuration. Red circles indicate disclinations. d)Schematic of the cross-section director field for the planar polar with line disclinations configuration.

an azimuthal component is added to the director field, so the director field has also a twist distortion which can reduce the overall energy in some cases [16].

Interestingly, since we only need to define the director field at the cross-section of the cylinder, this is equivalent to studying the possible configurations in a disk with homeotropic boundary conditions. Since the director field does not need to be tangent to the disk, the Poincaré-Hopf index theorem can not be applied to the director field itself. Nevertheless, it can still be applied to the projection of the director field in the cross-section. The projection field does not have to be normalized and can be zero when the director is perpendicular to the disk. The Euler characteristic of the disk is +1 so the total topological charge of the projection field has to be +1.

The first possibility to fulfill the topological charge constraint is to have a +1 disclination at the center. Since it is an integer strength disclination line, the singularity can be removed by escaping into the third dimension. This has the effect of removing the singularity in the projection field by making it go to 0 as we move to the center. This case, indeed, corresponds to the escaped radial configuration described before and is defect-free.

As a second possibility we can have two 1/2 disclination lines which have a non-removable singular core. When the disclination lines are inside the disk, the configuration is called planar polar with disclination lines (PPLD) [62, 63]. As shown in Figure 2.11d, this configuration has the director field better aligned in general that the escaped radial one with the extra cost of having singularities. In the limiting case, the disclination lines can be located on the surface leading to the planar polar configuration (PP) [62, 63], which aligns even better the director field at the cost of having singularities and breaking boundary conditions (Figure 2.11c).

It is worth noting that, although the periodic boundary conditions are met so the space is topologically equivalent to a torus, we can not apply the Poincaré-Hopf index theorem since it is only valid for configurations with isolated point defects and not for configurations with disclination lines.

In practice, the actual configuration which minimizes the energy depends on the physical properties of the material, anchoring and size [63, 64]. For example, for small enough cylinder sizes, the planar polar configuration is the ground state, while for large enough cylinders it is the escaped radial or any variant. This last case is the one usually observed through optical microscopy.

## 2.5 Why nematic tori?

In this work we will focus on the configurations of nematic toroidal droplets with different anchorings. The first interesting reason for studying toroidal droplets is that they are topologically different from spherical droplets, so the global properties given by the topology are intrinsically different. They are also more challenging to make experimentally, and thus have been less explored. This is because the surface tension energy is proportional to the area, such that a toroidal drop will tend to minimize the surface area of the volume, which is accomplished with the spherical shape [65, 66].

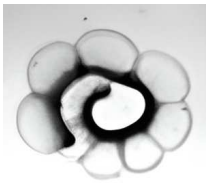
In addition, all the points in a perfect spherical surface are identical. The difference of a sphere with a plane is that the spherical surface has a Gaussian curvature different from zero, which is an intrinsic property that can be measured by two-dimensional "beings" living on the surface, and thus, can affect the global configuration. Nevertheless, since all the points have identical properties, a rotation of a given director field configuration around the center of the sphere will preserve its energy. In the case of the torus, the integrated Gaussian curvature is zero but there are regions with positive and negative curvature, outer and inner parts respectively, giving different local environments.

Moreover, in a torus there is a gradient of the curvature. This means that point features might be attracted to different regions to minimize their free energy. This is indeed the case of topological point defects, that reduce their

energy when they go to like-sign curvature areas. The higher the absolute value of the curvature the more the energy is reduced [11]. For 2D nematics on a thick enough torus, this can result in defect-populated states as the ones that minimize the energy although defects are not necessary in the configuration. This curvature attraction has been observed experimentally for 2D active nematic tori where the average topological charge in a region is proportional to the Gaussian curvature [67].

Toroidal confinement of nematic liquid crystals can also lead to an interesting interplay between the liquid crystal elasticity and the curvature of the confinement. For nematic solid tori with parallel and perpendicular anchoring, this interplay has resulted in the appearance of spontaneous twist in the defect free configurations, which in the extreme case of cylindrical confinement is not present.

Chapter 3



# Making and stabilizing toroidal droplets and a bit of polymer physics, hydrogels, their behavior and an upscale method for their production

## 3.1 Introduction

In this chapter we introduce the technique for making and stabilizing toroidal droplets which will be the object of study of most of the thesis. We stabilize the nematic toroidal droplets through a hydrogel-based yield-stress material. Taking advantage of this we will also talk about other projects related to hydrogels that have advanced along the thesis. We start by describing how toroidal droplets are made and introduce some basics on polymer physics. After that, we talk about one project regarding the generation of spherical hydrogels, studies on the evaporation of water and an upscaled prototype for their production. This project has been joint work with other people of the group: Alexis de la Cotte, Jyothishraj Nambisan and Adrià Meca Montserrat. After that, we explain the method used to stabilize toroidal droplets and in general, non-spherical droplets and finish the chapter by discussing experimental work on the deformation of cylindrical gels due to a constant volume phase transition that induces phase

separation into swollen and shrunk regions. This last project has been a joint collaboration with Adrián Arenas-Gullo, another graduate student in the group, whom I greatly thank for sharing this project with me.

## 3.2 Making toroidal droplets

### 3.2.1 Fundamentals

The procedure to make toroidal droplets relies on the observation that a toroidal droplet can be regarded as a jet that bends into itself. It is known that to generate a jet from an injector, surface tension needs to be overcome avoiding the formation of droplets at the tip that grow until they detach. It has been shown in microfluidic devices [68] that the capillary force can be overcome in two different ways to form jets. The first one is by having big enough inertia such that capillary forces are not able to stop the outcoming fluid that forms a jet. This is the usual case we observe in kitchen faucets. The second way is by means of an immiscible co-flowing liquid that exerts a shear stress on the injected fluid large enough to overcome capillarity and produce a jet.

This second case is the one that can be exploited to generate toroidal droplets. If the outer fluid instead of flowing straight, flows around a point, streamlines close onto themselves forming circles so a jet formed in such a flow profile would also close onto itself forming a toroidal droplet [65, 69]. This flow profile can be easily generated by rotating the outer medium, which can be placed in a cuvette. Then, for high enough rotation speeds, if we inject a fluid inside the rotating outer medium, the jet naturally tends to close onto itself and form a toroidal droplet, as schematically shown in Figure 3.1a. In practice, the tip is positioned parallel to the rotation axis such that it does not disturb significantly the jet allowing it to merge and form the toroidal droplet.

Liquid jets, nevertheless, are not stable and break due to a Rayleigh-Plateau instability. To generate toroidal droplets, the rotation speed needs to be high enough to induce jetting and to make a whole turn before the jet breaks. The first condition is fulfilled when the outer capillary number, which is a measure of the ratio between shear and capillary forces, is larger than order 1: $\mathrm{Ca}_{out} = \eta_{out} u_{out}/\gamma \geq O(1)$ with $\eta_{out}$ the outer fluid dynamic viscosity, $u_{out}$ the outer fluid velocity and $\gamma$ the surface tension between both fluids [68]. The second condition is obtained by comparing the jet break-up time $t_b$ with the time it takes to make a full rotation $T$. The breaking time is obtained from balancing inertial and surface forces so $t_b \approx \eta_{out} a_{tip}/\gamma$ where $a_{tip}$ is the tip radius, while the time it takes to make a full rotation is expressed as $T = 2\pi R/u_{out}$ where $R$ is the distance from the needle to the rotation axis. Imposing the rotation period time $T$ to be smaller than the break-up time $t_b$ we get the condition

$\mathrm{Ca}_{out} \geq 2\pi R/a_{tip} > O(1)$ [65]. Since $R > a_{tip}$, the second condition is more restrictive than the first one and the angular velocity $\omega$ necessary to generate a toroidal droplet becomes:

$$\omega > 2\pi \frac{\gamma}{\eta_{out} a_{tip}} \tag{3.1}$$

### 3.2.2 Experimental setup

To make toroidal droplets in the lab, we use a rotating stage on top of which we place a cuvette with the outer medium [70]. The simplest version of a rotating stage consists on a small DC motor and a toy gear box that mechanically transmit the rotation into the rotating stage that is held in place by a ball bearing (Figure 3.1b). While this setup works very well for making toroidal droplets with millimeter size tube radius, when dealing with tori with handle sizes of the order of hundreds of microns, mechanical vibrations can result in difficulties to get good toroidal droplets[1]. To get good small toroidal droplets we use a second rotating stage setup consisting on a ceiling fan motor fixed to a custom frame and having a custom stage added to the rotor for setting the outer medium cuvette. The rotation speed is controlled with the electric input frequency by a frequency variable drive (Figure 3.1c). Since the rotation is directly driven by the motor without any mechanical transmission the rotation is smoother, with less vibrations, making it easier to get good small toroidal droplets.

Now that we have the rotating outer medium, the toroidal droplet fluid is injected with a syringe pump connected via polyethylene tubing to a tip. The size of the tip determines the order of magnitude of the tube diameter. To generate toroidal droplets with millimeter tube diameters, we use syringe metal tips[2] that we obtain from melting the plastic part. To get smaller diameter tips in a more controlled way, we use a pipette puller (P-1000 Sutter instrument) to pull round glass capillaries and use a microforge (MF2 Narishige) to cut them to the desired size. For the nematic small toroidal droplets, we cut them to around $100\mu m$ outer diameter.

The tip is then placed in position with an alligator clip connected to a micromanipulator which controls the position of the tip. In this way, we can control the distance between the tip and the axis of rotation which determines the torus radius $R$. The control parameters for the toroidal droplet generation are the volume injected, which for a fixed $R$ will determine the torus tube radius

[1] This becomes especially relevant when using a yield stress material as the outer medium to stabilize the tori

[2] We use G27 (0.41mm diameter) or G20 (0.91mm diameter) syringe tips which are the ones that fit in our tubing BTPE-20 and BTPE-90, respectively

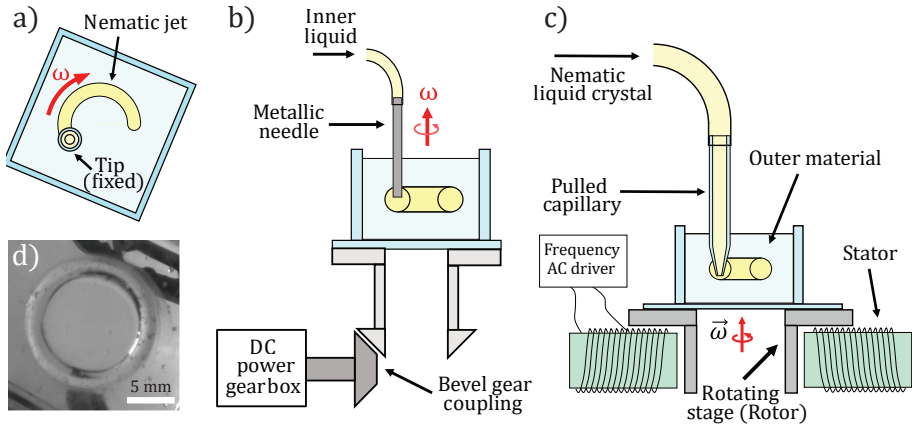



**Figure 3.1:** a) Top view schematic of the generation of a jet on a rotating bath. After one rotation the jet closes onto itself. b) Schematic of the mechanical rotation setup where the DC power gear box transmit the mechanical rotation through a bevel gear coupling. c) Schematic of the magnetic rotation setup. The electromagnetic forces of the electromagnets induce the rotation of the rotor where the cuvette is placed. d) Example of a millimeter size glycerol toroidal droplet in a bath of 60000 cSt silicon oil made in the mechanical setup with a G20 metallic tip.

$a$, the rotation speed, which has to be set high enough for the jet to form and the injection rate, which has to be large enough so the initial jet has a big enough diameter so it does not break before completing a turn and low enough such that the whole volume is not injected before the first turn is completed. More details on the experimental setup can be found in Appendix A. An example of a millimeter size toroidal droplet of glycerol in a bath of 60000 cSt silicon oil, made with a G20 tip in the rotating setup with mechanical transmission is shown in Figure 3.1d.

### 3.2.3 Stability

When making a toroidal liquid droplet inside another fluid, the resulting droplet is not stable and ends up transforming into one or more spherical droplets due to surface tension instabilities. This can happen via the Rayleigh-Plateau instability, resulting in the breaking of the torus into different droplets [65], or a shrinking instability whereby the center hole of the torus contracts until it disappears to result in a single spherical droplet [66]. To stabilize our toroidal droplets [71] we use a yield-stress material as the outer material such that below a certain stress, called the yield stress, it behaves as a solid stabilizing the droplet against surface tension forces, while it behaves as a liquid for larger stresses and thus allowing the generation procedure for making toroidal droplets to work.

To make our water-based yield stress material we use a solution of granular-sized hydrogels. To better understand the properties of the constituents making up the continuous phase in which the toroidal droplets are embedded, we now take a detour into the physics of hydrogels and the production and evaporation of spherical gels. This is also motivated by a collaboration with the company Agrobio S.L. The aim of this collaboration is to encapsulate liquids in polymer hydrogels for feeding predatory insects that eat plagues at greenhouses.

## 3.3 Polymer physics and hydrogels

Polymer gels are three-dimensional polymer networks. On the contrary to rubbers, which also fit into this definition, polymer gels are highly porous and are embedded in a solvent that fills the pores and permeate the whole network. For hydrogels, this solvent is water. The behavior of polymers in solution is dominated mainly by thermal fluctuations. As a result, the entropy of the system is a key factor to understand their physics and behavior.

The main difference between a hydrogel and a polymer solution resides in the fact that the polymer chains in the hydrogel are crosslinked, forming an interconnected network able to withstand shear stresses. Hydrogels, as opposed to polymer solutions, are elastic solids. Unlike conventional solids whose behavior is mainly described by means of the interaction energy between their constituents, hydrogels are dominated by the entropic part of their free energy, making entropy a cornerstone to understand hydrogel physics. In this section, following [72] and [73] we briefly describe the Flory-Rehner free energy of hydrogels and describe some of its most relevant features for this work.

### 3.3.1 Free energy of hydrogels

To describe the free energy of hydrogels we will consider a hydrogel as a polymer network made of polymer chains that are joined at each of their ends to other polymer chains (see Figure 3.2a). The junctions between different chains are named crosslinks. We will assume that the contribution of the dangling chains to the free energy, which are polymer chains only crosslinked in one end, is negligible.

In this approximation we have two main contributions to the free energy. The first one comes from the mixing of the solvent and the polymer. In this case we have both an energetic contribution due to the different molecular interactions between monomers and solvent molecules and a entropic contribution which favors mixing. This free energy is called mixing free energy and depends on the volume fraction of solvent, and thus, on the hydrogel network swelling state. The other contribution comes form the crosslinked character of the network

and thus it is related to its elastic behavior. Although elasticity is traditionally assigned to the energy of the material, in this case, deformations of the network induce a change in the entropy of the individual polymer chains. We will refer to this free energy contribution as the elastic free energy.

#### 3.3.1.1 Mixing free energy

Having a polymer network filled with solvent can be regarded as a system where polymer and solvent is mixing. The energy of interaction will depend on the amount of solvent in the hydrogel, and thus on the polymer volume fraction $\phi$. We use a mean field approach such that the interaction energy depends only on the average densities of solvent and monomer so fluctuations and inhomogeneities are not taken into account. This, together with the assumption that the monomer and solvent molecules have a similar volume $\nu$, results in the following form for the mixing energy:

$$E_{mix} \approx V \frac{k_B T}{2\nu} \left[ \chi_{m-m} \phi^2 + 2\chi_{m-s} \phi(1-\phi) + \chi_{s-s}(1-\phi)^2 \right] \tag{3.2}$$

where $V$ is the volume of the system, $k_B$ Boltzmann's constant, $T$ the temperature and $\chi_{m-m}, \chi_{m-s}$ and $\chi_{s-s}$ are the monomer-monomer, monomer-solvent and solvent-solvent interaction strengths relative to $k_B T$. These interaction strengths take into account, in a mean field way, van der Waals, excluded volume and possible hydrophobic interactions.

Since we are interested in the case of mixing, we compute the difference in energy between the mixed case and the separated case, $\Delta E_{mix}$. This gives the simple result:

$$\Delta E_{mix} = N k_B T \chi \phi (1-\phi) \tag{3.3}$$

where $N = n_s + n_m$ is the total number of solvent molecules and monomers and $\chi \equiv \chi_{m-s} - \chi_{m-m}/2 - \chi_{s-s}/2$ is the Flory parameter. This parameter accounts for the change in energy when a solvent molecule next to another solvent molecule is exchanged by a monomer which is next to another monomer. This breaks both a solvent-solvent and a monomer-monomer pair to form two monomer-solvent pairs. If $\chi < 0$, this exchange reduces energy, and thus mixing is favored, with the minimum energy obtained when $\phi = 1/2$. If $\chi > 0$ mixing is not favorable and, energetically, the system will tend to phase separate.

To estimate the entropy contribution to the mixing free energy we first simplify the system by considering a system of monomers and solvent molecules in a cubic grid. The total number of microstates is given by:

$$\Omega = \frac{N!}{n_m! n_s!} \tag{3.4}$$

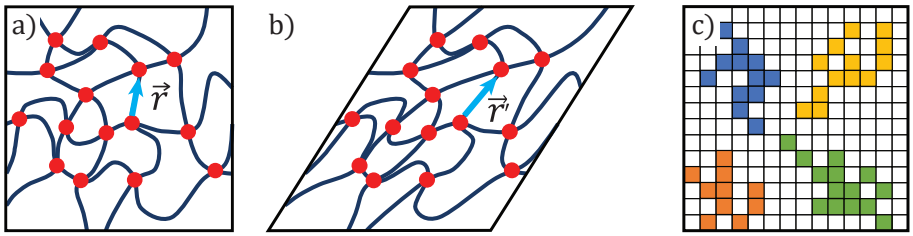



**Figure 3.2:** a) Schematic of a hydrogel region made of crosslinked polymer chains. The cross-linking points are marked with red dots and $\vec{\mathbf{r}}$ is an example of an end to end vector in the undeformed state. b) Affine transformation of the gel in a) where $\vec{\mathbf{r}'} = \Lambda\vec{\mathbf{r}}$ is the new end to end vector. c) Cubic grid representing each step used to compute the mixing entropy of polymers in solution. The polymers are colored while white regions correspond to solvent molecules.

Using the Stirling's approximation, the entropy is:

$$S_{latt} = k_B \ln \Omega \approx -Nk_B \left[(1-\phi)\ln(1-\phi) + \phi \ln \phi\right] \tag{3.5}$$

Nevertheless, in this case we have assumed the monomers behave independently and are able to explore the whole space. If we consider now a system of polymer chains made of $\mathcal{N}$ monomers (see Figure 3.2c), the monomers are required to be adjacent to other monomers while the polymer as a whole has full translational freedom. We can assume that the entropy of the individual monomers is negligible compared to the translational entropy of the polymer. We can then approximate the entropy as:

$$S_{latt} \approx -Nk_B \left[(1-\phi)\ln(1-\phi) + \frac{\phi}{\mathcal{N}} \ln \frac{\phi}{\mathcal{N}}\right] \tag{3.6}$$

As done with the mixing energy we can now compute the mixing entropy:

$$\begin{aligned} \Delta S_{mix} &= \frac{1}{V}\left[S(\phi) - \nu n_s S(\phi=0) - \nu n_m S(\phi=1)\right] \\ &\approx -Nk_B \left[(1-\phi)\ln(1-\phi) + \frac{\phi}{\mathcal{N}} \ln \phi\right] \end{aligned} \tag{3.7}$$

A system of polymers in solution is still not the same as our crosslinked polymer network. When crosslinks are considered, the polymer network can be considered as a very large polymer occupying the whole volume and thus losing its translational degrees of freedom. The entropy, then, comes from the solvent alone. This can be obtained from the previous equation taking the limit $\mathcal{N} \to \infty$. The result is the mixing entropy:

$$\Delta S_{mix} \approx -Nk_B(1-\phi)\ln(1-\phi) \tag{3.8}$$

Finally, the mixing free energy can be written as:

$$\Delta F_{mix} = \Delta E_{mix} - T\Delta S_{mix} = Nk_BT\left[(1-\phi)ln(1-\phi) + \chi\phi(1-\phi)\right] \tag{3.9}$$

This free energy is the free energy coming from the mixing of polymer and solvent. While for a polymer solution, the polymer volume fraction is typically fixed, for hydrogels it can change when placed in a water bath. The solvent is allowed to enter/escape the hydrogel through the porous network. This in turn increases/decreases the pore size resulting in swelling/shrinking of the gel. This mixing term is, therefore, relevant in determining the equilibrium size of the hydrogel.

#### 3.3.1.2 Elastic free energy

The second important contribution to the hydrogel free energy is the elastic free energy. We call it elastic in analogy with the elastic free energy of conventional solids since it takes into account the energy cost of elastic deformations. By contrast to conventional solids though, the hydrogel is made of polymer chains that when deformed, change their end to end distance. The free energy increase comes from the change in the number of possible configurations when the end to end distance of the polymer chains changes. This is a purely entropic contribution. We assume a phantom chain model so there is no energy of interaction of the chain with itself.

To compute the free energy, we initially consider just a single polymer chain confined to volume V with an end to end distance given by the vector $\vec{\mathbf{r}}$. We take the random walk approximation and call $a$ the length of each random walk step and consider that the chain takes a total of $N_i$ steps along direction $i$. The number of possible configurations, in this case, can be expressed as:

$$\Omega_1(\vec{\mathbf{r}}) = \frac{V}{\nu}\prod_{i=1}^{3}\frac{N_i!}{\left(\frac{N_ia+r_i}{2a}\right)!\left(\frac{N_ia-r_i}{2a}!\right)} \tag{3.10}$$

where the prefactor $V/\nu$ takes into account the translational freedom of one end. If we assume that the polymer explores all of 3D space isotropically the number of steps in each direction is the same and $N_1 = N_2 = N_3 = N/3$ with $N$ the number of steps. Using Stirling's approximation, the entropy of a single chain as a function of its end to end vector is:

$$S_1(\vec{\mathbf{r}}) = S_0 - \frac{3k_B|\vec{\mathbf{r}}|^2}{2R_0^2} + k_B \ln \frac{V}{\nu} \tag{3.11}$$

where $S_0$ is a constant depending on the number of steps in the chain, and $R_0 = \sqrt{N}a$. The second term takes into account the elasticity of the chain resulting from the number of possible configurations for a given end to end vector. The last term takes into account the translational entropy of the chain.

As in the previous case, we are interested in the change of entropy with respect to the initial configuration where the polymer has an end to end vector $\vec{\mathbf{r}}$. We can express the new end to end vector as $r'^i = \Lambda_{ij} r^j$ where $\Lambda_{ij}$ is a deformation matrix. The change in entropy becomes:

$$\Delta S_1(\vec{\mathbf{r}}) = -\frac{3k_B}{2R_0^2}(\Lambda_{ki}\Lambda_{kj} - \delta_{ij}) r^i r^j + k_B \ln\big(V'/V\big) \tag{3.12}$$

where we have used Einstein's summation convention and $\delta_{ij}$ is Kronecker's delta. The total entropy is the sum of the contributions of the $n_c$ chains. If we assume affine deformations, the end to end distance change of each chain is given by the same deformation matrix $\Lambda$ corresponding to the deformation matrix in the continuum approach (see Figure 3.2b). The entropy can be expressed as:

$$\Delta S_{n_c} = -\frac{3k_B}{2R_0^2}(\Lambda_{ki}\Lambda_{kj} - \delta_{ij})(r_1^i r_1^j + ... + r_{n_c}^i r_{n_c}^j) + n_c k_B \ln(\det \Lambda) \tag{3.13}$$

where the volume accessible for each chain $V'$ is related to the original volume via $V' = V \det \Lambda$. In order to get an analytic and tractable equation that is valid for different networks, we make the assumption that the region with the same deformation matrix is large enough such that all possible different end to end vectors appear in a statistically significant way, and that there is no chain deformation due to steric repulsion so that the entropy of a single chain is a valid approximation. Statistically, averaging over the equilibrium probability distribution gives the entropy change associated with the polymer chains:

$$\Delta S_{net} = \langle \Delta S_{n_c} \rangle = -\frac{1}{2} n_c k_B \left[ \mathrm{tr}\Lambda^T \Lambda - 3 - 2 \ln \det \Lambda \right] \tag{3.14}$$

So far, we have not taken into account the crosslinks between chains which reduces their conformational freedom and thus their entropy. In a simplistic way, this can be taken into account by equally dividing the population into two types of polymer chains A and B such that while the A chains retain their entropy freedom in their free end, the other one is completely determined by the first one. This is equivalent to establishing a set of constraints. The number of constraints can be estimated to be $n_c/2$ so that the entropy is reduced by

$(n_c k_B/2) \ln \det \Lambda$ [73, 74]. The total entropy reduction can then be expressed as:

$$\Delta S_{net} = -\frac{1}{2} n_c k_B \left[ \mathrm{tr}\Lambda^T \Lambda - 3 - \ln \det \Lambda \right] \tag{3.15}$$

The elastic free energy can be then expressed as:

$$\Delta F_{el} = -T S_{net} = \frac{1}{2} n_c k_B \left[ \mathrm{tr}\Lambda^T \Lambda - 3 - \ln \det \Lambda \right] \tag{3.16}$$

The free energy depends mainly on the deformation matrix $\Lambda$. It is important to note that this deformation matrix is not independent of the polymer volume fraction. Indeed, its determinant is equal to the relative volume change $V'/V$ and thus can be related to the volume fraction via $\det \Lambda = \phi_0/\phi$, where $\phi_0$ is the initial polymer volume fraction and $\phi$ the polymer volume fraction in the deformed state. We realize that the elasticity coming from the network results in an elastic response to swelling and shrinking. This avoids, for example, infinite swelling of the hydrogel in the solvent when the mixing conditions are favorable.

It is important to note that for deriving the free energy we have made an important number of assumptions, including the affine deformation of the chains. This assumption has indeed been proven inaccurate [75]. Along our derivations, the assumptions taken simplify the system so microscopic details are sometimes ignored; recall, we have assumed a mean field approach to the energy of mixing and considered ideal random-walk chains. Nevertheless, while we can not expect the Flory-Rehner free energy to perfectly describe the behavior of hydrogels, this free energy can be regarded as a semi-empirical model that provides insight into the main phenomena of hydrogels and their physical origin while simplifying the microscopic details of the gel. Additional energetic terms that can have an effect on the behavior of the hydrogel can be added to the theory, including the contribution of electrostatic charges for the case of charged polymers [76, 77], osmotic pressure contributions from molecules in suspension and ions in solution.

### 3.3.2 Shrinking and swelling

The most simple case we can study is an isotropic hydrogel inside a solvent bath without any other external forces. In this case, the deformation matrix is isotropic and the polymer volume fraction is homogeneous throughout the gel. The deformation matrix can be written as:

$$\Lambda = \left( \frac{\phi_0}{\phi} \right)^{1/3} \mathbb{I} \tag{3.17}$$

where $\mathbb{I}$ is the identity matrix. In this case, the relationship between the deformation matrix and polymer volume fraction is automatically fulfilled so the

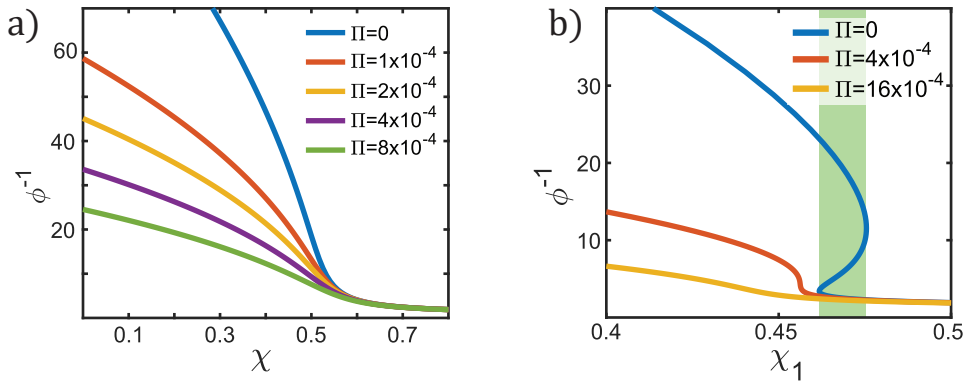



**Figure 3.3:** a) Plot of the isobars obtained from the Flory-Rehner equation of state 3.20 taking $\nu_0\nu = 10^{-4}$ and $\phi_0 = 0.1$. The osmotic pressure value is normalized by $k_BT/\nu$. b) Isobars of the modified Flory-Rehner equation keeping the previous parameter and taking $\chi_2 = 0.56$. For pressures larger than a critical one, the isobars are multivalued with respect the Flory parameter. The green region shows the multivalued region of Flory parameter for the isobar $\Pi = 0$. At this pressure, when the Flory parameter belongs in this range, phase coexistence is possible.

corresponding Lagrange multiplier does not need to be added to the free energy. Considering all contributions, the free energy density becomes:

$$\Delta\mathcal{F} = \frac{\nu_0\phi}{2\phi_0}k_BT\left[3\left(\frac{\phi_0}{\phi}\right)^{2/3} - 3 - \ln\left(\frac{\phi_0}{\phi}\right)\right] + \frac{k_BT}{\nu}[(1-\phi)\ln(1-\phi) + \chi\phi(1-\phi)] \tag{3.18}$$

where $\nu_0 = n_c/V_0$, with the subindex 0 indicating the value in the reference state. From basic thermodynamics [72], the osmotic pressure $\Pi$ can be obtained from the derivative of the free energy with respect to the number of solvent molecules resulting in:

$$\Pi(T,\phi,\Lambda) = -\left(\frac{\partial(\phi^{-}1\Delta\mathcal{F})}{\partial(\phi^{-}1)}\right)_{T,\Lambda} \tag{3.19}$$

$$\Pi(T,\phi) = \frac{k_BT}{\nu}\left[\nu_0\nu\left(\frac{\phi}{2\phi_0} - \left(\frac{\phi}{\phi_0}\right)^{1/3}\right) - \phi - \ln(1-\phi) - \chi(T)\phi^2\right] \tag{3.20}$$

This equation is the so-called Flory-Rehner equation of state. This equation relates the osmotic pressure, the Flory $\chi$ parameter and the polymer volume fraction. Thus, we can calculate the polymer volume fraction as a function of $\chi$ and osmotic pressure. If we set the osmotic pressure to be 0, we can see that the

volume fraction increases with increasing $\chi$ which means that the gel shrinks and expels solvent since the mixing becomes less favorable energetically. The isobars of the equation of state are shown in Figure 3.3a showing a continuous transition from the swollen high $\phi$ state to the shrunk low $\phi$ state as $\chi$ increases. Moreover, as the osmotic pressure increases at low $\chi$, the gel becomes less swollen due to the compressive forces of the osmotic pressure.

The dependence of the gel behavior with temperature is encoded in the dependence of $\chi$ with temperature. Indeed, the dependence of the Flory parameter with temperature is observed for some polymer solutions. This is the case of poly-isopropylacrilamide (pNIPAM) solutions. In this case, for low temperatures the solution is completely transparent indicating the polymer mixes completely with the solvent. As the temperature increases above $\sim 33°C$ the solution starts getting cloudy and whitish [78, 79]. This temperature is called the cloud point and is the manifestation of the collapse and aggregation of the polymer chains. The Flory parameter $\chi$ decreases as the temperature increases so polymers chains prefer to be in contact with other polymers rather than with water molecules and, at the cloud point, the system starts to phase separate. When the polymer aggregates grow to a size similar to the wavelength of light, they start scattering light resulting in the milky aspect of the solution.

If we crosslink the pNIPAM polymers to make a hydrogel, we obtain a thermorresponsive gel, a hydrogel whose size changes as a function of temperature. As the temperature increases, $\chi$ increases and the polymer volume fraction increases resulting in gel shrinking. Contrary to what the simple Flory-Rehner model tells us, in certain circumstances the experimentally observed transition is discontinuous and a sharp change in size is observed at a certain transition temperature [80]. This first order transition can be easily captured theoretically for the case of charged hydrogels when adding the osmotic pressure contribution of the counter ions, $\Pi_{ion}$ [80, 81]. Nonetheless, the Flory-Rehner equation of state can still capture the first order phase transition if we allow $\chi$ to depend on concentration. This is confirmed by measurements which show that $\chi$ has a non-linear dependence on $\phi$ [82, 83]. Expanding $\chi$ in Taylor series around $\phi = 0$ allows us to express it as:

$$\chi \approx \chi_1 + \chi_2\phi + \chi_3\phi^2 \tag{3.21}$$

It has been shown that only retaining the first two terms with only the first one depending on temperature is enough to recover a first order transition [84]. An example of the isobars with the modified Flory parameter are shown in Figure 3.3b.

In first order phase transitions, phase coexistence is possible in the range of values where the equation of state is multivalued (green area of Figure 3.3b). This means that, for a constant osmotic pressure, shrunk and swollen regions

can possibly coexist in this range of temperatures. This temperature range of coexistence has been observed in ionic pNIPAM gels [85] while it has been experimentally elusive to observe in neutral pNIPAM gels. This has been attributed to a very narrow coexistence region [85]. Nevertheless, in these neutral gels, applying an external stress can widen the coexistence region and phase coexistence driven by external stresses in cylindrical gels has been experimentally observed [86].

The swelling state of a hydrogel not only depends in general on temperature but can also depend on other external conditions. In the case of charged hydrogels, there is another contribution to the osmotic pressure coming from the counter-ions. The swelling state will then depend also on the amount of these ions and thus can be controlled by changing the pH of the sample and its salt concentration.

### 3.3.3 Out of equilibrium phenomena in hydrogels

The previously derived equation of state predicts the equilibrium state of a hydrogel. Nevertheless, there are other interesting phenomena which occur due to out-of-equilibrium processes. In the previous calculation of the equilibrium polymer volume fraction we have implicitly assumed that solvent can diffuse in and out the gel up to when the corresponding chemical potentials match.

In the case of thermoresponsive pNIPAM gels this is indeed observed when the temperature is changed. As soon as the temperature changes, the gel starts deswelling. However, this process is not immediate since it takes some time for the water to diffuse and for the polymer to relax. The associated time scale increases with the square of the size of the gel [87, 88]. For microgels this time scale is in the order of seconds, while for millimeter size macrogels it can be as large as hours. Hence, if we increase the temperature over the phase transition temperature slow enough such that we fall in the quasistatic regime, we will observe the expected equilibrium behavior of the gel, where it shrinks. In contrast, if we increase the temperature over the phase transition temperature fast enough, the gel slightly shrinks and stalls at a given size [89].

This behavior is attributed to the formation of an impermeable polymer layer on the gel surface. When the temperature is increased fast over the phase transition temperature, the polymer at the surface immediately expels water, collapsing to form a very dense polymer layer so that water molecules inside the gel can not get out of the gel. This impermeable layer fixes the inside volume such that shrinking of a part of the gel needs to be accompanied by swelling of another part. The free energy minimum corresponds to phase separation and shrunken/swollen coexistence inside the gel. This has been experimentally observed in spherical hydrogels where a "bubbling instability" occurs such that the surface becomes decorated with swollen "bubbles" [89] and in cylinders

where different instability patterns appear depending on the external conditions that drive the phase transition [90].

But, how does the gel chooses where to shrink and swell? This was theoretically studied for the case of gels with circular cross-sections and curvature [72, 91]. In this case, in a first order approximation, the energy is reduced when the dense polymer layer in the outside grows inhomogeneously, with one part growing thicker. Moreover, if there is curvature already present, the free energy is minimized when the gel shrinks in the region of negative Gaussian curvature and expands in the region of positive Gaussian curvature. For the case of a toroidal gel, a bend instability is predicted resulting in a saddle-shape[1] deformation of the gel. This was indeed confirmed in experiments [92]. This effect has received the name of extreme thermodynamics, since the thermodynamic instability associated to phase separation couples with the gel shape to induce large deformations.

A different and more familiar out-of-equilibrium phenomena of hydrogels is when the hydrogel is taken out of the solvent and left to dry. In this case, kinetic phenomena drives the evaporation of water such that the gel starts shrinking until it collapses. On the contrary to water droplet evaporation, the interaction between the solvent and the polymer network can affect the kinetics of the process, potentially slowing them down and in extreme cases even favoring the absorption of water from the environment. This evaporation of hydrogels have been extensively studied for applications in water retention and water harvesting and exploited in commercial applications like plant watering [93, 94].

## 3.4 Water evaporation of spherical hydrogels

In this section, motivated by a collaboration with AgroBio S.L. aimed at containing inside gels liquid diet for predators that eat plagues at greenhouses, we present the development of a fabrication setup for chitosan spherical hydrogels and study the water evaporation from these gels, since this can be relevant for their potential use. Additionally, we propose, fabricate and test a prototype for upscaling the production of hydrogels to industrially relevant levels.

We chose hydrogels to contain the liquid diet since gels are highly porous materials composed in their majority by solvent[2] all the while being mechanically solid and easy to manipulate. Chitosan has been chosen as the hydrogel polymer due to its biocompatible, biodegradable, antifungal and antibacterial properties [95, 96].

[1] In the original papers it was referred to as Pringle shape.

[2] Typically, between 90% and 99.9% of the hydrogel mass corresponds to the solvent.

### 3.4.1 Fabrication of chitosan spherical gels

Chitosan is an aminopolysaccharide polymer that is obtained through the deacetylation of chitin, a natural polymer that forms the exoskeleton of crustaceans. The molecular weight and properties of chitosan polymers depend on the degree of deacetylation, which determines the number of amine groups in the chain, which in turn affects their solubility in water. Although there are some physical gelation mechanisms that allow making gels directly from a chitosan polymer solution exploiting intermolecular interactions that can be tuned through external conditions like pH [97, 98], we are interested in chemical cross-linking between chains that can be induced with UV illumination. To achieve this, the chitosan polymers have to be functionalized with acrylate groups that can be covalently bonded through a free-radical polymerization reaction started by a photo-initiator when the solution is illuminated with UV light. Based on [99, 100] we first create a protocol for producing a UV photopolymerizable chitosan solution that can be used to produce our spherical gels.

#### 3.4.1.1 Photopolymerizable solution

To obtain a photopolymerizable solution we first synthesize methacrylated chitosan. In the process, acrylate reactive groups are added to the chain. To this end, commercial low molecular weight chitosan (Sigma-Aldrich, molecular weight, $50 - 190kDa$, >76% deacetylation) is first dissolved in a 4% acetic acid (Sigma-Aldrich, 99% pure) solution in deionized (DI) water at a concentration of 1.5 wt%. Chitosan is poorly soluble in DI water, so acetic acid is added to lower the pH, protonating the chitosan amine groups ($NH_3^+$) and increasing the solubility of chitosan significantly. After stirring overnight to ensure the chitosan polymer is fully dissolved, methacrylic anhydride (Sigma-Aldrich, 94% pure) is added as purchased at a 5.58 v/v% which roughly corresponds to 8 methacrylate molecules per monomer. The reaction is left stirring overnight at $50°C$. The resulting solution of methacrylated chitosan has a milky aspect due to the poor solubility of the methacrylic anhydride which forms an emulsion under stirring. The number of methacrylated units of the polymers will in general depend on the amount of methacrylic anhydride used. Since the cross-linking is produced between methacrylated monomers, this can also have an impact on the final crosslinking density of the gel.

To get rid of the unreacted methacrylic anhydride and acetic acid molecules, the methacrylated chitosan solution is transferred into dialysis tubing (RC tubing MWCO: 12-14 $kDa$) and dialyzed against DI water for 3-4 days changing the water bath every 12 hours. The volume of the DI water bath is ten times larger than the volume we intend to dialyze. The solution is collected in 50 mL Falcon tubes, frozen overnight and freeze-dried (Labconco Freezone 2.5L-50C)

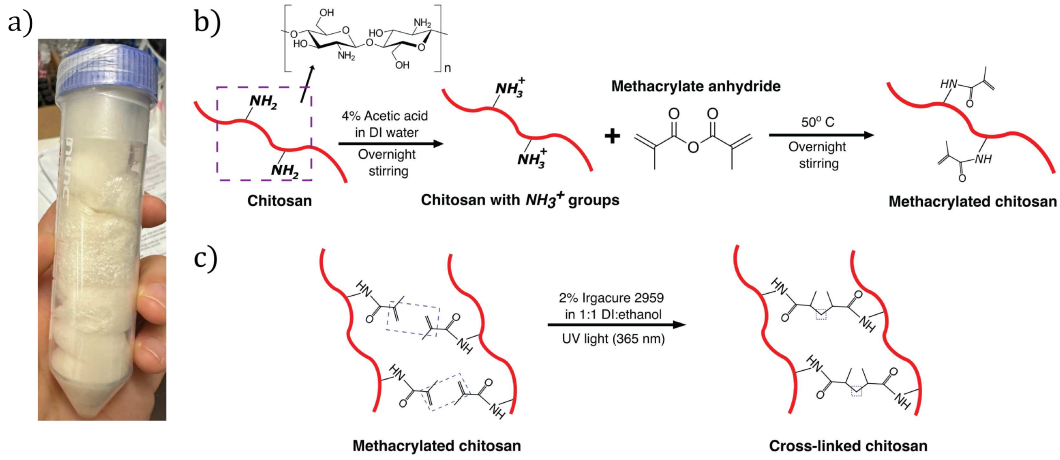



**Figure 3.4:** a) Schematic of the reaction to produced methacrylated chitosan. b) Schematic of the crosslinking reaction between methacrylate group induced by UV excitation of the photoinitiator. c) Image of the methacrylated chitosan in a falcon tube after freeze-drying.

over 3-4 days to recover the methacrylated chitosan, which has a white foamy texture (see Figure 3.4a). The freeze-dried samples are sealed and stored at room temperature.

With the methacrylated chitosan we can make the photopolymerizable solution whenever we need to make gels. First, the methacrylated chitosan is redissolved in DI water at the desired concentration. We use a 1.5 wt% concentration in our experiments. It is important to note that methacrylated chitosan is still not very soluble in water and can take a long time to redissolve in water under stirring. This process can take up to a week depending on the outer solution and can be sped up by separating the foam into small pieces and shaking the flask from time to time. Even then, chitosan does not completely dissolve and some micrometer aggregates are still present. Finally, a 2wt% solution of photo-initiator (Irgacure 2959, 2-Hydroxy-4'-(2-hydroxyethoxy)-2-methylpropiophenone, Sigma-Aldrich) in a 1:1 water/ethanol mixture is added to the methacrylated chitosan solution in a 1:10 ratio to get the final photopolymerizable solution.

Under UV illumination, the polymer in the solution crosslinks forming a hydrogel. UV illumination starts a free-radical polymerization reaction through the photo-initiator molecules that crosslinks adjacent methacrylate groups. A schematic of the methacrylated chitosan synthesis and cross-linking process between methacrylated chains is shown in Figure 3.4b,c.

#### 3.4.1.2 Spherical hydrogel fabrication

To make spherical hydrogels we exploit the surface tension driven tendency of fluids to form spheres when placed in an immiscible fluid. We first make droplets of the photopolymerizable solution on the top of a silicon oil column and illuminate them with UV as they fall. UV induces the crosslinking of the photopolymerizable droplet resulting in a chitosan gel.

To make larger amounts of spherical gels we use a custom setup (Figure 3.5a-c) consisting on a container with both an oil column on top where photopolymerization takes place and a water bath in the bottom where the solid gels get collected, and an injector device which generates the droplets of the photopolymerizable solution. The container consists on a 750 mL plastic jar with a circular whole on the lid where a UV transparent PMMA tube (Plexiglas 0A070GT) is glued. The oil column is made by filling the plastic jar first with water and adding silicon oil on top such that it fills the tube as shown in Figure 3.5b. Teflon tape is added to the lid thread to avoid leaks coming from hydrostatic pressure. A spigot is also added to the bottom of the jar to manually drain the container avoiding overflow of the solution at the column top as the level rises when polymer solution is injected.

To make the photopolymerizable droplets we use a simple device consisting on a pulled capillary tip connected to a syringe pump that pumps the solution at a fixed rate. The tip is placed at the top of the oil column and inside of it. The flow rate is chosen slow enough such that the solution is injected in the dripping regime and droplets attached to the tip grow until their weight overcomes surface tension. At this point, the drop detaches and starts falling through the oil column (see inset of Figure 3.5c). In this regime, the drop size is determined by the balance between gravitational and capillary forces such that $\gamma d_{tip} = \frac{\pi}{6}\Delta\rho g d_{drop}^3$ where $\gamma$ is the surface tension, $\Delta\rho$ the density difference between the polymer solution and outer oil, $d_{tip}$ and $d_{drop}$ the tip and droplet diameter respectively and $g$ the acceleration of gravity. Depending on the target gel size and the properties of the solutions, the tip diameter can be varied to produce droplets of the desired diameter.

Once the drop detaches from the tip, it starts falling through the oil column. The falling time is determined by the density difference between the polymer solution droplet and silicon oil which determines the falling force, the viscosity of the oil which determines the drag force (the more viscous the slower) and the length of the tube. In our setup the tube is $\sim 15\,cm$ long with an outer diameter of $40\,mm$ and we use silicon oil of 500cP viscosity (Calsil IP 500) to fill the column. As shown in figure 3.5a, as the drop falls, it is illuminated with UV light from a 75W point source (Dymax Bluewave 75) situated at $\sim 9\,cm$ from the tube center such that the tube is completely illuminated. We block the UV light path towards the tip to avoid polymerization of the forming drops

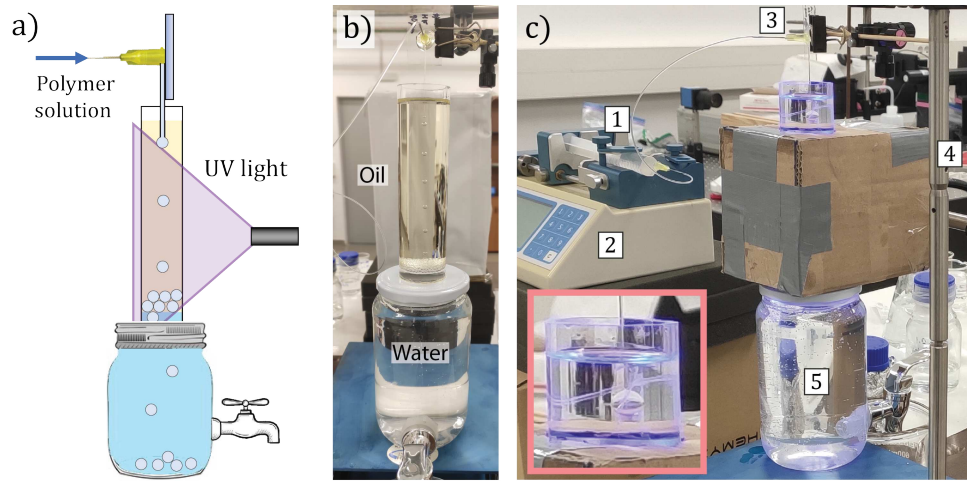



**Figure 3.5:** a) Schematic of the working principle of the setup. b) Image of the setup injecting water droplets which accumulate at the interface between the oil and the water. c) Image of the working setup. The cardboard box is added to contain the UV light. The numbers correspond to: 1. Syringe with polymer solution, 2. Syringe pump, 3. Microfluidic device consisting in an injecting tip, 4. UV optical guide (small cable) and 5. Water bath where gels are collected. Inset shows a magnification of a droplet being formed at the tip.

which could alter their shape.

Crosslinking takes place as the droplets fall through the oil column. Ideally, the falling time should be tuned by selecting the outer oil viscosity such that it is large enough so that droplets are fully cross-linked when exiting the oil column. For droplets of size $d_{drop} \approx 7 - 8mm$ produced from a $300\,\mu m$ pulled tip in $500\,cP$ silicon oil, the falling time is $\sim 60s$. This time is not enough to fully crosslink the droplets. Nevertheless, as the droplets get to the oil-water interface in the jar, they stay there for some time allowing for further crosslinking before crossing the interface. If the interface between water and oil is set in a region illuminated by UV, this gives enough extra polymerization time such that the gel becomes fully cross-linked. It is also important that consecutive droplets are not made too close since, if they get in contact too soon, they can coalesce before full polymerization forming a deformed blob. This can be controlled by setting the flow rate of the syringe pump. We make our gels using a flow rate of $8\,mL/h$.

To recover the resulting chitosan gels, we first extract the oil from the top with a syringe and use the spigot to drain some water until the level drops below the plastic jar height. Then, we can open the jar, scoop some of the extra floating oil and pour the solution into a coffee filter placed on a funnel. This

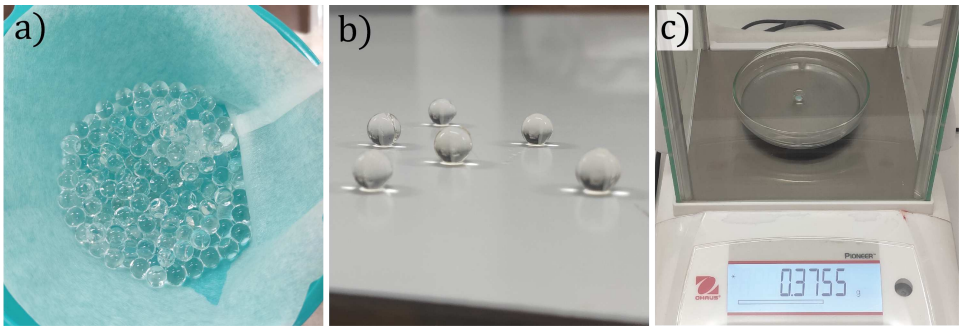



**Figure 3.6:** a) Chitosan gels on a coffee filter on top of a funnel after the collection bath is filtered out. b) Individual chitosan gels on a table where the spherical shape can be appreciated. c) Measurement setup for the mass evolution of a single gel as it dries. The gel is located at the center of a Petri dish. On top of the balance a big cardboard box is also added.

way, we can easily separate the gels from the solution (see Figure 3.6a). The gels can be stored in falcon tubes filled with water to prevent drying. An image of some spherical chitosan gels is shown in Figure 3.6b.

### 3.4.2 Single gel drying

#### 3.4.2.1 Experiments

To measure the water retention capabilities of our gels we first start studying the drying behavior of single gels. We monitor the weight as a function of time for a single gel placed on an analytical balance (OHaus Pioneer Precision PX). The weight is monitored with an external computer connected to the USB port of the balance through a custom made program that stores the measured weight as a function of time in a txt file.

Drying can indeed be affected by the external conditions such as air currents, temperature, local water vapor saturation in closed environments and relative humidity changes in the room. To get consistent data, we fix the room temperature with AC in the lab, leave the box of the analytical balance open such that there can be exchange of water vapor with the room and cover the whole balance with a big box to avoid air currents. The box is big enough such that there is not an observable change in relative humidity inside both the cardboard box and analytical balance cage during the single gel drying experiments[1]. With this last step, we avoid convection such that the main process affecting the gel evap-

[1]This has been verified experimentally by monitoring the relative humidity change during a single gel drying experiment.

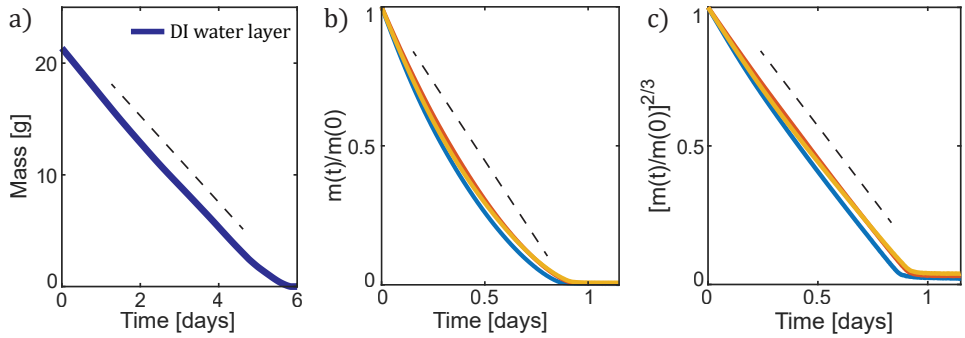



**Figure 3.7:** a) Mass evolution curve of a DI water layer. The dashed black line is a guide to the eye. b) Normalized mass evolution for the evaporation of single gels. The three curves correspond to different gels of the same batch. c) Scaled normalized mass evolution of graph b). The lines become more straight as can be seen by comparing with the dashed black line which serves as a guide to the eye.

oration becomes diffusion. The room external relative humidity is uncontrolled but monitored with a hygrometer.

We initially test our program by monitoring the mass evolution of a layer of DI water (Figure 3.7a). In this case the weight drops linearly, indicating that the evaporation rate is constant. This is expected since although water is evaporating, the interface shape and area does not change with time, so if the system is in steady state, the evaporation rate has to be constant.

We then study the evaporation of single gels from the same batch. The gels are made from a 1 wt% methacrylated chitosan photopolymerizable solution. The experiment is performed by placing a Petri dish on the balance, taring it and placing the gel in the middle as shown in Figure 3.6c. Before starting the measurement the extra water that can be outside the gel is absorbed with absorbent paper. In Figure 3.7b the normalized mass evolution of different gels from the same batch is shown. From this plot we can deduce two main things. First, the evaporation rate is not constant as shown by the non-linear profile, which indicates a dependence of the evaporation rate with respect to the size of the gel. Secondly, there is some variability in the evaporation rate between different gels even when they are from the same batch. This can be attributed to differences in the experimental conditions between experiments and/or differences between gels of the same batch. This last case is reasonable since not all the gels spend the same amount of time under UV illumination and we can also not guarantee that the methacrylated chitosan is completely dissolved in the photopolymerizable solution so that there might be small aggregates which will result in a somewhat inhomogeneous structure in the gel and further variability between gels.

#### 3.4.2.2 Maxwell's evaporation model

To understand the mass evolution of the gels during water evaporation we first resort on a simple model attributed to Maxwell [101, 102, 103]. In this model, we assume that the evaporation of the gel is limited by diffusion of the water molecules from the surface to infinity. Evaporation is taken to be effectively instantaneous so the water vapor concentration at the surface equals the saturation concentration corresponding to 100% relative humidity. The evaporation rate is given by the diffusion of the water vapor molecules out of the surface, since the water molecules that evaporate substitute the ones that leave the surface surroundings. The diffusion process can be modeled using Fick's laws for diffusion:

$$\vec{J} = -D\nabla c \tag{3.22}$$

$$\frac{\partial c}{\partial t} = D\Delta c \tag{3.23}$$

where $\vec{J}$ is the water vapor concentration flux, $c$ the water vapor mass concentration, $D$ the diffusion constant of water molecules in air and $\Delta$ the Laplacian. If we assume that the process is quasistatic, the profile at each time corresponds to the equilibrium profile that can be obtained by solving equation 3.23 with the time derivative equated to zero:

$$\Delta c(\vec{\mathbf{r}}) = 0 \tag{3.24}$$

which is Laplace's equation. Solving the equation we obtain the water vapor concentration profile. From this profile we can compute the evaporation rate by computing the water vapor flux at the surface and integrating it over the whole surface:

$$\frac{dm}{dt} = -\iint \vec{J} \cdot \hat{v} dA = D \iint \nabla c \cdot \hat{v} dA \tag{3.25}$$

where $\hat{v}$ is a vector normal to the surface pointing outwards and $dA$ the differential area element. In Maxwell's model, a floating sphere in space is assumed, so spherical symmetry is considered and the water vapor concentration is fixed both at the droplet surface where it has the saturation value $c(R) = c_v$ and at infinity, with the concentration given by the relative humidity at infinity $H$ as $c(\infty) = c_v \cdot H$. Fixing the relative humidity at infinity is a reasonable assumption since in experiments, infinity effectively corresponds to the room that has a constant water vapor concentration. Solving Laplace's equation and applying the boundary conditions results in the water vapor profile:

$$\begin{aligned} c(r) &= \frac{A}{r} + B \\ c(r) &= \frac{R}{r} c_v(1-H) + c_v H \end{aligned} \tag{3.26}$$

where A and B are integration constants. Introducing this concentration profile into equation 3.25 the rate of change of the mass becomes:

$$\frac{dm}{dt} = -4\pi D c_v (1-H) R \tag{3.27}$$

Since hydrogels are made of ∼99% of water we can assume that the density does not change significantly during the shrinking process until the very late stages and can be taken as the density of water. Using the relation between radius and mass $m = 4\pi\rho_w R^3/3$ and plugging it in the previous equation assuming that only the radius depends on time, we obtain a first order differential equation that gives the evolution of mass with time:

$$m(t) = \frac{4\pi}{3}\rho_w \left( R(0)^2 - \frac{2Dc_v(1-H)}{\rho_w} t \right)^{\frac{3}{2}} \tag{3.28}$$

where $\rho_w$ is the density of water and $R(0)$ the initial size of the gel. From this equation we can see that $m(t)^{\frac{2}{3}}$ should depend linearly on time. If we take the mass evolution data of Figure 3.7b and instead plot $m(t)^{\frac{2}{3}}$ vs $t$, we can see that the experimental profile indeed becomes linear (see Figure 3.7c) as predicted by this simple model. This indicates that the gel evaporation in our case is driven by a diffusion limited process.

The previous model, although describing the behavior of the data, makes the unrealistic assumption of a floating sphere. If we take now the real geometry of our problem, we can still use equation 3.24 to get the evaporation curve behavior. First, if $c_{sol}(\vec{\mathbf{r}})$ is a solution to the equation, then $c_{sol}(\vec{\mathbf{r}}/R)$ is also a solution of Laplace equation. This change of variables can be understood as an expansion/contraction of space. This means that if the system change over time can be described by a spatial contraction or expansion, we can use the solution of a system of size 1, $c_1(\vec{\mathbf{r}})$, to describe the solution at any time. We also need to make sure that the new boundary conditions are the same, which is immediately fulfilled if the boundary conditions impose a certain value of the concentration or zero flux through a surface. Then, the solution to the system of size R is indeed described by $c_1(\vec{\mathbf{r}}/R)$.

With this form of the solution in terms of the system radius, we can obtain the scaling of the mass time derivative with the gel radius as:

$$\frac{dm}{dt} \propto R^2 \cdot \frac{1}{R} \propto R \tag{3.29}$$

where the $R^2$ comes from the scaling of the surface area with the size of the system and the $1/R$ term comes from the scaling of the gradient of the concentration profile as a function of R: $\nabla_{\vec{\mathbf{r}}}\, c_1(\vec{\mathbf{r}}/R) = (1/R)\nabla_{\vec{\mathbf{u}}}\, c_1(\vec{\mathbf{u}})$ with $\vec{\mathbf{u}} = \vec{\mathbf{r}}/R$. From basic electrostatics we know that the electric field, which in our case is equivalent to the water vapor concentration flux, depends only on potential differences and not on the exact values at both boundaries. This comes from the fact that if $g(\vec{\mathbf{r}})$ is a solution, then $a \cdot g(\vec{\mathbf{r}}) + b$ is also a solution with $a$ and $b$ constants. Taking into account that the flux is proportional to the diffusion constant, the derivative of the mass with time can be written as:

$$\frac{dm}{dt} \propto -DR(c(R) - c(\infty)) = -DRc_v(1 - H) \tag{3.30}$$

where the minus sign is added to take into account that the mass decreases with time. With this, we can express the final differential equation as:

$$\frac{dm}{dt} = -4\pi DRc_v(1 - H)f \tag{3.31}$$

This equation has the same form as equation 3.27 except for a proportionality constant $f$ that captures the exact geometrical details of the problem.

The differential equation results in the same dependence of $m$ with $t$, but relies on the assumption of spatial expansion/contraction of the system with time. Interestingly, in our case, this is fulfilled since due to the solid nature of the gel, it remains spherical with time and thus, as it contracts, it shrinks. Also, since the gel is located on a flat surface, the whole system consisting on the flat plane plus the sphere can be seen as contracting as the sphere shrinks. Moreover, the boundary conditions are either no flux on the plane boundary or fixed concentration at the surface of the gel and at infinity.

In experiments regarding the drying of droplets on top of a surface, if the droplet is too large, gravity deforms the drop in a way that the shape could be dependent on its size; in this case the affine deformation assumption does not hold. The droplets need to be small enough for gravity to not play a role so that the shape is given by a spherical cap. In this case, the main parameter is the proportionality constant $f$, which depends on the contact angle $\theta$ for droplets on flat substrates [104, 105, 106]. Since our gels are mechanically solid, sphericity is maintained independently of their size. In our case, since we can also have the effect of the polymer in evaporation, we split the constant into the shape contribution coming from the sessile droplet experiments $f(\theta)$ and a contribution coming from the gel, $\alpha_{gel}$. The final form of the mass evolution with time is:

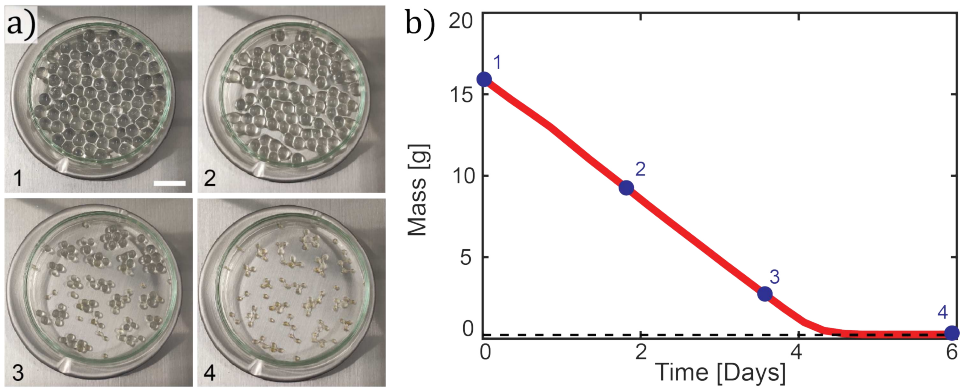



**Figure 3.8:** a) Images of the different stages during the evaporation of a layer of chitosan gels. Scale bar is $2\,cm$ b) Mass evolution curve of the gel layer shown in a). The dashed black line corresponds to the estimated polymer mass in the gels. The blue points correspond to the time where the images were taken.

$$m(t) = \frac{4\pi}{3}\rho_w \left( R(0)^2 - \frac{2Dc_v f(\theta)\alpha_{gel}(1-H)}{\rho_w} t \right)^{\frac{3}{2}} \tag{3.32}$$

For now, we define $\alpha_{gel}$ as a phenomenological parameter describing the possible slow down of evaporation due to the presence of the polymer network.

### 3.4.3 Effects of gel proximity on drying: Local saturation

We next study the effect of gel proximity on the drying curves. The extreme case corresponds to having the Petri dish completely filled with chitosan gels forming a layer. In this case, the mass evolution over time shows a linear relationship (Figure 3.8b), which implies a constant evaporation rate as in the case of a water layer. At the beginning, the constant evaporation rate can be rationalized by observing that the evaporation of the 2D lattice of gels can only take place in one dimension, from the top part like for the fluid layer. Contrary to the water layer where the surface covers the whole area of the Petri dish at all times, as the gels start shrinking they start separating from each other as shown in the experimental images of Figure 3.8a. Nonetheless, the evaporation rate remains constant, which indicates that the water evaporation is still effectively one dimensional. This means that although the gels are separated, the air in between them is saturated with water vapor, such that the water vapor flux is in the vertical direction through the whole surface of the Petri dish, keeping the evaporation rate constant.

When the gels completely dry, they become small stiff spheres that sometimes are attached to gels that were initially in contact with through thin filaments. This indeed can be understood as a result of aggregation between polymer chains of adjacent gels due to intermolecular interactions. This strong aggregation of chains can also explain the fact that a dried gel in water solution does not swell back to its original size but only swells a little to a non-spherical shape.

To further assess the local saturation effect between gels we measure the mass evolution curves of hexagonal arrays of gels with different lattice spacing (Figure 3.9a). The results show that as the gel separation is increased the evaporation rate also increases and the gels dry faster (Figure 3.9b). Indeed, when the separation between gels is $4\,cm$ the $m(t)^{2/3} \sim t$ scaling for single gels is recovered. At this separation, the nearby gels do not affect the evaporation rate any more and the gels behave as if they were effectively alone.

In this last case we obtain a evaporation curve which averages the variability between the individual gel experiments reported before. Using this curve we can fit our data to equation 3.32 to obtain a estimation for $\alpha_{gel}$. To fit the equation we use reported values of the parameters at $293K$: $D = 0.242\,cm^2/s$ [107] and $c_v = 17.3\,g/m^3$ [108]. The density of water is approximated by $\rho \approx 1000\,kg/m^3$ and we use as the relative humidity at infinity the characteristic one measured in the lab at the time of the experiments $H \sim 0.4$. For computing the constant $f(\theta)$ we use the polynomial fit $2f(\theta) = 0.00008957 + 0.633\theta + 0.116\theta^2 - 0.08878\theta^3 + 0.01033\theta^4$ [104] and measure the contact angle of our gels, which is $\theta = 142°$ (see inset Figure 3.9c).

We can see that if we do not take into account $\alpha_{gel}$, both the curves for the ideal case $f = 1$ and the model for a drop on a substrate $f(\theta = 142°)$ decay more rapidly than the experimental one (Figure 3.9c). When using the whole expression with $\alpha_{gel}$ as the fitting parameter the decaying slope is matched when $\alpha_{gel} \approx 0.75$ (Figure 3.9c). This indicates that the polymer network indeed plays a role in slowing down the evaporation rate.

### Physical origin of evaporation rate slow-down

To understand the physical origin of the evaporation slowdown when the polymer network is present, it is important to note that in the model used we have made the assumption that the water vapor concentration at the surface corresponds to the saturation concentration of pure water and that the evaporation rate from the gel was fast enough to ensure the saturation at the surface. The real effect of the polymer network can be reduced to a change in the water vapor concentration at the surface. This reduction can have two possible origins, a static one where the equilibrium vapor concentration for the polymer hydrogel is smaller than pure water, as for example occurs for supersaturated salt solu-

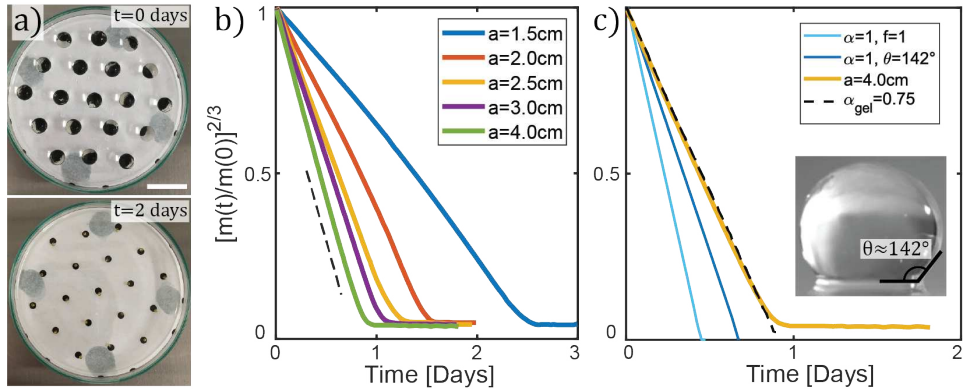



**Figure 3.9:** a) Example of lattice with spacing $2cm$ indicated by the black dot template. Top image shows initial placement of gels and bottom image show the gels after drying in the lattice arrangement. b) Scaled normalized mass evolution for different lattice spacing $a$. The cures shown correspond to an average of different experiments. The dashed black line is a guide to the eye for the slop of the green curve. c) Scaled normalized mass evolution of the experimental curve for spacing $4\,cm$ (yellow) together with the theoretical curves for the free floating sphere (light blue), droplet with contact angle $\theta = 142°$ (dark blue) and taking into account contact angle and $\alpha_{gel}$ (dashed lines). Inset shows a side image of a gel together with the contact angle measurement.

tions (Figure 3.10a), and a dynamic one, where the evaporation speed is not fast enough and becomes comparable to the diffusion rate at the surface. In this last case, the evaporation process is unable to keep the equilibrium concentration at the surface, $c(r = R) = c_v$, due to the presence of a barrier against evaporation. This barrier lowers the evaporation speed, thus lowering $c(r = R) < c_v$ to sustain a steady-state process.

We measure the equilibrium vapor concentration by placing hydrogels inside a closed container with a hygrometer and monitor the relative humidity evolution until it saturates. For a room relative humidity of 40 or 60%, $\alpha_{gel} = 0.75$ results in an relative humidity at the surface of 85 or 90%. The experiments show that the relative humidity always goes above these values up to 100% (Figure 3.10b), indicating that the effect of the polymer gel is not on the equilibrium water vapor concentration but on the evaporation rate.

The role of the chitosan polymer gel network can then be understood from the interaction between the solvent and the polymer network which affects the free energy of the water molecules. This potentially increases the energetic barrier the water molecules have to overcome to escape the gel and thus reduces the evaporation rate.

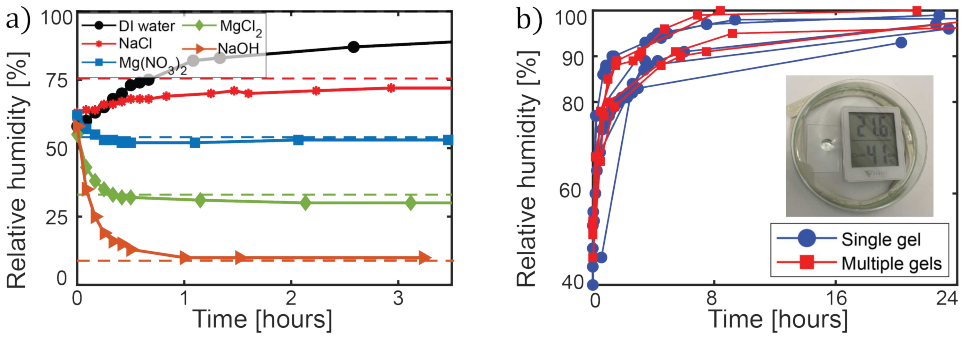



**Figure 3.10:** a) Measurements of the relative humidity evolution of a closed chamber with a solution of supersaturated salts in it. Solid lines with points represent the experimental data while the dashed lines correspond to the expected reported values in literature. DI water solution goes to 100% relative humidity at longer times. b) Evolution of the relative humidity of gels inside the closed container. Blue lines correspond to the evolution of the relative humidity for a single gel in a small chamber while red lines correspond to multiple gels in a larger chamber. All lines go above 90% with time and the longer measurements show saturation at 100% relative humidity. Inset image show the experimental setup for the single gel experiment.

The static change in the equilibrium water vapor concentration can be obtained for gels made of other materials [94]. If the polymer network is hygroscopic, the water vapor concentration in the atmosphere can be larger than the equilibrium one and the gels can absorb water from the surrounding atmosphere.

## 3.5 Upscaled prototype for the continuous production of spherical hydrogels

While the previous gel generation setup worked very well for laboratory scale production of chitosan gels, upscaling it for industrial application is desirable. For the size of gels of interest and an injection rate of $8\,mL/h$, we obtained a yield of $\sim 30$ gels/h with the laboratory scale setup, resulting in $\sim 250$ gels per 8 hours of work. Additionally, controlling the level by draining from the spigot to avoid overflow was required along the operation time. Finally, the setup had to be disassembled to recover the gels, cleaned and mounted back for subsequent gel generation rounds. In this section, we describe the operating principles, design and construction of an upscaled gel production setup and briefly describe tests on injection efficiency and gel polymerization performed.

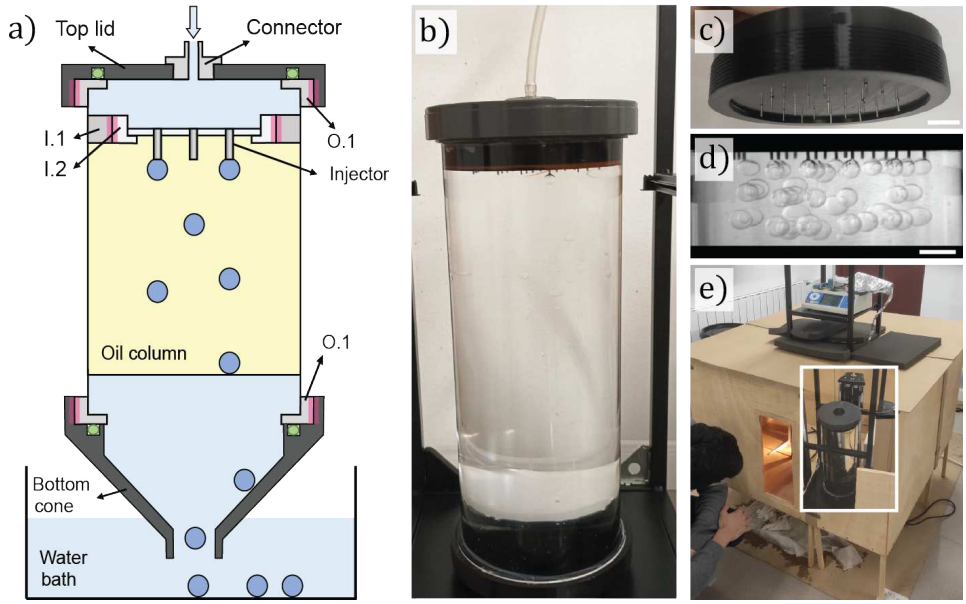



**Figure 3.11:** a) Schematic of the design for the upscale prototype with the more relevant parts labeled. The circles show the expected droplet path as it follow while polymerizing and cross the interface as a solid gel getting collected in the water bath. Green circles represent O-rings and pink areas depict regions where there is a thread. b) Image of the built prototype on a custom stand. c) Piece I.2 with 19 capillaries forming a hexagonal lattice arrangement with 2 cm separation. d) Experimental image showing the generation of droplets with the above capillaries. e) Custom wooden box to cover the setup while it is illuminated with UV. The white rectangle shows an image of the prototype inside the box. Scale bar is 2 cm.

### 3.5.1 Prototype: Principle of operation and design

A schematic of the upscaled prototype is shown in Figure 3.11a. The setup is very similar to the previous lab scaled prototype with a few key differences. First, the production rate is increased by parallelizing the drop generation using several injectors instead of the single one used for the lab scaled setup. This requires a bigger container for both the oil and water solutions. Second, the container is placed inside a water bath and opened from below. To keep the column in place, the container is air-tight such that the vacuum keeps the column together. This way, we do not have to periodically empty the container as the solution is pumped and the gels can get out of the container into an external one that can be retrieved during the setup operation. This will result in a setup that can produce gels continuously that are then stored out of the gel generation container.

To parallelize the injection we use a bigger UV transparent PMMA tube (150 mm outer diameter and 400 mm in length). Inside it, we glue on the top part a 3D printed (BCN3D Sigma D25) female thread (piece I.1). The multiple injectors are incorporated through a 3D printed disk with small holes forming a lattice where 1 $mm$ diameter 10 $mm$ long metal capillaries (Unimed AISI 304 tubing) are pressure fitted. The disk is glued to a male thread forming piece I.2 (see Figure 3.11c) which is then threaded to the female piece I.1. This separates the tube into two parts, a top one that will be filled with the solution to inject and the bottom one consisting on the oil column located on top of the water bath.

To seal the container, two outer male threads made from PVC are glued to the top and bottom part of the tube (piece O.1). On the bottom thread, a cone shaped piece with a cap is threaded (piece bottom cone) while the top part consists on a lid (piece top lid) that is threaded and has a threaded whole in the middle to put a custom designed connector (piece connector) that will interface with to the injection system. To ensure air-tightness, teflon tape is added to the threads and O-rings are used to seal the threaded pieces. Vacuum grease is used as a lubricant between pieces to facilitate the disassembling of the setup when necessary. The connector of the top lid is connected to plastic tubing through which the solution is injected. We explore two options for injecting the solution, either a flow controlled one using a peristaltic pump, or a hydrostatic pressure driven one controlled by the height of an outer reservoir connected to the connector piece. An image of the constructed upscaled prototype is shown in Figure 3.11b. More details on the pieces can be found in Appendix B.

For mounting the setup, we start with the container closed from below and fill it first with water until it reaches the level where we want to place the interface and then add 500cP silicone oil on top until it just reaches the thread level. We now screw in the piece with the capillary injectors until oil gets out of the capillaries. To avoid air pockets between the tips of the capillaries and the disk, before threading the disk, several capillaries are pushed back so air can escape through them while threading and once everything is in place they are pushed back to position. The top part is then cleaned from the extra oil and the rest of the tube is filled with the injection solution. The top lid is closed, the cylinder placed on a custom stand with the bottom part inside an outer water bath and the injection system is connected through the top connector making sure there is no air in between. Since the peristaltic pump acts as a check valve, the setup can now be opened from below and the column will hold in place.

From this point on, the injection can be tested. For the gel polymerization, a custom wooden box with a UV blocking watching window is built so the tube is placed inside together with the UV light sources (Figure 3.11e) . Inside the box there is enough place to fit 3 rectangular UV lamps (Spectro-UV XX-15A),

the point source Dymax Bluewave 75 and other sources if more power is needed. There is also the possibility to add ventilation to the setup if heating becomes an issue.

### 3.5.2 Injection tests

We first test the drop generation part of the setup injecting water. With these tests we want to assess whether the drop generation is satisfactory and if there is drop coalescence during falling. We initially use the peristaltic pump to control the flow rate. An experimental image of the drop formation using the upscaled prototype is shown in Figure 3.11d. In terms of coalescence, experiments with arrangements of 3 capillaries at different distances between them ($d = 1.5cm$, $d = 3.0cm$, $d = 5cm$) and with the wall (centered or close to the wall) have been done. Except for the case when the capillaries are close to the edge, falling drops do not coalesce. From now on, we will use a capillary separation of $d = 2cm$ and avoid positioning capillaries close to the wall.

When checking the drop generation process at different flow rates, we find that not all injectors produce drops simultaneously. At low flow rates only one capillary starts injecting while as the flow rate increases, the number of injectors increases. This can be especially seen when using a setup with 19 injectors forming a honeycomb lattice with separation $d = 2\,cm$. In this case, as the flow rate increases, the number of simultaneously working injectors, $N$, increases until it reaches a plateau of $N \approx 14 - 17$ at about $50\,mL/min$ (Figure 3.12a). At this plateau, not all injectors produce droplets. If the flow rate is increased further, $N = 19$ can be achieved, but at this point the injection occurs in the jetting regime.

We understand this effect by noticing that the capillaries are not independent but are connected through the water solution. To start the formation of a drop in a given capillary, the pressure difference between the water and oil bath has to be large enough to overcome the Laplace pressure difference of the smallest drop hanging from the tip, which has the diameter of the tip, $d_{min} = 1\,mm$: $\Delta P = 4\gamma/d_{min}$, with $\gamma$ the interfacial tension. If we think on the injection process, once we start the injection, the pressure increases until it overcomes the pressure threshold and a random injector starts injecting at the set flow rate. As the drop forms, the pressure is reduced and is not high enough to start injection from other capillaries. Increasing the flow rate increases the pressure until the threshold is overcome and another injector starts injecting. This explanation is supported by the occasional observation of a small droplet hanging on an injector being sucked back as bigger droplets are formed in other capillaries, which shows that the pressure on the smaller droplets is larger and favors the flow from small droplets to large droplets in a fashion reminiscent of "Ostwald ripening". Furthermore, the injecting capillaries are not always the

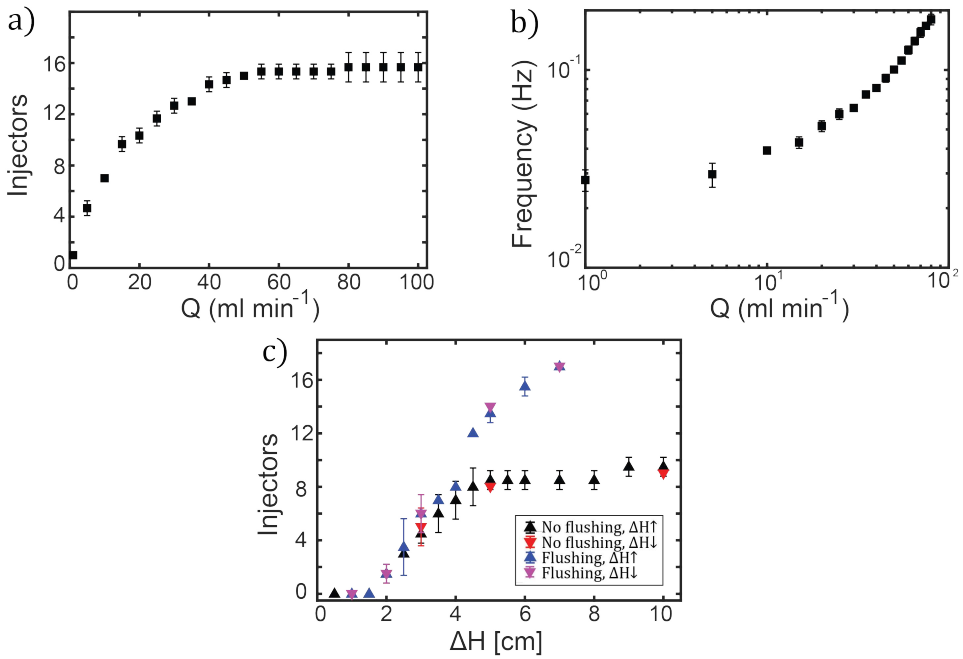



**Figure 3.12:** a) Number of simultaneous injectors as a function of the flow rate imposed by the peristaltic pump. b) Drop generation frequency per capillary as a function of the flow rate imposed by the peristaltic pump. c) Number of simultaneous injectors as a function of the height of the reservoir with respect the water bath.

same for the same flow rate and switch between different ones from time to time, indicating that it is not likely related to local differences between capillaries.

We can also study the drop frequency per injecting capillary as a function of the flow rate in the previous experiment. We can observe that it looks flat at the lowest flow rates probed. As the flow rate increases, the number of injecting capillaries also increases reducing the drop frequency per capillary leaving a flatter profile. As the number of injecting capillaries reaches the plateau, the drop frequency increases linearly with the flow rate, as expected by mass conservation considering a constant drop size (Figure 3.12b). This plot is relevant for tuning the polymerization process since the drop frequency has to be controlled to avoid coalescence before full crosslinking.

Ideally, for the best performance of our prototype, all capillaries should inject at all flow rates so the drop frequency generation can be easily controlled. The main problem with the flow control injection is that pressure is allowed to vary with time. To avoid this, we try using hydrostatic pressure based injection by

changing the height of the water reservoir. The peristaltic pump is used now just as a check valve. In this case, before injection, when the reservoir is elevated, the pressure increases at the capillaries so we expect that when it goes over the critical pressure all capillaries start injecting.

Nonetheless, when performing the experiment, we see that this is not the case and the number if simultaneous injectors increases continuously above a threshold given by Laplace pressure (Figure 3.12c). If we make the experiment after preparing the setup, the number of injectors plateaus at $N = 8$. We attribute this to silicone oil present in some capillaries making it more difficult to inject. When the system is initially brought to the jetting regime ensuring all capillaries can inject, repeating the experiment results in the same continuous increase in the number of simultaneous injectors, but this time the plateau is not observed and we get close to all capillaries injecting for high enough pressures (Figure 3.12c). The origin of this continuous transition in the number of injectors is still not clear.

### 3.5.3 Crosslinking tests

Since the oil column in the upscaled prototype is longer, instead of using a point UV source we use UV rectangular lamps (Spectro-UV XX-15A) that can illuminate the whole length of the column. These lamps are 47 cm long and consist on two 15W halogen tubes with emission peak 365nm, corresponding to the peak absorbance of the photoinitiator used. To test whether we can get full crosslinking with these lamps we test them with the laboratory scale setup positioning two of them at each side of the tube as shown in Figure 3.13a. We make tests with the lamps at two distances from the tube center (D=3.5cm and D=14cm) and two silicone oil viscosities (500cP and 5000cP), which affects the falling time. The injection rate is 8mL/h.

We find that the distance of the lamps does not affect significantly the crosslinking and that the largest change is observed when the falling time is changed. This is reasonable, since the intensity from a line source does not decay as fast with distance as for a point source. In Figure 3.13b we show the resulting gels for a distance D=14cm and the two silicone oil viscosities. As we can see, for low falling times with the 500cP silicone oil, we get solid gels, but before the crosslinking is fully completed, drops get in contact and merge, resulting in crosslinked blobs of merged gels. When the falling time is increased an order of magnitude by using the 5000cP silicone oil, the drops become more individual and merge less. Nevertheless, the high viscosity results in slightly deformed gels and merging is not completely avoided (Figure 3.13c).

We next test the polymerization with the upscaled prototype. To avoid wasting photopolymerizable solution, we use a single injector connected to our usual syringe pump by using a custom made piece. We place the 3 rectangular

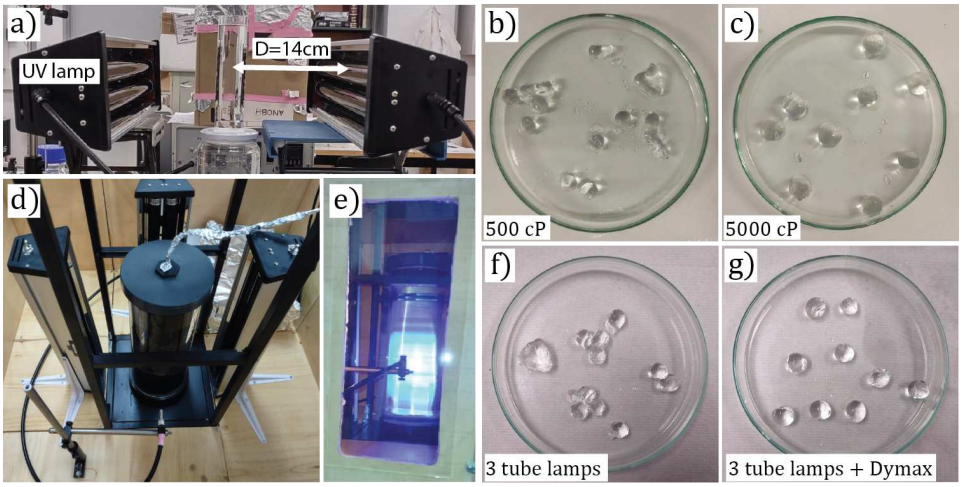



**Figure 3.13:** a) Experimental setup for testing tube UV lamps with laboratory prototype. b) Chitosan gels obtained for a distance D=14cm and 500cP silicone oil. The drops have merged at the interface forming blobs of crosslinked gels. c) Same as b) with 5000 cP silicone oil. Gels are more individual. d) UV lamp setup for crosslinking tests with the upscaled setup. e) Image of the upscaled setup while in the wooden box while UV is on. f) Results of crosslinking test of the upscaled setup using only the 3 tube lamps. Gels are individual but with a flat face. g) Same as before using the 3 tube lamps plus the point source on the bottom half as UV source. The gels are individual and more spherical.

lamps at a distance $\sim$ 20cm from the tube center at the center of three out of the four sides of a square. From the non-occupied edge we place the UV point source at a distance $\sim$ 20cm. Since the point source does not cover the whole length of the tube, we also have the freedom to change its height. Images of the system configuration and during operation is shown in Figure 3.13d,e. During all trials, the collection system worked as desired, with the gels crossing the interface sliding down the cone and falling in the water bath. If a beaker is placed inside the water bath, the gels can be taken out while the system keeps working.

If we only use the 3 rectangular lamps, the resulting gels are not spherical and are flattened on a side. This is due to the fact that the gels are not very crosslinked when they reach the interface and deform there, fully crosslinking in a deformed shape (Figure 3.13f). To add more UV power, we also use the point source. We try placing it both at the top, so it lights the drop while forming and during the first part of the falling, and at the bottom, so that it illuminates more during fall and at the bottom interface. The most spherical and individual gels are obtained when the point source is placed at the bottom half (Figure

3.13g). This test shows the potential of the system to produce chitosan gels in a continuous way when the UV light intensity is high enough for the gels to crosslink fast enough.

### 3.5.4 Overview and further work

The tests on our upscaled prototype for continuous production of spherical gels have proven the potential of the design. On the one hand, injection tests show the capacity for generating droplets from multiple capillaries simultaneously. On the other hand, polymerization tests show the potential for crosslinking the photopolymerizable solution when the UV power is high enough. Additionally, the setup has the capacity to recover the gels while it is in operation.

Although all this tests show that the prototype works according to its design, a full test with photopolymerizable solution and multiple injectors remains to be made to confirm that polymerization of multiple droplets falling simultaneously is possible. This will also allow an exploration of the parameter space to ensure that merging of droplets does not occur before full crosslinking. In this aspect, having enough UV intensity might be crucial, so more powerful UV sources might be needed for obtaining the best results.

## 3.6 Stabilization of non-spherical droplets in yield stress materials

To stabilize the toroidal droplets made using the technique described in section 3.2 we substitute the outer medium by a yield stress material [71]. Yield stress materials are a type of materials that behave as elastic solids below a certain stress, called the yield stress, but flow for larger stresses as non-Newtonian fluids. The shear forces of the tip while moving it through the yield stress material are high enough to locally fluidize the yield stress material allowing the toroidal droplet generation procedure to work. Once the droplet is generated, the main stress responsible for the droplet breakdown is surface tension through the Laplace pressure. If this pressure is higher than the yield stress of the outer material, surface tension is able to induce droplet deformation, potentially breaking up the droplet, while if the Laplace pressure is lower than the yield stress, the outer material will effectively behave as an elastic solid matrix preventing the droplet breakup. This condition can be written as $\Delta P = 2\gamma H = \tau_y$ where $H = (1/R_1 + 1/R_2)/2$ is the mean curvature of the surface, with $R_1$ nd $R_2$ the principal radii of curvature, $\gamma$ the surface tension and $\tau_y$ the yield stress of the outer material.

Small features on the droplet surface with a high enough radius of curvature such that the Laplace pressure is larger than the yield stress spontaneously

smooth down until the Laplace pressure and yield stresses are balanced. Additionally, if the yield stress is high enough such that these small features are stabilized, the formation of "bumpy" droplets is favored. Balancing Laplace pressure of the ideal toroidal droplet with the yield stress of the outer material becomes relevant to generate droplets with smooth surfaces.

### 3.6.1 Yield stress materials

Disregarding whether our droplets are made from a water-based or oil-based material, the outer yield stress medium should be immiscible with them. For the liquid crystal toroidal droplets we are interested in, a water-based yield stress material is needed, while for making hydrogels with different shapes, an oil-based yield stress material has to be used.

#### Water-based yield stress material

As the water-based yield stress material we use a solution of granular-sized acrylate hydrogels (Carbopol ETD 2020) that, when swollen, transition into a jammed state, resulting in the appearance of a macroscopic yield stress. To make the yield stress materials, the hydrogels are dispersed in a water based solution with ethanol, glycerol and surfactant overnight under constant stirring. The pH of the dispersed solution is around 3-4. At this pH the gels are not fully swollen, so we neutralize the solution by adding drops of 2M NaOH solution until pH 7 is achieved. At this pH the hydrogels swell significantly overnight, jamming and resulting in the desired yield stress material. The yield stress material will have air bubbles trapped in it (induced while stirring). We can get rid of them either by centrifuging or degassing the solution. The magnitude of the yield stress will depend on the degree of jamming, and thus, on the initial concentration of Carbopol. Surfactant is added to impose certain anchoring conditions on the director field of the nematic drops. We use polyvinyl alcohol (PVA) for planar anchoring and sodium dodecylsulfate (SDS) for homeotropic anchoring [9, 61].

The original recipe previously used for stabilizing nematic toroidal droplets is [9]:

- Carbopol ETD 2020: 0.5-2.0 wt%
- Glycerol: 2wt%
- Ethanol: 30 wt%
- Surfactant
- Ultrapure water: [100-Carbopol-Glycerol-Ethanol-Surfactant] wt%

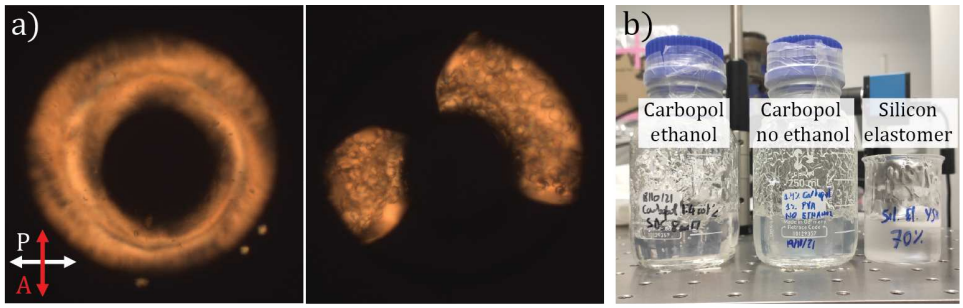



**Figure 3.14:** a) Experimental images of a nematic torus in a yield stress material with ethanol between crossed polarizers. The bright region in the left image corresponds to the nematic toroidal droplet. As time passes, some of it transitions to the isotropic phase becoming dark as shown in the right image. At the end, the whole torus becomes isotropic. b) Image of the different yield stress materials. Their transparency can be compared.

Although this yield stress material works very well for studying nematic tori after they are made giving information on the equilibrium configuration, if the tori are stored for longer times, we observe the spontaneous transition from the nematic to the isotropic phase at room temperature (see Figure 3.14a). This is seen when monitoring a nematic toroidal droplet evolution under crossed polarizers. In the nematic phase, the birefringence of the nematic phase makes the torus bright under crossed polarizers. After a day or two, the nematic torus starts transitioning to the isotropic phase and we observe coexistence between the nematic and the isotropic phase, which becomes dark (see Figure 3.14a right). The isotropic phase slowly grows until the whole torus becomes isotropic at room temperature. We attribute this phenomenon to the diffusion of ethanol inside the liquid crystal 4-Cyano-4'-pentylbiphenyl (5CB), which lowers its transition temperature below room temperature as its concentration increases [109].

Ethanol is added to the previous formulation to increase the transparency of the yield stress material by index matching the refractive index of the water-ethanol-glycerol mixture and the polymer. If ethanol is not added, the sample becomes more turbid due to light scattering. To keep nematic toroidal droplets for longer times we use the following formulation without ethanol:

- Carbopol ETD 2020: 0.5-2.0 wt%
- Glycerol: 2wt%
- Surfactant

- Ultrapure water: [100-Carbopol-Glycerol-Surfactant] wt%



The difference in transparency between the yield stress material with and without ethanol is shown in Figure 3.14b, where the Carbopol without ethanol looks more whitish. Nonetheless, for the length scales of our cuvettes this scattering becomes unimportant and does not affect our experimental observations. Another difference with this new preparation is that the absence of ethanol changes how swollen the gels can become. With just water and glycerol, the hydrogels are able to swell more, so less Carbopol needs to be used to obtain the same yield stress.

#### Oil-based yield stress material

If we want to make non-spherical water based droplets, like for the case of non-spherical hydrogels made by photopolymerization of a photopolymerizable solution, we use an oil-based yield stress material. This material is made from a mixture of a silicone elastomer blend (Dow Corning 9041) and 10cSt silicone oil. The yield stress is controlled by the percentage of silicone oil added, becoming lower for larger amounts of silicone oil. This solution is indeed much less transparent than the Carbopol yield stress material (Figure 3.14b) but still suitable for observation under the microscope.

### 3.6.2 Toroidal droplet generation in yield stress materials

While using a yield stress material as the outer medium allows stabilizing our toroidal droplets, being a more complex material also changes the details of the mechanism for making toroidal droplets. When we have a simple liquid as the outer medium, the cross-section of the toroidal droplet grows very circular, producing toroidal droplets very similar to ideal tori. Using a yield stress material as the outer medium makes the generation process more complicated.

During the droplet generation process, shear stresses are localized very close to the injection tip. This in turn implies that the part of the material that behaves as a liquid as the tip moves is a small cylindrical region around it, while the rest behaves as an elastic solid. When injecting the toroidal droplet fluid, this injected liquid will occupy the volume where it can displace yield stress material easier, corresponding to the fluidized part. This limits the lateral growth of the cross-section resulting in vertically elongated cross-sections [110, 111, 112]. If too much volume is injected, the cross-section grows continuously in the vertical direction forming a tube. In practice, if we want to obtain a toroidal droplet with a circular cross-section avoiding vertical elongation, the maximum diameter of the torus tube should be comparable to the tip diameter. From our experience,

the ideal tube diameter for a torus is around 2-3 times larger than the tip diameter.



Another relevant aspect is that a flowing tip on a yield stress material produces a crevice with its depth determined by the yield stress of the material and the tip speed [111]. For generating toroidal droplets, we should insert the tip deep enough such that the crevice does not reach the toroidal droplet. Sometimes we have also observed an effect where the generated jet does not close onto itself but goes up as the cuvette rotates forming a "helical" droplet.

Finally, even though the cross-section of our droplet tends to be elongated, if the yield stress is tuned to match the largest Laplace's pressure for the ideal torus we want to make, surface tension will smooth the surface towards the desired shape without been able to break the droplet. More details on the most common problems arising when making stable small toroidal droplets and how to solve them can be found in Appendix C.

### 3.6.3 Sample preservation: Cuvette sealing

An important problem of the water based yield stress material for preserving nematic tori for long times is that water evaporates with time, drying out the material and deforming the droplet, breaking it up eventually. To avoid this, we seal our cuvettes. We make custom cuvettes by gluing a 12.5mm side and 5mm length square glass tube on one side of a 12.5x25mm cut glass slide with 5 minutes bi-component epoxy (Devcon). We fill the cuvette with the Carbopol yield stress material and make our toroidal droplet inside it. To seal it, we clean the top edges of the square glass tube, add some epoxy to them and put a 12.5x12.5mm cut glass slide on top of it, not completely covering it letting a small aperture. The size of the top glass slide is chosen to allow placing the cuvette sideways on the microscope to get side view images. Through the aperture we use a pipette to inject 10cSt silicone oil while keeping the cuvette tilted such that it fills the space between the glass and the yield stress material and no air bubbles get trapped. Once the silicone oil slightly overflows, we slide the top glass square until it completely covers the cuvette. We keep it pressed until the epoxy glue fully cures.

With the sealed cuvettes, we can be preserve samples for months and perform repeated experiments with them. The silicone oil is added to roughly index match the yield stress material such that the bumpy interface does not distort the images taken from the microscope. An image of a toroidal nematic droplet in a sealed cuvette is shown in Figure 3.15a.

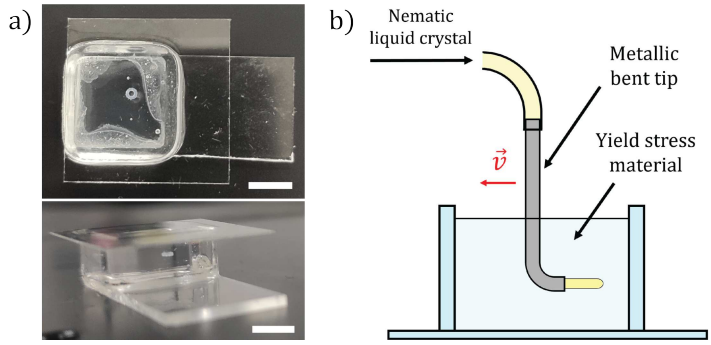



**Figure 3.15:** a) Top and side views of a sealed cuvette with a torus. The top lid for this cuvette is larger than the square tube so it can not be placed sideways. Scale bar is 5mm. b) Schematic of the procedure for generating cylindrical nematic droplets.

### 3.6.4 Generation of nematic cylinders

For generating nematic cylindrical droplets we use a simple modification of the tori generating setup. Instead of rotating the cuvette, this time we use a bent tip and manually move it horizontally with a micromanipulator during liquid crystal injection, as schematically shown in Figure 3.15b. To get good cylindrical tori the motion speed has to be chosen according to the injection rate and kept as constant as possible, so the injected volume substitutes the volume the tip frees up as it moves. The cylindrical droplet generation process can be improved by using a mechanical stage to move the tip [113].

## 3.7 Study of thermoresponsive cylindrical hydrogels: Extreme thermodynamics

Before going back to studying nematic toroidal droplets, we end this chapter talking about some experimental work on extreme thermodynamics of thermoresponsive pNIPAM polymer gels. In this section we study the shape change of cylindrical pNIPAM hydrogels due to phase separation at constant volume.

### 3.7.1 Previous work

As briefly discussed in section 3.3.3, the term extreme thermodynamics is used to refer to a constant-volume phase transition that results in phase separation of the hydrogel into shrunken and swollen regions that couples with the initial shape of the gel to result in large deformations.

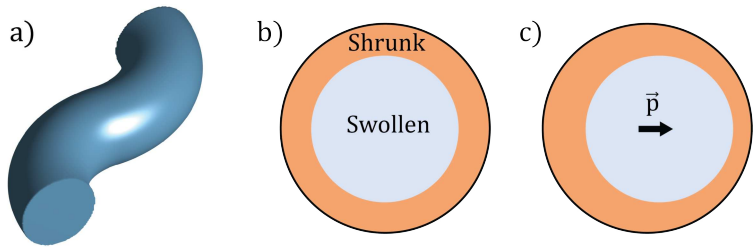



**Figure 3.16:** a) Schematic of a shape characterized by a center curve and circular cross-section. b) Schematic of axisymmetric phase coexistence in a circular cross-section of the gel. The shrunk region forms a layer at the surface (orange region) while the swollen region being circular and located at the center. c) Schematic of the phase-coexistence when the circular swollen region is displaced from the center. The vector $\vec{\mathbf{p}}$ is the polarization and indicates the displacement of the center of the swollen region with respect the center of the cross-section.

The effects of this phenomenon in gels with circular cross-section have been theoretically studied in [72]. To make the problem tractable, the following assumptions were made:

1. The initial shape of the gel is elongated and can be described by its center curve which, in general, has curvature. The cross-section is assumed circular. A schematic of a gel with these characteristics is shown in Figure 3.16a.

2. When the temperature increases a dense polymer shell forms at the surface and the gel phase separates into swollen and shrunk regions. The shrunk regions grow from the dense shell à la heterogeneous nucleation and does not spontaneously nucleate inside the swollen region.

3. The interface shape between swollen and shrunk regions is approximated by a circular region displaced from the center of the cross-section by the polarization vector $\vec{\mathbf{p}}$, as schematically shown in Figure 3.16b,c. This vector points from the thickest region of the shell to the thinnest. This is equivalent to describing the interface by a first order expansion in the angular coordinate.

4. Linear elasticity theory is used.

With these assumptions the free energy can be approximated and minimized with respect to the internal displacement field. This yields, to leading order, the free energy difference as a function of the initial curvature of the center curve, the change in this curvature and the polarization vector. This free energy

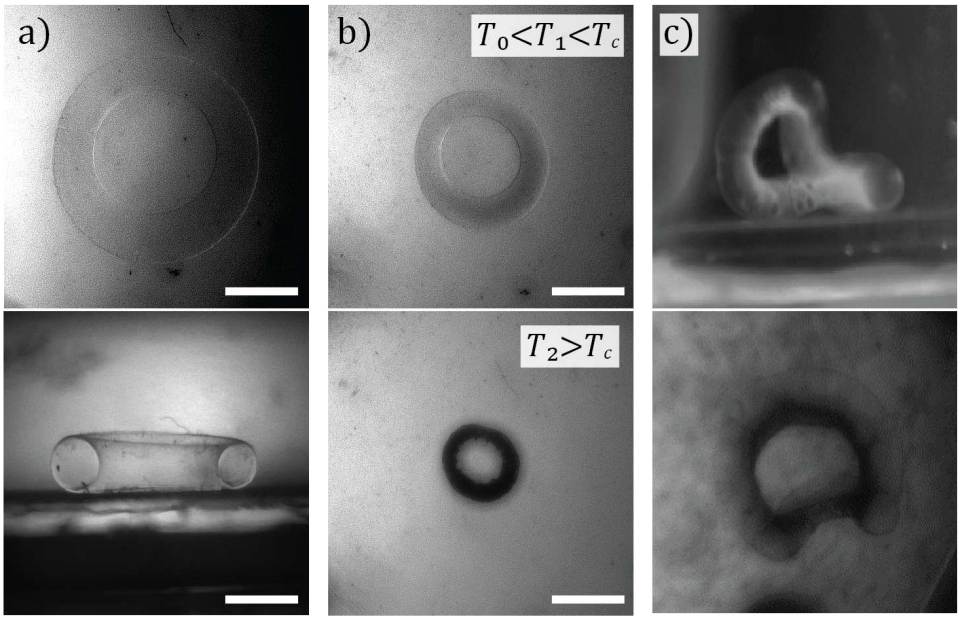



**Figure 3.17:** a) Top and side view of the synthesized toroidal hydrogel. b) Images of the same torus during quasistatic shrinking at a heating rate of $0.1°C/h$. Top image correspond to a temperature $T_1$ larger than room temperature $T_0$ but still lower than the transition temperature $T_c$. Bottom image shows the final state of the gel when the temperature $T_2$ is larger than the transition one. For the shrinkage during the phase transition, the heating rate is too fast and some small swollen bubbles get trapped inside the gel. Scale bars are 3mm. c) Side and top images of the torus deformation into a "Pringle" shape when the temperature is raised to 40°C as fast as possible. From the top image it can be seen that the whitish part corresponding to the shrunk region is at the inner part of the torus.

difference has four terms. The first two terms of the free energy are quadratic and correspond to the effective elastic cost of bending and twisting respectively. The third term refers to the coupling between the curvature and the polarization vector. This term minimizes the free energy when the shell is thicker in the negative Gaussian curvature region. The last term, surprisingly is a function only of the magnitude of the polarization vector squared and goes as $-r|\vec{\mathbf{p}}|^2$, with $r$ being a positive constant. This term always reduces the free energy when polarization is present, so the axisymmetric deformation state is indeed unstable.

Prior to the theoretical development, the coupling between curvature and polarizability was experimentally studied using pNIPAM toroidal gels [92]. When the toroidal gel was heated slowly enough, it shrunk affinely to the collapsed

state, as shown in Figure 3.17b. In contrast, when the gel was suddenly heated, the volume of the gel did not change significantly. It was observed that the shrunken region, which is seen whiter in the images due to the higher polymer density, was mainly located in the inner part of the torus as predicted by the coupling term. Also, the toroidal gels deformed into the predicted "Pringle" like shape (see Figure 3.17a,c). This deformation, indeed, increases the total amount of curvature reducing the free energy through the coupling term [72].

### 3.7.2 Hydrogel preparation

For our experiments, we prepare the hydrogels through photopolymerization of a precursor solution composed of monomer, crosslinker and photoinitiator. In this case, when UV illuminates the solution, the photoinitiator starts both the polymerization and crosslinking reaction, so polymer chains grow and get crosslinked simultaneously. The general process for getting hydrogels with different shapes consists on constraining the precursor solution to the desired shape and illuminating with UV light such that the solution turns into a solid hydrogel with that shape.

#### NIPAM precursor solution

For the precursor solution we use the same composition as for the toroidal hydrogels in [92]. We dissolve in deionized (DI) water, 5% (w/v) of the monomer N-isopropylacrylamide (NIPAM), 0.2% (w/v) of the crosslinker bis-acrylamide (BIS), and 0.2% (w/v) Irgacure 2959 as the photoinitiator.

It is important to note that when the precursor solution is illuminated with UV light, it heats up. Since NIPAM is a thermorresponsive monomer, if the temperature goes above the cloud point ($\sim$ 33°C) it will start aggregating, resulting in an inhomogeneous solution that produces an inhomogeneous whitish hydrogel when crosslinked. To keep the temperature low enough, the cuvette with the precursor solution is placed on top of an ice block. To improve heat conductivity between the cuvette and the ice block, a 50/50% water/ethanol solution is added between them.

To generate homogeneous pNIPAM hydrogels we illuminate the precursor solution with a 75W UV point source (Dymax BlueWave 75) at max power placed $\sim$ 85mm away from the sample[1] for $\sim$ 60$s$. This results in visually transparent hydrogels.

[1]This distance is chosen to ensure that the illumination area is much larger than size of the precursor solution such that the illumination is as even as possible.

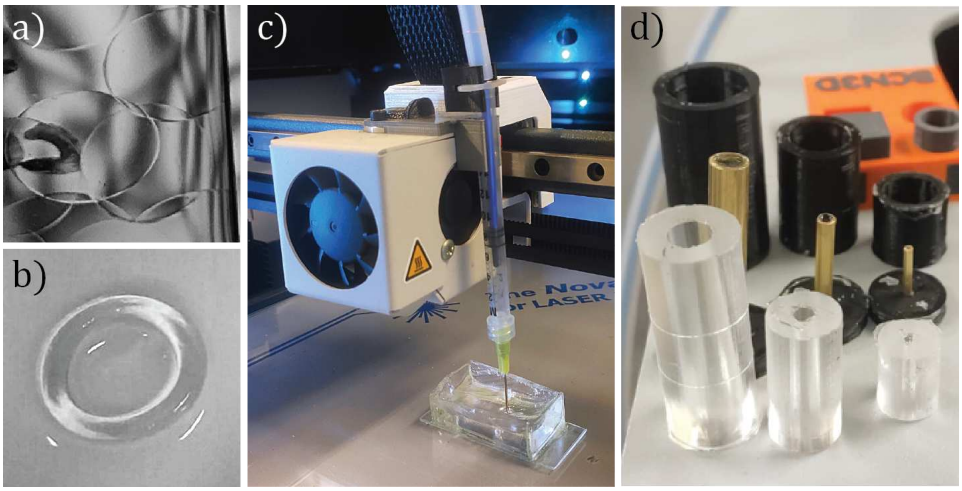



**Figure 3.18:** a) Spherical pNIPAM gels stored in a vial filled with DI water. b) Toroidal pNIPAM hydrogel on a plastic cuvette. c) Modified 3D printer for the injection of precursor solution inside a yield stress material. The tip is attached to the printing head so the generated shape can be controlled with the movement of the tip. d) PDMS molds for making pNIPAM cylinders of different size. The negatives used for making the PDMS mold are in the background and consist on a base with a cylinder attached to it and a circular wall for containing the PDMS while curing.

### Making gels with different shapes

Depending on the hydrogel desired shape, different methods are used. For making spherical gels the precursor solution is injected into a cuvette filled with 60000 cSt silicone oil. Due to the high viscosity, the sphere remains virtually floating while the shape becomes spherical. Once the gel is formed, we take it out with a spatula, put it on a weighting dish, remove as much oil as possible by sliding the gel around the dish, and transfer it to a water vial (Figure 3.18a). For making toroidal hydrogels (Figure 3.18b), we use our torus generating setups to make the precursor toroidal droplet inside the silicone elastomer yield stress material and polymerize it there. After taking the gel out of the silicone elastomer, the remaining yield stress material attached to the gel is more easily removed by first diluting it in 10cSt silicone oil.

If we want to make gels with a shape defined by an arbitrary non-intersecting center curve with circular cross-section we use a modification of the toroidal droplet generation procedure using a modified 3D printer (BCN 3D Sigma D25). The printer is modified such that a syringe with the precursor solution can be attached to the printing head and the filament is attached to the syringe piston

(Figure 3.18c). In this way, we have a moving injection tip where the filament movement controls the flow rate. By using custom written g-codes, the tip can be moved along the desired center curve while injecting the solution inside the silicone elastomer yield stress material [114]. Once the non-spherical droplet is generated we polymerize it inside the yield stress material as we did for the toroidal gels.

We can use the above method to generate cylindrical gels. Nevertheless, as discussed previously, when injecting fluids in yield stress materials it is very difficult to get circular cross-sections; these will typically be elongated. To get cylindrical gels with circular cross-sections we instead use a custom hydrophobic PDMS mold (Sylgard 184 Silicon Elastomer kit) with a cylindrical cavity (Figure 3.18d). The mold is made by filling with uncured PDMS a negative of the mold made with 3D printed pieces and a tube piece. PDMS is cured in an oven at 50°C overnight. The cylindrical hole in the mold is then filled with the precursor solution and illuminated from above with UV light to make the gels. For the correct polymerization of the gel it is important to make sure that the precursor solution surface at the top of the mold is flat. This ensures there are no lensing effects leading to inhomogeneous illumination. To retrieve the gel, the flexibility of the mold can be used to make some room between the gel and the walls to allow a stream of water to enter in between, facilitating the removal of the gel[1].

### 3.7.3 Temperature control setup

To study the shape change of our pNIPAM gels when the temperature is drastically increased we have made two experimental setups. The first one allows for the observation of the gel evolution with three cameras at right angles but has limited temperature profile control. The second one is simpler and allows for a better temperature control and sudden change of temperature, but the evolution of the gel is harder to follow, allowing for best observation of the final state of the gel.

#### Three camera setup

As shown in Figure 3.19a, this setup consists on three cameras placed at right angles and focusing at the sample which is placed inside a rectangular glass jar filled with water. The cameras are controlled through an Arduino Uno with a custom program to get images simultaneously. For improving the images of the cameras, the sample is illuminated through a light diffuser with three lamps pointing towards the cameras. Inside the jar, the sample is placed inside

[1] If the gel is too long for this method to work, one can also poke a hole with a thin needle at the bottom of the mold. The gel can then be retrieved by blowing some air into this bottom hole, pushing the gel out through the top part of the mold.

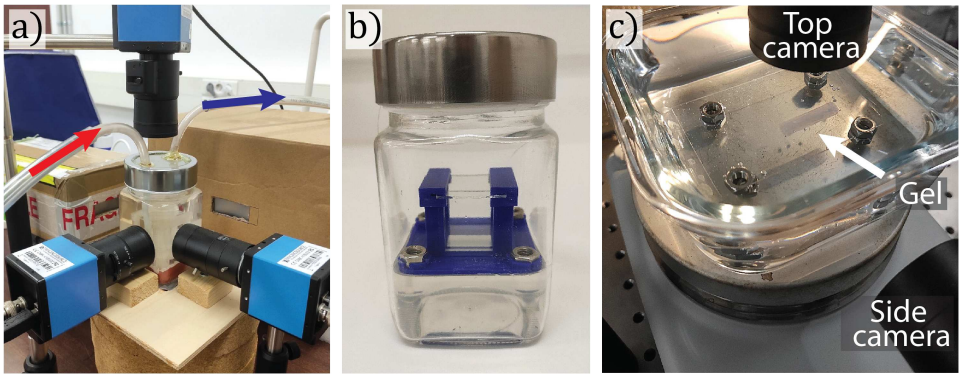



**Figure 3.19:** a) Three camera setup with the flask modified for water pumping. The pumping direction is shown with arrows. Opposite to each camera there is a diffuser (cardboard box with translucent plastic) from where the sample is illuminated. b) Last version of the rectangular flask without the tubes for pumping. The sample is place inside the blue cuvette that lies on a PDMS base. c) Temperature control setup where a borosilicate glass container is placed on top of a hot plate. A gel is placed on top of an elevated platform inside the container (white arrow) and two cameras record the evolution.

an elevated custom-made cuvette from glass slides and 3D printed pieces. For raising the temperature of the water and the gel two variations of this setup have been used.

The first consists on adding two tubes to the jar lid (see Figure 3.19a), and connecting them to a fish tank pump inside a temperature control bath (Huber Heating bath CC). Water at the temperature of the bath circulates inside the jar. The main limitations of this setup are that the quench rate is limited by the heating capacity of the bath and more importantly, the generated flow can disturb and even drag the gel out of the field of view, given that its density is very close to that of water. The problem of the sample being dragged with the flow was partially solved by using a closed cuvette. Nonetheless, in this case, the heat conduction inside the cuvette is worse. Also, frequent problems with leaks and glue deterioration made the setup difficult to operate.

The second variation consists on having the closed jar (Figure 3.19b) and using an external heat gun to suddenly raise the temperature. While this setup is less problematic, the temperature profile and evolution are completely uncontrolled. The sample is, however, not dragged and remains in place allowing captioning the gel evolution in time.

We use this three camera setup setup to test if we can reproduce previous results on pNIPAM tori. As shown in Figure 3.17a,b, for slow cooling ($< 0.1°C/h$) the toroidal gel undergoes affine shrinking keeping its aspect ratio constant. This

process is reversible and the swollen gel is recovered upon decreasing the temperature back to its original value. When temperature is raised fast enough, the toroidal gel keeps its volume and deforms into the "Pringle" shape (Figure 3.17c). More details on the test and further tests with spherical hydrogels are discussed in Appendix D.

#### Temperature quench setup

This second setup consists on a borosilicate container filled with water and placed on top of a hot plate. The water temperature is controlled through the hot plate dial and monitored with a thermocouple. Figure 3.19c shows a closeup picture of the experimental setup. Once the water is at the desired temperature the gel is dropped inside the hot water on top of a custom platform and a top and side camera are adjusted to observe its evolution. Because the gel is dropped in the hot water, it takes some time to put it in place and set the cameras. Sometimes, air bubbles get attached to the gels, making them float and complicating the observations.

### 3.7.4 Cylindrical gels

#### 3.7.4.1 Bending and bubbling

We start by "quenching" pNIPAM cylindrical gels generated with the modified 3D printer on the three camera setup. The cross-section diameter of the cylindrical gels generated is $\sim 1-2mm$ and their length is $\sim 15mm$. Independently of the way used to heat the container, the behavior of the gels is qualitatively the same. Figure 3.20 shows a series of images of the typical deformation process of a cylindrical gel when the temperature is suddenly increased. While initially the gel is swollen and transparent (Figure 3.20a), as the temperature goes above the transition temperature, the gel darkens and starts bending (Figure 3.20b). When looking closely at the gel in this state we can also observe that the region of negative Gaussian curvature is darker than the rest of the gel. The gel keeps bending and some transparent bubbles start to form in the region of positive curvature (Figure 3.20c). At the end of the process, the gel has a thick black region in the negative curvature region and bubbles in the positive curvature region (Figure 3.20d).

This behavior can be understood from the theoretical point of view by recalling the last term of the free energy, where a polarization of the interface between swollen and shrunk regions is energetically favored. This polarization is experimentally seen as the black line that appears on one side of the gel which corresponds to a larger shrunk region. Moreover, once the shrunk region grows larger, the energy is further reduced by bending towards the shrunk region. The

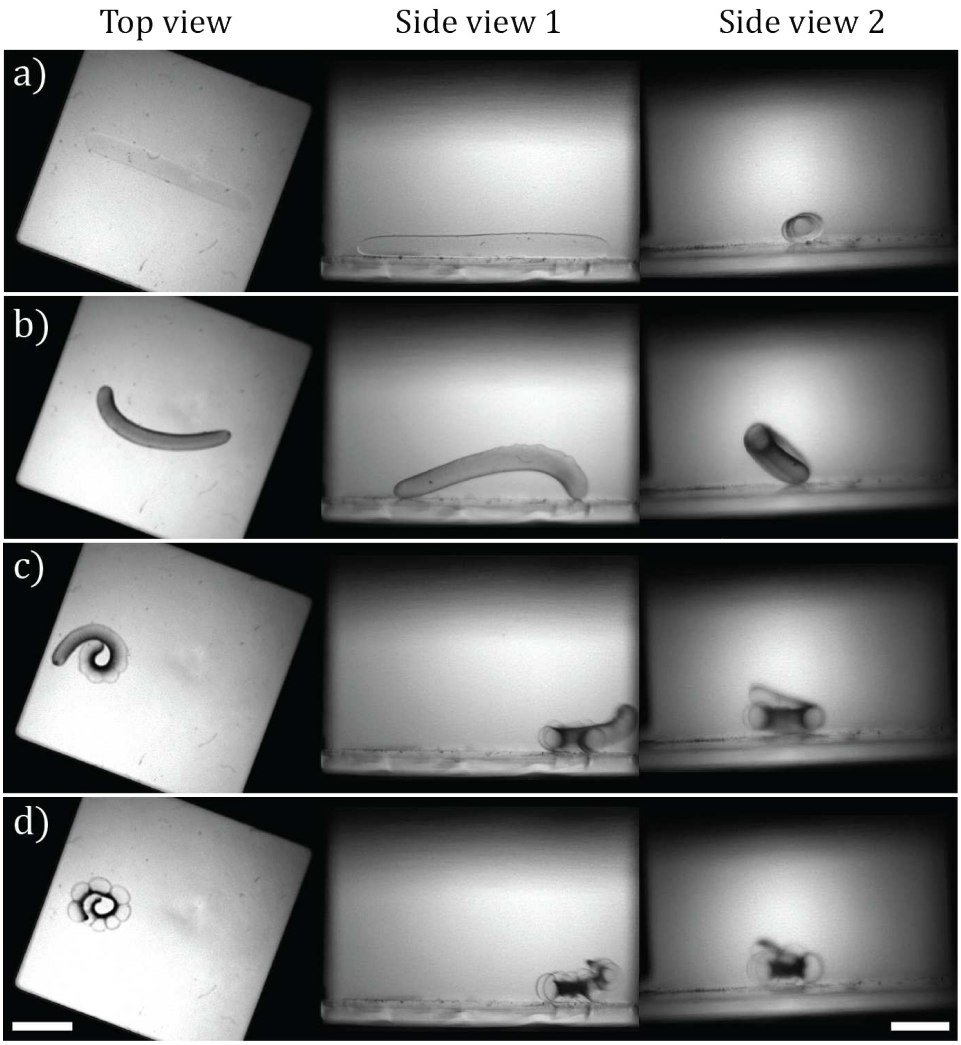



**Figure 3.20:** a)-d) From top to bottom, time series of the deformation of a cylindrical pNIPAM hydrogel when the temperature is suddenly increased. In each row the top and the two side views are shown. Scale bars are 5mm. The left one corresponds to the top view while the right one correspond to both side views.

bubbling instability appears at later stages and is similar to the one observed by Tanaka for pNIPAM spherical gels when the temperature is suddenly increased [89]. This instability has its origin in the extension force on the shrunk shell exerted by the swollen region. To maximize the volume of the swollen region while minimizing the lateral stretch of the shrunk layer, the ideal shape is the spher-

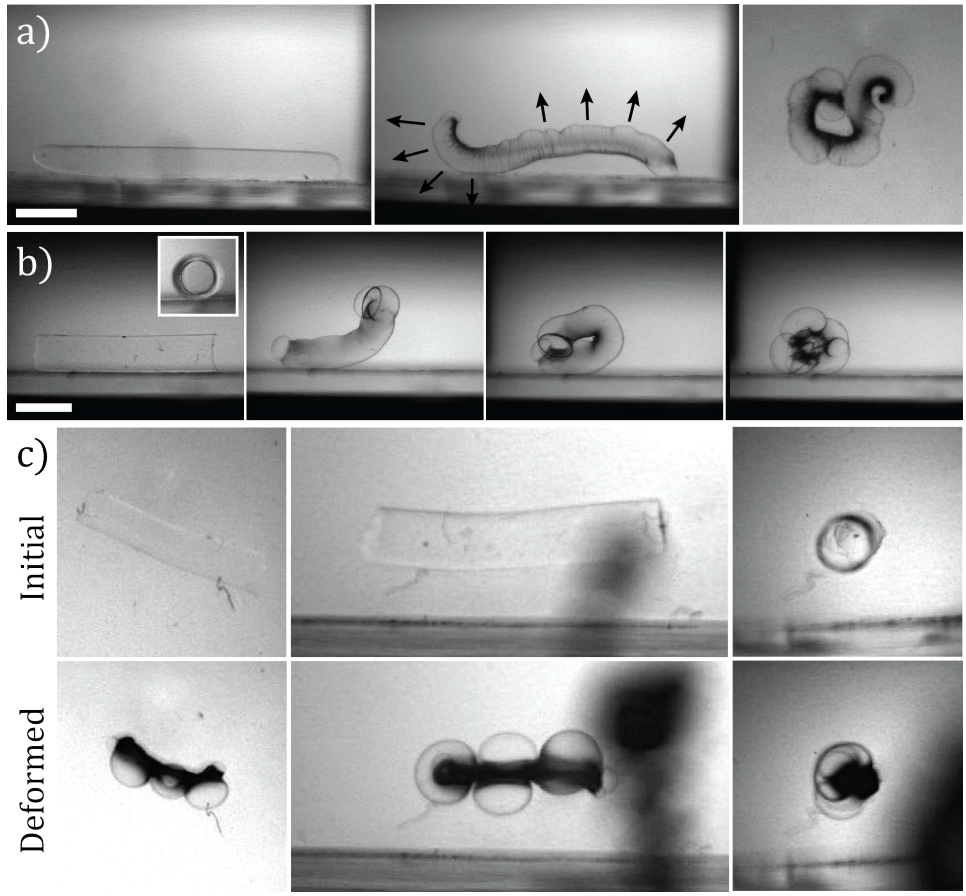



**Figure 3.21:** a) Time series of the deformation of a cylindrical gel into an "S" shape. The dark region appears in different parts of the cross-sections at each end. The first two images are side view of the gel while the last one is a top image of the final state. Arrows in middle image indicate the direction of the polarization vector at different points of the center curve. Scale bar is $3mm$. b) Side view time series of the deformation of a cylindrical gel made with a mold. Inset of the first image shows the circular cross-section. Scale bar is $3mm$. c) Top and side views of the initial and final state of a quenching experiment with a cylinder inside a yield stress material with no ethanol and glycerol and 0.1% Carbopol. The final shape barely shows any bending.

ical one. Since the gel is elongated the minimization of elongation is achieved by forming bubbles of a size similar to the cylinder diameter.

In another experiment, we observe a different polarization direction at each extreme of the cylinder (Figure 3.21a). This results in a final "S" shape, rather

than the spiral shape obtained for a single polarization since the bending direction is different for both parts. According to the theory, for an ideal cylinder, the polarization direction chosen should be random. This means that for a long enough cylinder, regions far away can be uncorrelated and the polarization can be different at different parts of the torus as is observed in this case for a cylinder of $\sim 1.5mm$ diameter and $\sim 15mm$ length. This can be understood as the nucleation of different domains of polarization. Nevertheless, due to the interconnected nature of the gel, the polarization vector needs to vary continuously between domains leading to a transition region. Experimentally, this is verified by the continuity of the dark line that transitions from one part of the cylinder cross-section to the other one (Figure 3.21a right).

Although the experiments are consistent with the theoretical predictions, there could be other experimental factors inducing the spontaneous polarization. One of this factors is the true geometry of the gels, which might not be perfect cylinders and may have elongated non-uniform cross-section. This could bias the polarization direction or directly trigger the appearance of the polarization through local curvature-polarization coupling. To rule out the role of the non-ideal geometry in the spontaneous polarization we generate cylindrical gels which a much better geometry (see inset Figure 3.21b) using our PDMS molds. The deformation of these gels when the temperature is suddenly increased also shows a spontaneous polarization resulting in bending towards the shrunk region (Figure 3.21b). This suggests that the spontaneous polarization does not stem from local geometrical imperfections of our cylindrical gels.

The bending of the cylindrical gel is a result of the appearance of a bending moment stemming from the uneven distribution of shrunk and swollen regions. We test this idea by filling the jar with a 0.1wt% Carbopol yield stress material without ethanol and glycerol[1] and placing the cylindrical gel inside (Figure 3.21c top). When the gel is heated, it barely bends, with the shrunk region forming a straight line surrounded by some swollen bubbles (Figure 3.21c bottom). This deformation resembles some of the shapes reported for pNIPAM cylinders immersed in a bath with acetone with their extremes fixed [90]. The yield stress of the outer medium is then able to compensate the bending moment keeping the straight shape of the gel. This, in fact, opens up the possibility of estimating the bending moment of a cylinder by finding the critical yield stress that prevents its deformation. More examples of the extreme thermodynamics experiments performed can be found in Appendix E.

[1]The presence of these other solvents can affect the behavior of the pNIPAM gels since the mixing free energy term could change.

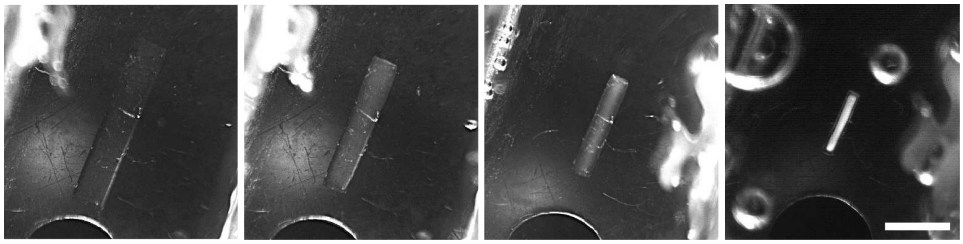


**Figure 3.22:** Size evolution of a $1.5mm$ in diameter cylindrical hydrogel when the temperature is increased slowly enough such that the shrinking process is quasistatic. Scale bar is $3mm$.

#### 3.7.4.2 Homogeneity test

Another possible origin for the spontaneous bending of our gels is that they are not homogeneous. This could result in regions with different polymer density that will shrink or swell by different amounts resulting in the deformation of the gel. The homogeneity of the gels can be tested by checking whether they keep their cylindrical shape or not while shrinking during quasistatic heating. We place one of our cylindrical gels in a closed custom water cuvette placed on top of a temperature control Peltier stage (Linkam T95-PE) and follow its evolution with a camera. The temperature is increased at an effective rate of 0.05°C/h. As shown in Figure 3.22, the gel shrinks affinely so it can be considered as homogeneous. Inhomogeneity can be ruled out as the cause of the cylinder gel bending.

#### 3.7.4.3 Temperature and size effects on instability

A drawback of the three camera setup is that the temperature distribution inside the jar can not be controlled. In fact, for the case of external heating the temperature gradient in the vertical direction close to the location of the gel has been estimated to be $\approx 0.02$°C/mm. This was done by following the temperature evolution during heating with two thermocouples placed at different heights and close to the location of the gel. Additionally, the temperature of the glass surface where the gel is placed could be different to that of the solution. A gradient in temperature could induce the spontaneous polarization of the gel by favoring the shrunk part of the gel to be located in the hottest part.

To eliminate the temperature gradient factor, we use the temperature quench setup where a water bath is heated to the desired temperature and the gel is dropped inside. We then monitor its evolution until it reaches the final deformed state. We also use this setup to study the effect of the temperature of the water bath and of the gel diameter in the final configuration of the gel.

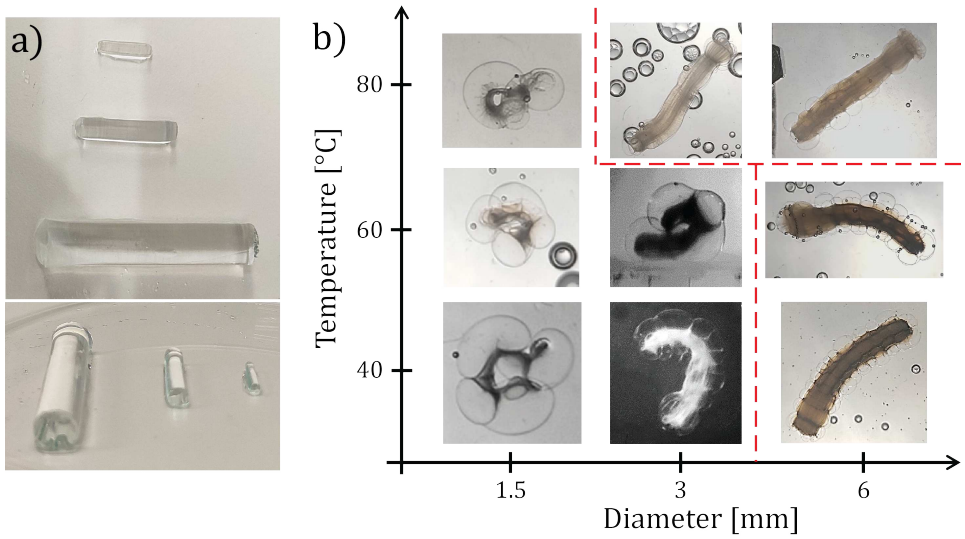



**Figure 3.23:** a) Images of the synthesized gels with diameters 1.5, 3 and 6$mm$. b) Phase diagram with images of the characteristic final shape of the gels as a function of the temperature of the bath and the diameter of the gel. Dashed red lines separates regions where different instabilities occur.

We make cylindrical gels with diameters 1.5, 3 and 6mm (Figure 3.23a). The length of the gels is chosen so that the aspect ratio (length/diameter) is constant and $\approx 5$. We heat the bath at three temperatures between the phase transition temperature of pNIPAM and the boiling temperature of water, 40, 60, and 80°C. We do experiments with three different gels for each combination of temperature and gel diameter and obtain the same results. The same experiment can not be repeated with the same gel since it internally breaks when extremely deformed. If the experiment is repeated the gel is now biased to repeat the same instability as before.

Figure 3.23b shows a representative picture of the final equilibrium shape for each combination of gel diameter and bath temperature. For all cylinders of diameter 1.5$mm$ and for the cylinders with diameter 3$mm$ at temperatures 40 and 60°C we observe the bending of the cylinder followed by the bubble instability, as before. This confirms that the spontaneous polarization of the gel is something intrinsic to the gel circular cross-section that lowers the free energy, as predicted by the theory and not a result of experimental limitations.

Interestingly, we also observe two more types of instabilities. For cylindrical gels of diameter 6$mm$ and temperatures 40 and 60°C the gel barely bends and the bubble instability forms a shape similar to a corncob and an opaque region at the center where the gel is greatly deswollen. This behavior is indeed not con-

templated in the theory since the shape of the interface between the shrunken and swollen regions in a cross-section is assumed to be a displaced circle neglecting any other shape. If the instability is dominated by a higher order term of the shape expansion, the polarity is lost and the gel does not break the necessary symmetry for bending. That would also explain the presence of several bubbles along the polar angle of the cylinder.

For a temperature of 80°C and gel diameter 3 and 6$mm$ a different scenario is observed. In this case, the bubbles barely appear and the gel becomes whitish with a filamentous structure in the axial direction. This could correspond to a theoretically described radial instability [115].

While the different types of instabilities of pNIPAM gels have been studied as a function of the acetone content of the bath where it is immersed and the elongation of the gels both in experiments and theory [90, 115], in this work we have studied the effects of the temperature of the bath and gel diameter. While the gel diameter was not reported to make a difference in the acetone case, in our case it makes a difference in the type of deformation of the gel. For low diameters, the gel bends and bubbles form, as predicted theoretically, while for the larger diameters and low temperatures a structure similar to a corncob is formed. Although the reason for this is unclear at the moment, if the bubbles have a characteristic length scale, several bubbles can fit around the polar angle of the cylinder for large enough diameters. This could favor the corncob instability. For large enough diameters and high temperatures, there is no bubbling instability and we observe an axial structure that resembles the one observed for high acetone content.

### 3.7.5 Other shapes

To finish this section, we briefly report on some quenching experiments with gels with curvature. The main goal of these experiments was to control the polarization direction which in turn would determine the deformation of the gel. We started making simple arcs. According to the theory in this case, the shrunk region would concentrate in the region of negative curvature making the arc bend even more. An experiment where this is observed is shown in Figure 3.24a. Nevertheless, this is not always the case and sometimes part of the gel bends in the opposite direction. This could be due to the poor control on the shape of the gel and homogeneity of the cross-section which tends to be larger at the center of the arc.

Another shape of interest is the "S" shape. In this case we have two regions that favor opposite polarization directions. By continuity the shrunk region will have to pass continuously from one to the other where the curvature changes. This in turn is predicted to generate a twist in the gel. In our preliminary experiment instead of two polarization domains, it formed four of them complicating

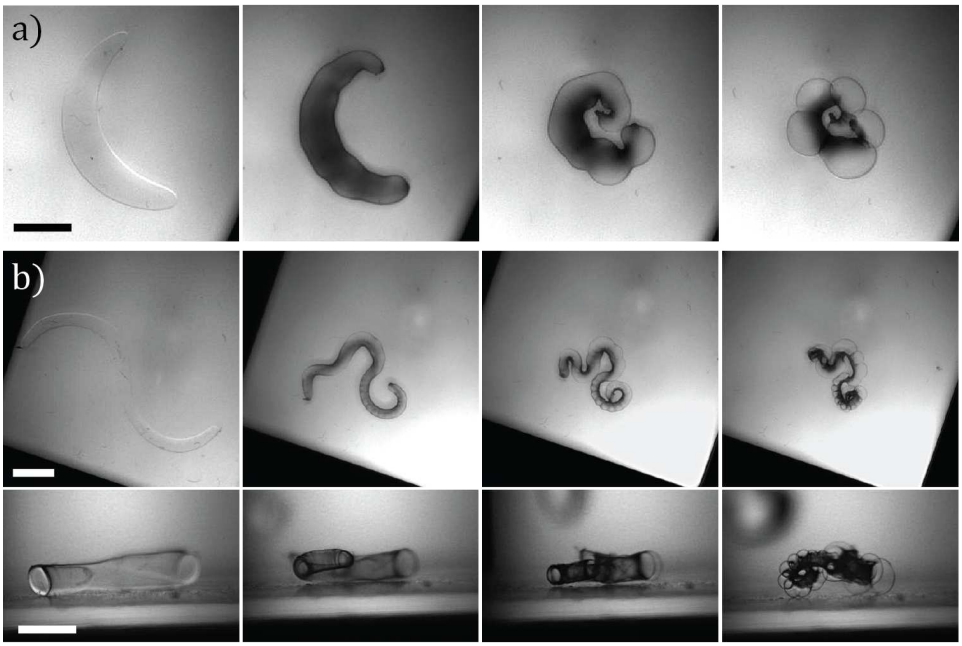



**Figure 3.24:** a) Top view time series of the deformation of an arc-shaped pNIPAM gel when increasing the temperature fast. b) Top and side view time series of the deformation of an "S"-shaped gel. Scale bars are $3mm$.

the analysis (Figure 3.24b). Nevertheless, in the later stages of the deformation it seems like there is some twist, which lifts the center of mass of the gel, as seen in the side view last image.

Although this data is interesting preliminary experiments, for a deeper analysis, more experiments should be made. Better control over the gel-making technique would allow better controlling their shape and the homogeneity of their cross-section.

## 3.8 Conclusions

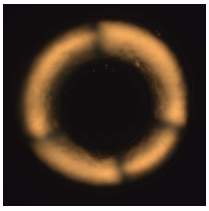
In this chapter we have described how to generate the toroidal droplets which are the main topic of the thesis. They are made by injecting a fluid in a rotating cuvette filled with an outer medium. We stabilize the non-spherical shape by using a yield stress material as the outer medium. This introduces differences in the generation process compared to using a simple fluid. For making nematic toroidal droplets we use a yield stress material based on hydrogels.

After introducing the main concept of hydrogel physics, we have described

the process to make spherical chitosan hydrogels and a first prototype to upscale their production. With these gels we have studied the evaporation behavior and found that they follow Maxwell's theory. Moreover, we have also assessed the effect of gel proximity on the evaporation time through local saturation and studied the origin of the drying slow down for single gels.

Finally, we have shown our results on the extreme thermodynamics of pNIPAM cylindrical gels, where, after suddenly increasing the temperature, phase separation at constant volume generates deformations of the gel that couple with the curvature. In the case of cylindrical gels, our experiments confirm the appearance of a spontaneous polarization in the shrunk region, which in turn induces the bending of the gel. We ended showing our preliminary results with arc-shaped gels and "S"-shaped gels which can further test more predictions of the theory proposed to explain and predict their deformation.

Chapter 4



# Planar nematic solid tori

## 4.1 Introduction

With the technique described in section 3.2 we can generate nematic toroidal droplets with parallel (tangential) anchoring conditions. We refer to these toroidal droplets as solid tori, following the mathematical language stressing that we do not have a 2D nematic on a toroidal surface, but rather a filled toroidal surface generated by the rotation of a disk around an axis of revolution. We then have an inherently three-dimensional object that can be described by a 3D director field. While the Poincaré-Hopf index theorem for a planar solid tori with tangential boundary conditions requires that the total topological charge is zero, this does not imply that no configurations with defects can exist but that the sum of their topological charges must be zero.

Nematic liquid crystals are by definition uniaxially anisotropic. This implies that their properties will depend on the direction relative to the director, with all the directions perpendicular to it being equivalent. For the specific case of the refractive index, the material is said to be uniaxially birefringent. This anisotropy is directly related to how light propagates through the material. The change in light polarization depends both in the initial polarization of the incident light and the orientation of the liquid crystal. This fact is used in polarized optical microscopy (POM) to study the director field configuration.

In this chapter, we study the different stable defect structures that appear in planar nematic solid tori using polarized optical microscopy and simulations.

## 4.2 Polarized optical microscopy

### 4.2.1 Fundamentals



In its simplest case, polarized light can be described as a sinusoidal monochromatic wave propagating in a certain direction [116, 117]. Polarized light consists on an oscillating electric and magnetic field perpendicular to each other and to the traveling direction (see Figure 4.1a). This wave is characterized by the angular frequency $w = 2\pi f$ and wavelength $\lambda$. For simplicity, we set the propagation direction to be $\hat{z}$. In that case, the electric and magnetic field lie in the the x-y plane. For a given propagation direction, given the electric field, the magnetic field is completely determined so the polarization state can be completely described with the electric field only. The electric field can point in any direction of the perpendicular plane, and thus in the most general case, polarized light can be described by the sum of two perpendicular sinusoidal components with different amplitudes and phases:

$$\vec{E}(z) = E_x e^{i(\frac{2\pi z}{\lambda} - wt + \phi_x)}\hat{x} + E_y e^{i(\frac{2\pi z}{\lambda} - wt + \phi_y)}\hat{y} \tag{4.1}$$

where $i$ is the imaginary unit number, and $E_n$ and $\phi_n$ represent the electric field amplitude and phase in the $n = \{x, y\}$ direction. Since we are adopting a complex analysis approach, to obtain the actual electric field one just has to take the real part of the expression. Note that, from the form of the exponents in equation 4.1, the phase of both components depends on the choice of origin, so only the phase difference $\delta = \phi_y - \phi_x$ between components is needed to describe the polarization state. Also that the polarization state does not depend on any prefactor, since it only indicates the amplitude of the electric field. Another relevant factor that determines the polarization state of light is the ratio of amplitudes between components; this is given by $\frac{E_y}{E_x} = \tan\theta$[1]. The electric field can then be written as:

$$\begin{aligned}\vec{E}(z) &= E_0(\cos\theta e^{i(\frac{2\pi z}{\lambda} - wt)}\hat{x} + \sin\theta e^{i(\frac{2\pi z}{\lambda} - wt)}e^{i\delta}\hat{y}) \\ &= E_0 e^{i(\frac{2\pi z}{\lambda} - wt)}(\cos\theta\hat{x} + \sin\theta e^{i\delta}\hat{y})\end{aligned} \tag{4.2}$$

where $E_0 = \sqrt{E_x^2 + E_y^2}$. The polarization state is, thus, determined by the phase difference between components $\delta$ and the ratio of magnitudes given by the angle $\theta$. It can be expressed by a complex vector called the Jones vector:

[1] If we plot the vector $\vec{E}_{plane} = E_x\hat{x} + E_y\hat{y}$ in the x-y plane, $\theta$ is the angle this vector forms with the x axis.

**Table 4.1:** Special types of polarized light

| Polarization | Characteristics | Jones vector |
|---|---|---|
| Elliptical | General case | $\begin{pmatrix} cos(\theta) \\ sin(\theta)e^{\delta} \end{pmatrix}$ |
| Linear | $\delta = 0$ | $\begin{pmatrix} cos(\theta) \\ sin(\theta) \end{pmatrix}$ |
| Right circular | $\theta = \frac{\pi}{4}$ and $\delta = -\frac{\pi}{2}$ | $\frac{1}{\sqrt{2}}\begin{pmatrix} 1 \\ -i \end{pmatrix}$ |
| Left circular | $\theta = \frac{\pi}{4}$ and $\delta = \frac{\pi}{2}$ | $\frac{1}{\sqrt{2}}\begin{pmatrix} 1 \\ i \end{pmatrix}$ |

$$J = \begin{pmatrix} \cos\theta \\ \sin\theta e^{i\delta} \end{pmatrix} \tag{4.3}$$

If one looks at a fixed point in space and checks the trajectory of the electric field vector[1], in general it will form an ellipse, so a general polarization state is said to be elliptical. There are, however, some special cases of interest (Table 4.1). If the electric field oscillates in a single direction, the polarization is said to be linear; this can be considered as the simplest mode. If the electric field describes a circle, the polarization is called circular. We refer to right/left polarization to an electric field that rotates clockwise/counterclockwise (Figure 4.1b).

When polarized light of a given frequency goes through a real material it interacts with it. From a microscopic point of view the electric field excites molecular electric dipoles that re-emit radiation at the same frequency. When the material is isotropic, its reaction does not depend on the orientation of the electric field and the polarization is indeed preserved. The only difference is the exponent in equation 4.2 associated to the wavelength, which changes from $\lambda$ to $\lambda/n$, where $n$ is the index of refraction of the material. This wavelength reduction also implies that the speed of the light wave is reduced by a factor n. We can see that the polarization preservation in isotropic materials comes from the fact that when introducing the new wavelength in equation 4.2 the last

[1]This is also equivalent to fixing the time and following the tip of the electric field as we move in the propagation direction, $z$. The only difference is the rotation sense, which becomes opposite.

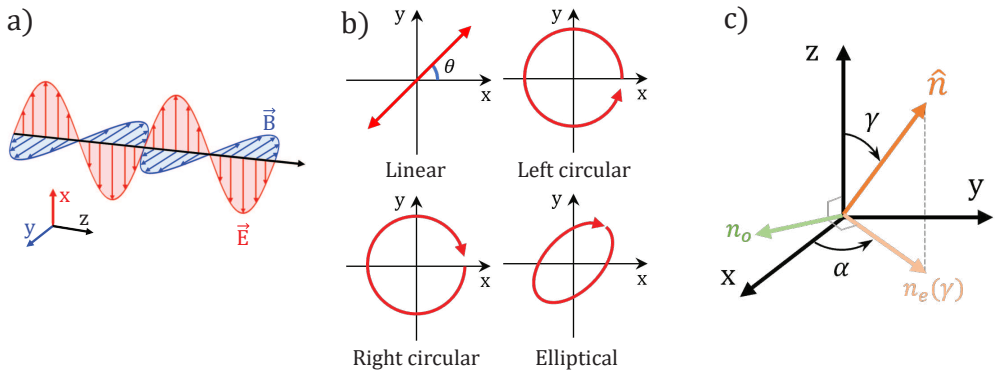



**Figure 4.1:** a) Linearly polarized electromagnetic wave propagating in the z direction. The polarization direction is given by the oscillation direction of the E field, the x axis in this case. b) Line path of the electric field at a certain point in space for different types of polarization. c) Coordinate system where z corresponds to the propagation direction of the light and $\hat{n}$ is the director direction. $n_o$ marks the principal direction in the x-y plane with ordinary refractive index while $n_e(\gamma)$ marks the other main direction in the x-y plane.

equality still holds since the exponential factor for both components is still the same and can be taken out as a common factor.

When the material is not isotropic, its interaction with polarized light will depend in general on the relative orientation between the material and the propagation direction, and on the polarization state of the light. Fortunately, since the propagation of light can be written in terms of the dielectric tensor, there are always at least three principal directions defining three principal indexes of refraction. The index of refraction of a principal direction is the index of refraction seen by linearly polarized light with the electric field oscillating in that principal direction, independently of the propagation direction. Also, when light propagates in a certain direction, there are always two perpendicular main axis where linear polarization is preserved. The effective refractive index in this directions can be written as a function of the principal indexes of refraction and the propagation direction. When all three principal indexes of refraction are different the material is called biaxial, while if two of them are equal it is called uniaxial. The case when all of them are equal reduces to the isotropic case.

Nematic liquid crystals are by definition uniaxial, meaning that there is a distinct principal direction, with all perpendicular directions to this one being equivalent. In this case, we can assign an index of refraction, called extraordinary index of refraction $n_E$, to the director direction, and an ordinary index of refraction $n_o$ to all the directions perpendicular to the director. In this case,

all directions in the plane perpendicular to the director are principal directions. The extraordinary axis is also called the optic axis since when light travels in that direction, any polarization state is preserved, since all perpendicular directions where the electric field oscillates have the same index of refraction.

A polarized beam of light propagating in the $\hat{z}$ direction that goes through a uniaxial slab of thickness $d$ will suffer a change in polarization that will depend in the initial polarization and the angle the optic axis makes with respect to the propagation direction $\gamma$. It is interesting to note that independently of the orientation of the director, there is always a direction perpendicular both to the director and to the propagation direction that corresponds to a principal direction. The component of the polarized light in this direction will see the ordinary index of refraction (see Figure 4.1c). We can redefine our $\hat{y}$ and $\hat{x}$ to point in this ordinary principal direction and its normal in the perpendicular plane, respectively, which is the other direction where linear polarization is preserved. The effective refractive index seen by the electric field component in this normal direction depends on the angle $\gamma$ and is given by [117]:

$$n(\gamma) = \frac{n_o n_E}{\sqrt{n_o^2 \sin^2\gamma + n_E^2 \cos^2\gamma}} \tag{4.4}$$

When $\gamma = 0$, light propagates through the optic axis, and the main axis coincides with an ordinary principal axis with $n(0) = n_o$. When $\gamma = \pi/2$, the electric field oscillates around the extraordinary direction with $n(\pi/2) = n_E$. For any other angle, the effective index of refraction takes an intermediate value. We can now rewrite equation 4.2 for the light beam exiting the uniaxial material applying the appropriate phase shift to each component:

$$\begin{aligned}\vec{E}(d) &= E_0 e^{-iwt}\left(\cos\theta \cdot e^{i(\frac{2\pi n(\gamma)d}{\lambda})}\hat{x} + \sin\theta \cdot e^{i(\frac{2\pi n_o d}{\lambda})}e^{i\delta}\hat{y}\right) \\ &= E_0 e^{i(\frac{2\pi n_o d}{\lambda} - wt)}\left(\cos\theta \cdot e^{i(\frac{2\pi (n(\gamma)-n_o) d}{\lambda})}\hat{x} + \sin\theta \cdot e^{i\delta}\hat{y}\right)\end{aligned} \tag{4.5}$$

The Jones vector has changed by a complex exponential factor that represents an extra phase shift $\Delta = \frac{2\pi(n(\gamma)-n_o)d}{\lambda}$ between the components. This change can be expressed in matrix form as:

$$\begin{aligned}J' &= \begin{pmatrix}\cos\theta \cdot e^{i(\frac{2\pi(n(\gamma)-n_O)d}{\lambda})} \\ \sin\theta \cdot e^{i\delta}\end{pmatrix} = \begin{pmatrix}e^{i(\frac{2\pi(n(\gamma)-n_O)d}{\lambda})} & 0 \\ 0 & 1\end{pmatrix}\begin{pmatrix}\cos\theta \\ \sin\theta \cdot e^{i\delta}\end{pmatrix} \\ &= \begin{pmatrix}e^{i\Delta} & 0 \\ 0 & 1\end{pmatrix} J = MJ\end{aligned} \tag{4.6}$$

**Table 4.2:** Jones calculus operators for common optical elements

| Optical Element | Jones Matrix |
|---|---|
| Linear polarizer with axis of transmission horizontal ($\hat{x}$) | $\begin{pmatrix} 1 & 0 \\ 0 & 0 \end{pmatrix}$ |
| Linear polarizer with axis of transmission vertical ($\hat{y}$) | $\begin{pmatrix} 0 & 0 \\ 0 & 1 \end{pmatrix}$ |
| Linear polarizer with axis of transmission at $\pm 45^\circ$ with the horizontal | $\frac{1}{2}\begin{pmatrix} 1 & \pm 1 \\ \pm 1 & 1 \end{pmatrix}$ |
| Left circular | $\frac{1}{2}\begin{pmatrix} 1 & \pm i \\ \mp i & 1 \end{pmatrix}$ |

The polarization state after going through an uniaxial material changes by a matrix multiplication given by M. To compute the change in polarization in a practical way, we first express the Jones vector in the coordinates coinciding with the local principal axis, apply matrix M and finally rotate back to our original axis. In a general sense, any optical device that changes the device polarization can be expressed in terms of a matrix and thus the calculation of polarization change is reduced to matrix multiplication. The Jones matrices for some basic optical elements are listed in table 4.2.

Since nematic liquid crystals are uniaxial materials where the polarization change is a function of the angle the director makes with the propagation direction, studying the change in polarization as light goes through the material allows us to study its director field configuration.

### 4.2.2 Microscope setup

To study our nematic solid tori we use one of the simplest forms of polarized optical microscopy. We illuminate our sample with linearly polarized light and study the output polarization by means of a polarizer called analyzer, which probes the polarization component in one direction.

We use the inverted transmission microscope Axio Observer from ZEISS (Figure 4.2a). The sample is illuminated from above with a mercury lamp. Light passes through a first polarizer whose orientation can be manually controlled giving linearly polarized light in a certain direction that then passes through a condenser and illuminates the sample. The condenser can be moved up and down to ensure Köhler illumination, which guarantees even illumination by appropriately placing the lenses so the inhomogeneity of the illumination

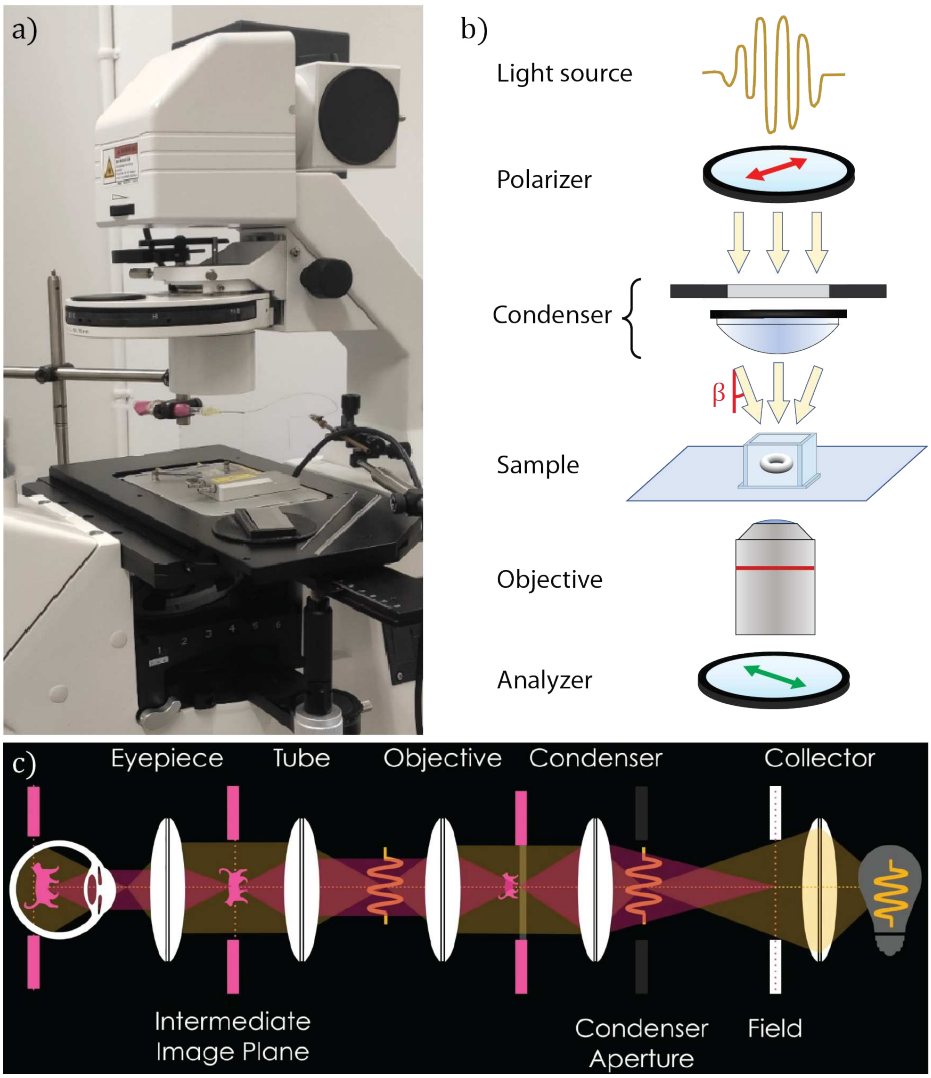



**Figure 4.2:** a) Inverted bright field Axio Observer 3 microscope. b) Simplified schematic of polarized optical microscopy used to study nematic tori. The optics related to Köhler illumination are omitted for clarity. The polarization axis of polarizer and analyzer are indicated by a double arrow. $\beta$ corresponds to the numerical aperture angle. c) Schematic of the Köhler illumination configuration. The sample plane coincides with the conjugated plane of the light source such that the illumination becomes parallel. Pink and yellow/gray paths correspond to the illumination from a point source in the sample and the light bulb respectively. Image extracted from [118].

source is lost in the sample plane. The condenser has a diaphragm, also called condenser aperture, that controls the numerical aperture of light, which is the angle $\beta$ of the cone of light illuminating the sample. The smaller the angle, the more parallel the light rays will be. Once the polarized light goes through our sample the image of the sample is gathered by the objective and passes through the analyzer. The analyzer can be rotated to change the component of the polarized light probed. After that, light goes to the camera (ZEISS Axiocam 512 color) and the image is displayed in the computer through the software ZenCore. A simplified schematic of the optical system used can be seen in Figure 4.2b. Another schematic with the details of Köhler illumination is shown in Figure 4.2c.



### 4.2.3 Two dimensional flat samples

To gain insight on how the director configuration of a nematic liquid crystal affects the texture observed, it is interesting to study the case of a flat sample of thickness $d$ with the director parallel to the boundaries and uniform across the thickness of the sample. In this case, we have a 2D director field with flat interfaces and polarized light propagating in the perpendicular direction. Each point of the plane behaves as a uniaxial material with its optic axis given by the director and thickness $d$. This case corresponds to an angle $\gamma = \pi/2$ with the two main axis always having refractive indices $n_O$ and $n_E$. It is, then, the angle the director makes with respect the incident polarization what determines the polarization as light exits the sample.

One of the simplest configurations to study nematic liquid crystals is crossed polarizers. This consists on having the polarizer and analyzer in perpendicular orientations (Figure 4.3a), meaning that if the light polarization does not change the analyzer blocks the incident light, resulting in black regions. in contrast, if the outer polarization is linear in the perpendicular direction to the original light direction, the intensity captured will be maximum.

The typical texture observed in this configuration, is often called Schlieren texture, and typically contains many topological defects (Figure 4.3b). At the defects, where the orientation is not defined, the refractive index changes in a very short distance, of the order of the wavelength of visible light (from the defect core to the ordered regions) producing light scattering. This in turns means that when looking at the sample in bright field, defects will appear as dark spots (Figure 4.3c).

We set the polarizer direction to be the $\hat{x}$ direction and describe the director field by the angle $\theta$ relative to the x axis. We can now use Jones calculus to compute the exit configuration for monochromatic illumination. First, we compute the Jones vector of the incident polarization in the basis of the main axis of the nematic liquid crystal in the x-y plane. This can be done by multiplying

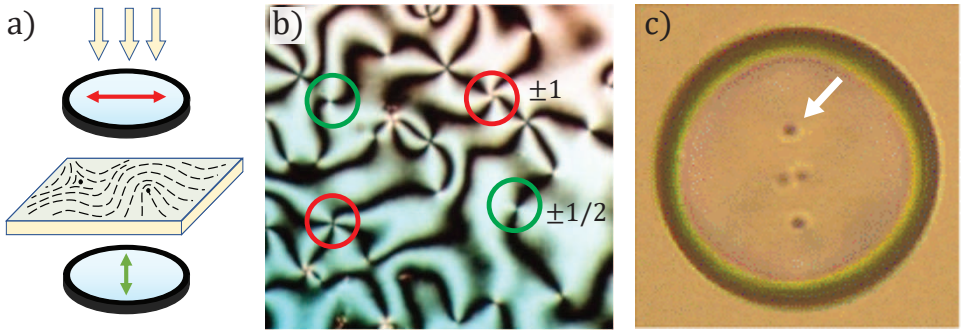



**Figure 4.3:** a) Crossed polarizer setup for a 2D sample. The director field is shown as dashed arrows. b) Typical Schlieren texture. Black regions corresponds to the director being parallel or perpendicular to the polarizer and analyzer. Circles show point defects with their topological charge inferred from the number of brushes. Color gradient indicates thickness gradient in the sample. Image adapted from [119]. c) Bright field image of a nematic shell with four defects appearing as dark spots. White arrow points to one of the defects. Image adapted from [57].

the Jones vector by the rotation matrix $R(-\theta)$. In the 2D case, the basis of the main axis is just the director and its normal:

$$J' = R(-\theta)J = \begin{pmatrix} \cos\theta & \sin\theta \\ -\sin\theta & \cos\theta \end{pmatrix} \begin{pmatrix} 1 \\ 0 \end{pmatrix} = \begin{pmatrix} \cos\theta \\ -\sin\theta \end{pmatrix} \tag{4.7}$$

Now the polarization is multiplied by the matrix corresponding to a birefringent material. In this case, since $\gamma = \pi/2$, we have $\Delta = 2\pi(n_E - n_o)d/\lambda$. Finally we have to rotate back our output polarization to the initial coordinate basis. This is done multiplying by $R(\theta)$:

$$\begin{aligned} J_{sample} = R(\theta)MJ' &= \begin{pmatrix} \cos\theta & -\sin\theta \\ \sin\theta & \cos\theta \end{pmatrix} \begin{pmatrix} e^{i\Delta} & 0 \\ 0 & 1 \end{pmatrix} \begin{pmatrix} \cos\theta \\ -\sin\theta \end{pmatrix} \\ &= \begin{pmatrix} 1 + \cos^2\theta(e^{i\Delta} - 1) \\ \frac{1}{2}\sin 2\theta(e^{i\Delta} - 1) \end{pmatrix} \end{aligned} \tag{4.8}$$

We then add the effect of analyzer, which is set in the $\hat{y}$ direction, by multiplying by the corresponding matrix (Table 4.2). The end result is:

$$J_{out} = \begin{pmatrix} 0 & 0 \\ 0 & 1 \end{pmatrix} \begin{pmatrix} 1 + \cos^2\theta(e^{i\Delta} - 1) \\ \frac{1}{2}\sin 2\theta(e^{i\Delta} - 1) \end{pmatrix} = \begin{pmatrix} 0 \\ \frac{1}{2}\sin 2\theta(e^{i\Delta} - 1) \end{pmatrix} \tag{4.9}$$

The only remaining component of the electric field is the y component, as a result of the presence of the analyzer. The final light intensity is proportional to the square modulus of the output polarization vector. The prefactors consist on constants and the amplitude of the incident light. The intensity at each point will depend on the director angle and is given by:



$$I \propto \frac{1}{4}\sin^2 2\theta(e^{i\Delta}-1)^2 \tag{4.10}$$

From this equation we can see that the intensity vanishes in two cases:

1. $\theta = q\pi/2$, with $q \in \mathbb{Z}$. This case corresponds to the case where the director is either parallel or perpendicular to the polarizer axis. In those cases, the electric field oscillates in one of the main directions of the liquid crystal and thus, the polarization of the incident light does not change and does not go through the analyzer.

   This allows characterizing the winding number of 2D topological defects, since the winding number indicates the number of rotations of the director around the defect. For each half rotation, the director field becomes parallel and perpendicular to the polarizer once, giving two black brushes. A topological defect of winding number $p/2$ will have $2p$ brushes emanating from it. In particular a $\pm\frac{1}{2}$ defect features 2 black brushes, while a $\pm 1$ defect features 4 (Figure 4.3b). To determine the sign of the defect one has to check the sense of rotation of the brushes as one rotates the crossed polarizer and analyzer together. If the brushes rotate in the same sense, the defect is positive, while it is negative otherwise.

2. $e^{i\Delta} = 1 \implies \lambda = (n_E - n_o)d/q = \Delta n d/q$ with $q \in \mathbb{Z}$. We can see that this condition does not depend on the angle $\theta$ of the director but on the wavelength of the light and the thickness of the sample. This means that certain wavelengths are always extinguished.

   If instead of monochromatic illumination we use white light, the extinction of some wavelengths can lead to a colored output, where the color corresponds to the wavelengths that pass through the analyzer. This color output has been used traditionally in optical mineralogy [120, 121] by means of the Michel-Lévy chart (Figure 4.4). Given the color output, if you know the thickness of your sample, you can deduce the birefringence $\Delta n$ and thus identify the mineral, whereas if you now the mineral you can use the color to find the thickness.

   The colors appear when the extinction in the visible regime correspond to low q. In this case, if we want the first extinction to be at $\lambda = 500nm$ for a sample of 5CB that has a birefringence of $\Delta n \approx 0.2$, the sample

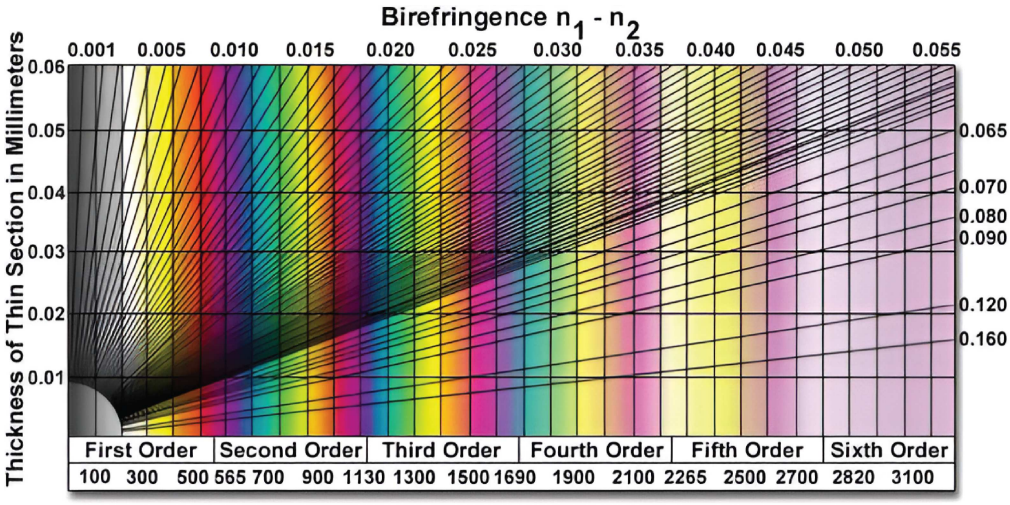



**Figure 4.4:** Michel-Lévy chart used in optical mineralogy. Image adapted from [122].

thickness should be of the order of $2.5\mu m$. We can see that vivid colors for a flat parallel sample of 5CB would occur for very small thicknesses. If we observe a color gradient, this indicates that the thickness is not constant; this is the case for the sample shown in Figure 4.3b.

We can see that the crossed polarizer setup does not provide information on which is the fast (smaller $n$) and slow (larger $n$) axis when extinction occurs in the first case. This is because extinction occurs with the polarizer both parallel and perpendicular to the director. To distinguish them, other optical elements like quarter wave-plates and universal compensators can be used in different configurations to get unambiguously which is the fast axis and thus the director orientation [39, 123, 124, 125].

### 4.2.4 Thick samples with curved boundaries

The previous section provided us with some basics to interpret polarized optical microscopy for 2D flat samples. Nevertheless, our nematic solid tori are different in some aspects:

1. The director field is not necessarily homogeneous along the $\hat{z}$ direction and can point in any direction in 3D. This makes the cross-polarizer images harder to interpret, since the birefringence changes as light propagates. The result is an output polarization that integrates all the information of

the director field along the path traveled. In that sense, there is not a one to one dependence between the output polarization and the director field the light traverses.

This implies that dark regions in cross-polarizers will usually be regions where the main birefringence axis of the director are either parallel or perpendicular to the polarizer axis through the whole sample. Moreover, point defects can not be characterized by the numbers of dark brushes since above and/or below them there is still birefringent material that might change the output polarization. Nevertheless, they will usually have two dark brushes and the rotation of polarizer and analyzer can give us a hint on their topological character depending on the rotation sense of the brushes. However, the correspondence is not one to one as in the 2D case, since, for example, negative defects can give both rotation senses depending on the plane we may be probing; see schematics in Figure 2.6.

Our procedure for finding and discerning the director field configuration of nematic solid tori consists on gathering some experimental data that can provide some hints on the possible configuration, propose an ansatz for the director field and compare with simulations of the textures for the proposed ansatz.

2. The nematic tori generated are "thick" and have a typical tube diameter of $\approx 300\mu m$. This size is at least an order of magnitude larger than the one needed to see vivid interference colors from the Michel-Lévy chart for 5CB. At these thicknesses, there are a lot of wavelengths extincted distributed along the visible spectrum resulting in a paler color, which corresponds to the far right part of the chart.

   Nevertheless, if the birefringence is low enough, the first extinction occurs for larger thicknesses. In this case, since the director field can point in any direction in 3D (except at the boundary) and the effective birefringence is given by $n(\gamma) - n_o$, when the angle $\gamma$ between the director and light propagation direction $\hat{z}$ is small, $n(\gamma) \sim n_o$ and the birefringence can be small enough to give interference colors for those thicknesses. This can be summarized by saying that interference colors can appear if the director field is nearly vertical.

3. The toroidal droplet interface is not flat and its index of refraction is different from the one of the medium surrounding it. This means that refraction effects can be important, specially in the inner and outer regions of the torus where the light incidence angle is larger with respect to the surface normal. This deviates the light trajectory at those regions (see Figure 4.5a) leading to a dark contour in the inner and outer regions

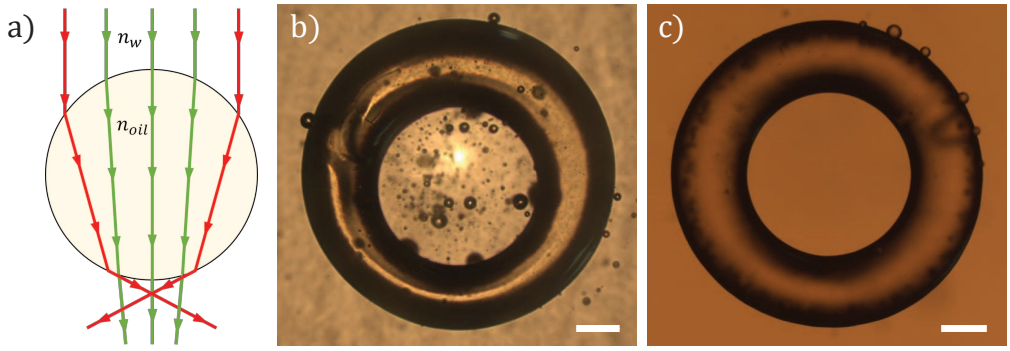



**Figure 4.5:** a) Schematic of refraction in a cross-section of the torus. Green arrows indicate light paths that are captured by the camera while red arrows indicate light paths that do not reach the camera leading to black regions. $n_{oil}$ and $n_w$ indicate the index of refraction of the liquid crystal and the exterior medium. $n_{oil} > n_w$. b) Bright field image of a torus with the smallest possible numerical aperture for the illumination (parallel rays). c) Bright field image of a torus with the highest possible numerical aperture for the illumination. Scale bar is $200\mu m$.

(left and right areas in the schematic). This is also typically observed in droplets, where the outer edge becomes darker and the thickness of this dark region depends on the difference of refractive index between the droplet fluid and the outer medium. Moreover, in the case of a birefringent material, the ordinary ray will follow Snell's law but not the extraordinary ray. As a result both rays could, in general, separate.

While for the flat sample one ideally needs parallel illumination, so that the assumptions in the theoretical treatment hold as best as possible, in our case, parallel illumination results in poor images filled with speckles and large dark regions (Figure 4.5b). This is due to the large volume of material surrounding the torus and the dust and small particles that can get there during the fabrication process. If the illumination is perfectly parallel, once the light scatters in these objects it won't get to the objective and dark spots coming from dust out of the plane will be very visible . Nevertheless, if we increase the numerical aperture of the illumination there will be more rays coming from different directions illuminating the same point so the dust out of the focal plane will have a negligible effect on the image. Moreover, the black regions resulting from refraction become smaller, since light at different angles illuminates every point of the surface (Figure 4.5c).

In this way, setting the numerical aperture to the maximum improves the quality of the image at the cost of not having a perfectly parallel illumina-

tion. Due to the difficulties of identifying the director configuration, even in the most ideal cases, we assume that this is a minor effect that will not affect the discussion of all previous points.

Although it might seem that thick 3D samples are more complicated to interpret when illuminated between crossed polarizer and analyzer, there is a case where the output polarization can be computed in a very simple way. This is the case where the nematic liquid crystal acts as a waveguide. This happens when the incident linearly polarized light is parallel/perpendicular to the main axis of the director in the x-y plane. In this case, as the polarized light goes through the sample it remains linearly polarized and parallel/perpendicular to the director at all points. As a result, the output polarization is linear and parallel/perpendicular to the main axis of the director at the exit point.

In order for the nematic liquid crystal to act as a wave guide the director twist around the $z$ direction, $\phi$, must be much smaller than the phase retardation induced by the birefringence in the same distance $\Delta = \frac{2\pi(n(\gamma)-n_o)d}{\lambda}$. This is called the Mauguin limit [117, 126] and can be written as:

$$\frac{\phi}{\Delta} = \frac{\phi\lambda}{2\pi d(n(\gamma) - n_o)} \ll 1 \tag{4.11}$$

### 4.2.5 Temperature control

To heat and cool the nematic tori in a controlled way, the standard microscope stage is substituted by a microscope Peltier stage Linkam T95-PE that heats and cools down in a controlled way according to custom made programs. On top of the stage, we place the cuvette with the nematic droplet. Since the torus is at a certain distance from the stage we can expect the temperature to be slightly smaller than the stage temperature due to heat conduction. Nevertheless, since we are only interested in controlling the cooling rate, we heat our sample and keep it at a certain temperature for around 15 minutes to ensure that the temperature has stabilized and then reduce the temperature of the stage at a controlled rate. If we assume that the temperature difference between the stage and the sample remains constant the sample will cool at the same rate. This is true when the cooling is slow enough for the temperature profile to have time to equilibrate. For fast cooling, the cooling rate is approximate and refers to the Peltier stage temperature change.

## 4.3 Defect-free planar tori

With the toroidal droplets generation and stabilization techniques discussed in sections 3.2 and 3.6, we generate stable nematic toroidal droplets with planar

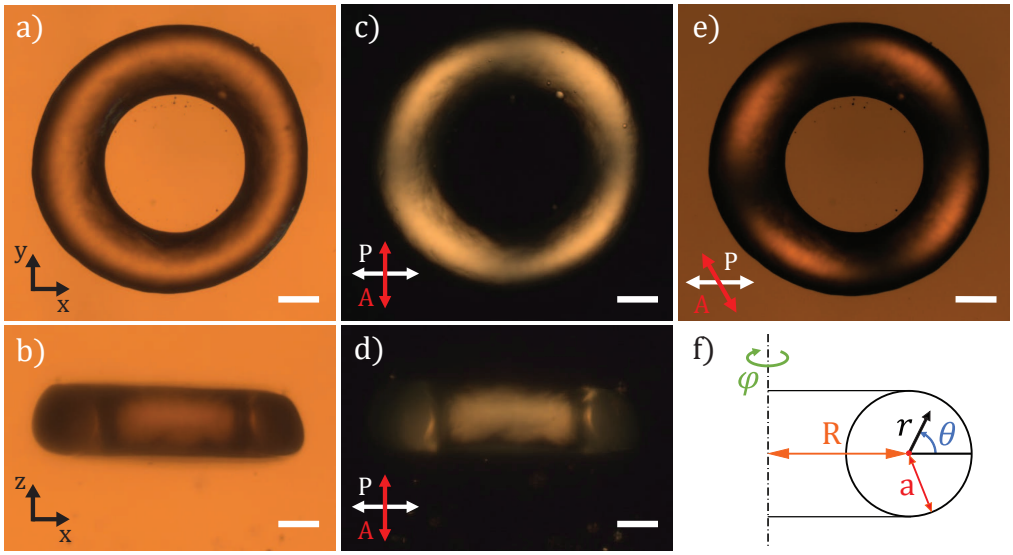



**Figure 4.6:** a) Top view bright field image of nematic torus. b) Bright field side view. c) Crossed polarizers top view. d) Crossed polarizers side view. e) Polarized optical microscopy with the polarizer horizontal and analyzer rotated until the dark regions become as dark as possible. All scale bars are 220$\mu m$. A gamma=0.45 correction has been applied to the crossed-polarizer images for visualization purposes. f) Schematic of simple toroidal coordinates.

anchoring (see Figure 4.6 a and b for top and side view bright field images). For these experiments we use a yield stress material with 1 wt% Carbopol (ETD 2020 from Lubrizol), 2 wt% glycerol, no ethanol and 1 wt% polyvinyl alcohol (PVA) as a surfactant to impose the planar anchoring. By using no ethanol we avoid the spontaneous transition of the nematic to the isotropic phase at room temperature, allowing us to preserve samples in sealed cuvettes for months.

### 4.3.1 Double-twisted configuration

After generating the nematic toroidal droplets and waiting for them to relax into a stable configuration, which happens in a time span of ≈1 hour, we obtain, in the vast majority of cases, the same defect-free configuration. When imaged between crossed polarizers, the observed texture consists on four darker regions at 90° from each other separated by bright areas as shown in Figure 4.6c. From a naive perspective one could think that the configuration of the director field consist on the simple axial configuration, with the director field pointing along the azimuthal direction $\varphi$ (Figure 4.7a). This would be equivalent to a cylinder in the axial configuration (Section 2.4.2) bent until it closes onto itself around

an axis of revolution.

Interestingly, the experimental observations are not consistent with this simple ansatz. If we had the axial configuration, the intensity in the dark regions when in crossed polarizers should vanish since the director field would be parallel or perpendicular to the polarization of the incident light and thus, its polarization would not change and light would be completely blocked by the analyzer. Also, if one rotates the analyzer in the right sense while keeping the polarizer fixed, one observes that the dark regions rotate and start becoming darker (Figure 4.6e) until a point where they start becoming brighter again. Finally, if one observes the sample from the side with crossed polarizers and the polarizer parallel to the x-y plane, the sample shows some brightness (Figure 4.6d), which should not appear if the configuration was perfectly axial.

This defect-free configuration was previously studied in the group experimentally [9, 70] and also theoretically by other groups [10]. The configuration of the director field was successfully described by a double-twisted configuration where the director points in the azimuthal direction at the center of the cross-section and rotates as we move towards the surface, as schematically shown in Figure 4.7b. This configuration spontaneously breaks chiral symmetry by means of the twist distortion. The most general two parameter ansatz proposed is expressed in toroidal coordinates (Figure 4.6f) as:

$$\begin{cases} n_r = 0 \\ n_\theta = w \dfrac{\xi \dfrac{r}{a}}{\xi + g \dfrac{r}{a} \cos(\theta)} \\ n_\varphi = \sqrt{1 - n_\phi^2} \end{cases} \tag{4.12}$$

where $\xi = R/a$ is the aspect ratio of the torus, with $R$ the torus radius and $a$ the tube radius, as shown in Figure 4.6f. $w = \sin\alpha$ controls the total twist, with $\alpha$ the angle of the director field at the surface with respect to the azimuthal direction, and $g$ is another parameter that allows for configurations with splay. The director field in this double-twisted configuration rotates $\phi = 2\alpha$ as we move vertically in the $z$ direction across the cross-section.

Since the director field depends on the aspect ratio $\xi$ of the torus, the values of the parameters $w$ and $g$ that minimize the energy will in general depend on $\xi$. It has been shown that the saddle-splay term had to be included in the free energy for the double-twisted configuration to be the ground state in comparison to the axial configuration, showing its key role in this system [10]. Indeed, as we will see in chapter 5, the origin of the double twist can be understood in pure bulk terms as a way of relieving bend and acquiring twist, reducing the overall free energy. The experimental results obtained for the twist angle $\phi$

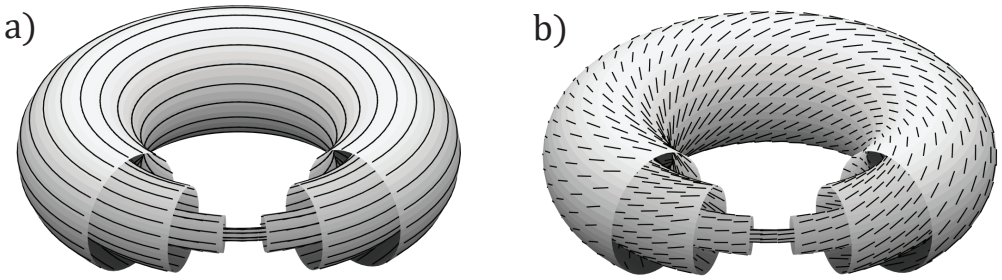



**Figure 4.7:** a) Axial configuration of a torus of aspect ratio $\xi = 2.5$. The director field is shown at different cylindrical surfaces. b) Double twist configuration. The configuration corresponds to the ansatz 4.12 with parameters $w = 0.5$ and $g = 0$. The director is axial at the cross-section center and twist as we move to the surface.

as a function of the aspect ratio were fitted in order to obtain a value for the saddle-splay constant $K_{24}$ for 5CB (Figure 4.9); the result was $K_{24} \approx 1.02K_2$ [9, 70].

To test that the nematic tori we generate behave consistently with previous results we will measure the twist angle. To do that in a simple way it is interesting to check whether the Mauguin limit is fulfilled for the light path going through the center of the cross-section along the vertical direction. In that case, if the incident polarization is parallel/perpendicular to the director at the entrance, the output polarization will be linear and pointing in the direction parallel/perpendicular to the director at the exit. The angle between the incident and output polarization will correspond to the twist angle. If we assume the twist angle $\phi$ is smaller than $\pi/2$, take $\lambda \sim 0.55\mu m$ as a typical wavelength, the birefringence of 5CB as $\Delta n \sim 0.15$, and the torus tube diameter to be $a \approx 300\mu m$ we obtain:

$$\frac{\phi}{\Delta} = \frac{\phi\lambda}{2\pi d\Delta n} \leq \frac{\lambda}{4d\Delta n} \sim \frac{1}{360} \ll 1 \tag{4.13}$$

Thus, the Mauguin limit is fulfilled and our nematic toroidal droplet can act as a waveguide. To find the twist angle we note that the ansatz has azimuthal symmetry[1]; this means that as one goes around the rotation axis of the torus, the director field at the top part rotates one turn and thus becomes parallel or perpendicular to the incident polarization four times. This means that when illuminating the sample with polarized light there will automatically be four regions where the director at the entrance is parallel to it.

[1] One can also observe experimentally that the texture observed is invariant under sample rotation and rotates when rotating simultaneously both polarizer and analyzer

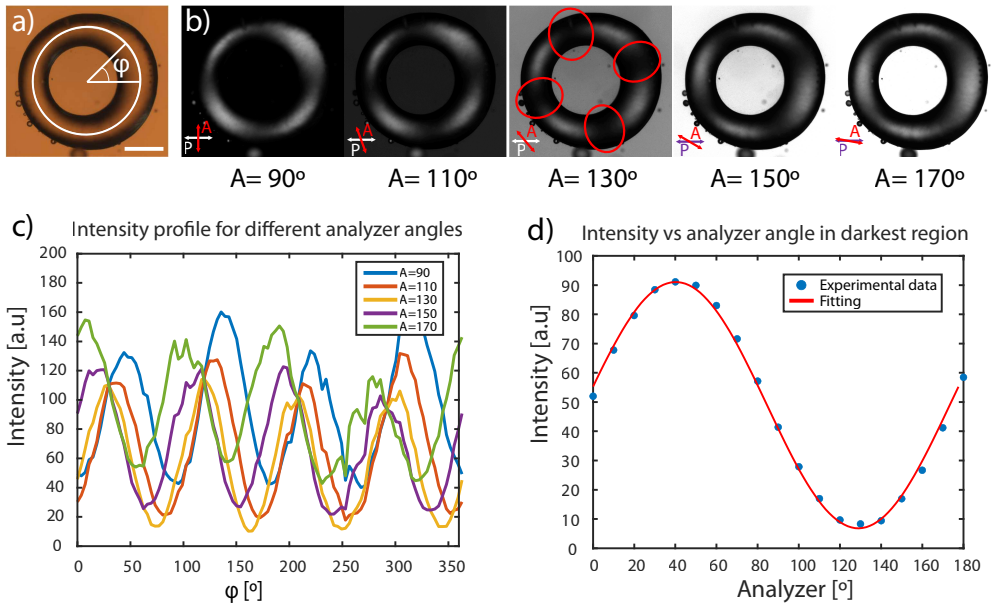



**Figure 4.8:** a) Bright field image of a defect free nematic torus. Scale bar is $400\mu m$. b) Images of the torus with the polarizer fixed at 0° and rotating the analyzer. The original color images from the microscope are converted to black and white and the intensity is scaled. Red circles correspond to the darkest regions of the torus. c) Intensity profile around the white circle of figure a for different analyzer angles. At each point the intensity is averaged over an area of 39x39 pixels. d) Intensity profile at one of the darkest regions in b) as a function of of the analyzer angle. The intensity is averaged over an area of 31x31 pixels. The red line is the fitting to a Malus' law plus a constant.

We take pictures of the sample for different angles of the analyzer, A, keeping the polarizer at 0° and the illumination constant. We plot the intensity profile as we go around the torus in the circle shown in white in Figure 4.8a for different angles of the analyzer (Figure 4.8c). We see that the minimum intensity changes as we rotate the analyzer, and that it reaches a minimum at a certain analyzer angle. This angle corresponds to when the darkest regions are observed, as shown with red circles in Figure 4.8b and the analyzer is perpendicular to the output polarization where the director is parallel to the polarizer. The twist angle will in fact correspond to the angle the polarizer forms with the direction perpendicular to the analyzer.

We can further corroborate our reasoning by monitoring the intensity as a function of the analyzer angle at one of the darkest regions. If the output polarization is linear, the intensity should follow Malus' law. We can check this

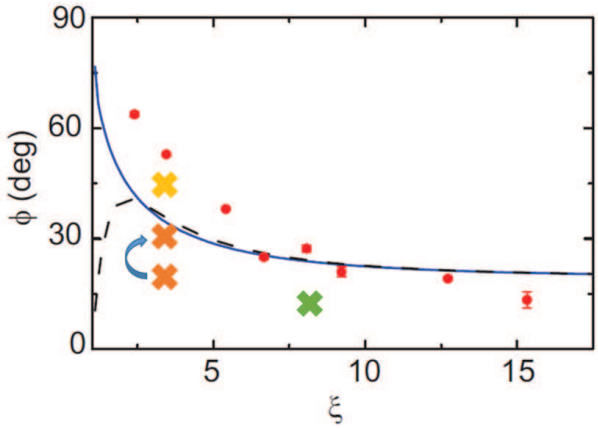



**Figure 4.9:** The data for our tori is shown on the same graph published in [9]. Each torus is shown as a cross with different colors. The torus corresponding to the orange cross was measured thrice, once after made and two other times after heating and cooling resulted in the defect free configuration. The blue arrow points from the first measurement to the second an third which yielded the same result.

by fitting the experimental data to the function $I(A) = I_0 + Bcos^2(A - \phi_0)$[1], which corresponds to Malus' law plus a background intensity that accounts for non-idealities in the light path discussed in 4.2.4. The experimental data is well fitted by this function as shown in Figure 4.8d; the fitting parameters are $I_0 = 6.9$, $B = 84.2$ and $\phi_0 = 40.7°$. The angle $\phi_0$ corresponds to the director angle at the exit.

Finally, we can see how our data compares with the previous experimental data (Figure 4.9). We use data for three different tori, two thick ones with $\xi \approx 3$, and one slender one with $\xi \approx 3$. Also, one of the tori was heated to the isotropic phase and cooled back to the nematic phase returning to the defect free configuration twice and yielding a twist angle a bit different from the initial one. We can see that the twist angle follows the trend observed in prior work, decreasing as the aspect ratio increases. Note the variability for the same aspect ratio is relatively quite high. This might result from the fact that our nematic toroidal droplets are not perfect. Shape changes might have an impact on the

[1]This functional form is also valid for a general elliptical polarization going through a polarizer. The extreme case of circular polarization, for example, would have $B = 0$ and the intensity is constant. Linear polarization is characterized by $I_0 = 0$ and $I_{max} = I_{input}$. Nevertheless, since we do not know the value of $I_{input}$, for low values of $I_0$ it is hard to distinguish between slightly elliptical polarization and non-idealities that give rise to a constant background intensity. In any case, the experimental evidence is consistent with the proposed ansatz, so we consider it a good description of the system.

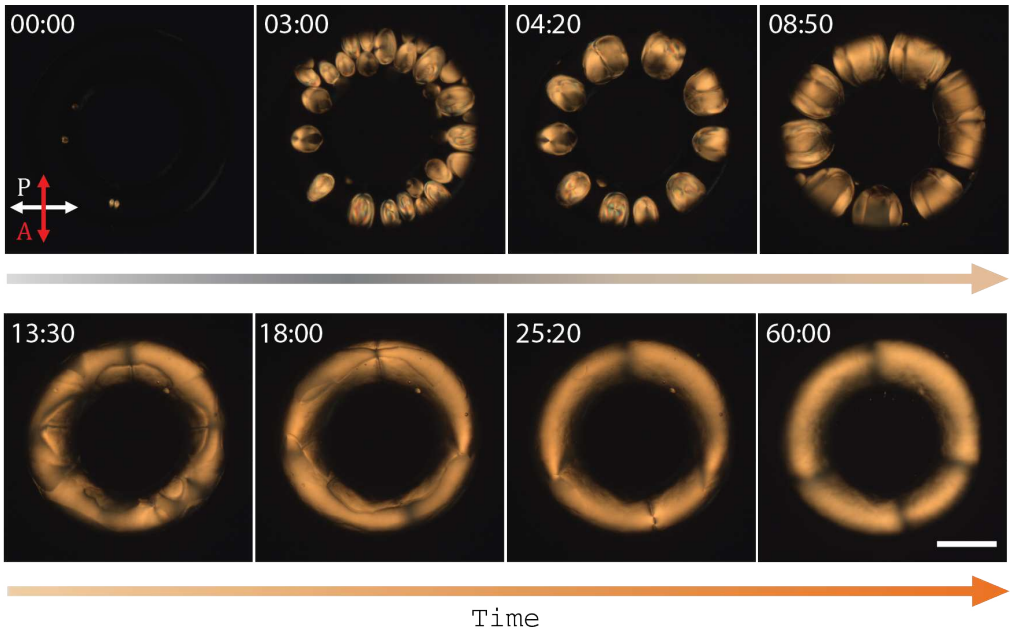



**Figure 4.10: Isotropic-nematic transition of a nematic torus at a cooling rate of $2°C/h$.** Time evolution snapshots of the isotropic-nematic transition in crossed polarizers. Time labels are in minutes. Scale bar is $400\mu m$. Gamma=0.45 for visualization purposes.

final twist angle. There is also the possibility that the torus resides in metastable states of twist, as the heating and cooling experiment suggests. Nevertheless, we do observe the double twist character of our nematic tori seen before.

### 4.3.2 Generating stable defect configurations by heating and cooling cycles

After making the nematic tori, most of them acquire the defect-free double-twisted configuration. In order to test whether there is a bias in the making procedure towards this configuration we heat the nematic toroidal droplet to the isotropic phase and cool it back, so that it randomly nucleates into the nematic phase and the memory of the making procedure is lost. To heat and cool our nematic tori we place the cuvette with the tori on top of a Peltier stage as described in 4.2.5. The tori are heated at $38°C$ for around 15 min. After this time the torus has become isotropic and when imaged between crossed polarizers the sample appears completely dark. Subsequently, we cool the sample down to room temperature at a controlled rate. In this work, we explore two different

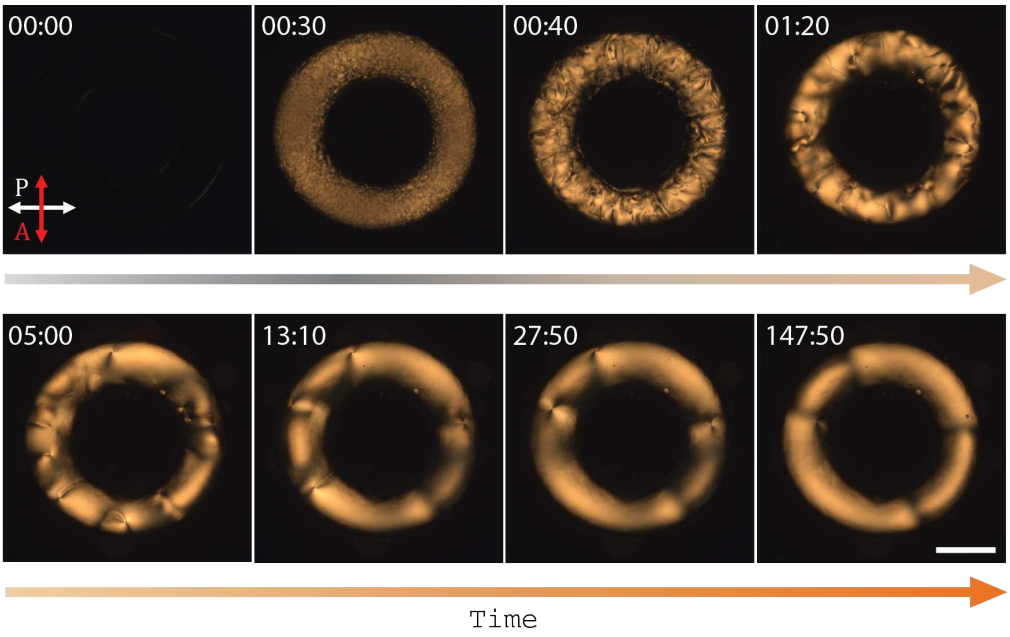



**Figure 4.11: Isotropic-nematic transition of a nematic torus at a cooling rate of 2°$C/min$.** Time evolution snapshots of the isotropic-nematic transition in crossed polarizers. Time labels are in minutes. Scale bar is 400$\mu m$. Gamma=0.45 for visualization purposes.

cooling rates, a slow one at 2°$C/h$ and a fast one at 2°$C/min$:

1. **2°C/h**: In this case, since the isotropic-nematic transition is a first order transition and the cooling rate is small, we observe the appearance of a few nematic domains that start growing as the cooling process proceeds. These domains are located on the top part of the torus since that is the coldest part due to the vertical temperature gradient. Initially, many of them appear close and merge when growing, resulting in a few stable domains. These nematic domains grow slowly until they get in contact with each other and merge. The situation is then reversed and we observe a few isotropic islands in a continuous nematic background. The isotropic islands then shrink until the whole torus becomes nematic (Figure 4.10). In this case it is interesting to note two things. First, the initial domains look elongated along the polar direction $\hat{\theta}$, which could be either because of the nematic elasticity favoring the elongation of tactoids [127, 128] and/or because of the heterogeneous nucleation on a curved interface with different principal curvatures. Second, the phase transition takes around an hour, and thus the nucleated domains have time to relax before merging. The fi-

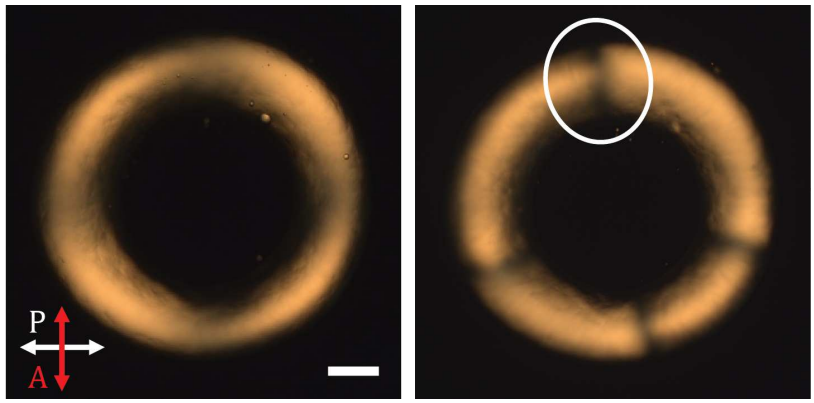



**Figure 4.12:** Left: Double-twisted configuration in crossed polarizers. Right: Configuration with localized featured obtained after heating and cooling the torus on the left. One out of the four features is marked with a white ellipse. Scale bar is $200\mu m$. Gamma=0.45 for visualization purposes.

nal stable configuration is usually reached soon after the torus has become completely nematic with very small changes occurring in the time-span of another hour.

2. **2°C/min**: In this case, the torus transitions completely to the nematic phase in a very short time leading to a configuration full of disclination lines and point defects through the nematic version of the Kibble-Zurek mechanism [129]. As time passes the nematic liquid crystal starts relaxing and the disclination lines and point defects start annihilating and thus the defect density reduces with time. This process continues until a final stable configuration is reached (Figure 4.11). In this case, although the full transition of the toroidal droplet into the nematic phase is very fast, it usually takes longer, around 2-3 hours, to arrive to the stable configuration due to the large distortions that are present in the nematic.

Independently of the nucleation mechanism the final configuration in both cases rarely corresponds to the defect-free double-twisted configuration, presenting localized features which are stable throughout the life of the torus[1]. The comparison between the double-twisted texture and the stable texture resulting from the heating and cooling cycles under crossed polarizers is shown in Figure 4.12, where one out of the four new features in the torus is highlighted with a

[1]Our nematic tori can be preserved for months. The main reason for their breakup is the evaporation of the water in the yield stress material, or the growth of air bubbles that distort the yield stress material. No spontaneous change of configuration has been observed experimentally.

white circle. Moreover, the same type of stable localized features are observed for both cooling rates, supporting the idea that they correspond to stable or metastable director field configurations.

## 4.4 Defect pairs



### 4.4.1 Observations

To understand the nature of the localized features that appear when heating and cooling nematic toroidal droplets with parallel boundary conditions (see 4.3.2), it is important to take into account the following experimental observations:

1. If the heating and cooling experiment is repeated several times for the same torus we find that the number and location of the features change (Figure 4.13a). However, all of the features have the same texture when rotating the crossed polarizers. Since the orientation of a feature depends on its position, the important parameter to compare textures is the relative angle of polarizer and analyzer with respect to the feature.

2. The total topological charge of the feature is zero. The Poincaré-Hopf index theorem applied to a solid-torus with parallel anchoring conditions shows that the total topological charge must be zero. Since we find that after heating and cooling repeatedly the same torus, there are instances where the configuration has only one localized feature, as shown in figure 4.13a left, its total topological charge needs to be zero. This does not imply that the feature is defect free since we can have defects with positive and negative topological charges, so a defect populated configuration is possible as long as the sum of the charges is zero.

3. No defect points or lines are observed from the top view. In the cooling videos we observe that in the late stages, when the features are formed, one can sometimes observe two point-like features moving to the inner and outer rings of the torus (Figure 4.13b). These point-like features are possible candidates to be topological defects. Their positioning in the inner and outer rings would explain why they are not seen from the top view, since they lie in the optically inaccessible regions due to refraction. This is further confirmed by looking at the relaxed torus from the side between crossed polarizers. In this case, two point defects can be seen at different focal planes corresponding to the inner and outer ring of the torus (Figure 4.13c).

4. The texture between crossed polarizers when the polarizer is aligned parallel or perpendicular to the cross-section consists on a dark thin line going

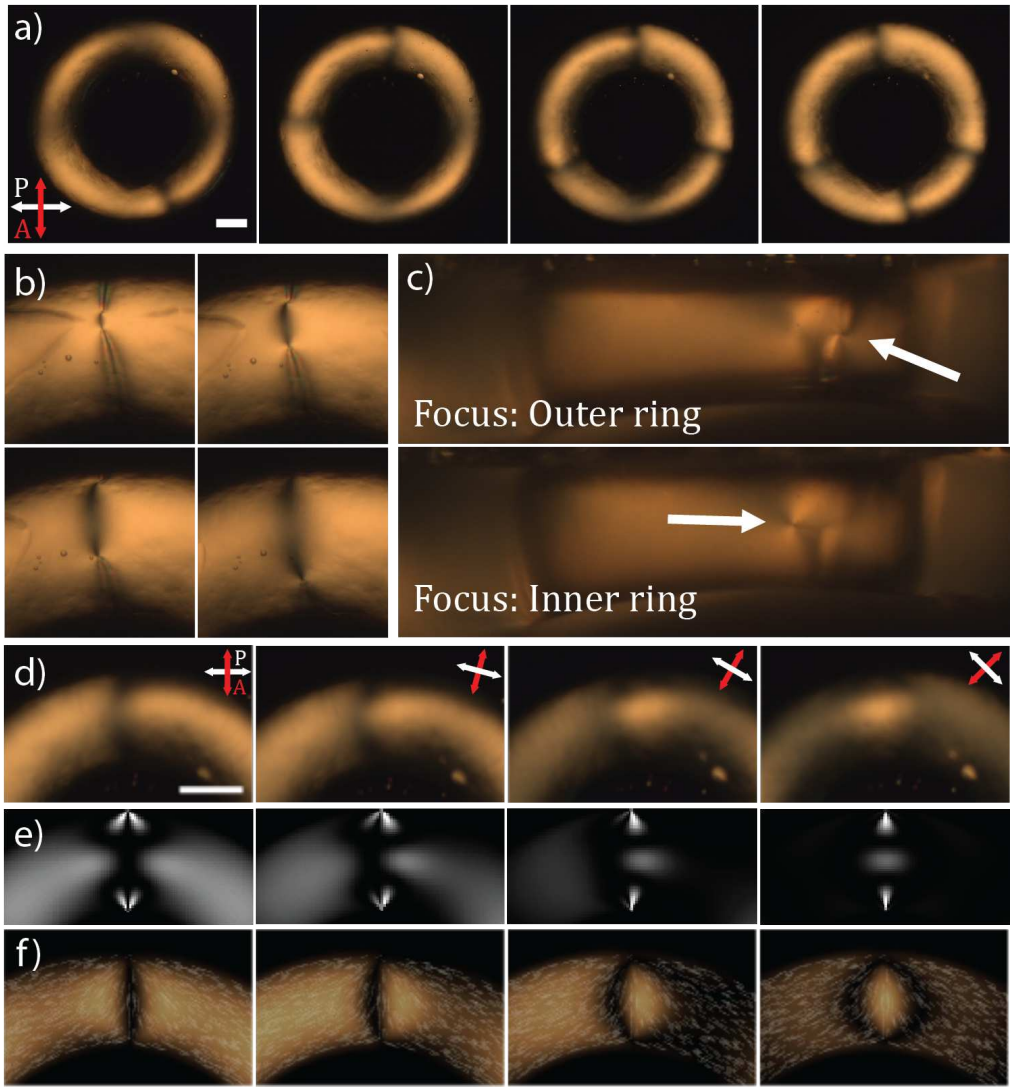



**Figure 4.13:** a) Stable configurations with different number and location of defect pairs after different heating and cooling cycles of the same torus. There is only one defect pair on the left image. b) Formation of a defect pair during the isotropic-nematic transition. Two point-like features can be seen to move to the outer and inner ring respectively between crossed polarizers. c) Side view of a torus between crossed polarizers where the point like features of a defect pair are observed at different focal planes. d) Experimental texture of a defect pair when rotating crossed polarizers. Each image correspond to an extra rotation of 15° clockwise. e)Single wavelength Jones matrix simulation of the proposed ansatz. f) Jones matrix simulation for the defect pair configuration from the Lattice-Boltzmann simulations (extracted from [130]). Scale bars are 200$\mu m$.

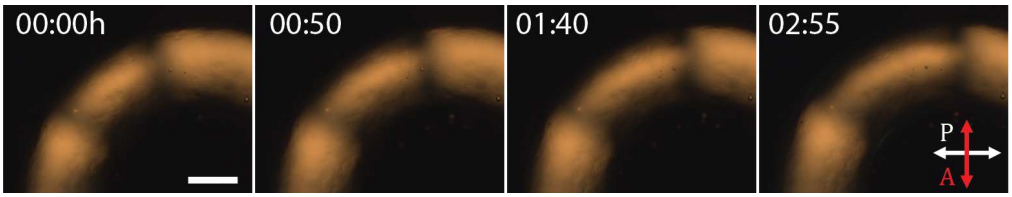



**Figure 4.14:** Time sequence showing the separation of defect pairs with time after formed. Scale bar is $200\mu m$.



from the inner ring to the outer ring of the torus. As we rotate the crossed polarizers, the thin line starts deviating for its straight shape while keeping its end points at the inner and outer rings fixed. One can see that it rotates in the same/opposite sense as the crossed polarizers with respect to the fixed point in the outer/inner ring respectively (Figure 4.13d). The dark line ends up breaking up and appearing from the other side as the rotation angle becomes larger than 45°. As seen in sections 4.2.3 and 4.2.4 the rotation sense might indicate that the inner defect is negative while the outer defect is positive. This is consistent with the zero total topological charge constraint.

5. When two features are formed close enough they seem to slowly repel until they stabilize at a given distance (see Figure 4.14). This could indicate that the localized features have an interaction width and thus a characteristic width where the director differs from the defect-free one.

### 4.4.2 Proposed model

The previous observations allow proposing a model for the localized features consisting on two defects located in the inner ($\theta = \pi$) and outer ($\theta = 0$) ring. We assume that both defects are located on the torus surface (boojums), since point defects lower their energy by half when they are on the surface. We also assume that the topological defects are $\pm 1$, the lowest possible charge, since splitting of point defects into several point defects with smaller charge reduces the energy in all cases. Additionally, $\pm 1/2$ defects would imply the presence of disclination lines ending at the surface which are not observed. Finally, to fulfill the topological constraint we can assign the defects opposite charges, assigning the boojum in the outer/inner ring a charge of $+1/-1$ respectively. This configuration will be referred to as a defect pair configuration from now on.

We can easily imagine a director configuration compatible with the above description that also complies with the tangential boundary conditions. The cross-section has a bipolar configuration, as shown in Figure 4.15a, with the

director field tangent to the cross section at all points. The director field at the equatorial plane, $r \sin\theta = 0$, which corresponds to the symmetry plane of the torus perpendicular to the rotation axis, is also tangent to it. The director field resembles the one corresponding to a pair of $\pm 1/2$ defects separated by a distance $2a$, as schematically shown in Figure 4.15b.



#### 4.4.2.1 Analytical ansatz derivation

To derive an analytical ansatz for the defect pair we first note that we can easily construct a feasible configuration if we have a mathematical expression for the director field in both the cross-section and equatorial plane. Since both planes are perpendicular between them and the director field is tangential to them, from each of them we get one angle describing the director field. From the cross-section we get the polar angle $\Theta(r, \theta)$ that tells us how much the director field tilts away from the radial direction, while from the equatorial plane we get the azimuthal angle $\Phi(r\cos\theta, \varphi)$ that indicates how much the director field tilts away from the azimuthal $\hat{\varphi}$ direction. We then can compute the director field at each point by assigning the polar angle from the corresponding position of the cross-section and the azimuthal angle from the one at the closest point in the equatorial plane (vertical projection of the point on the equatorial plane). The director field can be written as:

$$\begin{cases} n_r(r,\theta,\varphi) = \sin(\Phi(r\cos\theta,\varphi))\cos(\Theta(r,\theta)) \\ n_\theta(r,\theta,\varphi) = \sin(\Phi(r\cos\theta,\varphi))\sin(\Theta(r,\theta)) \\ n_\varphi(r,\theta,\varphi) = \cos(\Phi(r\cos(\theta),\varphi)) \end{cases} \tag{4.14}$$

We can easily verify that the anchoring conditions are fulfilled since for each point on the surface the director field is given by a linear combination of the $\hat{\theta}$ and $\hat{\varphi}$ components. Since the tangential plane is determined by both vectors, any linear combination belongs to the tangential plane.

The bipolar configuration is a well-known configuration with an analytical expression resulting from the energy minimization in the one-constant approximation [131, 132]. For perfect planar boundary conditions the polar angle $\Theta$ can be written as:

$$\Theta(r,\theta) = \begin{cases} -\tan^{-1}\left(\tan(\theta)\dfrac{a^2+r^2}{a^2-r^2}\right) & \text{if } \dfrac{\pi}{2} < \theta < \dfrac{3\pi}{2} \\ -\tan^{-1}\left(\tan(\theta)\dfrac{a^2+r^2}{a^2-r^2}\right) + \pi & \text{else} \end{cases} \tag{4.15}$$

We have used a piece-wise function to rotate the vector field $\pi$ where needed to get a continuous vector field pointing from the outer to the inner ring. The

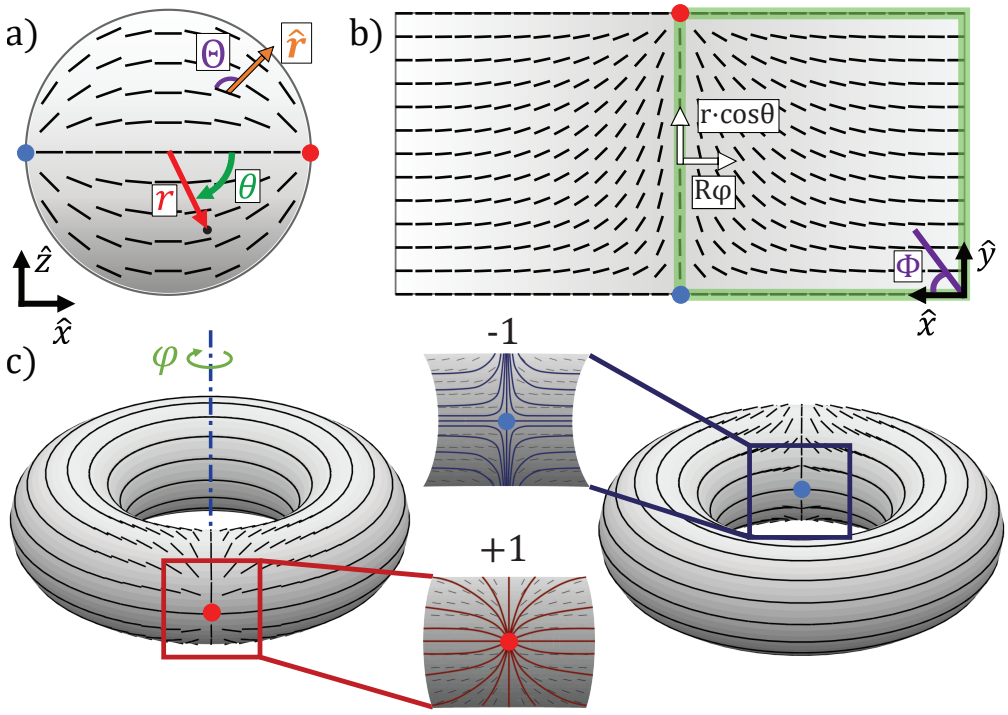



**Figure 4.15:** a) Ansatz director field at the cross-section. b) Ansatz at the equatorial plane drawn on a rectangle with basis $\hat{\varphi}$ and $\hat{r}$ and $R\varphi$ and $a\cos\theta$ their coordinates respectively. c) Director field at the surface of the torus with the $\pm 1$ defects magnified.

director field does not change because of its symmetry but continuity in the vector field description is need for equation 4.14 to give a continuous vector field. A section of the equatorial plane can be first approximated by a rectangle with the horizontal coordinate $x$ corresponding to $R\varphi$ and the vertical one $y$ to $r\cos\theta$ (Figure 4.15b). We characterize the director field by the angle with the horizontal direction $\hat{x}$. The point defects are located in the middle line, where the director field is along $\hat{y}$. Sufficiently to the left and right of this line, the axial configuration is recovered, with the director pointing in the $\hat{x}$ direction. By symmetry we only have to consider one half of the rectangle; we choose the right one marked by the green box in 4.15b. The other half is simply obtained by a reflection across the vertical central line. The boundary conditions are given by $\Phi = 0$ in the horizontal boundaries due to the anchoring conditions and in the right boundary since we assume we recover the axial configuration at a finite distance $L$. $\Phi = \pi/2$ in the left boundary since it corresponds to the line joining defects.

If we assume a 2D vector field in the one constant approximation, minimizing the free energy results in a differential equation for the angle of the director with the horizontal direction $\hat{x}$. This equation is Laplace's equation, $\nabla^2\Phi = 0$. We set the origin of coordinates in the lower right corner, being the $x$ coordinate positive as we go to the left, and the $y$ positive as we go up (see figure 4.15b). By using separation of variables $\Phi(x, y) = X(x)Y(y)$ we get the differential equation:

$$\frac{1}{Y}\frac{\partial^2 Y}{\partial y^2} = -\frac{1}{X}\frac{\partial^2 X}{\partial x^2} = -k^2 \tag{4.16}$$

where $k$ is a real or complex number. By assuming $k^2 > 0$ the solutions can be written as [133]:

$$\begin{cases} X(x) = A\cosh(kx) + B\sinh(kx) \\ Y(y) = C\cosh(ky) + D\sinh(ky) \end{cases} \tag{4.17}$$

The boundary at the top, bottom and right boundaries provide the following restrictions:

$$\begin{cases} \Phi(x,0) = 0 \Longrightarrow Y(0) = 0 \Longrightarrow C = 0 \\ \Phi(x,2a) = 0 \Longrightarrow Y(2a) = 0 \Longrightarrow k = \dfrac{n\pi}{2a}, \quad n = 1,2,3... \\ \Phi(0,y) = 0 \Longrightarrow X(0) = 0 \Longrightarrow A = 0 \end{cases} \tag{4.18}$$

The angle can then be written as:

$$\Phi(x,y) = \sum_{n=1}^{\infty} D_n sin\left(\frac{n\pi y}{2a}\right) sinh\left(\frac{n\pi x}{2a}\right) \tag{4.19}$$

Imposing on this form of the solution the last boundary equation, we get:

$$\Phi(L,y) = \sum_{n=1}^{\infty} D_n \sin\left(\frac{n\pi y}{2a}\right) \sinh\left(\frac{n\pi L}{2a}\right) = \frac{\pi}{2} \tag{4.20}$$

This expression corresponds to a Fourier sine series in the $y$ variable. Since a Fourier sine series describes antisymmetric functions we can extend the function to the $-2a \leq y \leq 0$ interval and obtain the coefficients from Fourier analysis [133]:

$$\sinh\left(n\pi\frac{L}{2a}\right) D_n = \frac{\pi}{2a}\int_0^{2a} \sin\left(\frac{n\pi y}{2a}\right) dy = \begin{cases} \dfrac{2}{n}, & \text{n odd} \\ 0, & \text{n even} \end{cases} \tag{4.21}$$

Finally, we can change to simple coordinates[1]. By setting the defect pair location to $\varphi = 0$, with $\phi$ increasing to the right, we get $x = L - R\varphi$. The $y$ coordinate is transformed according to $y = a - r\cos\theta$. With these changes, the final expression for the director field at the equatorial plane becomes:

$$\Phi(\varphi, r\cos(\theta)) = \sum_{\text{n odd}} \frac{2}{n} \frac{1}{\sinh\left(n\pi \dfrac{R\varphi_{max}}{2a}\right)} \sin\left(\frac{n\pi(a - rcos(\theta))}{2a}\right) \sinh\left(n\pi\left(\varphi_{max} - \varphi\right)\frac{R}{2a}\right) \tag{4.22}$$

where $\varphi_{max} = L/R$ is the azimuthal angle where the axial configuration is recovered. In the limit $L \to \infty$ the expression can be simplified to[2]:

$$\Phi(\varphi, r\cos\theta) = \sum_{\text{n odd}} \frac{2}{n} \sin\left(\frac{n\pi(a - r\cos\theta)}{2a}\right) e^{-n\pi\frac{\varphi R}{2a}} \tag{4.23}$$

From this last equation we can see that the azimuthal angle of the director field decreases as we move away from the defect pair as a sum of decreasing exponentials. From these ones, the slowest decay is given by the term $n = 1$, so we can assign an angular width[3] based on the angle where the slowest exponential becomes $1/e$:

$$\Delta\varphi_{\text{defect pair}} \sim \frac{2}{\pi}\frac{2a}{R} = \frac{4}{\pi\xi} \tag{4.24}$$

Since $\xi \geq 1$ for a torus, the angular width is always smaller than $4/\pi \approx 1.27$ which is always significantly smaller than the maximum angular width allowed for the torus: $2\pi \approx 6.28$. This angular width gives an interaction distance between defect pairs. Defect pairs will interact if the distance is smaller than the width of a defect pair. Nevertheless, we will let $\varphi_{max}$ as a free parameter controlling the defect pair width since our ansatz is based on º simplifications and the real width can indeed be smaller.

[1] We have used a simple linear coordinate transformation for simplicity. The 2D equilibrium configuration for the defect pair configuration in the equatorial plane can be obtained by using the conformal mapping $w = e^{-i\alpha z + \delta}$, with $\alpha = \frac{1}{2a}\ln\left(\frac{R+a}{R-a}\right)$ and $\delta = \ln(R-a)$. The map transforms the initial rectangle into an annular region, which corresponds to half the equatorial plane when $L = \pi/\alpha$. This mapping gives the equilibrium configuration, since in the one constant approximation, the angle of the director field with the azimuthal direction, $\Phi$, fulfills Laplace's equation with the right boundary conditions.

[2] The simplification is based on the fact that $\sinh x \to \frac{1}{2}e^x$ for $x \to \infty$

[3] We use twice this value because of the defect pair symmetry.

The final expression for the defect pair ansatz is then obtained by simply plugging equations 4.15 and 4.22 into equation 4.14. The director field on the surface of the torus obtained from this ansatz is shown in Figure 4.15c, where the insets show the director field around the point defects. This surface director field resembles the one reported for toroidal colloidal inclusions in a nematic liquid crystal with parallel anchoring conditions [134]. In order to numerically compute the director field, we truncate the summation series to the first 100 terms. This number is chosen, since larger numbers can cause numerical instabilities, while assuring good and fast convergence. For the largest values of $\varphi_{max}$, a lower number of terms should be used for numerical convergence.

As a final remark we have not included twist in the ansatz for simplicity of the analysis. The difference between the double-twisted and the axial director field could be added to our ansatz as a first approach to incorporate twist.

#### 4.4.2.2 Jones Matrix simulations

As a first test to our ansatz we perform Jones Matrix simulations [117, 135] to see if we can reproduce qualitatively the experimentally observed texture near the defect pair when rotating crossed polarizers. Jones Matrix simulations consists on breaking the continuous director field into voxels[1]. In each of the voxels, the continuous director field is substituted by a constant field given by the director field at the center. Each of these voxels can be considered as a uniaxial medium so the transmission of polarized light is given by multiplying the Jones vector of the incident light by the matrix (see 4.2 and equations 4.7 and 4.8):

$$\phi_i = R(\theta_i) M_i R(-\theta_i) \tag{4.25}$$

where the subindex $i$ refers to the specific voxel from top to bottom, $R$ is the rotation matrix, $\theta_i$ is the angle of the director projection onto the horizontal plane with respect to the $\hat{x}$ direction, and $M$ the phase shift matrix in its diagonal form (see equation 4.6). The phase shift will depend on the angle the director makes with the horizontal plane and the wavelength of light (see equation 4.4). When light propagates through each voxel we multiply the polarization of light entering the voxel by the corresponding matrix, which is equivalent to multiplying the initial polarization by the matrix resulting from multiplying the voxels matrices in the following way:

$$\Psi(x_i, y_i) = \phi_N ... \phi_{i+1} \phi_i \phi_{i-1} ... \phi_1 \tag{4.26}$$

[1] Voxel is the name given to 3D pixels. They can be considered as boxes, or in general, as right parallelepipeds.

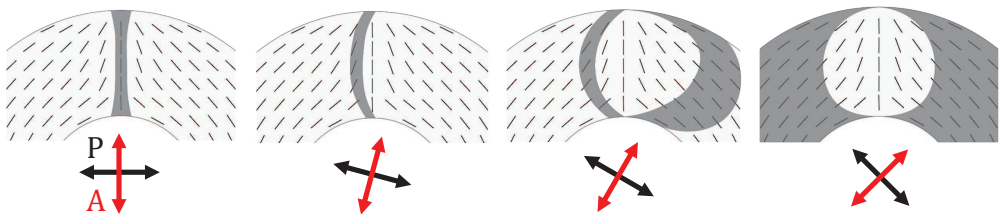



**Figure 4.16:** Schematics of the expected texture for our defect pair ansatz under crossed polarizer for different angles of the polarizers.

We then have to compute the corresponding matrix for each voxel column to get the whole 2D image. The final intensity at each pixel is obtained by multiplying the output polarization by the matrix corresponding to the analyzer (Table 4.1) and obtaining the modulus square of the resulting complex vector. In order for the discretization to not affect the final texture obtained, the voxel size has to be small enough so the director field barely changes inside the voxel.

We simulate the texture resulting from the defect free ansatz director field between crossed polarizers with a custom made Python script[1]. We use the simplest approach of single wavelength ($\lambda = 0.65\mu m$) and do not take into account any refraction effects, so that light propagates in the vertical direction without deviation. For our simulations, the voxel size is set to: $\Delta z = 0.012a$ and $\Delta x = \Delta y = 0.022(R + a)$. The simulation results and comparison with the experiments are shown in Figure 4.13e. There is qualitative agreement with the experiment in some important aspects. Mainly the dark line joining defects changes in the same way as the crossed polarizers are rotated. A simpler way to predict the texture in crossed polarizers from the ansatz is by using a quasi 2D approach where we just take the director field at the equatorial plane as representative of the director field[2]. For a given polarizer angle the dark regions correspond to where the director is parallel or perpendicular to the initial polarization (see Figure 4.16). This proves the compatibility of the proposed defect pair configuration for describing the experimental texture and director field.

#### 4.4.2.3 Further confirmation: Lattice-Boltzmann simulations

Final support for the defect pair configuration was provided by Luca Giomi's group [130]. They performed Lattice Boltzmann simulations to mimic the

[1] Credit to Alexis de la Cotte for developing the program used.

[2] In this case, this is a good representation, since the director at a given point only deviates from the configuration at the closest equatorial plane by tilting out of the plane. As a result, the main axis remain the same all along z.

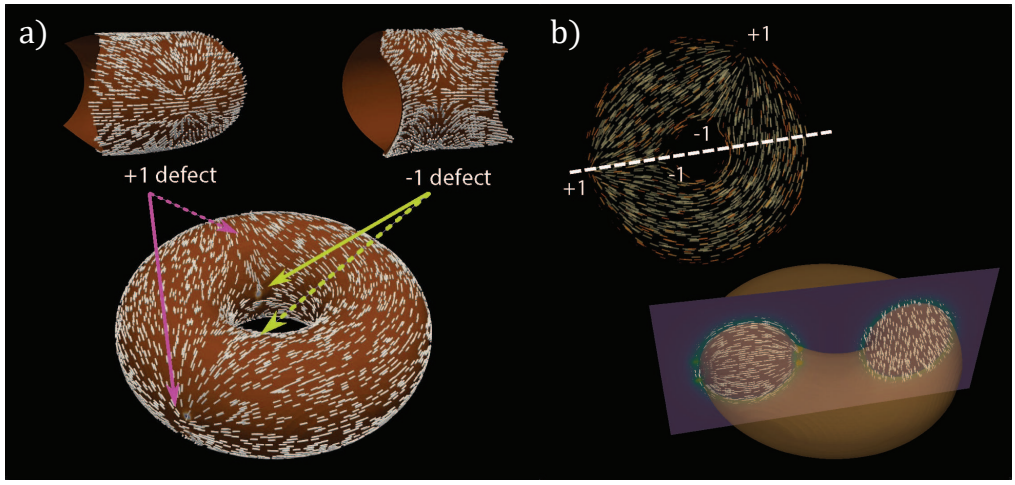



**Figure 4.17:** a) Director field configuration on the surface of the torus. $pm1$ defects are label and enlarged on the top. b) Director field at the equatorial plane and cross section of a defect pair. Image adapted from [130].

isotropic-nematic transition for a toroidal droplet. The simulations first thermalized the non-spherical droplet to get phase separation between the inside of the droplet and the outer material. The Q-tensor was then randomly initialized inside the droplet, set to 0 outside, and allowed to evolve by solving the nematohydrodynamics equations [136]. These equations account for advection-diffusion of the concentration field, the Q-tensor evolution through the Beris-Edwards equation, and flow thorough a modified version of the incompressible Navier-Stokes equation. Simulations were carried out until the total free energy variation between iterations was less than 0.1%. More details on the simulation procedures and equations can be found in the Supplemental Material of [130].

Simulations were performed for toroidal droplets with aspect ratios $\xi$ in the range $[2, 6]$ and different values for the Frank elastic constant. In all cases, simulations show that defect pairs are stabilized, with the positive/negative defect located in the outer/inner ring of the torus, consistent with the proposed ansatz and experimental observations. The director field obtained from the simulations is shown in Figure 4.17 for a torus with two defect pairs. The simulated configuration for a defect pair is very similar to the one obtained from the ansatz in figure 4.15.

To compare with experimental images, Jones Matrix simulations were performed for the simulated configuration. Since the Q tensor of the configuration is computed, the simulations are improved by using the dielectric anisotropy tensor $\epsilon_{ij}$:

$$\epsilon_{ij} - \frac{Tr\boldsymbol{\epsilon}}{3} = Q_{ij} \tag{4.27}$$

The simulated images are shown in Figure 4.13f. The visual agreement with the experimental images is very good, supporting the interpretation of the simulation results, and consistent with other Monte Carlo simulations [137]. These last ones focus on cholesteric tori, but find metastable structures for planar nematic tori like those found here.



### 4.4.3 Role of curvature

The description of defect pairs matching the experimental observations consists on the positive/negative defect being located at the outer/inner ring of the torus. In our initial experiments with thick tori, $\xi \approx 3$, almost all the defect pairs observed are consistent with this configuration, which we will refer to as the "canonical" configuration from now on (Figure 4.18a). The minority of cases where defect pairs are found in other configurations will be discussed in 4.4.6.

Note that for the canonical defect pair, the positive/negative point defects are located in the surface regions of higher positive/negative Gaussian curvature, respectively. This is reminiscent of the theoretically predicted case for a 2D nematic on the surface of a torus [11]. In this case, when the torus is thick enough, $\pm 1/2$ defect pairs with the positive/negative defects in the outer/inner rings are predicted to populate the ground state. This is based in the fact that for a 2D nematic there is an interaction with the underlying curvature such that positive defects are attracted to regions of positive Gaussian curvature while negative defects are attracted to regions of negative Gaussian curvature. Since the torus has a gradient in Gaussian curvature, been negative and the lowest in the inner ring and positive and the highest in the outer ring, this induces an unbinding force for defect pairs. In the theory, when the torus is thick enough, $\xi \leq \xi_c$, the unbinding force is large enough to hinder the elastic attraction and induce the spontaneous defect pair separation. This curvature-induced unbinding was experimentally detected for a 2D active nematic system on the surface of a torus, where the positive/negative defect density increased for increasing/decreasing Gaussian curvature [67].

Our experimental results differ in some fundamentals aspects from the 2D nematic on a torus surface. In our case we have a solid torus with nematic material in the inside whose elasticity can play an important role. Also, and because of this, the defect pairs consist on $\pm 1$ defects, rather than $\pm 1/2$. The relevant parameter determining the stability of defect pairs in [11] is the aspect ratio, so in order to experimentally test whether the Gaussian curvature of the surface plays a role in the generation and/or stability of our defect pairs, we generate nematic solid tori with larger aspect ratios, $\xi \approx 8$. When heating and

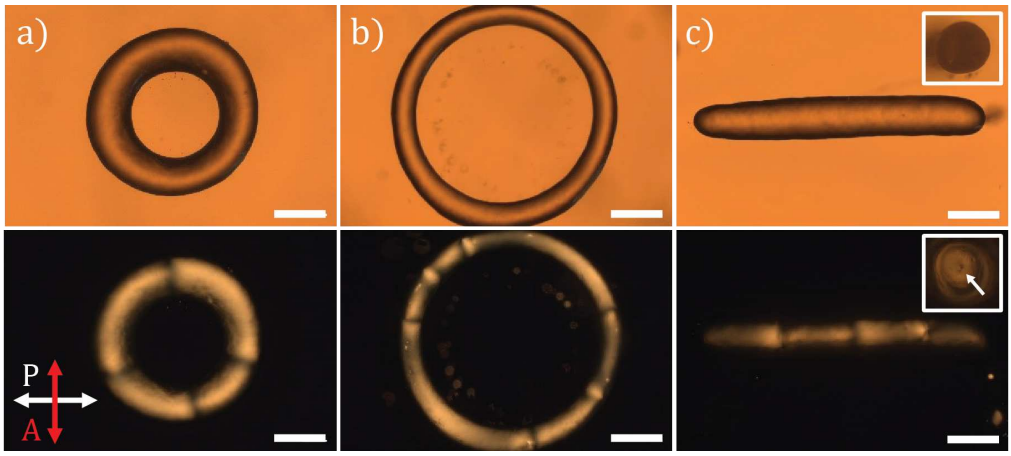



**Figure 4.18:** Bright field (top) and crossed polarizer (bottom) images of: a) Thick nematic torus $\xi \approx 3$, b) Slender nematic torus $\xi \approx 8$ and c) nematic cylinder. Images correspond to configurations obtained after a heating and cooling cycle. Insets of figure c) correspond to view of the nematic cylinder from the axial direction. A point defect can be seen at the center as indicated by the white arrow. All scale bars are $400\mu m$.

cooling these slender tori we still observe stable defect pairs in the equilibrium configuration (see Figure 4.18b).

Since making more slender tori becomes a challenge, either in terms of field of view for increasing $R$, or in terms of their generation for decreasing $a$, we generated some nematic solid cylinders which would correspond to the case $\xi \to \infty$ and zero Gaussian curvature, except at the rounded caps of the cylinder edges. Note that these cylinders are topologically equivalent to a sphere so for parallel anchoring conditions the total topological charge should be +2. We observe that to fulfill this topological constraint, a +1 defect is located at each cap, where the curvature is largest (inset Figure 4.18c). This means that the cylindrical section starts defect free and is similar to a torus with infinite aspect ratio. After heating and cooling our solid cylinders, we see that stable defect pairs still appear (Figure 4.18c), indicating that Gaussian curvature does not play a role in the generation and stabilization of defect pairs for solid nematic tori. One could argue that our nematic cylinders are not perfect and present bumps on the surface with curvature, and that those could act as attraction regions for defects. Simulations, on the contrary, show that for perfect cylinders, stable defect pairs are also formed, proving that our results are not a result of experimental non-idealities.

Interestingly, while for the nematic tori the canonical defect pair configuration is the one observed in the majority of cases, the orientation of the defect

pairs in the cylinder does not seem to show any preferential polar angle (see section 4.4.5.3 for a statistical analysis). This is expected, since the nematic cylinder presents rotational symmetry around its axis and the energy should not change with the polar location of the defects as long as they are kept diametrically opposed. Gaussian curvature, despite not playing a role in the generation and stability of the defect pairs, might play a role in positioning the point defects through Gaussian curvature attraction.

However, as we will see in section 6.3.1, one can also qualitatively explain the observed defect position in relation to bulk energy differences due to the curvature of the center-line of the torus. This is further exemplified by the results in [138], where they confine rod-like viruses forming a nematic liquid crystal into a 2D annulus. This system is indeed a 2D nematic confined to the equatorial plane of a torus with planar boundary conditions. Their experimental results show the presence of stable $\pm 1/2$ defect pairs with a director field like the one previously derived for the equatorial plane. In this case, there is no Gaussian curvature, yet defect pairs are formed, illustrating that the main role in the defect positioning might be related to the curvature of the center-line. Ths is further supported by theoretical and simulation work describing the 2D defect pair configuration [139, 140].

### 4.4.4 Stability of defect pairs

It is now clear that defect pairs are stable configurations and do not spontaneously annihilate into the defect-free configuration. This means that there is an energy barrier for any path between the defect pair and the defect-free configurations. To estimate this energetic barrier we can imagine, encouraged by simulations, that in order to annihilate, each point defect splits into two 1/2 defects of the same sign connected by a disclination line; see schematics in Figure 4.19a. These charge-like half integer defects start separating from each other until they meet the oppositely charged half-integer defect at the top/bottom part of the cross-section, where they annihilate leading to the defect free configuration; see schematics in Figure 4.19a. During the defect separation, the associated disclination lines grow. For simplicity, we assume these lines are straight. Interestingly, for micrometer-sized nematics confined to toroidal cavities with nearly square cross-section and subjected to tangential boundary conditions, the pair disclination lines with small separation angle are stable against the formation of the boojum pair [60], emphasizing the significance of the lines as an intermediate configuration for the system to transition to the defect-free state.

To analytically compute the energy[1], we need to compute the energy for

[1]Credit to Ludwig A. Hoffmann for performing the analytical calculations during his PhD work in Luca Giomi's group.

both the defect pair and the case with two disclination lines. For the defect pair configuration, we assume its energy is a sum of the bulk energy $E_0^{bulk}$, computed as the 2D energy of the bipolar configuration multiplied by the width of the defect pair $\ell_c$, in the azimuthal direction; the surface energy $E_0^{int}$ resulting from the 2D elastic interaction energy of the point defects on the surface [141], and the defect core energy, $E_{core}^s$:

$$\begin{cases} E_0^{bulk} = \dfrac{\pi K \ell_c}{2} \ln \dfrac{a}{4r_0} \\ E_0^{int} = \pi K \left( \sum\limits_i s_i \right)^2 \ln \dfrac{\ell_c}{r_0} + 2\pi K \sum\limits_{i>j} s_i s_j \ln \dfrac{r_0}{D_{ij}} \\ E_{core}^s = \dfrac{\pi K s^2}{2} \end{cases} \tag{4.28}$$

where $\ell_c$ represents the characteristic length comparable to the width of the defect pair as defined in equation 4.24, $r_0$ is the defect core size, $K$ a characteristic value for the elastic constant, $s$ the 2D topological charge of the defect, and $D_{ij}$ the separation between defect $i$ and $j$. Taking into account that $D = \pi a$, the final energy of the canonical defect pair can be expressed as [130]:

$$E_0 = \frac{\pi K \ell_c}{2} \ln \frac{a}{4r_0} - 2\pi K \ln \frac{r_0}{\pi a} + \pi K \tag{4.29}$$

For the case with disclination lines, the bulk energy $E^{bulk}$ can be approximated by the energy of the two disclination lines of width $\ell_c$, since the director field in simulations can be seen to be pretty homogeneous far from them:

$$E^{bulk} = 2E^{line} = 2\pi K s^2 \mathcal{L} \ln \frac{\ell_c}{r_0} + 2E_{core}^{1/2} \mathcal{L} \tag{4.30}$$

with $\mathcal{L}$ the length of the disclination lines. The surface and core energies can be obtained from the expressions in equation 4.28, taking into account we have four half integer defects whose distance will depend on the separation angle $\alpha$ as shown in the inset of Figure 4.19a:

$$E^{int} + E^{core} = \pi K \ln \left[ \frac{\pi a (\pi - 2\alpha)}{2 r_0 \alpha} \right] + 4E_{core}^{1/2} \tag{4.31}$$

If we plot the free energy of the configurations with disclination lines relative to the defect-free configuration free energy, as a function of the separation angle between sign-like half integer defects $\alpha$, we can see that there is an energy barrier between the defect pair and defect-free configurations (see Figure 4.19a). The dashed line of the relative free energy curve joins the energy of the limit state with half integer sign-like defects get very close and the free energy of

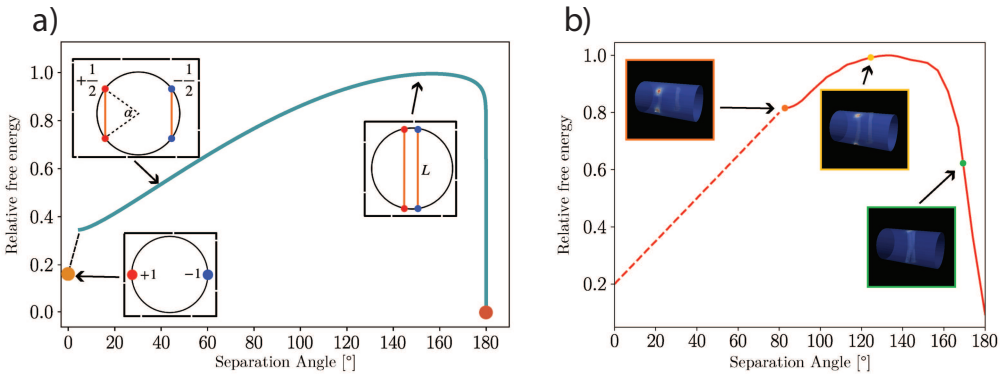



**Figure 4.19:** a) Energy barrier for the annihilation process of a defect pair by the formation of two straight disclination lines that get closer. The separation angle $\alpha$ corresponds to the angle between defects of the same size. Inset shows the annihilation process b) Energy barrier for the annihilation process observed in simulations. Figure adapted from [130].

the defect pair configuration where these half integer defects have merged and the disclination line has disappeared. As shown in Figure 4.19a, the defect pair state has a larger energy than the defect free one, therefore corresponding to a metastable state. Nevertheless, as the defects split into disclination lines and these get closer, the energy grows significantly until they merge and annihilate reducing the energy to the one of the defect free configuration. We can see that the barrier height is much larger than the difference in energy between the defect pair and the defect free configurations. Moreover, we can estimate the order of magnitude of the barrier height by noticing that the largest contribution comes from the energy of disclination lines. The height of the barrier will then correspond to the state where the disclination lines are the longest. This occurs when the lines span the whole diameter of the cross-section of the torus, leading to $\Delta E_{barrier} \sim K \cdot 2a$[1]. If we take $K \approx 5pN$ and $a \approx 160\mu m$, we obtain $\Delta E_{barrier} \sim 2 \times 10^{-16} J \gg kT \approx 4 \times 10^{-21} J$ . The barrier height is thus orders of magnitude larger than thermal energy. Hence, thermal fluctuations can not induce defect pair annihilation. Defect pairs are then stable, as observed experimentally.

Finally, annihilation of disclination lines in a fashion similar to the one described before was observed in simulations in cylinders. In this case, the system started from a state with two disclination lines close to the maximum of the

[1] We can see that this is a lower estimate of the barrier, since the logarithmic term contribute to increase its value, given that the size of the system is orders of magnitude larger than the defect core size.

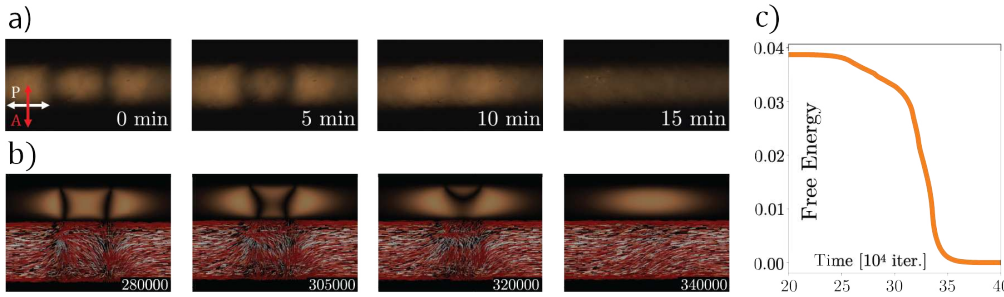



**Figure 4.20:** a) Experimental images of the annihilation process in crossed polarizers. b) Simulation snapshots of the annihilation process. c) Free energy evolution graph for the simulated annihilation process. The graph is monotonically decreasing. Figure adapted from [130].

energy barrier and was able to overcome the barrier to result in the defect-free configuration through annihilation of disclination lines. The energy profile is shown in Figure 4.19b, where the insets show the simulation situation at different separation angles $\alpha$. The shape of the curve is qualitatively similar to the analytically derived one with a similar relative energy barrier. The main difference between the curves is that in the simulation, the peak of energy is reached sooner, at $\alpha \sim 120°$. This is likely due to the simplifications in the analytical treatment, which assumed straight non interacting disclination lines.

In the end, both the analytical approximation and the numerical simulations show that the high energy barrier responsible for the stability of defect pairs comes from the energetic cost of rearranging the bulk director field in the defect annihilation process.

When such an energy barrier does not exist, annihilation takes place spontaneously. This occurs for example when we have two defect pairs in a cylinder where each of the defects of one pair is close to the opposite signed defect of the other pair. In this case, defects with opposite charge attract and annihilate leading to a defect-free configuration. This is indeed observed both experimentally and in simulations. Figure 4.20 shows experimental images of this defect pair annihilation process under crossed polarizers (panel a), and the simulation snapshots of the same process (panel b). The energy evolution in the simulations is shown in panel c. We can see that it continuously decreases until the configuration relaxes to the defect-free state.

### 4.4.5 Statistics of defect pair generation

Sealing our nematic tori in cuvettes with ethanol-free yield stress material allows storing them for long periods of time. Consequently, we can repeat the heating-

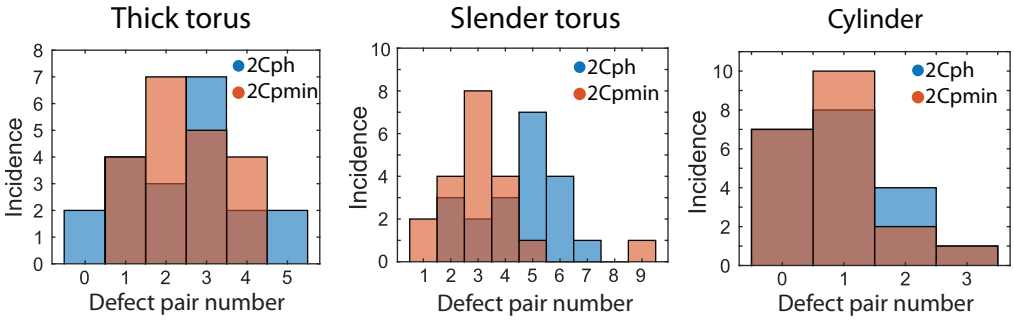



**Figure 4.21:** Histograms for the number of defect pairs after each heating and cooling cycle for the three samples. The results for slow and fast cooling rates are shown in the same histogram with different colors.

cooling experiment for the same torus allowing us to get some statistics. We obtain our statistics by repeating the experiments 20 times for each cooling speed, slow ($2C^{\circ}/h$) and fast ($2C^{\circ}/min$). The isotropic-nematic transition is recorded for each cycle to be sure that we arrive to the equilibrium configuration. When we are sure the configuration is the equilibrium one, we take crossed-polarizer images to identify the patterns. This is done for all two tori and cylinder shown in 4.18 to explore the role of Gaussian curvature. The parameters of the samples are:

1. Thick torus: Radius $R \approx 20\mu m$, tube radius $a \approx 170\mu m$, and aspect ratio $\xi \approx 3$.
2. Slender torus: Radius $R \approx 810\mu m$, tube radius $a \approx 101\mu m$, $\xi \approx 8$.
3. Cylinder: Length $L \approx 2400\mu m$, $a \sim 165\mu m$.

As mentioned briefly in the previous chapter, in some occasions we end up with defect pairs where the positive/negative defects are not located in the outer/inner ring. For the defect pair number statistics we will include these non-canonical defect pairs since we assume that for perfect tori they would have evolved into a canonical defect pair. Nevertheless, we will not take them into account for defect pair location since they seem to appear in some preferential places as opposed to canonical defect pairs. This is further discussed in Section 4.4.6.

#### 4.4.5.1 Defect pair number

We first measure the defect pair number per cooling cycle. The corresponding histograms for all three samples and cooling rates are shown in Figure 4.21.

**Table 4.3:** Mean defect pair number per heating and cooling cycle. The discrepancy tells us whether the means can be considered equal or not

| Sample | Slow cooling $(2C^\circ/h)$ | Fast cooling $(2C^\circ/min)$ | Discrepancy |
|---|---|---|---|
| Thick torus | 2.5 ±0.3 | 2.5 ±0.2 | 0 |
| Slender torus | 4.5 ±0.3 | 3.2 ±0.4 | 2.58 |
| Cylinder | 0.95 ±0.20 | 0.85 ±0.18 | 0.37 |

While for the thick torus and the cylinder the cooling rate does not seem to affect the final distribution, the histogram for the slender torus seems different for different cooling rates, leading to a larger number of defect pairs for slow cooling.

To compare distributions, we study whether the mean of the distributions for both cooling speeds is the same for each sample. To do that, we first compute the mean estimator of the distribution with its standard deviation[1], $(\mu \pm \sigma)$. To compare the means, we can use the discrepancy test. This test, valid for independent samples, considers that the means of two distributions are different if the absolute value of the difference is larger than twice the standard deviation of the difference. We compute the discrepancy as:

$$\text{Discrepancy} = \frac{|\mu_1 - \mu_2|}{\sqrt{\sigma_1^2 + \sigma_2^2}} \tag{4.32}$$

If the discrepancy is larger than 2 we can consider the means different, while if it is smaller than 2 the results are compatible. The obtained values, shown in Table 4.3, show that for the thick torus and cylinder there is no difference in the mean for each cooling speed, while the means clearly differ for the slender torus. We can additionally make box plots comparing the results for different cooling rates (Figure 4.22a). In these plots, the median is shown as a red line, the upper and lower limits of the box correspond to the 75 and 25 percentiles of the data respectively, and the black lines are extended towards the limiting values of the data that are not considered atypical values of the distribution. Atypical values[2] are marked with a red $'+'$. Visually we see that the results agree with the discrepancy test.

To further compare the distributions, we also Gaussian fit the data and compare the results using the two-sample t-test to address whether the distributions

[1]The standard deviation of the mean estimator is estimated as the standard deviation of the data divided by the square root of the number of data points.

[2]A value is considered atypical if it is larger than $q_3 + 1.5(q_3 - q_1)$ or smaller than $q_1 - 1.5(q_3 - q_1)$ with $q_1$ and $q_3$ the 25 and 75 percentiles of the data respectively.

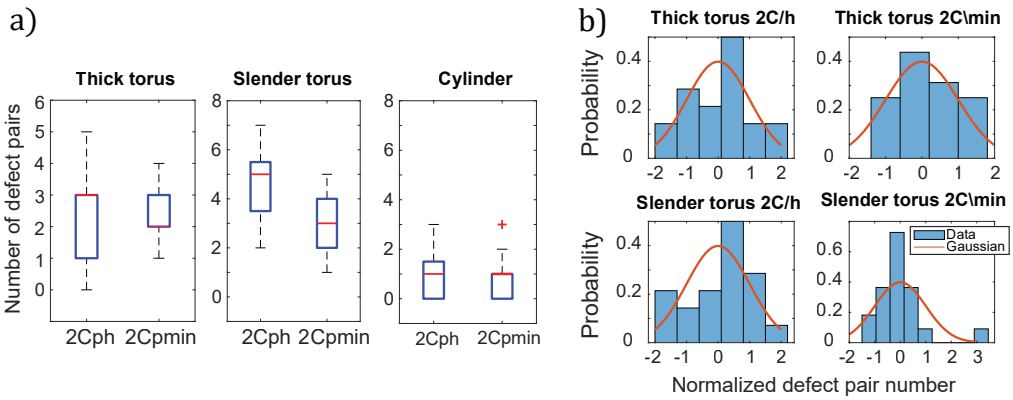



**Figure 4.22:** a) Box plot histograms of the defect pair number distributions comparing both slow and fast cooling for all samples. b) Gaussian fit of the normalized histograms. The histograms have been shifted by their mean and scaled by the standard deviation so the distribution showed have zero mean and standard deviation 1. Orange line corresponds to a normalized Gaussian distribution. Image adapted from [130].

.

can be considered different [142]. We do this despite our data being discrete. In principle we would need a very large number of datasets for the central limit theorem to apply, nevertheless, we perform this continuous test and assume the outcomes are mostly qualitative. To assess whether our distributions are different from Gaussian, we use the Kolmogorov-Smirnov test with a 5% significance [142]. This test measures the maximum distance between the cumulative distribution function (CDF) of the empirical distribution and the proposed distribution (in our case a Gaussian). If the probability of obtaining at least this maximum distance is lower than the significance level, the null hypothesis is rejected and the distributions can be considered different. The results indicate, for both thick and slender tori, that the null hypothesis of the distributions being Gaussian can not be ruled out. Hence, we assume our distributions can all be described as Gaussians. These are shown in Figure 4.22b.

To test whether the distributions for different cooling rates are the same we use the two sample t-test. This test checks as a null hypothesis whether two sets of data come from the same Gaussian distribution, with equal mean and variance. The alternative hypothesis is that the two sets of data come from distributions with different mean. Using a 5% significance level we find that the null hypothesis indicates that, for the thick torus, both distributions are statistically the same, while for the slender torus, they are statistically different, having different mean. This is all consistent with our prior statistical analysis.

Finally, we see that the mean defect number is different for the three samples. To compare them we can divide the number by the length $L = 2\pi R$ associated to a torus. The defect pair number per unit length is $0.74mm^{-1}$ for the thick torus, $0.90mm^{-1}$ and $0.64mm^{-1}$ for the slender torus for slow and fast cooling rates, respectively, and $0.38mm^{-1}$ for the cylinder. The defect number per unit length is similar for both tori while it is significantly lower for the cylinder. Although we only have 3 data points, the similarity of defect pair density in the tori could indicate that the probability of appearance of defect pairs per unit length is equal and independent of aspect ratio. For the cylinder case, this number could be lower due to annihilation between defect pairs in opposite configurations or annihilation of defect pairs at the edge of the cylinder, both observed experimentally.

#### 4.4.5.2 Defect pair position

We now look at the spatial distribution of the defect pairs. To measure the azimuthal position of a defect pair we first fit the inner ring to a circle to get the center of the torus. We then draw a segment joining the center and the defect pair. The position of the defect pair is given by the angle of the segment with respect the horizontal axis. The location of a defect pair is then essentially given by the azimuthal angle of the torus where it is positioned. If we plot the defect pair distribution for both thick and slender tori at both cooling rates (Figure 4.23a), we see that the points are scattered all around the torus in a seemingly random and uniform way for all cases.

To quantitatively assess the uniformity of the experimental data we use the Kolmogorov-Smirnov test with a 5% significance level. Figure 4.23b shows the CDF of the data together with the CDF obtained from the uniform distribution. To plot the empirical CDF distribution, we use the Kaplan-Meier estimator [143]. The standard deviation of this estimator is approximated using the Greenwood formula to obtain upper and lower bounds [144]. When plotting the Kaplan-Meier estimator plus/minus the approximated standard deviation, we find that the theoretical CDF for a uniform distribution lies between the boundaries of the experimental ones. The results of the test for all distributions allows rejecting the non-uniformity. Hence, nothing in our data indicates that the defect pairs are preferentially located somewhere along the torus. This also indicates that, as discussed in previous sections, defect pairs are not a result of non-idealities of the experimental system or bumps on the torus, In contrast, they appear everywhere and are consistent with being uniformly distributed.

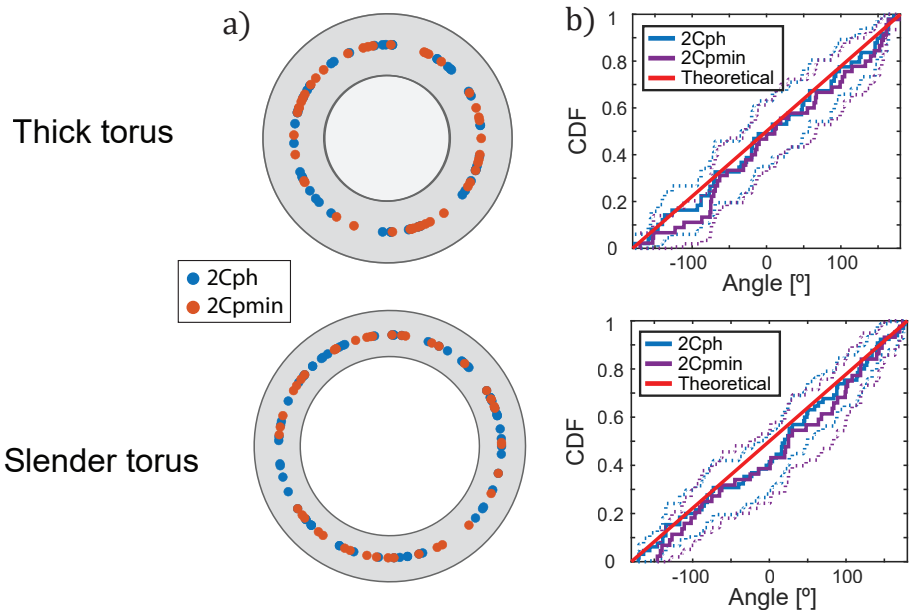



**Figure 4.23:** a) Polar plot of the azimuthal distribution of defect pair for both tori and both cooling rates. b) Experimental CDF for both tori and both cooling rates. Dashed lines correspond to upper and lower boundaries given by the estimated standard deviation. The red line corresponds to the theoretical CDF of a uniform distribution. Image adapted from [130]

.

#### 4.4.5.3 Defect pair orientation in nematic cylinders

As mentioned in previous sections, for defect pairs in nematic cylinders, the polar angle of the defects in the cross-section looks random, with the two defects being located a diameter away. To study whether the distribution of defect pairs is consistent with a random polar angle we classify the defect pairs into three categories based on their top and side view between crossed polarizers:

1. **Horizontal**: The top view corresponds to the standard defect pair texture observed in tori. A thin dark line crosses the cylinder from bottom to top (Figure 4.24a). The side view shows the presence of the defects with a highly distorted texture (Figure 4.24b). In this case the defects are located close to the equatorial plane.

2. **Vertical**: In this case, the top texture shows the defect with the highly distorted texture while the side view texture corresponds to the typical texture from defect pairs on the torus seen from the top. The defects are

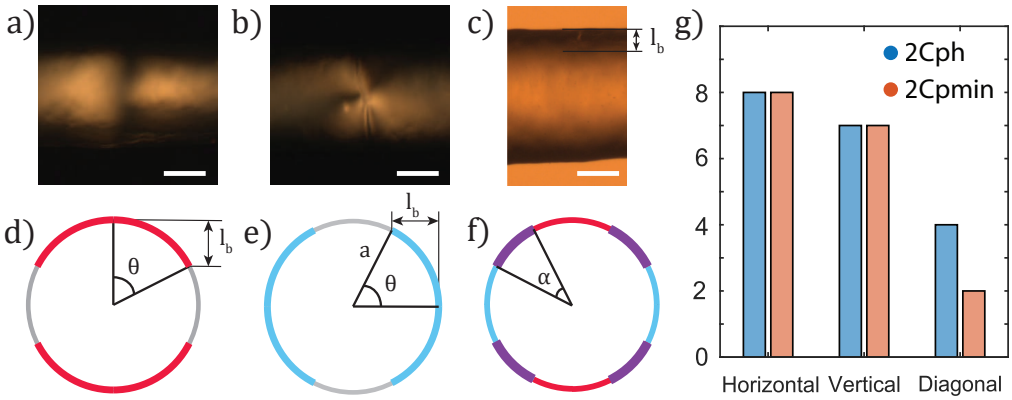



**Figure 4.24:** a) and b) Usual defect pair texture with the defects on the top and bottom part of the image.b) Texture of the defect pairs when the defects are located in top and bottom. c) Bright field image of cylinder showing blind region. Scale bars are $100\mu m$ d)-f) Schematics of the blind regions when observed from the side, top and in both cases respectively. g) Experimental histogram of the number of horizontal, vertical and diagonal defect pair for both cooling rates. Figure adapted from [130].

located in the top and bottom part of the surface of the torus.

3. **Diagonal**: In this case both top and side views correspond to the standard defect pair texture. This is associated to the defects been located in a region that is not observed from either the top and side due to refraction.

If the defect pair angular distribution was to be uniform around the circular cross-section, the number of horizontal and vertical defect pairs should be the same. For the diagonal defects the proportion of defect pairs in the diagonal configuration should be equal to the length of the blind area divided by the total length. This can be estimated by the dark band length $l_b$ in bright field (Figure 4.24c). If we assume that this length gives the region that is not observable, we can compute the size of the blind regions from the side (red) and top (blue) views, as shown in Figure 4.24d-e. The invisible region is the overlap region between these two, as shown with purple lines in Figure 4.24f. It is worth noting that for the blind regions to overlap, the condition $l_b > (1 - 1/\sqrt{2})a$ needs to be fulfilled. This is equivalent to imposing that the angle $\theta > \pi/4$, where $\theta$ is the angle of the blind region as shown in Figure 4.24. The percentage of the diagonal defect pairs can be computed as a function of $l_b$ from simple trigonometry as:

$$\frac{N_{diag}}{N_{tot}} = \frac{4\alpha}{2\pi} = \frac{4}{\pi}\arccos\left(1 - \frac{l_b}{a}\right) - 1 \tag{4.33}$$

When we plot the experimental histogram showing the number of horizontal, vertical and diagonal defects for both cooling rates (Figure 4.24g), we find that for both cooling rates the number of vertical and diagonal defect pairs is similar and the proportion of diagonal defect pairs is 21% for slow cooling and 12% for fast cooling. From the bright field image (Figure 4.24c), we estimate the dark band length $l_b$ to be around $60\mu m$. With a cylinder diameter estimation of $320\mu m$, and using equation 4.33, we obtain a theoretical fraction of diagonal defect pairs of 14% which is consistent with the experimental findings. The exact theoretical value obtained is actually quite sensitive to the value chosen for $l_b$. If instead of $60\mu m$ we had taken $55\mu m$ or $65\mu m$, the calculated percentage would be 8% and 19%. Overall, the experimental findings in a nematic solid cylinder seem consistent with axial symmetry, highlighting the role of curvature for the positioning of defects in solid nematic tori.



### 4.4.6 Non-canonical defect pairs

Experimentally, the most commonly observed feature is the canonical defect pair. Nevertheless, some of the features are compatible with a defect pair configuration with positive/negative point defects not located in the outer/inner ring of the torus. We call these types of defect pairs non-canonical defect pair. We focus on these on this section.

#### 4.4.6.1 Types

Since non-canonical defect pairs are formed by a pair of $\pm 1$ defects where the location of the positive and negative defects is different from the canonical case, we can classify them as a function of their position:

1. **Inverse defect pairs**: This is the extreme case where the positive and negative defects are switched in position. The positive defect is located in the inner ring of maximum negative Gaussian curvature while the negative defect is located in the outer ring of maximum positive Gaussian curvature. The observed texture under crossed polarizers from above is very similar to that of the canonical defect pair. The difference comes from two thick and slightly dark bands that appear on each side of the usual thin line, and the fact that the deflection direction is different as the cross-polarizers are rotated. This is shown in Figure 4.25a where the arrows on the left image show the slightly dark bands and the top part of the image correspond to the inner part of the torus. As the crossed polarizers are rotated in the

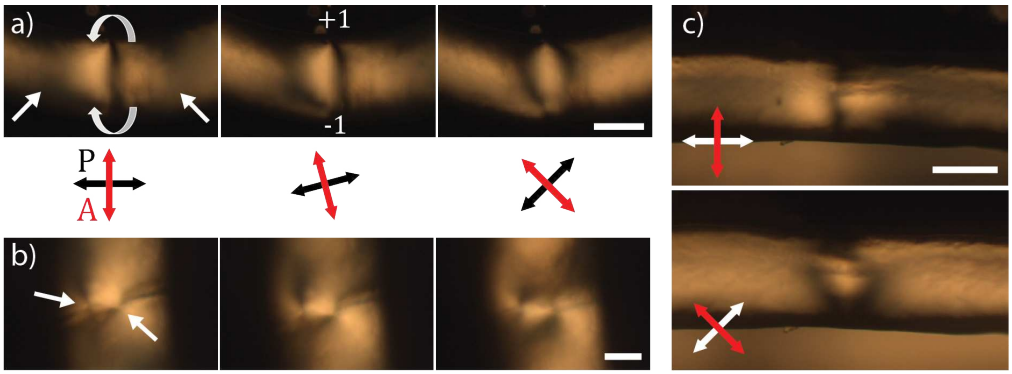



**Figure 4.25:** a) Inverse defect pair. The positive/negative defect is in the top/bottom which correspond to the inner/outer ring respectively. Bent arrows indicate rotation sense of brushes when rotating crossed polarizers counterclockwise. Straight arrows indicate the location of the slightly dark bands. Scale bar is $100\mu m$. b) Defect pair in other configuration. Both point defects can be clearly seen from the top with the brushes rotating. Arrows indicate the location of tehd efects. Scale bar is $50\mu m$. c) Side view of defect pairs in other configurations. The texture is the same as for canonical defect pairs seen from the top. Scale bar is $200\mu m$.

counterclockwise sense, the dark band on the left starts moving towards the center, which will imply a clockwise/counterclockwise rotation around the defect at the outer/inner ring respectively. This suggests that the defect at the inner/outer rings have a $+1/-1$ topological charge.

2. **Other configurations**: This encompasses any other case, with the most typical case when the defects are located in the top and bottom of the cross-section. The texture in this case is similar to the one shown in Figure 4.24b for vertical defect pairs when both defects are aligned. When they are not very aligned the individual defects can be seen, as shown in Figure 4.25b. Another possibility observed experimentally is having the two defects close to each other in a region of like-signed curvature. The defect pair nature of these configurations is further proved when observing the texture between crossed polarizers from the side. As shown in Figure 4.25c, the texture observed is the same as the canonical defect pair texture from above.

**Table 4.4:** Percentage of defect structures of different types experimentally observed for different aspect rations and cooling rates

| $\xi$ | Cooling rate | Canonical defect pairs | Inverse defect pairs | Defect pairs: Other configurations | X patterns * |
|---|---|---|---|---|---|
| 3 | $2C°/h$ | 96% | 0% | 0% | 4% |
| 3** | $2C°/min$ | 88% | 2% | 6% | 2% |
| 8 | $2C°/h$ | 68.4% | 8.4% | 17.9% | 5.3% |
| 8** | $2C°/min$ | 55% | 10% | 15% | 18.75% |



#### 4.4.6.2 Statistics: Number and location

With this classification, we can look at defect pair types and their statistics. We start by looking into the number of non-canonical defect pairs that appear for both thick and slender tori at both cooling rates. The results are summarized in Table 4.4. We can see that for the thick torus with $\eta = 3$, the non-canonical defects barely appear and the canonical defect pairs are the predominant feature. Indeed, non-canonical defect pairs only appear for the fast cooling rate accounting for an 8% of the total features. On the contrary, for the slender torus, although canonical defect pairs are still the main type observed, $\approx 25\%$ of the features correspond to non-canonical defect pairs, independent of the cooling rate. We argued previously that curvature favors the positioning of the defects in the canonical configuration, therefore, for more slender tori, this effect is weaker and other details and non-idealities can affect the equilibrium configuration; these include as bumps or irregularities on the surface of the torus that could effectively pin defects by curvature attraction.

We can further test this argument by looking into the azimuthal distribution of non-canonical defect pairs for the slender torus. As shown in Figure 4.26a the distribution of inverse defect pairs looks segregated into a few small regions. This might indicate that the inverse defect pair stabilization is related to the local geometrical features of those regions. For the defect pairs in other configurations (Figure 4.26b) we see that although it does not look as segregated as for the inverse defect pairs, the distribution still looks concentrated into wider sectors with a region where no defect pairs of this type are found. This can be related to the fact that the category of other configurations encompasses a lot of different types that can be promoted by local geometry details in more regions. The azimuthal distribution of non-canonical defect pairs does not look

*See Section 4.5

**The shown percentages do not add up to 100%. This is because there was one pattern that we were not able to identify and has not been included in any type

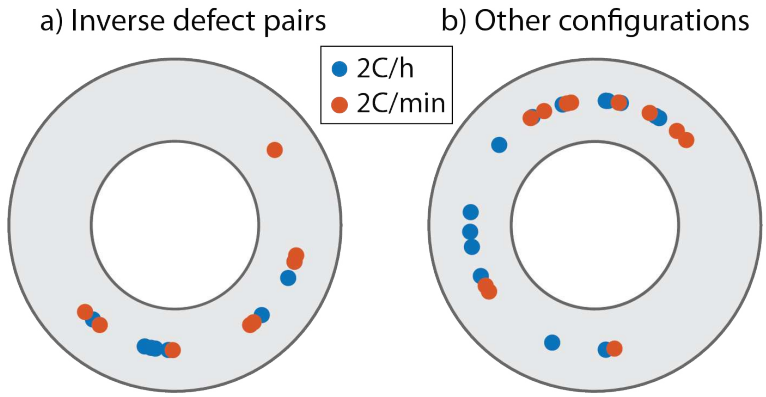



**Figure 4.26:** a) Inverse defect pair azimuthal distribution. b) Other defect pair configurations distribution. The data shown corresponds to the experiments with the slender torus, $\xi \approx 8$.

homogeneous. Furthermore, they have not been found in simulations. For these reasons, we consider the stability of both, inverse defect pairs and defect pairs in other configurations, a localized phenomena due to the shape imperfections of our toroidal droplets. While we consider that for an ideal torus these defect configurations would evolve into canonical defect pairs to minimize the energy therefore counting them as defect pairs for the histogram statistics, we do not consider them for the positional statistics due to their localized nature.

## 4.5 An unknown pattern

While defect pair configurations are the most common type of feature observed when heating and cooling nematic solid tori and cylinders, in fewer occasions a different pattern appears. This pattern is also stable and clearly different from any observed type of defect pairs. We name this unknown localized feature "X pattern" for its aspect in bright field. Although the director field configuration for the X pattern remains unknown, in this section, we describe it in this section.

### 4.5.1 Observations

The main features of the X pattern in bright field and between polarizers are:

1. The pattern presents a distinct texture in bright field. This texture consists of two thin lines forming an elongated X shape crossing at the center of the cross-section. Interestingly, this same bright field texture is seen both from the top and the side, as shown in the left and right images of

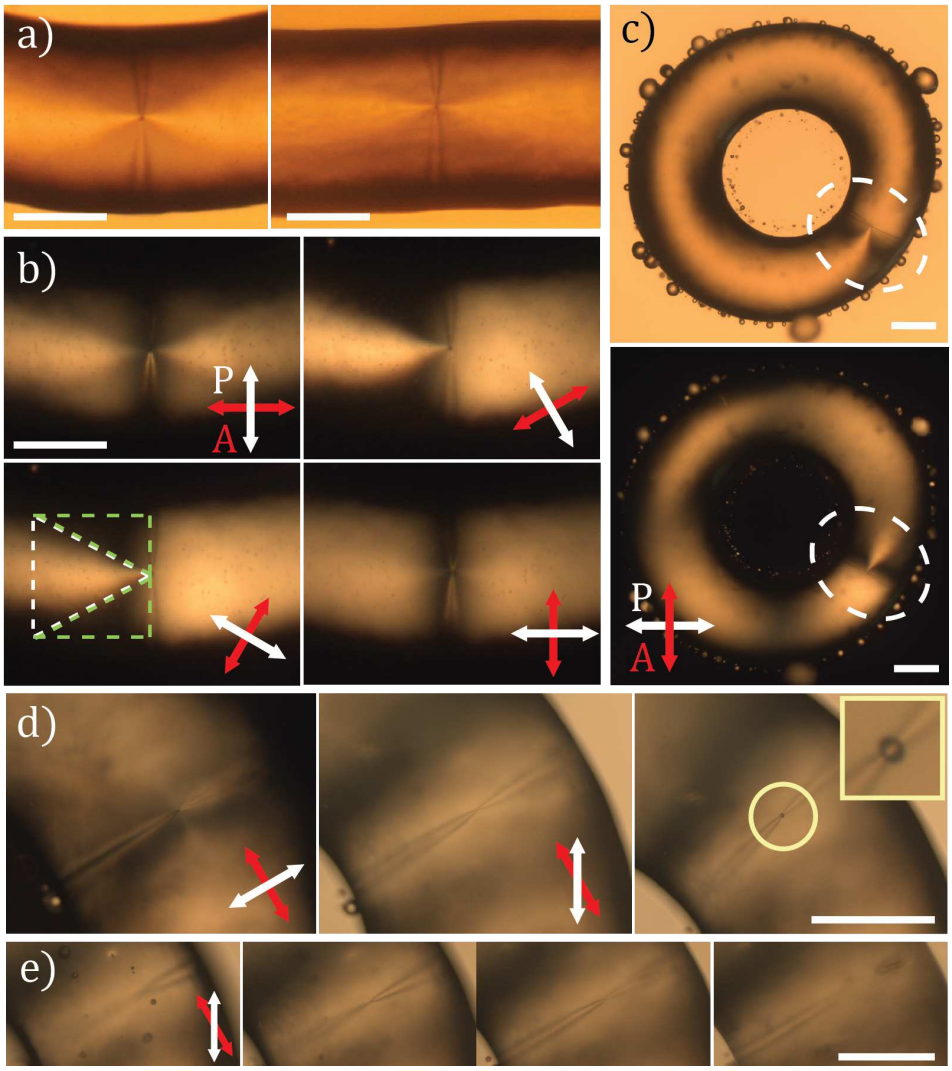



**Figure 4.27:** a) Bright field view of top (left) and side (right) view. b) Texture of X pattern for rotating crossed polarizers in one sense. When rotated in the opposite sense, the mirror symmetric texture is observed. c) Bright field and crossed polarizer view of torus with only one X pattern. d) Texture of X pattern in for special polarizer and analyzer angles. Inset of right most image shows the appearance of a circle pattern at the center of the cross after a couple of days passed which is not present in center image. e) X pattern images with different focal planes. From left to right the focal plane is rising. Scale bars are $100\mu m$ for panels a) and b) and $200\mu m$ for the rest.

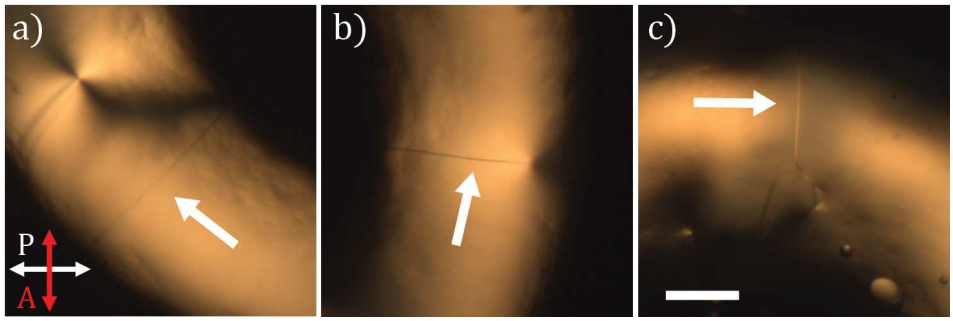



**Figure 4.28:** Crossed polarizer images of disclination lines formed between domains during the isotropic-nematic cooling process. White arrows indicate the location of the disclination lines a) Disclination line going from the inner to the outer ring. b) Disclination line ending in a point defect on the surface. c) Bright disclination line. Scale bar is $100\mu m$

Figure 4.27a respectively. These thin lines, nevertheless, do not look like disclination lines. They are much thicker and not as sharp as the disclination lines observed during the isotropic-nematic phase transition (see Figure 7.10).

2. Between crossed polarizers, when the polarizer is either parallel or perpendicular to the cross-section, the texture looks symmetric with respect to the cross section passing through the center of the X. The texture is nevertheless different for each orientation of the polarizers. When the crossed polarizers are rotated counter-clockwise the texture becomes asymmetric, with the region at one side looking bright and the region in the other side presenting two dark triangles at the edges separated by a bright triangle. If the crossed polarizers are rotated in the opposite sense, the bright region and the region with triangles exchange side. The experimental images between cross-polarizers are shown in Figure 4.27b.

3. The total topological charge of the X pattern is 0. As for the defect pair case, this is proved by the fact we observe some configurations with only one X pattern (Figure 4.27c); the Poincaré-Hopf index indicate its topological charge must be zero.

4. When the polarizer is parallel to the cross-section and the analyzer perpendicular to it, the pattern of the X is inverted, in the sense that the thin black lines in bright field become bright and the region in between the X lines becomes dark (Figure 4.27d left). Furthermore, if both polarizer and analyzer are approximately perpendicular to the cross section, the texture

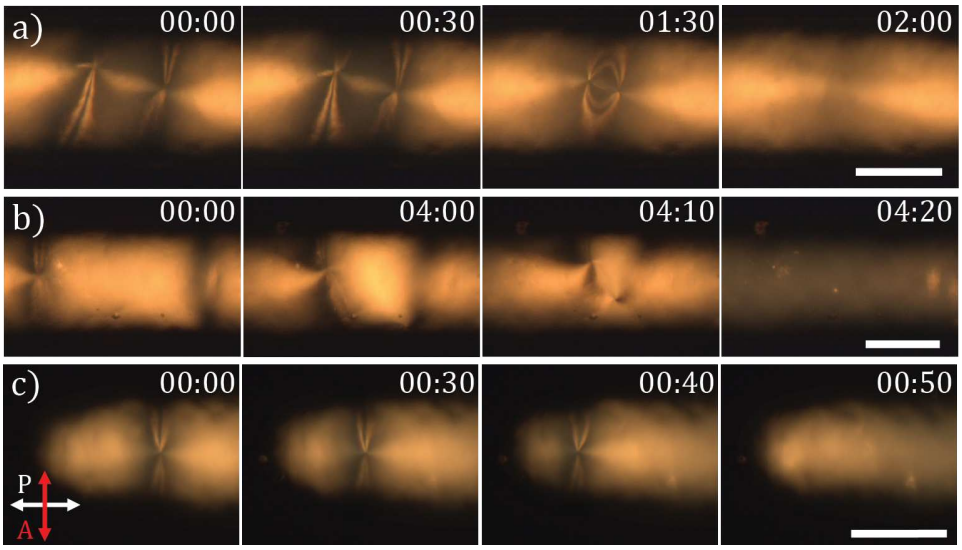



**Figure 4.29:** Crossed polarizer images of: a) Annihilation of two X patterns, b) annihilation of an X pattern with a defect pair and c) annihilation of an X pattern at the cylinder edge. Time stamp is in minutes and scale bars are 200$\mu m$.

shows the two dark lines forming the X in a bright background (Figure 4.27d middle).

5. While the X pattern looks like two lines crossing, after a couple of days, the intersection of the cross evolves into a circular pattern. This is shown in Figure 4.27d right, which is the same image as the middle one but taken two days after. The inset shows the dark circle that appears.

6. The dark lines of the X are not horizontal but have some vertical component as suggested by the side view in bright field. This can also be seen when using higher magnification, 20x, so the focal depth is smaller than the tube diameter, and setting the polarizer and analyzer almost perpendicular to the cross-section. When changing the focal plane from bottom to top of the cross-section one can see that the lines first gets in focus from the outer region and as the focal plane goes up the best focused region is moved towards the inner region. This is shown in the sequence of images in Figure 4.27e.

7. Annihilation events involving tentative X patterns are observed during the relaxation phase in the isotropic-nematic transition. These events include annihilation of two X patterns, an X pattern and a defect pair, and an X pattern at the edge of the cylinder, as shown in Figure 4.29.

8. The rate of appearance of X patterns in our experiments amounts to around a 5% of all generated patterns (see Table 4.4). The case for fast cooling in the slender torus shows an anomalously high value compared to the other three cases, with 18.75% of the features observed being X patterns.



### 4.5.2 Discussion

The above observations can guide us into some of the properties of the director field. First, and most interestingly, the texture observed is the same when looked from the top or from the side. This might indicate that the director field has rotational symmetry around the center-line of the torus, since in that case the texture should remain the same independent on the angle of observation of the X pattern, and in particular, for the top and side views. Moreover, the mirror symmetry with respect to the cross section as we rotate cross-polarizers might be indicative of the same mirror symmetry for the director field. Note that the mirror image of the director field of a +1 point defect corresponds to a -1 defect, so if the mirror symmetry is fulfilled, having a +1 defect at a distance from the symmetry plane automatically fulfills the zero topological constraint since a mirror -1 defect needs to appear at the other side of the plane. This is indeed the case of a toron which has a pair of $\pm 1$ defects in the bulk separated a certain distance.

The observation of black lines in bright field, different from disclination lines, indicates that the director field likely varies significantly in a distance comparable to the light wavelength, leading to some scattering and the corresponding loose of intensity. The X pattern configuration possibly corresponds to a highly distorted director field confined to a thin slab parallel to the cross-section. This high distortion implies a high elastic energy for the X pattern which would justify why it appears so scarcely compared to defect pairs.

A similar texture in bright field was found in [145] (see Figure 4.30a). In this case, they use a chromonic lyotropic liquid crystal with a chiral dopant confined to a cylinder with parallel anchoring conditions, so that the equilibrium configuration corresponds to a double-twisted configuration where the equilibrium twist from the center to the surface corresponds to $3\pi/2$[1]. The characteristic pattern appears when a metastable double-twisted domain with $\pi/2$ twist appears between two domains in the ground state. The domains are separated between them by point defects at the middle of the cross-section. Since the low twist domain costs more energy, it shrinks until both defects at the boundaries,

[1]The rotation for different domains is expressed as $(k + 1/2)\pi$, since the $K_{24}$ term favors a director field pointing in the polar direction at the surface making this rotation angles local minima.

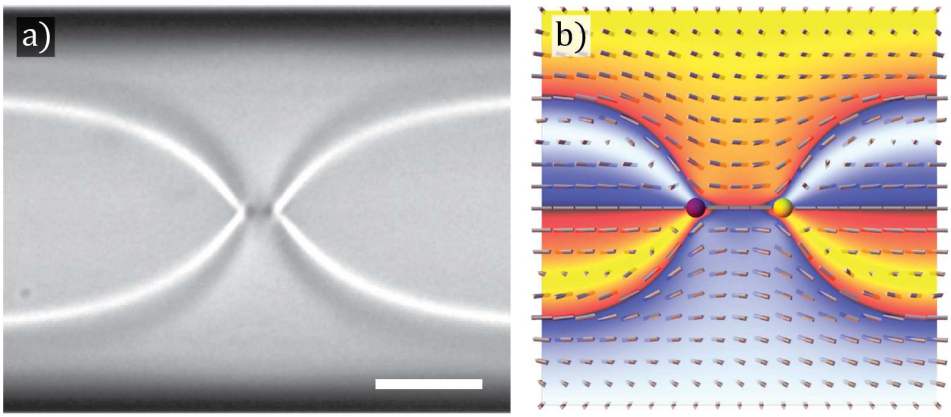



**Figure 4.30:** a) Bright field image of a metastable configuration of the cholesteric chromonic liquid crystal confined to a round capillary with planar anchoring which resembles the X pattern observed. Scale bar is $50\mu m$. b) Schematic of the simulated configuration with a $\pm 1$ pair of defects separated at a distance. Images adapted from [145].

a pair of $\pm 1$ defects, get close enough. They nevertheless do not annihilate due to an energy barrier that appears to be related to the cholesteric nature of the liquid crystal.

This configuration is inherently highly twisted also due to the cholesteric nature of the liquid crystal. Nevertheless, the similarities with the texture we observe could be taken to suggest that the X pattern could be a double-twisted domain with $\approx \pi$ twist, sandwiched between domains in the ground state corresponding to the usual double twist. In this way, the director field is continuous at the surface and the domains are separated by point defects at the center line, with the $\pm 1$ pair of defects getting very close but unable to annihilate.

From a different perspective, the X pattern occupies a thin slab of the torus. Far from it, the director field recovers the double-twisted configuration, so if we neglect the small twist and assume an axial ground configuration this would be equivalent to the slab having homeotropic anchoring conditions. Moreover, the finite size of the cross-section and continuity imposes the director field being axial at the surface. Such a configuration is equivalent to a director field confined between homeotropic layers with a localized distorted configuration. This constraints are similar to the ones imposed in cholesteric liquid crystals where solitonic configurations appear [146, 147]. This solitonic configurations correspond to localized highly distorted configurations and can be of different types,some with point defects, like the torons, or defect-free, like the hopfions. Out of these configurations, the toron configuration with two point defects sep-

arating a region with a twist of around $\pi$ is the configuration we propose for the X pattern based on the results in [145].

Therefore, we hypothesize that the X pattern corresponds to a solitonic configuration, most likely a toron, based on the similarities with [145]. Nevertheless, the appearance of solitonic structures of this kind, and for the toron, its stability against annihilation, is based on the chirality of the cholesteric liquid crystal. However, we use an achiral liquid crystal, and we know the curvature does not play a role, as the X patterns are also observed in cylinders. Despite this, 5CB presents a very low and maybe negative double twist elastic constant $K_2 - K_{24}$ (see chapter 5 for more details), which could induce the metastability of double-twisted domains and occasionally stabilize the structure.



## 4.6 Conclusions

In this chapter we have studied the configurations that appear on a toroidal nematic droplet with tangential boundary conditions after heating it to the isotropic phase and cooling back to the nematic phase. These configurations are localized features and can be classified in two main types.

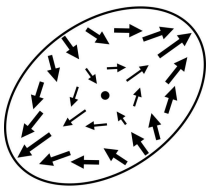
The first type corresponds to a defect pair configuration where two $\pm 1$ point charges are located on the surface and on the outer and inner rings of the torus. The stability of this configuration does not come from the Gaussian curvature of the torus but rather from the high energetic barrier the bulk rearrangement imposes for the defects to annihilate. This is further proved by showing that defect pairs also appear in cylindrical nematic droplets where Gaussian curvature does not play a role. Nevertheless, the curvature of the torus induces a preferential positioning of the point defects, which can be attributed to the Gaussian curvature attraction of point defects and/or to the curvature of the center-line, resulting in an asymmetry in the bulk energy as a function of the position of the point defects. Less frequently, defect pairs in nematic tori with the point defects out of the canonical position are observed. We associate them to metastable states due to the non-idealities of our toroidal droplets.

The second type, which we call X pattern, is observed as two dark lines forming an elongated "X" in bright field images. It appears much less frequently than defect pairs. The exact nature of the configuration is unknown, but our current hypothesis is that it could correspond to a solitonic configuration, probably a toron, due to the resemblances with other reported configurations [145]. Other non-singular solitonic configurations like hopfions could also be compatible.

Although the role of the saddle-splay elastic term has not been discussed for the defect-populated configurations, prior work showed that it plays a key role in inducing a spontaneous double twist. The effect of the saddle-splay term in defect-free nematic solid tori was interpreted as a surface term that coupled

with the curvature of the surface, favoring the alignment of the director towards the direction of largest curvature. In the next chapter, we make a quick detour before continuing our studies with nematic toroidal droplets, and present the view of the saddle-splay term as a bulk term and its interpretation in terms of local deformations. We use this interpretation to derive the compatibility conditions for a nematic liquid crystal in a simple and intuitive way.

Chapter 5





# $K_{24}$ as a bulk deformation mode: Compatibility conditions

## 5.1 The traditional view: $K_{24}$ as a surface term

In the Frank-Oseen elastic free energy density expansion introduced in section 2.2.2, there are three terms, splay, twist and bend, corresponding to pure bulk deformation modes. There is an additional fourth term, saddle-splay, which is expressed as a pure divergence. This last term is written as [148]:

$$f_{24} = -K_{24}\nabla \cdot [\hat{\mathbf{n}}\nabla \cdot \hat{\mathbf{n}} + \hat{\mathbf{n}} \times \nabla \times \hat{\mathbf{n}}] \tag{5.1}$$

When integrating the saddle-splay free energy over the whole sample volume and applying Gauss' divergence theorem, the saddle-splay term can be reduced to a surface term. It is important to take into account that the theorem applies for a volume with a continuous and differentiable director field inside. When defects are present in the sample, the saddle-splay term is computed by excluding the defects; this is effectively done by surrounding the defects with a surface that will also contribute to the free energy. This total saddle-splay energy is expressed as:

$$\begin{aligned} F_{24} &= -K_{24} \int_V \nabla \cdot [\hat{\mathbf{n}} \nabla \cdot \hat{\mathbf{n}} + \hat{\mathbf{n}} \times \nabla \times \hat{\mathbf{n}}] dV \\ &= -K_{24} \oint_{\partial V} \hat{\mathbf{v}} \cdot [\hat{\mathbf{n}} \nabla \cdot \hat{\mathbf{n}} + \hat{\mathbf{n}} \times \nabla \times \hat{\mathbf{n}}] dA \end{aligned} \tag{5.2}$$

where $\hat{\mathbf{v}}$ is a normal to the surface pointing outwards, $V$ is a defect free sample volume and $\partial V$ the surface enclosing this defect free volume. Traditionally, this term is neglected unless necessary to explain experimental results. Indeed, it can be completely disregarded when the boundary conditions are fixed and no defects are present in the sample. In this case, the saddle-splay free energy is constant and independent of the director field configuration inside the sample, which in turn is determined by the balance between splay, twist and bend energies. When the director at the surface is not fixed and can vary, the saddle-splay free energy will depend on the orientation of the director at the boundary, and thus it will affect the final configuration. A particular case of this is when the anchoring is planar degenerate. In this case, the director is tangential to the confining surface and the saddle-splay energy can be written in terms of the principal curvatures of the surface [10]:

$$F_{24} = -K_{24} \oint_{\partial V} [\kappa_2 n_2^2 + \kappa_1 n_1^2] dA \tag{5.3}$$

where $\kappa_i$ are the principal curvatures and $n_i$ the component of the director in the i-th principal curvature direction. In this case, the energy is minimized when the director field points in the direction of the maximum curvature. This explains why the saddle-splay term is necessary to explain the double-twisted configuration observed in planar nematic tori irrespective of the aspect ratio [9, 10]. In the generated tori, the curvature of the circular cross-section is the largest, and the saddle-splay term favors the director field being along it. The balance between energies results in a double twist whose magnitude depends on the aspect ratio of the torus.

In the same fashion, the double-twisted configuration has been observed for lyotropic chromonic liquid crystals (LCLC) confined to cylinders with planar anchoring. LCLCs are lyotropic liquid crystals made of nematogens that are formed by the dynamic self assembly of anisotropic particles. These materials have a very low twist elastic constant compared to other materials. This low twist combined with the saddle-splay elastic term results in a highly double-twisted structure [15, 17].

Saddle-splay elasticity also plays a role in the case of weak anchoring and can affect the stability of different configurations. This is the case of nematic homeotropic droplets, where a shift in the boundaries in the stability phase

diagram is predicted when including the saddle-splay constant [149, 150]. The same happens in cylindrical confinement with weak homeotropic anchoring [151, 152]. This has indeed been used to obtain an experimental estimation of $K_{24}$ by observing the configuration transition from homeotropic to planar in nanopores as a function of the pore diameter [153].

Using the saddle-splay term together with the usual splay, twist and bend terms results in a complete phenomenological first order description of the free energy. Nevertheless, while the splay, twist and bend distortions have a clear bulk deformation associated (see Figure 2.2), the interpretation of the saddle-splay term is not straightforward and is typically associated to an effective surface term. Nonetheless, as the other three terms, it appeared when taking into account the first derivatives of the director field at a certain point and thus, represents a local bulk property of the nematic liquid crystal which becomes hard to visualize due to the mathematical form used.



In this chapter, we follow the 1990 work of Schmidt [154] and the 2019 work of Selinger [155], and decompose the nematic distortion into normal modes, with one of them corresponding to the saddle-splay deformation. We continue with an analogy of the normal modes with 2D elastic deformations and discuss the effects of $K_{24}$ from an energetic point of view. We then use this local decomposition into normal deformation modes to obtain the compatibility conditions for the distortion fields both in 2D and 3D. The compatibility conditions are a set of equations that reflect the uniqueness of $\hat{\mathbf{n}}$. They must be fulfilled by the magnitudes of the normal deformation modes and their derivatives for any continuous and differentiable director field. Previous approaches in 3D used differential geometry or pure calculus methods to derive them [156, 157]. Unlike them, we use a more intuitive approach by imposing that the variation of the director field is the same when following two distinct infinitesimal paths towards the same point. We first use this construction to proof the equality of mixed partial derivatives for a function of several variables and then use it for a director field in 2D to obtain the already known compatibility equations [158] together with an interpretation of how Gaussian curvature enters the equation when extending the expression to curved spaces. We finish the chapter by deriving the first six compatibility equations for a 3D director field in Euclidean space and discussing some of the consequences resulting from imposing them. The missing three compatibility equations can also be derived using the same construction.

## 5.2 Decomposing nematic deformations into normal modes

As shown in Section 2.2.2 we can locally describe the deformation state of a director field by the components of the gradient tensor $\nabla\hat{\mathbf{n}} \equiv \partial_i n_j$. From these components, only six are independent due to the normalization condition $n_i n_i = 1$. If we set our coordinates axis at the evaluation point such that the director field points in the z direction, $\partial_i n_z = 0$ and the six non-zero independent components become [154]:



$$a_1 = \frac{\partial n_x}{\partial x},\ a_2 = -\frac{\partial n_y}{\partial x},\ a_3 = \frac{\partial n_x}{\partial z},\ a_4 = \frac{\partial n_y}{\partial y},\ a_5 = \frac{\partial n_x}{\partial y},\ a_6 = \frac{\partial n_y}{\partial z} \tag{5.4}$$

Expanding to first order, the director field around a point can be expressed as [154]:

$$\begin{aligned}\hat{\mathbf{n}} \approx &(a_1 x + a_5 y + a_3 z)\ \hat{\mathbf{x}} + (-a_2 x + a_4 y + a_6 z)\ \hat{\mathbf{y}} \\ &+ \sqrt{1 - (a_1 x + a_5 y + a_3 z)^2 - (-a_2 x + a_4 y + a_6 z)^2}\ \hat{\mathbf{z}}\end{aligned} \tag{5.5}$$

We can now compute the expression for the splay free energy in terms of the independent components defined in equation 5.4 [154]:

$$f_1 = \frac{1}{2}K_1(\nabla \cdot \hat{\mathbf{n}}) = \frac{1}{2}K_1(a_1 + a_4)^2 \tag{5.6}$$

The only derivatives entering this expression are $a_1$ and $a_4$. This means that to first order, the components of the expansion of the director field to first order of equation 5.48 that contribute to splay are:

$$a_1 x\ \hat{\mathbf{x}} + a_4 y\ \hat{\mathbf{y}} = \frac{1}{2}(a_1 + a_4)(x\ \hat{\mathbf{x}} + y\ \hat{\mathbf{y}}) + \frac{1}{2}(a_1 - a_4)(x\ \hat{\mathbf{x}} - y\ \hat{\mathbf{y}}) \tag{5.7}$$

This deformation field can be split into two terms. By computing the splay free energy associated to each term, we see that only the first one contributes to the free energy[1]. The deformation corresponding to the first term corresponds then to the splay normal mode, which will be called "double splay" from now on:

$$\frac{1}{2}(a_1 + a_4)(x\ \hat{\mathbf{x}} + y\ \hat{\mathbf{y}}) \tag{5.8}$$

[1]It is important to note that we can not take $x\ \hat{\mathbf{x}}$ and $y\ \hat{\mathbf{y}}$ as independent modes due to the coupling term $K_1 a_1 a_4$ that appears when expanding the splay free energy.

For this deformation mode, the gradient when moving in any direction perpendicular to the director field points in the moving direction and has the same magnitude everywhere. The magnitude of this gradient measures how fast the director changes and is the only degree of freedom.

We can now repeat the same process for the twist energy:

$$f_2 = \frac{1}{2}K_2(\hat{\mathbf{n}} \cdot \nabla \times \hat{\mathbf{n}}) = \frac{1}{2}K_2(a_2 + a_5)^2 \tag{5.9}$$

The only term affecting the twist are $a_2$ and $a_5$. The deformation associated to these terms can be expressed as:



$$a_5 y\ \hat{\mathbf{x}} - a_2 x\ \hat{\mathbf{y}} = \frac{1}{2}(a_5 + a_2)(y\ \hat{\mathbf{x}} - x\ \hat{\mathbf{y}}) + \frac{1}{2}(a_5 - a_2)(y\ \hat{\mathbf{x}} + x\ \hat{\mathbf{y}}) \tag{5.10}$$

Again, only the first term contributes to the twist free energy while the second one give has no twist free energy cost. The twist normal mode, from now on called "double twist", can be written as:

$$\frac{1}{2}(a_5 - a_2)(y\ \hat{\mathbf{x}} + x\ \hat{\mathbf{y}}) \tag{5.11}$$

In this deformation mode, when we move in a direction perpendicular to the director it starts rotating around the movement direction in the same sense independently of the direction chosen. As for the splay case, the amplitude is the only degree of freedom.

Finally, we can do the same analysis for the bend deformation mode:

$$f_3 = \frac{1}{2}K_3|\hat{\mathbf{n}} \times \nabla \times \hat{\mathbf{n}}|^2 = \frac{1}{2}K_3(a_3^2 + a_6^2) \tag{5.12}$$

We can immediately see that there are two independent bend distortion modes, such that any bend distortion can be written as a linear combination of these terms:

$$a_3 z\ \hat{\mathbf{x}} \quad \text{and} \quad a_6 z\ \hat{\mathbf{y}} \tag{5.13}$$

So far, we have found four out of the six independent normal modes. From the decomposition of the splay and twist deformation we have found the following two deformations that do not contribute to neither the splay, twist and bend free energy:

$$\begin{cases} \frac{1}{2}(a_1 - a_4)(x\ \hat{\mathbf{x}} - y\ \hat{\mathbf{y}}) \\ \frac{1}{2}(a_5 - a_2)(y\ \hat{\mathbf{x}} + x\ \hat{\mathbf{y}}) \end{cases} \tag{5.14}$$

These two deformations correspond to the same type. Dropping the prefactors, the vector fields transform into each other under a 45° rotation. In fact, any linear combination of these two deformations results in a deformation of the same type, but with different magnitude and angle. This mode has two degrees of freedom, magnitude and rotation angle, and is independent of the other three, as it does not contribute to the energy associated to them. This deformation mode has two perpendicular axis where the director field makes single splay of opposite sign and two other perpendicular axis forming 45° with the previous ones where the director field makes single twist in opposite direction. Since this deformation does not contribute to the splay, twist or bend energy, it must contribute to the saddle-splay free energy term and, thus, can corresponds to the normal saddle-splay mode.



Using these simple arguments, we have derived the normal deformation modes in the frame of reference having the director pointing in the $z$ direction. For a more systematic approach that works in any coordinate axis, we now follow the tensorial derivation of Selinger [155]. We start by decomposing the gradient tensor $\partial_i n_j$. Note that the normalization condition of the director field implies that this gradient is perpendicular to the director, $n_j \partial_i n_j = 0$. As a result, the gradient of the director field has to be perpendicular to the director itself along any direction, as $|\hat{\mathbf{n}}|$ can not grow in magnitude. Furthermore, these 3 constraints reduces the number of degrees of freedom of the gradient tensor from 9 to 6. Considering now the direction along which we compute the gradient, we divide the tensor in a component parallel and another perpendicular to the director field:

$$\partial_i n_j = -n_i B_j + \alpha_{ij} \tag{5.15}$$

where $\mathbf{B}$ is a vector perpendicular to $\hat{\mathbf{n}}$, and $\alpha_{ij}$ a tensor in the plane perpendicular to $\hat{\mathbf{n}}$, $n_i \alpha_{ij} = 0$. The minus sign is added such that the definition of the bend vector coincides with the traditional one. If we contract both sides with $n_i$, the $\alpha_{ij}$ term cancels out and we get an expression for the vector $\mathbf{B}$:

$$\mathbf{B} = -(\hat{\mathbf{n}} \cdot \nabla)\hat{\mathbf{n}} \tag{5.16}$$

which corresponds to the usual bend vector in liquid crystal physics. This vector is the one obtained by the linear combination of the two independent bend in from Schmidt's derivation and, hence, has two degrees of freedom.

The tensor $\alpha_{ij}$ has then the other four degrees of freedom. We can further decompose it into a symmetric $\gamma_{ij}$ and an antisymmetric part $\beta_{ij}$. The antisymmetric part can be written using the Levi-Civita symbol and a pseudoscalar $T$, all the while being perpendicular to $\hat{\mathbf{n}}$:

$$\partial_i n_j = -n_i B_j + \frac{1}{2} T \epsilon_{ijk} n_k + \gamma_{ij} \tag{5.17}$$

Contracting both sides with $\epsilon_{ijm} n_m$ eliminates the bend term and the symmetric tensor, resulting in the following expression for the pseudoscalar T:

$$T = \hat{\mathbf{n}} \cdot (\nabla \times \hat{\mathbf{n}}) \tag{5.18}$$

which corresponds to the typical twist term and has one degree of freedom. We now have a symmetric tensor $\gamma_{ij}$ with 3 degrees of freedom. This tensor can be broken into an isotropic part in the plane perpendicular to $\hat{\mathbf{n}}$ and a traceless part:



$$\partial_i n_j = -n_i B_j + \frac{1}{2} T \epsilon_{ijk} n_k + \frac{1}{2} S(\delta_{ij} - n_i n_j) + \Delta_{ij} \tag{5.19}$$

Taking the trace of the gradient tensor cancels out all terms except the isotropic one; this allows getting an expression for the scalar S:

$$S = \nabla \cdot \hat{\mathbf{n}} \tag{5.20}$$

The scalar S corresponds to the splay term and has one degree of freedom. For the last traceless term, which corresponds to the normal mode accounting for saddle-splay, an explicit expression can be computed by adding the gradient to its transpose [155]:

$$\Delta_{ij} = \frac{1}{2}[\partial_i n_j + \partial_j n_i - n_i n_k \partial_k n_j - n_j n_k \partial_k n_i - \delta_{ij} \partial_k n_k + n_i n_j \partial_k n_k] \tag{5.21}$$

This mode has two degrees of freedom. As a traceless symmetric tensor perpendicular to $\hat{\mathbf{n}}$, it can always be diagonalized into perpendicular eigenvectors such that one of them corresponds to $\hat{\mathbf{n}}$ with eigenvalue 0. The other two eigenvectors belong to the plane perpendicular to $\hat{\mathbf{n}}$ and have eigenvalues $\pm\Delta$. This gives the two other degrees of freedom, the magnitude of $\Delta$ and the orientation of the eigenvectors perpendicular to $\hat{\mathbf{n}}$.

### 5.2.1 Normal deformations as 2D elastic deformations

So far, we have decomposed the gradient tensor into four different modes. From these four modes, the bend mode is different from the other three since it accounts for the gradient along $\hat{\mathbf{n}}$ and has two degrees of freedom indicating the tipping direction of the director[1] and how large the gradient is (Figure 5.1a).

[1] This direction is perpendicular to the director.

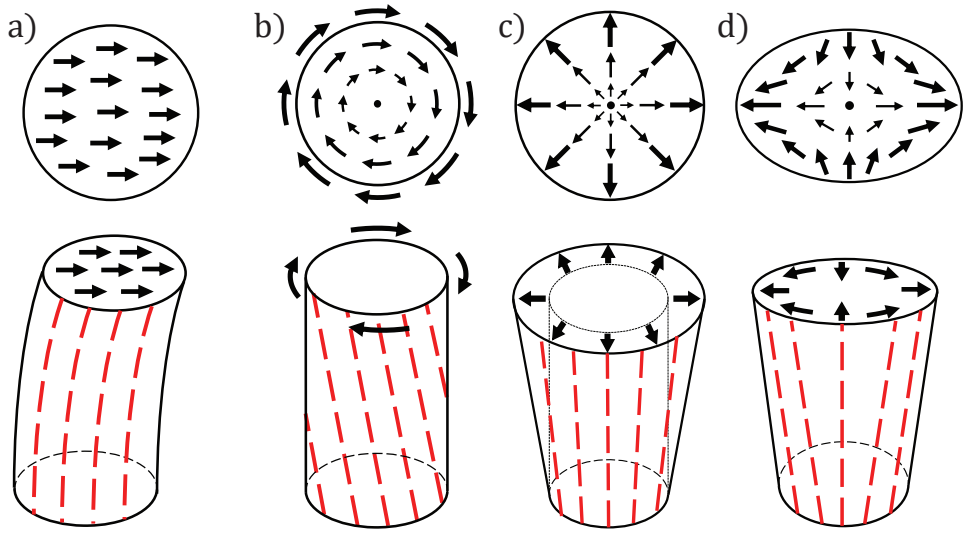



**Figure 5.1:** Schematic of the different normal distortion modes. Top schematics show the deviation of the tips of the director field in the neighborhood of the point in a plane perpendicular to the director field, akin to a displacement field. Bottom schematics show the streamlines of $\hat{\mathbf{n}}$ in a circle around the point of study and perpendicular to $\hat{\mathbf{n}}$ (bottom circle) and the deformation it produces for each normal mode on that region (top ellipse). Red dashed lines show the stream lines emanating from the bottom circle. a) Bend mode. The deformation occurs as we move parallel to the director field and can be described by a single vector. b)-d) Double twist, double splay and biaxial splay normal modes. The equivalence to 2D elastic deformations is apparent from the top schematic. For the biaxial splay mode, the orientation of the ellipse has been chosen for visualization purposes but in general the deformation can be represented by an ellipse pointing in any direction perpendicular to $\hat{\mathbf{n}}$

The other three modes are tensors perpendicular to the director field, and describe the distortions in the plane perpendicular to the director (Figure 5.1b-d).

If we now choose a coordinates axis such that one of the axis points along $\hat{\mathbf{n}}$, the tensors of the perpendicular modes can be expressed as 2x2 matrices which represent the deformations in the perpendicular plane. This is true because the gradient vector of $\hat{\mathbf{n}}$ along any direction is always perpendicular to $\hat{\mathbf{n}}$, and thus tangent to the perpendicular plane. If we look at the deformations in the perpendicular plane, the gradients of the director field belong to this plane and we can make the analogy with the gradient of the displacement field or strain tensor in 2D elasticity.

In this frame of reference, the decomposition of the tensor in the perpendicular plane can be expressed as:

$$\boldsymbol{\alpha} = \frac{1}{2}T\begin{pmatrix} 0 & -1 \\ 1 & 0 \end{pmatrix} + \frac{1}{2}S\begin{pmatrix} 1 & 0 \\ 0 & 1 \end{pmatrix} + \begin{pmatrix} \Delta_1 & \Delta_2 \\ \Delta_2 & -\Delta_1 \end{pmatrix} \tag{5.22}$$

As we can see, from the elasticity point of view, the matrix is decomposed into an antisymmetric part corresponding to a pure rotation, an isotropic part which accounts for the area change and a deviatoric component which corresponds to a traceless symmetric tensor accounting for deformations that preserve area and account for shear.



In our case, since we are setting one of the coordinate axis parallel to the director at the point of study, the deformation at the origin in the perpendicular plane is zero. We can now represent the deformations resulting from each part of the gradient tensor. The antisymmetric part corresponds to the double twist mode and consists on a rotation of the tip displacement vector around the point, as shown in Figure 5.1b. The resultant configuration is referred to as double twist. The isotropic part corresponds to an expansion or contraction of the tips in the perpendicular plane. As shown in Figure 5.1c the tip displacement vector points in the radial direction and the deformation is isotropic. For this reason and in analogy to double twist, we call this deformation mode double splay.

The deviatoric term can always be diagonalized into two perpendicular axis where the displacement vector performs single splay in opposite directions. This is shown in Figure 5.1d where one of the axis "expands" while the other "contracts", forming an ellipse. Because of this, the name "biaxial splay" was suggested to describe this deformation and will be used from now on [155]. For any direction in between the two principal ones, there is a "shear" component of the displacement of the tips. This mode has two degrees of freedom, the rotation angle of the resulting ellipse ($\omega$), and the other the magnitude of elongation ($\Delta$).

All in all, we have obtained that the local deformation of the director field can be determined by specifying the values of the bend vector $\mathbf{B}$, twist amplitude $T$, splay amplitude $S$, biaxial splay amplitude $\Delta$, and biaxial splay main axis orientation.

### 5.2.2 The free energy of the normal modes

While the double splay, double twist and bend modes present the same form as in the classical Frank-Oseen theory, the biaxial splay term is indeed different from the traditional saddle splay one. To see how this term enters the free energy density, we can decompose the saddle-splay divergence term into the normal deformations:

$$\nabla \cdot [\hat{\mathbf{n}}(\nabla \cdot \hat{\mathbf{n}}) + \hat{\mathbf{n}} \times (\nabla \times \hat{\mathbf{n}})] = \frac{1}{2}S^2 + \frac{1}{2}T^2 - \mathrm{Tr}\ (\boldsymbol{\Delta}^2) \tag{5.23}$$

where Tr $(\boldsymbol{\Delta}^2) = \Delta_{ij}\Delta_{ji} = 2\Delta^2$. As we can see, the saddle-splay divergence term includes not only biaxial splay but also double twist and double splay. We can now plug this into the standard Frank-Oseen free energy to obtain an expression for the energy as a function of the normal modes:

$$\begin{aligned} f_{el} =& \frac{1}{2}K_1 S^2 + \frac{1}{2}K_2 T^2 + \frac{1}{2}K_3|\mathbf{B}|^2 - K_{24}\left[\frac{1}{2}S^2 + \frac{1}{2}S^2 - \text{Tr }(\boldsymbol{\Delta}^2)\right] \\ =& \frac{1}{2}(K_1 - K_{24})S^2 + \frac{1}{2}(K_2 - K_{24})T^2 + \frac{1}{2}K_3|\mathbf{B}|^2 + K_{24}\text{Tr }(\boldsymbol{\Delta}^2) \end{aligned} \tag{5.24}$$

where the elastic coefficients in the first row correspond to the usual ones in the Frank-Oseen free energy while the ones in the second are the elastic coefficients for each normal mode. The elastic modulus for double twist and double splay is thus $K_2 - K_{24}$ and $K_1 - K_{24}$, respectively, and are lower than their single twist and single splay counterparts, given that $K_{24} > 0$ [155]. In fact, as shown by Selinger, the usual twist $(K_2)$ and splay $(K_1)$ elastic constants account for the elastic cost of single twist and single splay, and include the double twist/splay constant plus the biaxial splay constant. The bend modulus remains the same and the elastic modulus describing the biaxial splay deformation is $K_{24}$.

It is interesting to note that when $K_{24} > K_2$ the double twist elastic modulus becomes negative. Having a negative elastic modulus results in a decrease of free energy as the deformation increases. This typically leads to an instability that grows and leads to drastic changes in the material like in the case of the gas to liquid phase transition. in this case, as the temperature drops, the compressibility of the gas phase decreases until it becomes negative, resulting in a decrease of energy as the molecules get together. This results in the condensation of the gas phase into the liquid phase.

Interestingly, this is not always the case. Sometimes one modulus can become negative while the material remains stable thanks to other elastic moduli that are able to counteract the instability. This is the case in thermoresponsive polymer gels, where the bulk modulus $K$ can become negative as long as the longitudinal modulus $K + 4\mu/3$ remains positive, with $\mu > 0$ the shear modulus [72]. This is possible due to the stabilization effect of the shear rigidity that is able to withstand the instability and collapse of the material for small negative values of $K$.

In the case of a negative double twist modulus, and as we will see later, we can not have a director field with pure double twist everywhere in space, and other elastic deformations need to appear, ultimately stabilizing the material. This is indeed the case in chromonic liquid crystals where $K_2$ is so low that $K_2 - K_{24}$ is negative [15, 17]. Instead of rendering the material unstable, the negative double twist modulus manifests in ground states different from the

uniform one. Cylindrical confinement with parallel degenerate anchoring, for example, can result in the spontaneous appearance of double twist. In the extreme case that $K_{24}$ becomes very low for a cholesteric liquid crystal, the continuity of the director field is broken and new phases filled with topological defects and double-twisted structures, called blue phases appear [155, 159].

The use of the normal elastic modulus instead of the standard ones can give insight into the behavior of some materials. This is the case for 5CB, the liquid crystal used in this work, which has similar elastic constants $K_1 \sim K_2 \sim K_3$, being the twist one the lowest. Experimental measurements of the saddle-splay constant show that it has a value similar to the twist elastic constant $K_{24} \approx K_2$ [9, 153]. This in turn means that the double twist constant can become significantly lower than the other three elastic constants. This in turn is reflected in the clear double-twisted configuration that appears when it is confined to a torus with parallel anchoring conditions. In fact, a small double twist, with a twist angle $\approx 7°$ has been observed in planar 5CB cylinders [113], suggesting the biaxial splay constant is slightly larger than the single twist one $K_{24} > K_2$, thus making the double twist elastic constant slightly negative.



## 5.3 Compatibility conditions for nematic liquid crystals

Local deformations for a nematic director field can be completely described in terms of the bend vector $\mathbf{B}$, the double splay amplitude $S$, the double twist amplitude $T$ and, the biaxial splay magnitude $\Delta$ and orientation $\omega$. While for a given point, any combination of these deformations in principle is possible, not all combinations of deformations fields are in reality truly possible since continuity of the director field needs to be guaranteed. It is well known, for example, that a constant pure bend state can not exist in Euclidean space. The same happens for a constant pure double twist or double splay state [160].

The set of equations that relate the deformation fields for a continuous director field are called compatibility conditions. These conditions have been derived previously both in 2D [158] and 3D [156, 161] for a general curved manifold using differential geometry. For Euclidean space in 3D they have also been derived using tools in pure calculus for both the uniform distortion and the general case [157, 162], exploiting the fact that the rotational of the gradient is zero. In this section, we derive the compatibility equations in 2D and 3D Euclidean space by imposing that the variation of the director field when moving along two different infinitesimal paths arriving at the same point, is the same. This method, while equivalent to the one used in [157] gives more insight on the origin of the different terms and the meaning of each equation. Additionally, for the 2D case,

it also allows discussing how the Riemann curvature tensor enters the equations from simple arguments using the concept of parallel transport.

### 5.3.1 Equality of mixed partial derivatives



Before deriving the compatibility conditions for the 2D and 3D nematic, we start by using the proposed method to prove the symmetry of second order partial derivatives for a function of several variables. The standard proofs of this equality rely on either using the mean value theorem for certain functions (Schwarz's proof) [163], or applying Green's theorem to the gradient of the function [164]. For these proofs to work, the function $f$ is assumed to be differentiable in a neighborhood of the point, with continuous second partial derivatives. Our construction to proof the equality of mixed partial derivatives is akin to the Green's function method and can be regarded as a infinitesimal approach to it.

We start by defining two infinitesimal paths stemming from point P; see Figure 5.2a. One path consists of a displacement $\Delta x$ along x, to arrive at point A, and a displacement $\Delta y$ along y, to arrive at point Q. The second path consists of a displacement $\Delta y$ along y, to arrive at point B, and a displacement $\Delta x$ along x, to arrive at point Q. The two paths end at the same point, forming a rectangle of sides $\Delta x$ and $\Delta y$.

Assuming the length of the paths is infinitesimal, we can approximate, to first order the value of the function $f$ at $A$ and $B$ using the expansion around P along x and y:

$$\begin{cases} f_A(y) &= f(x_0+\Delta x, y) \approx f(x_0, y) + \left.\dfrac{\partial f}{\partial x}\right|_{(x_0,y)} \Delta x \\ f_B(x) &= f(x, y_0+\Delta y) \approx f(x, y_0) + \left.\dfrac{\partial f}{\partial y}\right|_{(x,y_0)} \Delta y \end{cases} \tag{5.25}$$

where $(x_0, y_0)$ are the coordinates of point P. It is important to note that we have left $f_A$ as a function of $y$ and $f_B$ as a function of $x$, so we can expand them further. We now expand theses functions around $A$ and $B$ to obtain the value of the function at point $Q$ for the two paths, while retaining only first order and second order terms:

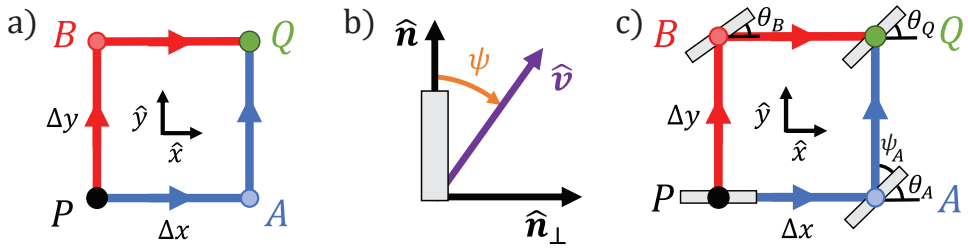



**Figure 5.2:** a) Schematic of the two paths taken from $P$ to $Q$. Solid blue line corresponds to the first path that passes through $A$ and the solid red line to the second path passing through $B$. b) Schematic of the direction $\hat{\mathbf{v}}$ along which we compute the gradient. $\psi$ is the angle between $\hat{\mathbf{v}}$ and $\hat{\mathbf{n}}$. c) Schematic of the two infinitesimal path construction for the 2D nematic case. Grey rectangles represent the director and $\theta_i$ is the director angle at point $i$.



$$\begin{cases} f_Q &= f(x_0+\Delta x, y_0+\Delta y) \approx f_A(y_0) + \left.\dfrac{\partial f_A}{\partial y}\right|_{y_0} \Delta y \\ &= f_P + \left.\dfrac{\partial f}{\partial x}\right|_{(x_0,y_0)} \Delta x + \left.\dfrac{\partial f}{\partial y}\right|_{(x_0,y_0)} \Delta y + \left.\dfrac{\partial}{\partial y}\dfrac{\partial f}{\partial x}\right|_{(x_0,y_0)} \Delta x \Delta y \\ f_Q &= f(x_0+\Delta x, y_0+\Delta y) \approx f_B(x_0) + \left.\dfrac{\partial f_B}{\partial x}\right|_{x_0} \Delta x \\ &= f_P + \left.\dfrac{\partial f}{\partial y}\right|_{(x_0,y_0)} \Delta y + \left.\dfrac{\partial f}{\partial x}\right|_{(x_0,y_0)} \Delta x + \left.\dfrac{\partial}{\partial x}\dfrac{\partial f}{\partial y}\right|_{(x_0,y_0)} \Delta x \Delta y \end{cases} \tag{5.26}$$

This expression can be interpreted as follows. For the first path, the value of $f_P$ is initially increased by the value of its $x$ derivative multiplied by the step size $\Delta x$. At point $A$, when we move vertically, the new increase can be split into two components, the vertical increase at the origin P giving the first derivative with respect to $y$ multiplied by $\Delta y$, and the increase in this derivative when moving from $f_P$ to $f_A$ which corresponds to the second derivative. The process on the second path is analogous, exchanging the $x$ and $y$ coordinates.

By continuity, both expressions should give the same value of $f_Q$. Comparing the expressions we can see that the second order term $\Delta x \Delta y$ is the only one different in the two expressions. Equating them we find the equality between second partial derivatives:

$$\frac{\partial^2 f}{\partial x \partial y} = \frac{\partial^2 f}{\partial y \partial x} \tag{5.27}$$

Instead of equating the value at $Q$ obtained from following two different infinitesimal paths, we can also use this method to measure the increase in

the function as we go around the loop. This interpretation works since the increase when moving from one point to another is opposite to the increase when reversing the path. In this sense, the equality of mixed second partial derivatives is a necessary condition to ensure that the value of the function when going through a loop is the same. Since this is true for any infinitesimal circuit, which can be arbitrarily small, the equality holds as long as the function is differentiable and has continuous first and second derivatives.

### 5.3.2 Compatibility conditions for a 2D nematic



Using this method we now derive the compatibility conditions for a 2D nematic. Since $|\hat{\mathbf{n}}| = 1$, we have one degree of freedom associated to the rotation of the director. To derive the compatibility conditions, we impose that the rotation of the director when moving in the two infinitesimal paths described previously is the same (Figure 5.2a).

We start by deriving the rotation rate of the director field when we move in an arbitrary direction $\hat{\mathbf{v}}$ forming an angle $\psi$ with respect to the director; seen Figure 5.2b. In the 2D case, the gradient tensor has four components and there are two constraints from the normalization condition. As a result, there are two degrees of freedom. A similar analysis as previously done for the gradient tensor in 3D reveals that the gradient tensor can be decomposed into two normal modes: Bend ($b$), which accounts for the director gradient as we move along $\hat{\mathbf{n}}$, and single splay ($s$), which accounts for the director gradient in the perpendicular direction, $\hat{\mathbf{n}}_\perp$:

$$\begin{cases} \vec{\mathbf{B}} &= \hat{\mathbf{n}} \cdot \nabla \hat{\mathbf{n}} = b\hat{\mathbf{n}}_\perp \\ \vec{\mathbf{S}} &= \hat{\mathbf{n}}_\perp \cdot \nabla \hat{\mathbf{n}} = s\hat{\mathbf{n}}_\perp \end{cases} \tag{5.28}$$

where $\vec{\mathbf{B}}$ and $\vec{\mathbf{S}}$ correspond to the parallel and perpendicular components to $\nabla\hat{\mathbf{n}}$. These vectors are both perpendicular to $\hat{\mathbf{n}}$ due to the normalization condition. The magnitudes $b$ and $s$ are scalars that account for the magnitude of these gradients. The deformation state of a 2D nematic can be completely characterized by specifying the scalar fields $b$ and $s$. Using equation 5.28, we can compute the gradient in the $\hat{\mathbf{v}} = \cos\psi\hat{\mathbf{n}} + \sin\psi\hat{\mathbf{n}}_\perp$ direction:

$$\begin{aligned} \nabla_{\hat{\mathbf{v}}}\hat{\mathbf{n}} = \hat{\mathbf{v}} \cdot \nabla\hat{\mathbf{n}} &= \cos\psi\hat{\mathbf{n}} \cdot \nabla\hat{\mathbf{n}} + \sin\psi\hat{\mathbf{n}}_\perp \cdot \nabla\hat{\mathbf{n}} \\ &= (b\cos\psi + s\sin\psi)\hat{\mathbf{n}}_\perp \end{aligned} \tag{5.29}$$

where the gradient points in the perpendicular direction to $\hat{\mathbf{n}}$ and its magnitude depends on the bend and splay magnitudes $b$ and $s$, as well as on the angle $\psi$. From this expression, if we move in the $\hat{\mathbf{v}}$ direction an infinitesimal amount

$\Delta r\ \hat{\mathbf{v}}$, the new director field at the end of the path can be approximated to first order by:

$$\hat{\mathbf{n}}(\vec{\mathbf{r}}_0 + \Delta r\hat{\mathbf{v}}) \approx \hat{\mathbf{n}}(\vec{\mathbf{r}}_0) + \Delta r(b\cos\psi + s\sin\psi)\hat{\mathbf{n}}_\perp(\vec{\mathbf{r}}_0) \tag{5.30}$$

where $\vec{\mathbf{r}}_0$ sets the starting point. When $\Delta r$ is infinitesimal, the variation of the director field in the perpendicular direction goes as the rotation angle $\Delta\theta$ to first order. The angle the director rotates when we move $\Delta r\ \hat{\mathbf{v}}$ can be written as:

$$\Delta\theta \approx \Delta r(b\cos\psi + s\sin\psi) \tag{5.31}$$



Recall $b$ and $s$ have dimensions of 1/length. We now make our two different paths taking the $x$ direction to point along $\hat{\mathbf{n}}$ and the direction $y$ to be perpendicular to $\hat{\mathbf{n}}$, as shown in Figure 5.2c. Repeating the same analysis as for the mixed partial derivatives, we find that at points $A$ and $B$ the director can be approximated as:

$$\begin{cases} \hat{\mathbf{n}}(A) & \approx \hat{\mathbf{n}}(P) + \Delta x\ b(P)\hat{\mathbf{y}} \\ \hat{\mathbf{n}}(B) & \approx \hat{\mathbf{n}}(P) + \Delta y\ s(P)\hat{\mathbf{y}} \end{cases} \tag{5.32}$$

The infinitesimal rotation angle the director has made when moving from point $P$ to points $A$ and $B$ results from equation 5.31:

$$\begin{cases} \Delta\theta_{P-A} & \approx \Delta x\ b(P) \\ \Delta\theta_{P-B} & \approx \Delta y\ s(P) \end{cases} \tag{5.33}$$

For the second segment of the paths, the director makes an angle $\Delta\theta$ with respect to the $x$ direction. If we take the second segment of the path from $A$ to $Q$, we now move an infinitesimal amount $\Delta y$ in the y direction; $\hat{\mathbf{v}}$ then corresponds to $\hat{\mathbf{y}}$ and the angle $\psi$ at A is $\psi_A \approx \pi/2 - \Delta\theta_{P-A}$ (Figure 5.2c). Knowing this angle, we can approximate the rotation angle from $A$ to $Q$ using equation 5.31. For the segment $B - Q$, the angle the director makes with respect to the path direction is $\psi_B \approx -\Delta\theta_{P-B}$. The rotation angle along these segments becomes:

$$\begin{cases} \Delta\theta_{A-Q} & \approx \Delta y[b(A)\cos(\pi/2 - \Delta\theta_{P-A}) + s(A)\sin(\pi/2 - \Delta\theta_{P-A})] \\ \Delta\theta_{B-Q} & \approx \Delta x[b(B)\cos(-\Delta\theta_{P-B}) + s(B)\sin(-\Delta\theta_{P-B})] \end{cases} \tag{5.34}$$

which can be further simplified as:

$$\begin{cases} \Delta\theta_{A-Q} & \approx \Delta y[b(A)\sin(\Delta x\ b(P)) + s(A)\cos(\Delta x\ b(P))] \\ \Delta\theta_{B-Q} & \approx \Delta x[b(B)\cos(\Delta y\ s(P)) - s(B)\sin(\Delta y\ s(P))] \end{cases} \tag{5.35}$$

Since $\Delta x$ and $\Delta y$ are infinitesimal, we can expand to first order the sine and cosine functions such that $\cos(x) \approx 1$ and $\sin(x) \approx x$. We then have:

$$\begin{cases} \Delta\theta_{A-Q} & \approx b(A)b(P)\Delta x\Delta y + s(A)\Delta y \\ \Delta\theta_{B-Q} & \approx b(B)\Delta x - s(P)s(B)\Delta x\Delta y \end{cases} \tag{5.36}$$

The resultant expressions depend on the values of splay and bend at the point of evaluation $P$ and at neighboring points $A$ and $B$. We can approximate these neighboring values by a first order expansion of the fields around the evaluation point $P$:



$$\begin{cases} \Delta\theta_{A-Q} & \approx b^2\Delta x\Delta y + s\Delta y + \dfrac{\partial s}{\partial x}\Delta x\Delta y \\ \Delta\theta_{B-Q} & \approx b\Delta x + \dfrac{\partial b}{\partial y}\Delta x\Delta y - s^2\Delta x\Delta y \end{cases} \tag{5.37}$$

where the bend, splay and their derivatives are evaluated at $P$. Finally, the total rotation angle for paths $P-A-Q$ and $P-B-Q$ can be written as the sum of the rotation angle in both segments:

$$\begin{cases} \Delta\theta_{P-A-Q} & \approx b\Delta x + s\Delta y + \left(b^2 + \dfrac{\partial s}{\partial x}\right)\Delta x\Delta y \\ \Delta\theta_{P-B-Q} & \approx b\Delta x + s\Delta y + \left(\dfrac{\partial b}{\partial y} - s^2\right)\Delta x\Delta y \end{cases} \tag{5.38}$$

Imposing that the rotation angle has to be the same independently of the path taken results in the 2D compatibility equation:

$$b^2 + s^2 + \frac{\partial s}{\partial x} - \frac{\partial b}{\partial y} = 0 \tag{5.39}$$

which can be written in vectorial form as:

$$b^2 + s^2 + \hat{\mathbf{n}} \cdot \nabla s - \hat{\mathbf{n}}_\perp \cdot \nabla b = 0 \tag{5.40}$$

This equation is the same as the one previously derived in [158] and indeed, as pointed out there, can be understood as a result of the equality of mixed partial derivatives of the director field angle $\theta$. In this article, they also derive the compatibility conditions in the case of a curved manifold. In this case, the Gaussian curvature of the surface enters in the equation in a very simple form [158]:

$$b^2 + s^2 + \hat{\mathbf{n}} \cdot \nabla s - \hat{\mathbf{n}}_\perp \cdot \nabla b = -K \tag{5.41}$$

In deriving this expression, the authors used the metric of the manifold, somewhat obscuring, in our opinion, the intuition on how the Gaussian curvature

of the surface enters the equation. It is important to note than when dealing with a curved manifold, the tangent plane is different at different points and the standard derivative must be substituted by the covariant derivative which accounts for the vector change rate compared to a parallelly transported vector [8].

In this case instead of imposing the equality on the angle change between the two paths we can directly travel the whole loop $P-A-Q-B-P$, while computing the director field rotation, exploiting that $\Delta\theta_{P-B} = -\Delta\theta_{P-B}$:

$$\begin{aligned}\Delta\theta_{P-A-Q-B-P} &= \Delta\theta_{P-A} + \Delta\theta_{A-Q} - \Delta\theta_{B-Q} - \Delta\theta_{P-B} \\ &= \left(b^2 + s^2 + \hat{\mathbf{n}} \cdot \nabla s - \hat{\mathbf{n}}_\perp \cdot \nabla b\right) \Delta x \Delta y\end{aligned} \tag{5.42}$$

One of the interesting consequences of curvature is the fact that when transporting parallelly a vector around a closed loop, the vector would in general have rotated after returning back to the starting point. This angle the director rotates when going around the loop is called holonomy and can be related to the total Gaussian curvature of the encircled area. In our derivation we are using an infinitesimal loop that can be made arbitrarily small, and thus the holonomy can be approximated by[1] [8]:

$$\Delta\theta_{holonomy} = K\Delta x\Delta y \tag{5.43}$$

with $K$ the Gaussian curvature at point $P$. Combining equations 5.42 and 5.43, we see that in order for the director field to be continuous and return to its original position when going around the closed circuit, the rotation of the director $\Delta\theta_{P-A-Q-B-P}$ must compensate the holonomy associated to parallel transport. As a result:

$$\begin{aligned}\Delta\theta_{P-A-Q-B-P} &= -\Delta\theta_{holonomy} \\ b^2 + s^2 + \hat{\mathbf{n}} \cdot \nabla s - \hat{\mathbf{n}}_\perp \cdot \nabla b &= -K\end{aligned} \tag{5.44}$$

which is the same equation as derived in [158]. In fact, the concept of holonomy can be used to proof the Gaussian curvature metric formula [8], which is the one used in [158] to derive the compatibility conditions for curved manifolds.

Our reasoning indicates that the role of Gaussian curvature in the compatibility conditions can be then attributed to holonomy, so that the liquid crystal deformations need to compensate the rotation of the director field when parallelly transported to guarantee continuity. This concept of holonomy can indeed

[1] We have taken the first order approximation of the area, corresponding to the Euclidean case. Higher orders are not needed for this argument to work.

be used to understand in an intuitive manner why positive/negative 2D point defects energetically prefer regions of positive/negative Gaussian curvature [11], since in these regions, the curvature of space favors the rotation of the director field in the same direction as the winding of the defects when parallelly transported in a loop around the defect. Locating positive/negative defects in regions of positive/negative Gaussian curvature then lower the nematic elastic free energy.



### 5.3.3 Compatibility conditions for a 3D nematic

We now move to the case of a 3D director field in Euclidean space. In this case, the two path construction can still be used for any pair of spatial coordinates. Since we now consider a liquid crystal in 3D, we have three spatial coordinates $(x, y, z)$ and thus, three possible pairs of them. We construct the three orthogonal loops shown in Figure 5.3a, and equal the variation of the director as we move along two different paths ending at the same point. Although the gradient of the director field has to be perpendicular to $\hat{\mathbf{n}}$, the second order mixed term can have a component parallel to the director field which can result in 9 compatibility conditions. In our case, as we will see, the only different components are the ones perpendicular to the director field. This results in two equations for each of the three circuits, yielding six compatibility conditions.

To simplify the calculations, we choose a local coordinate system with an orthonormal vector basis $(\hat{\mathbf{x}}_1, \hat{\mathbf{x}}_2, \hat{\mathbf{x}}_3)$ such that the first coordinate points along $\hat{\mathbf{x}}_1 \equiv \hat{\mathbf{n}}$. The other two vectors $\hat{\mathbf{x}}_2, \hat{\mathbf{x}}_3$ belong to the perpendicular plane. From the analysis of the deformation modes, only bend and biaxial splay are anisotropic in the perpendicular plane. For simplicity, we choose $\hat{\mathbf{x}}_2 = \hat{\mathbf{n}}_2$ to point in the direction of the eigenvector with positive eigenvalue of the biaxial-splay deformation. The vector $\hat{\mathbf{x}}_3 = \hat{\mathbf{x}}_1 \times \hat{\mathbf{x}}_2 = \hat{\mathbf{n}}_3$ is defined to be perpendicular to the other two forming a right-handed triad, as shown in Figure 5.3a. This vector points in the direction of the eigenvector with negative eigenvalue of the biaxial-splay deformation.

As in the 2D case, we start computing the gradient of the director field as we move in an arbitrary direction given by the unitary vector $\hat{\mathbf{v}}$ (Figure 5.3b). Due to the linearity of the directional derivative, we can decompose the vector into its three components $(v_1, v_2, v_3)$ in the principal directions $(\hat{\mathbf{n}}, \hat{\mathbf{n}}_2, \hat{\mathbf{n}}_3)$. The gradient when moving in the $\hat{\mathbf{n}}$ direction is given by the bend deformation as:

$$\nabla_{v_1\hat{\mathbf{n}}}\ \hat{\mathbf{n}} = -v_1\mathbf{B} = -v_1(b_2\hat{\mathbf{n}}_2 + b_3\hat{\mathbf{n}}_3) \tag{5.45}$$

The bend vector $\mathbf{B}$ is decomposed into a component $b_2$ pointing along $\hat{\mathbf{n}}_2$ and a component $b_3$ pointing along $\hat{\mathbf{n}}_3$. To compute the gradient due to the component of $\hat{\mathbf{v}}$ perpendicular to $\hat{\mathbf{n}}$ we can use the explicit expression of the

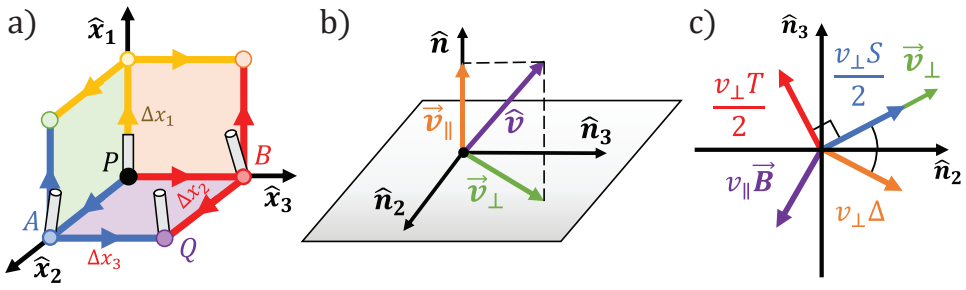



**Figure 5.3:** a) Schematic of the different infinitesimal paths. There are in total six paths belonging to perpendicular points. For each plane there are two points leading to the same path. The points are labeled for the paths in the $\hat{\mathbf{x}}_2 - \hat{\mathbf{x}}_3$ plane. Cylinders represent the nematic for the path in the horizontal plane. b) Schematic of the direction $\hat{\mathbf{v}}$ where the gradient of the director field is computed in the frame of reference of the deformation main directions. c) Schematic of the gradient components associated to each deformation. The only gradient that does not depend on the direction of $\hat{\mathbf{v}}$ is the bend one.



perpendicular gradient tensor when the axis coincide with the main directions of the biaxial splay tensor:

$$\boldsymbol{\alpha} = \frac{1}{2}S\begin{pmatrix}1 & 0\\ 0 & 1\end{pmatrix} + \frac{1}{2}T\begin{pmatrix}0 & -1\\ 1 & 0\end{pmatrix} + \Delta\begin{pmatrix}1 & 0\\ 0 & -1\end{pmatrix} \tag{5.46}$$

The gradient in the component of $\hat{\mathbf{v}}$ perpendicular to $\hat{\mathbf{n}}$ can then be expressed as:

$$\begin{aligned}\nabla_{(v_2\hat{\mathbf{n}}_2+v_3\hat{\mathbf{n}}_3)}\hat{\mathbf{n}} = &\left(v_2\frac{1}{2}S - v_3\frac{1}{2}T + v_2\Delta\right)\hat{\mathbf{n}}_2\\ &+\left(v_3\frac{1}{2}S + v_2\frac{1}{2}T - v_3\Delta\right)\hat{\mathbf{n}}_3\end{aligned} \tag{5.47}$$

Adding both parallel and perpendicular components of $\hat{\mathbf{v}}$ and rearranging, we obtain the gradient of the director field along direction $\hat{\mathbf{v}}$:

$$\begin{aligned}\nabla_{\hat{\mathbf{v}}}\hat{\mathbf{n}} = &\left[-v_1b_2 + v_2\left(\frac{1}{2}S + \Delta\right) - v_3\frac{1}{2}T\right]\hat{\mathbf{n}}_2\\ &+\left[-v_1b_3 + v_3\left(\frac{1}{2}S - \Delta\right) + v_2\frac{1}{2}T\right]\hat{\mathbf{n}}_3\end{aligned} \tag{5.48}$$

The directional derivative depends only on the deformation fields $\mathbf{B}$, $S$, $T$, $\Delta$ and the components of $\hat{\mathbf{v}}$, and it is perpendicular to $\hat{\mathbf{n}}$. We can further decompose this vector into the terms associated to each deformation, as shown in Figure 5.3c. For the deformations associated to the perpendicular component of $\hat{\mathbf{v}} \to \hat{\mathbf{v}}_\perp$, the gradient vectors are related to this direction. The term associated to double splay points in the $\hat{\mathbf{v}}_\perp$ direction, the double twist one is perpendicular to $\hat{\mathbf{v}}_\perp$, and the one associated with biaxial splay points in the symmetric direction of $\hat{\mathbf{v}}_\perp$ with respect $\hat{\mathbf{n}}_2$. The bend component of the gradient is associated to the parallel component of $\hat{\mathbf{v}} \to \hat{\mathbf{v}}_\parallel$ and has two degrees of freedom. As a result, it can point anywhere in the perpendicular plane.



With the expression for the directional derivative of the director field we can start computing the compatibility equations. We start by focusing on the $\hat{\mathbf{x}}_2 - \hat{\mathbf{x}}_3$ plane. We draw our two infinitesimal paths ending at the same point Q, as for the 2D case (Figure 5.3a). One path first moves $\Delta x_2$ in the $\hat{\mathbf{x}}_2$ direction towards point $A$ and then $\Delta x_3$ in the $\hat{\mathbf{x}}_3$ direction to point $Q$. The second moves first $\Delta x_3$ in the $\hat{\mathbf{x}}_3$ direction to point $B$ and then $\Delta x_2$ in the $\hat{\mathbf{x}}_2$ direction ending also in $Q$.

We now compute the first order approximation of the director field at point $A$ using equation 5.48, noticing that $\hat{\mathbf{v}} = \hat{\mathbf{x}}_2$:

$$\hat{\mathbf{n}}(A) \approx \hat{\mathbf{n}}(P) + \Delta x_2 \nabla_{\hat{\mathbf{x}}_2} \hat{\mathbf{n}} = \hat{\mathbf{x}}_1 + \left[ \left( \frac{1}{2} S + \Delta \right) \hat{\mathbf{x}}_2 + \frac{1}{2} T \hat{\mathbf{x}}_3 \right] \Delta x_2 \tag{5.49}$$

In the infinitesimal limit, this corresponds to a director rotation of angle $\theta_A \approx \sqrt{T^2/4 + (S/2 + \Delta)^2} \Delta x_2$ towards the direction given by $(S/2 + \Delta)\, \hat{\mathbf{x}}_2 + T/2 \hat{\mathbf{x}}_3$. In order to approximate the director variation in the segment $A - Q$ using equation 5.48, we first need to know the direction of all the main directions of the gradient tensor at point $A$. While for the 2D case the perpendicular direction to the director is completely determined by the director orientation, in the 3D case, the director completely determines the perpendicular plane, but not the directions of the other two principal directions, $\hat{\mathbf{n}}_2(A)$ and $\hat{\mathbf{n}}_3(A)$, in this plane.

The final orientation of these two vectors can be computed from $\hat{\mathbf{x}}_2$ and $\hat{\mathbf{x}}_3$ by two infinitesimal rotations. A first one that rotates the vectors around an axis perpendicular to the director, transforming $\hat{\mathbf{n}}(P)$ into $\hat{\mathbf{n}}(A)$, and a second one that rotates the vectors around the $\hat{\mathbf{n}}(A)$ direction. The first operation can be regarded as torsion free, since any vector perpendicular to $\hat{\mathbf{x}}_1$ tips in the direction perpendicular to the plane; it can be seen as a pure tilt of the plane. The second rotation corresponds to a pure rotation of the perpendicular plane around $\hat{\mathbf{n}}(A)$. This second rotation is relevant and will completely determine the orientation of the main axis, which is necessary to compute the biaxial splay

component of the gradient. We will consider that the angle characterizing the orientation of the biaxial splay main axis, $\omega$[1], is constant if there is no rotation around $\hat{\mathbf{n}}(A)$ of the axis. The second rotation angle as we move in direction $\hat{\mathbf{x}}_i$ can then be approximated by $(\partial\omega/\partial x_i)\Delta x_i$. As we will see later, this angle gradient can be computed from the analytical expression for $\hat{\mathbf{n}}_2$.

We now compute the first rotation by using the rotation matrix corresponding to a rotation of angle $\theta_A \approx \sqrt{T^2/4 + (S/2+\Delta)^2}\Delta x_2$ around the axis given by the unit vector $[-T/2\hat{\mathbf{x}}_2 + (S/2+\Delta)\,\hat{\mathbf{x}}_3]/\sqrt{T^2/4 + (S/2+\Delta)^2}$ which is perpendicular to the director tipping direction. Retaining up to first order, the rotation matrix becomes:



$$R_1 = \begin{pmatrix} 1 & -\left(\frac{1}{2}S+\Delta\right)\Delta x_2 & -\frac{1}{2}T\ \Delta x_2 \\ \left(\frac{1}{2}S+\Delta\right)\Delta x_2 & 1 & 0 \\ \frac{1}{2}T\ \Delta x_2 & 0 & 1 \end{pmatrix} \tag{5.50}$$

We now use this matrix to obtain the rotated vectors $\hat{\mathbf{x}}_2'$ and $\hat{\mathbf{x}}_3'$ to first order:

$$\begin{cases} \hat{\mathbf{x}}_2' \approx R_1 \cdot \begin{pmatrix} 0 \\ 1 \\ 0 \end{pmatrix} = \hat{\mathbf{x}}_2 - \left(\frac{1}{2}S+\Delta\right)\Delta x_2 \hat{\mathbf{x}}_1 \\ \hat{\mathbf{x}}_3' \approx R_1 \cdot \begin{pmatrix} 0 \\ 0 \\ 1 \end{pmatrix} = \hat{\mathbf{x}}_2 - \frac{1}{2}T\Delta x_2 \hat{\mathbf{x}}_1 \end{cases} \tag{5.51}$$

where the first order term corresponds to tipping in the $\hat{\mathbf{x}}_1$ direction. The second rotation matrix can be computed by a rotation of angle $(\partial\omega/\partial x_2)\Delta x_2$ around $\hat{\mathbf{n}}(A)$. To first order, the rotation matrix becomes:

$$R_2 = \begin{pmatrix} 1 & 0 & 0 \\ 0 & 1 & -\frac{\partial\omega}{\partial x_2}\Delta x_2 \\ 0 & \frac{\partial\omega}{\partial x_2}\Delta x_2 & 1 \end{pmatrix} \tag{5.52}$$

[1]We note that the definition of this angle is difficult to be extended to the whole sample and may not be possible in general. Nevertheless, in a local environment, we can always define it in the proposed way to account for the second rotation.

which corresponds to a rotation around $\hat{\mathbf{n}}$. Applying the second rotation to vectors $\hat{\mathbf{x}}_2'$ and $\hat{\mathbf{x}}_2'$ we obtain, to first order, deformation main directions of deformation at A:

$$\begin{cases} \hat{\mathbf{n}}_2(A) & \approx \hat{\mathbf{x}}_2 - \left(\frac{1}{2}S + \Delta\right)\Delta x_2 \hat{\mathbf{x}}_1 + \frac{\partial \omega}{\partial x_2}\Delta x_2 \hat{\mathbf{x}}_3 \\ \hat{\mathbf{n}}_3(A) & \approx \hat{\mathbf{x}}_3 - \frac{1}{2}T\Delta x_2 \hat{\mathbf{x}}_1 - \frac{\partial \omega}{\partial x_2}\Delta x_2 \hat{\mathbf{x}}_2 \end{cases} \tag{5.53}$$

We can now use equation 5.48 to compute the gradient in the second segment taking into account that $v_1$, $v_2$ and $v_3$ are the projections of $\hat{\mathbf{v}}$ onto the deformation main directions $\hat{\mathbf{n}}(A)$, $\hat{\mathbf{n}}_2(A)$, and $\hat{\mathbf{n}}_3(A)$, respectively. The director field value at point $Q$ can be expressed to second order as:

$$\begin{aligned} \hat{\mathbf{n}}(Q) \approx & \hat{\mathbf{n}}(A) + \nabla_{\hat{\mathbf{x}}_3}\hat{\mathbf{n}}(A)\cdot\Delta x_3 = \hat{\mathbf{n}}(A) - \frac{1}{2}T\ \mathbf{B}_A \Delta x_2 \Delta x_3 \\ & + \left[\left(\frac{1}{2}S_A + \Delta_A\right)\frac{\partial \omega}{\partial x_2}\Delta x_2 \Delta x_3 - \frac{1}{2}T_A \Delta x_3\right]\hat{\mathbf{n}}_2(A) \\ & + \left[\left(\frac{1}{2}S_A - \Delta_A\right)\Delta x_3 + \frac{1}{2}T_A \frac{\partial \omega}{\partial x_2}\Delta x_2 \Delta x_3\right]\hat{\mathbf{n}}_3(A) \end{aligned} \tag{5.54}$$

As in the 2D case, this expression not only takes into account the deformation state at $P$, but also the deformation state at $A$ which is indicated by the subindex "$A$". As an example, the bend vector at point A is expressed in terms of the main directions at that point $\mathbf{B}_A = b_2(A)\hat{\mathbf{n}}_2(A) + b_3(A)\hat{\mathbf{n}}_3(A)$. We can now approximate the values of our deformation fields at $A$ by a Taylor expansion around point $P$, such that we only retain first order and crossed second order terms to obtain the final expression:

$$\begin{aligned} \hat{\mathbf{n}}(Q) \approx & \hat{\mathbf{x}}_1 + \left[\left(\frac{S}{2} + \Delta\right)\hat{\mathbf{x}}_2 + \frac{T}{2}\hat{\mathbf{x}}_3\right]\Delta x_2 + \left[\left(\frac{S}{2} - \Delta\right)\hat{\mathbf{x}}_3\right. \\ & \left. - \frac{T}{2}\hat{\mathbf{x}}_2\right]\Delta x_3 + \left[\left(-\frac{T}{2}b_2 + 2\Delta\frac{\partial \omega}{\partial x_2} - \frac{1}{2}\frac{\partial T}{\partial x_2}\right)\hat{\mathbf{x}}_2\right. \\ & \left. + \left(-\frac{T}{2}b_3 + \frac{\partial}{\partial x_2}\left(\frac{S}{2} - \Delta\right)\right)\hat{\mathbf{x}}_3 + T\Delta\ \hat{\mathbf{x}}_1\right]\Delta x_2 \Delta x_3 \end{aligned} \tag{5.55}$$

The director change $\hat{\mathbf{n}}(Q) - \hat{\mathbf{x}}_1$ is a vectorial quantity, so when imposing equality with the expression obtained from the second path, all of the components of this vector have to be equal.

We now compute the variation of $\hat{\mathbf{n}}$ along the second path in an analogous way to the first path. The director field at $B$ to first order becomes:

$$\hat{\mathbf{n}}(B) \approx \hat{\mathbf{n}}(P) + \Delta x_3 \nabla_{\hat{\mathbf{x}}_3} \hat{\mathbf{n}} = \hat{\mathbf{x}}_1 + \left[ \left( \frac{1}{2} S - \Delta \right) \hat{\mathbf{x}}_3 - \frac{1}{2} T \hat{\mathbf{x}}_2 \right] \Delta x_3 \tag{5.56}$$

This corresponds to a rotation of angle $\theta_B \approx \sqrt{T^2/4 + (S/2 - \Delta)^2} \Delta x_3$ towards the $-T/2\hat{\mathbf{x}}_2 + (S/2 - \Delta)\,\hat{\mathbf{x}}_3$ direction. As for the previous path, we can compute the change of the triad related to the deformation main directions by two rotations, a first one of angle $\theta_B$ around the axis $[-(S/2 - \Delta)\,\hat{\mathbf{x}}_2 - T/2\hat{\mathbf{x}}_3]/\sqrt{T^2/4 + (S/2 - \Delta)^2}$ and another one of angle $(\partial\omega/\partial x_3)\Delta x_3$ around $\hat{\mathbf{n}}(B)$. To first order, the rotations matrices corresponding to these operations are:



$$R_1 = \begin{pmatrix} 1 & \frac{1}{2} T\ \Delta x_3 & -\left( \frac{1}{2} S - \Delta \right) \Delta x_3 \\ -\frac{1}{2} T\ \Delta x_3 & 1 & 0 \\ \left( \frac{1}{2} S - \Delta \right) \Delta x_3 & 0 & 1 \end{pmatrix} \tag{5.57}$$

$$R_2 = \begin{pmatrix} 1 & 0 & 0 \\ 0 & 1 & -\dfrac{\partial \omega}{\partial x_3} \Delta x_3 \\ 0 & \dfrac{\partial \omega}{\partial x_3} \Delta x_3 & 1 \end{pmatrix}$$

The eigenvectors of the biaxial-splay deformation perpendicular to the gradient tensor at point $B$ are:

$$\begin{cases} \hat{\mathbf{n}}_2(B) & \approx \hat{\mathbf{x}}_2 + \dfrac{1}{2} T \Delta x_3 \hat{\mathbf{x}}_1 + \dfrac{\partial \omega}{\partial x_3} \Delta x_3 \hat{\mathbf{x}}_3 \\ \hat{\mathbf{n}}_3(B) & \approx \hat{\mathbf{x}}_3 - \left( \dfrac{1}{2} S - \Delta \right) \Delta x_3 \hat{\mathbf{x}}_1 - \dfrac{\partial \omega}{\partial x_3} \Delta x_3 \hat{\mathbf{x}}_2 \end{cases} \tag{5.58}$$

With these, the value of $\hat{\mathbf{n}}(Q)$ can be approximated from the second path as:

$$\begin{aligned} \hat{\mathbf{n}}(Q) \approx & \hat{\mathbf{n}}(B) + \nabla_{\hat{\mathbf{x}}_2} \hat{\mathbf{n}}(B) \cdot \Delta x_2 = \hat{\mathbf{n}}(B) + \frac{1}{2} T\ \mathbf{B}_B \Delta x_2 \Delta x_3 \\ & + \left[ \left( \frac{1}{2} S_B + \Delta_B \right) \Delta x_2 + \frac{1}{2} T_B \frac{\partial \omega}{\partial x_3} \Delta x_2 \Delta x_3 \right] \hat{\mathbf{n}}_2(B) \\ & + \left[ \left( -\frac{1}{2} S_B + \Delta_B \right) \frac{\partial \omega}{\partial x_3} \Delta x_2 \Delta x_3 + \frac{1}{2} T_B \Delta x_2 \right] \hat{\mathbf{n}}_3(B) \end{aligned} \tag{5.59}$$

Expanding this equation to second order around $P$ results in:

$$\begin{aligned}\hat{\mathbf{n}}(Q) \approx & \hat{\mathbf{x}}_1 + \left[\left(\frac{S}{2}+\Delta\right)\hat{\mathbf{x}}_2 + \frac{T}{2}\hat{\mathbf{x}}_3\right]\Delta x_2 + \left[\left(\frac{S}{2}-\Delta\right)\hat{\mathbf{x}}_3\right. \\ & \left. - \frac{T}{2}\hat{\mathbf{x}}_2\right]\Delta x_3 + \left[\left(\frac{T}{2}b_2 + \frac{\partial}{\partial x_3}\left(\frac{S}{2}+\Delta\right)\right)\hat{\mathbf{x}}_2\right. \\ & \left. + \left(\frac{T}{2}b_3 + 2\Delta\frac{\partial\omega}{\partial x_3} + \frac{1}{2}\frac{\partial T}{\partial x_3}\right)\hat{\mathbf{x}}_3 + T\Delta\ \hat{\mathbf{x}}_1\right]\Delta x_2\Delta x_3\end{aligned} \tag{5.60}$$

5

If we now equate the expression for $\hat{\mathbf{n}}(Q)$ obtained from the two paths (equations 5.55 and 5.60) we can see that the zeroth and first order terms are the same. Also, from the crossed second order term, the component in the $\hat{\mathbf{x}}_1$ direction is the same. The only different terms are the perpendicular components in the second order crossed term resulting in the two compatibility conditions:

$$\begin{cases} Tb_2 + \frac{1}{2}\frac{\partial T}{\partial x_2} + \frac{1}{2}\frac{\partial S}{\partial x_3} + \frac{\partial\Delta}{\partial x_3} - 2\Delta\frac{\partial\omega}{\partial x_2} = 0 \\ Tb_3 + \frac{1}{2}\frac{\partial T}{\partial x_3} - \frac{1}{2}\frac{\partial S}{\partial x_2} + \frac{\partial\Delta}{\partial x_2} + 2\Delta\frac{\partial\omega}{\partial x_3} = 0 \end{cases} \tag{5.61}$$

The same process can be repeated for the other two circuits in the planes $\hat{\mathbf{x}}_1-\hat{\mathbf{x}}_2$ and $\hat{\mathbf{x}}_1-\hat{\mathbf{x}}_3$. The detailed calculations in these two circuits can be found in Appendix F. We end up with the six compatibility conditions for a unitary vector field in Euclidean space:

$$Tb_2 + \frac{1}{2}\frac{\partial T}{\partial x_2} + \frac{1}{2}\frac{\partial S}{\partial x_3} + \frac{\partial\Delta}{\partial x_3} - 2\Delta\frac{\partial\omega}{\partial x_2} = 0 \tag{5.62a}$$

$$Tb_3 + \frac{1}{2}\frac{\partial T}{\partial x_3} - \frac{1}{2}\frac{\partial S}{\partial x_2} + \frac{\partial\Delta}{\partial x_2} + 2\Delta\frac{\partial\omega}{\partial x_3} = 0 \tag{5.62b}$$

$$b_2b_3 + \frac{1}{2}TS + 2\Delta\frac{\partial\omega}{\partial x_1} + \frac{1}{2}\frac{\partial T}{\partial x_1} + \frac{\partial b_3}{\partial x_2} + b_2\frac{\partial\omega}{\partial x_2} = 0 \tag{5.62c}$$

$$b_2b_3 - \frac{1}{2}TS + 2\Delta\frac{\partial\omega}{\partial x_1} - \frac{1}{2}\frac{\partial T}{\partial x_1} + \frac{\partial b_2}{\partial x_3} - b_3\frac{\partial\omega}{\partial x_3} = 0 \tag{5.62d}$$

$$b_2^2 + \left(\frac{1}{2}S+\Delta\right)^2 - \frac{1}{4}T^2 + \frac{\partial b_2}{\partial x_2} + \frac{\partial(S/2+\Delta)}{\partial x_1} - b_3\frac{\partial\omega}{\partial x_2} = 0 \tag{5.62e}$$

$$b_3^2 + \left(\frac{1}{2}S-\Delta\right)^2 - \frac{1}{4}T^2 + \frac{\partial b_3}{\partial x_3} + \frac{\partial(S/2-\Delta)}{\partial x_1} + b_2\frac{\partial\omega}{\partial x_3} = 0 \tag{5.62f}$$

where equations 5.62a,b correspond to the paths in the $\hat{\mathbf{x}}_2 - \hat{\mathbf{x}}_3$ plane, equations 5.62c,e to the paths in the $\hat{\mathbf{x}}_1 - \hat{\mathbf{x}}_2$ plane, and equations 5.62d,f to the paths in the $\hat{\mathbf{x}}_1 - \hat{\mathbf{x}}_3$ plane.

We can first confirm that these equations fulfill the symmetry under a $\pi/2$-rotation of the coordinate system around $\hat{\mathbf{n}}$, which transforms $\hat{\mathbf{x}}_2 \to -\hat{\mathbf{x}}_3$ and $\hat{\mathbf{x}}_3 \to \hat{\mathbf{x}}_2$. This corresponds to swapping the perpendicular axis and should not change the equations. The change of coordinates transform the bend vector components in the same way: $b_2 \to -b_3$ and $b_3 \to b_2$. For the deformations in the perpendicular plane, double splay $S$ is unchanged since it is isotropic. This is also true for the double twist term $T$, since the vector system is also kept right-handed. For this last reason, the gradient in angle $\partial\omega/\partial x_i$ is also unchanged. In addition, the double splay magnitude changes sign ($\Delta \to -\Delta$), since the new $\hat{\mathbf{x}}_2$ axis is the one with the negative eigenvalue. Performing this change in the compatibility equations, the equations transform into each other by pairs, resulting in the same set of compatibility conditions. In particular, there is an exchange of equations 5.62a↔5.62b, 5.62c↔5.62d and 5.62e↔5.62f.

We can also verify that these equations result in the 2D compatibility equation in the limiting case where the director field lies in a plane and only varies within that plane. In that case we can take $\hat{\mathbf{x}}_2$ to be the direction perpendicular $\hat{\mathbf{n}}$ in the plane where it lies. This implies that $b_2 = b_{2D}$ and $b_3 = 0$, and that the partial derivative with respect to $x_3$ is zero. The planar deformation is only fulfilled when $T = 0$ and there is single splay, which occurs when $S/2 = \Delta$, so that the single splay is given by $s_{2D} = (S/2 + \Delta)$. Moreover, the rotation of the frame of main directions around the director is zero, so $\partial\omega/\partial x_i = 0$. When considering all these facts in the compatibility conditions, equations 5.62a,b,c,d and f are automatically satisfied. Equation 5.62e, on the other hand transforms into the 2D compatibility equation 5.39.

If instead of Euclidean space we now think in a curved manifold, the curvature of the manifold is given by the Riemann tensor $R_{ijkl}$. This tensor has in general 9 independent components, which is further reduced to 6 when the first Bianchi identity is fulfilled [156]. As in the 2D case, these 6 independent components have a very clear interpretation in terms of parallel transport around loops. Indeed, the term $R_{ijkl}$ corresponds to the angle per unit area a vector pointing in the $k$ direction has rotated towards direction $l$ when performing a loop in the $ij$ plane [8]. This implies that when curvature is present, the director field deformation when going around a loop should compensate the rotation angle due to parallel transport as in the 2D case, with the only difference that we now have 6 components of the curvature accounting for each loop and tilting direction. Nonetheless, passing from 2D to 3D is typically not straightforward mathematically, so a deeper analysis needs to be done to check which are the modifications to the equations in Euclidean space necessary to account for the

curvature of the space.

All in all, we have obtained six compatibility equations when imposing continuity of the director field. This continuity can also be expanded to other vectors in our triad. Once the director continuity is imposed, since the other vectors are perpendicular to $\hat{\mathbf{n}}$ and perpendicular between them, their orientation only has one degree of freedom corresponding to rotations around $\hat{\mathbf{n}}$. This results in one extra compatibility equation per loop, adding three extra compatibility equations, which can be derived using the same approach.



Importantly, the obtained compatibility equations are expressed in terms of the deformation fields of the nematic liquid crystal. Before studying them in more detail, it is interesting to first relate them to the director field, so they can be checked with different director fields. While the double twist, double splay and bend can be described by their well know expressions, in the case of the biaxial splay, its magnitude $\Delta$ has to be computed from the largest eigenvalue of the biaxial-splay tensor. Finally, the other important term is the rotation of the frame associated to the main directions around the director when moving in a certain direction, $\partial\omega/\partial x_i$. We can derive an expression for this by noticing that this term appears in the change of the vector $\hat{\mathbf{n}}_2$ in the $\hat{\mathbf{n}}_3$ direction when moving along $\hat{\mathbf{n}}_i$. This gives the following expressions for the deformation fields:

$$\begin{cases} T & = \hat{\mathbf{n}} \cdot (\nabla \times \hat{\mathbf{n}}) \\ S & = \nabla \cdot \hat{\mathbf{n}} \\ b_2 & = [-(\hat{\mathbf{n}} \cdot \nabla)\hat{\mathbf{n}}] \cdot \hat{\mathbf{n}}_2 \\ b_3 & = [-(\hat{\mathbf{n}} \cdot \nabla)\hat{\mathbf{n}}] \cdot \hat{\mathbf{n}}_3 \\ \Delta & = \text{ Largest eigenvalue of } \boldsymbol{\Delta} \\ \dfrac{\partial \omega}{\partial x_i} & = (\hat{\mathbf{n}}_i \cdot \nabla \hat{\mathbf{n}}_2) \cdot \hat{\mathbf{n}}_3 \end{cases} \tag{5.63}$$

where $\hat{\mathbf{n}}$ is the director field, $\hat{\mathbf{n}}_2$ the eigenvector of the biaxial-splay tensor with positive eigenvalue and $\hat{\mathbf{n}}_3 = \hat{\mathbf{n}} \times \hat{\mathbf{n}}_2$.

### 5.3.4 3D compatibility equations: Cases of study

We end this section by applying the compatibility equations to some particular director field cases.

#### Uniform deformation

We start by studying the case of uniform deformation everywhere in the sample. In this case we consider as uniform deformations those where the magnitude of the deformation fields is constant. This implies that $T$, $S$, and $\Delta$ are constant.

Since the bend deformation is described by a vector perpendicular to $\hat{\mathbf{n}}$, we fix its modulus $b = \sqrt{b_2^2 + b_3^2}$. It is important to note that $\partial w/\partial x_i$ can still be different from zero, since we can allow the main biaxial-splay eigenvectors to rotate around $\hat{\mathbf{n}}$. The equations simplify to:

$$\begin{cases} Tb_2 - 2\Delta\dfrac{\partial\omega}{\partial x_2} = 0 \\ Tb_3 + 2\Delta\dfrac{\partial\omega}{\partial x_3} = 0 \\ b_2 b_3 + \dfrac{1}{2}TS + 2\Delta\dfrac{\partial\omega}{\partial x_1} + \dfrac{\partial b_3}{\partial x_2} + b_2\dfrac{\partial\omega}{\partial x_2} = 0 \\ b_2 b_3 - \dfrac{1}{2}TS + 2\Delta\dfrac{\partial\omega}{\partial x_1} + \dfrac{\partial b_2}{\partial x_3} - b_3\dfrac{\partial\omega}{\partial x_3} = 0 \\ b_2^2 + \left(\dfrac{1}{2}S + \Delta\right)^2 - \dfrac{1}{4}T^2 + \dfrac{\partial b_2}{\partial x_2} - b_3\dfrac{\partial\omega}{\partial x_2} = 0 \\ b_3^3 + \left(\dfrac{1}{2}S - \Delta\right)^2 - \dfrac{1}{4}T^2 + \dfrac{\partial b_3}{\partial x_3} + b_2\dfrac{\partial\omega}{\partial x_3} = 0 \end{cases} \tag{5.64}$$

Moreover, fixing the value of $b$ results in the following constraints for the derivatives of $b_2$ and $b_3$:

$$\begin{cases} b_2\dfrac{\partial b_2}{\partial x_2} + b_3\dfrac{\partial b_3}{\partial x_2} = 0 \\ b_2\dfrac{\partial b_2}{\partial x_3} + b_3\dfrac{\partial b_3}{\partial x_3} = 0 \end{cases} \tag{5.65}$$

We can start studying the case where we have only one deformation present. For the case of bend, degeneracy of the biaxial-splay eigenvectors in the perpendicular plane allows us to choose $b_3 = 0$ so that $b_2 = \pm b$. From the previous constraints this implies that, if $b_2 \neq 0$, $\partial b_2/\partial x_2 = \partial b_2/\partial x_3 = 0$. Then, for any single deformation we choose, the fifth equation becomes $b_2^2 = S^2 = T^2 = \Delta^2 = 0$ such that no pure uniform deformation state can exist in Euclidean space.

If we now focus on combinations of uniform deformations, we can see that for any combination of bend, double splay, and double twist, the biaxial-splay eigenvectors are degenerate so that we can take $b_3 = 0$, $b_2 = \pm b$ and $\partial b_2/\partial x_2 = \partial b_2/\partial x_3 = 0$. The fourth equation results in $S \cdot T = 0$ so double splay and double twist can not coexist simultaneously. From the first equation, $T \cdot b_2 = 0$, so that bend and double twist are incompatible. Since double twist is incompatible with both double splay and bend, we set $T = 0$. Equation five results in $b_2^2 + S^2/4 = 0$, which can only be fulfilled if $b_2 = S = 0$. Thus, no uniform distortion state without biaxial splay can exist.

Taking into account biaxial splay together with the other deformations complicates significantly the analysis of the equations. Nevertheless, it has been

shown that the only possible configuration with uniform distortions must fulfill the condition $T = 2\Delta$ [162]. Indeed, the case with $T = 2\Delta$, $b_2 = -b_3$ and $\partial\omega/\partial x_1 = 0$ corresponds to the relatively recently discovered twist-bend nematic phase [162, 165].

### Non-uniform double splay

If we now consider the case of having a non-uniform double splay deformation, the third and four compatibility equations are automatically satisfied and the remaining equations become:



$$\begin{cases} \dfrac{\partial S}{\partial x_3} = \dfrac{\partial S}{\partial x_2} = 0 \\ \dfrac{\partial S}{\partial x_1} = -\dfrac{1}{2}S^2 \end{cases} \tag{5.66}$$

Since in this case we do not have bend deformation, the director field streamlines are straight lines such that $x_1$ can be considered a coordinate in a straight line. In this case the second equation can be solved resulting in:

$$S = \frac{2}{x_1 - C} \tag{5.67}$$

with C an integration constant. We can choose the origin of the straight line such that $C = 0$ and the double splay becomes:

$$S = \frac{2}{r} \tag{5.68}$$

where $r = x_1 - C$. This expression has a singularity at $r = 0$ and the coordinate $r$ measures the distance from this singularity. We then have a point of the line with an infinite distortion. This indeed corresponds to a defect region where continuity can not be satisfied. To get a full director field configuration we need to fill space with streamlines that can not cross each other. Also, the streamlines can not be parallel to each other since in this case the director field would be constant, implying $S = 0$, and thus, incompatible with finite double splay.

If we now look at the first equation in 5.66 we can see that the double splay is constant when moving in a direction perpendicular to $\hat{\mathbf{n}}$. This in turn implies that two neighboring streamlines are at the same distance from the singularity. One easy way to fulfill this is to have all streamlines emanating from the same singularity corresponding to the origin. This corresponds to a radial hedgehog configuration with director field $\hat{\mathbf{n}} = \hat{\mathbf{r}}$. We can compute $S$ from this director field which results in the previously obtained expression $S = 2/r$.

### Non-uniform pure bend

We can now look at the case of having a pure non-uniform bend distortion. In this case, we can choose the bend direction to point in the $\hat{\mathbf{x}}_2$ direction such that $b_3 = 0$. The compatibility equations simplify to:

$$\begin{cases} b_2 \dfrac{\partial \omega}{\partial x_2} = b_2 \dfrac{\partial \omega}{\partial x_3} = 0 \\ \dfrac{\partial b_2}{\partial x_3} = 0 \\ b_2^2 + \dfrac{\partial b_2}{\partial x_2} = 0 \end{cases} \tag{5.69}$$



The first equation implies that, if the bend is not zero, the triad does not rotate when moving perpendicular to $\hat{\mathbf{n}}$. Since there is only bend, the director field is parallel when moving in the perpendicular direction which implies that $x_2$ and $x_3$ form straight lines. Additionally, solving last equation along $x_2$ results in:

$$b_2 = \frac{1}{x_2 - C} = \frac{1}{r} \tag{5.70}$$

where in the last equality we have chosen a coordinate origin such that $C = 0$ and $r$ measures the distance from the singularity point. As the simplest case, we can think of a plane distortion which occurs in the plane $\hat{\mathbf{n}} - \hat{\mathbf{x}}_2$. In this case, since the streamlines corresponding to $\hat{\mathbf{n}}_2$ are straight lines and $b_2$ presents a singularity, an analogous reasoning as for the double splay shows that these lines form a radial structure meeting at the singularity. This case corresponds to a circular director field $\hat{\mathbf{n}} = (-y\hat{\mathbf{x}} + x\hat{\mathbf{y}})/\sqrt{x^2 + y^2}$. We then see that this field has an integer disclination line at $x = y = 0$. Computing the magnitude associated to bend distortions for this director field, equation 5.70 is recovered.

### Escaped radial configuration

We finish by checking that our compatibility conditions are fulfilled for a more complex continuous director field called escaped radial configuration, which is typical for cylinders with homeotropic anchoring conditions, as we will see later in the thesis, in Section 7.3, and Figure 7.7. For a cylinder of radius 1, this field is given by:

$$\hat{\mathbf{n}} = \frac{1}{1 + x^2 + y^2}(2x\hat{\mathbf{x}} + 2y\hat{\mathbf{y}} + (1 - x^2 - y^2)\hat{\mathbf{z}}) \tag{5.71}$$

where $x, y, z$ are the Cartesian coordinates, with the $z$ direction pointing along the cylinder axis. This director field has no dependence on $z$. Using equation 5.63 we can compute the values of twist, splay and bend:

$$\begin{cases} T = 0 \\ S = \dfrac{4}{(1+x^2+y^2)^2} \\ \mathbf{B} = \dfrac{4}{(1+x^2+y^2)^3} \begin{pmatrix} x(1-x^2-y^2)\hat{\mathbf{x}} \\ y(1-x^2-y^2)\hat{\mathbf{y}} \\ -2(x^2+y^2)\hat{\mathbf{z}} \end{pmatrix} \end{cases} \tag{5.72}$$

To obtain the biaxial-splay eigenvectors, we first obtain the biaxial-splay deformation tensor in Cartesian coordinates:

$$\begin{cases} \Delta_{xx} = \dfrac{2[4x^2(x^2+y^2) - (1+x^2+y^2)^2(x^2-y^2)]}{(1+x^2+y^2)^4} \\ \Delta_{xy} = \Delta_{yx} = \dfrac{4xy[(x^2+y^2)^2+1]}{(1+x^2+y^2)^4} \\ \Delta_{yy} = \dfrac{2[4y^2(x^2+y^2) + (1+x^2+y^2)^2(x^2-y^2)]}{(1+x^2+y^2)^4} \\ \Delta_{xz} = \Delta_{zx} = \dfrac{-4x[(x^2+y^2)^2 - x^2 - y^2]}{(1+x^2+y^2)^4} \\ \Delta_{yz} = \Delta_{zy} = \dfrac{-4y[(x^2+y^2)^2 - x^2 - y^2]}{(1+x^2+y^2)^4} \\ \Delta_{zz} = -\Delta_{xx} - \Delta_{yy} = \dfrac{-8(x^2+y^2)^2}{(1+x^2+y^2)^4} \end{cases} \tag{5.73}$$

Although this tensor looks lengthy, its eigenvectors, $\hat{\mathbf{n}}_2$, and $\hat{\mathbf{n}}_3$, have simple expressions. $\hat{\mathbf{n}}_2$ points in the polar direction in the $x-y$ plane, and $\hat{\mathbf{n}}_3$ is perpendicular to both $\hat{\mathbf{n}}$ and $\hat{\mathbf{n}}_2$:

$$\begin{cases} \hat{\mathbf{n}}_2 = \dfrac{1}{\sqrt{x^2+y^2}}(-y\hat{\mathbf{x}} + x\hat{\mathbf{y}}) \\ \hat{\mathbf{n}}_3 = \dfrac{1}{(1+x^2+y^2)\sqrt{x^2+y^2}} \begin{pmatrix} x(x^2+y^2-1)\hat{\mathbf{x}} \\ y(x^2+y^2-1)\hat{\mathbf{y}} \\ 2(x^2+y^2)\hat{\mathbf{z}} \end{pmatrix} \end{cases} \tag{5.74}$$

The biaxial splay becomes:

$$\Delta = \frac{2(x^2+y^2)}{(x^2+y^2)^2 + 1 + x^2 + y^2} \tag{5.75}$$

With the eigenvectors $\hat{\mathbf{n}}_2$ and $\hat{\mathbf{n}}_3$, we can obtain the components of the bend vector in those directions:

$$\begin{cases} b_2 = 0 \\ b_3 = \dfrac{4\sqrt{x^2+y^2}}{(1+x^2+y^2)^2} \end{cases} \tag{5.76}$$

Using equation 5.63, we obtain the expressions for $\partial\omega/\partial x_i$:

$$\begin{cases} \dfrac{\partial \omega}{\partial x_1} = 0 \\ \dfrac{\partial \omega}{\partial x_2} = \dfrac{x^2+y^2-(x^2+y^2)^2}{(1+x^2+y^2)\sqrt{(x^2+y^2)^3}} \\ \dfrac{\partial \omega}{\partial x_3} = 0 \end{cases} \tag{5.77}$$

Finally, we calculate the directional derivatives of the scalar fields $S$, $\Delta$ and $b_3$ along $\hat{\mathbf{n}}$, $\hat{\mathbf{n}}_2$ and $\hat{\mathbf{n}}_3$:

$$\frac{\partial f}{\partial x_i} = \hat{\mathbf{n}}_i \cdot \nabla f \tag{5.78}$$

where $f$ represents the scalar field. Computing the terms that appear in the compatibility equations we get:

$$\begin{cases} \dfrac{\partial S}{\partial x_3} = -16\dfrac{(x^2+y^2)^2-x^2-y^2}{(1+x^2+y^2)^4\sqrt{x^2+y^2}} \\ \dfrac{\partial \Delta}{\partial x_3} = -4\sqrt{x^2+y^2}\dfrac{(1-x^2+y^2)^2}{(1+x^2+y^2)^4} \\ \Delta\dfrac{\partial \omega}{\partial x_2} = 2\sqrt{x^2+y^2}\dfrac{1-x^2+y^2}{(1+x^2+y^2)^3} \\ \dfrac{\partial S}{\partial x_2} = \dfrac{\partial \Delta}{\partial x_2} = \dfrac{\partial b_3}{\partial x_2} = 0 \\ b_3\dfrac{\partial \omega}{\partial x_2} = -4\dfrac{x^2+y^2-1}{(1+x^2+y^2)^3} \\ \dfrac{\partial b_3}{\partial x_3} = -4\dfrac{3(x^2+y^2)^2-4(x^2+y^2)+1}{(1+x^2+y^2)^4} \\ \dfrac{\partial S}{\partial x_1} = -32\dfrac{x^2+y^2}{(1+x^2+y^2)^4} \\ \dfrac{\partial \Delta}{\partial x_1} = -8\dfrac{(x^2+y^2)^2-x^2-y^2}{(1+x^2+y^2)^4} \end{cases} \tag{5.79}$$

We can confirm that the compatibility conditions hold everywhere by plugging these analytical expressions into equations 5.62 and checking that they are fulfilled everywhere. Using this more complicated director field allows us to further check the correctness of the derived equations.

## 5.4 Conclusions

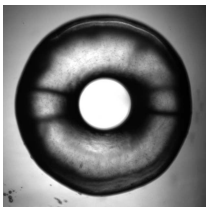


In this chapter we have derived the compatibility conditions of a nematic liquid crystal in 2D and 3D by imposing continuity of the director field when moving in two infinitesimal paths that finish at the same point. We also presented a brief analysis of some particular cases. Deriving the compatibility conditions in this way is possible thanks to the normal mode decomposition of the local deformation, which is presented at the beginning of the chapter. Compared to previous methods, our method highlights the origin of each equation and term in a simple and intuitive way.

Moreover, if instead of using two paths ending at the same point we use a closed loop, it is easy to see how the curvature of space enters the equation. This is specially shown for the 2D case where the curvature produces a net rotation of a vector when parallel transporting it around a closed loop, which is called holonomy. This results in a rotation of the director field when going around a loop that needs to be compensated by the director field distortion to ensure continuity. This argument can also be extended to 3D where the components of the Riemann curvature tensor take into account the plane of the loop, direction of the director and rotation direction.

For the 3D case, we have derived six compatibility equations by imposing continuity of the director field. Using this same method, we plan to derive the other three compatibility equations that result from the continuity conditions of the eigenvectors of the biaxial-splay deformation. These calculations are lengthier, since imposing the equality of $\hat{\mathbf{n}}_2$ when going to two paths ending at the same point results in two equations. Nevertheless, we only have one extra degree of freedom so these equations have to be manipulated with the previously derived 6 to obtain an independent equation with a form as simple as possible.

Chapter 6



# Magnetic field effects in planar nematic solid tori



One of the most interesting characteristics of liquid crystals is their interaction with external fields, which can reorient the director. In this chapter, we go back to toroidal nematic droplets and study the effects of an external magnetic field in the configuration of the planar nematic toroidal droplets studied in Chapter 4. The magnetic anisotropy of the liquid crystal used (5CB) is positive, and as a result, the director will tend to align with the external magnetic field. Interestingly, the texture observed both for defect-free and defect-populated tori can be understood in terms of stable alignment inversion walls. The experimental work presented in this chapter was conducted in the group of Arjun Yodh at the University of Pennsylvania (UPenn).

## 6.1 Experimental setup

Conceptually, the experimental setup consists of a system of two Helmholtz coils[1] that apply uniform magnetic fields up to 1T to samples located between them and a simple custom microscope setup to observe the samples that are loaded in the magnetic field region with custom sample holders. An image of

[1] A pair of Helmholtz coils is composed of two identical coils at the optimal separation to produce a practically constant field in the largest volume possible. This optimal distance corresponds to where the second and third derivatives of the magnetic field are zero midway between the coils.

the real experimental setup is shown in Figure 6.1a. The sample cuvettes are placed on sample holders and the magnetic field applied is perpendicular to the symmetry axis of the torus, tangential to the horizontal plane. A front view schematic of the system with the magnetic field direction is shown in Figure 6.1b. The inset shows the microscope view with the magnetic field direction. From now on, we will refer to different regions of the torus by the azimuthal angle $\Phi$, with $\Phi = 0$ corresponding to the line measured from the center of the to toroidal "hole" parallel to the magnetic field. We now describe each part of the system in more detail:

### Helmholtz coils



The Helmholtz coils system consists on a tabletop Alpha Magnetics electromagnet that creates uniform magnetic fields up to 1T[1] over the entire imaging area. Each Helmholtz coil has a truncated conical iron pole piece that concentrates the magnetic flux by 12 times to a $2.54cm$ region. Due to the high intensity needed to get such high magnetic fields, both Helmholtz coils are water cooled. The DC current for the Helmholtz coil is supplied by a unipolar high intensity power supply Kepco KLP 75-33-1200 (Voltage: 0-75V and Intensity: 0-33.3A), which is controlled remotely via a GPIB interface. The applied magnetic field is measured with calibrated Hall sensors through an oscilloscope, providing a feedback loop for setting the desired magnetic field. The sample is placed between the iron poles through a rail and a custom-made sample holder (Figure 6.1d left).

### Microscope system

The imaging system is composed of a 4-Wavelength High-Power LED Source from ThorLabs, which is used in the four wavelengths mode (470, 590, 617 and 660 nm) for broadband illumination. The light is directed towards the sample with a 45° mirror. The final image of the sample is collected through a 5x objective and a Kiralux 8.9Mp Monochrome CMOS camera from ThorLabs. The objective can be moved up and down to set the focal plane where desired. The optical components and modular pieces are assembled with a ThorLabs 30-mm cage system. To get polarized optical microscopy images, a fixed polarizer with its axis perpendicular to the B field is set after the 45° mirror and the analyzer is placed before the camera. The orientation of the analyzer can be set parallel, perpendicular or at 45° to the polarizer.

In this case, the illumination is basically parallel. This leads to poor imaging of our torus as explained in section 4.2.4. To improve imaging, a spherical lens

[1]For reference, the Earth's magnetic field at the surface ranges from 25 to 65$\mu T$.

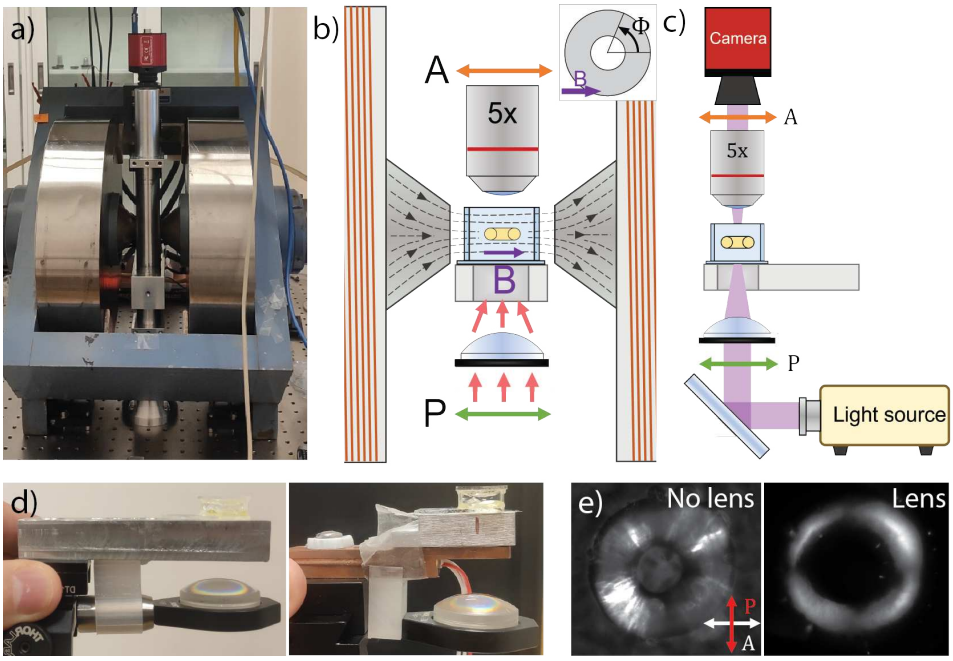



**Figure 6.1:** a) Image of experimental setup in the laboratory. b) Front view schematic of Helmholtz coils and optical system. Inset shows schematic of microscope view. $\Phi$ represents the azimuthal angle. c) Side view of microscope system. d) Sample holders. Left: Standard one. Right: Temperature controlled stage. e) Crossed polarizer images of tori on the magnetic setup. The left image was taken without the spherical lens while the right was taking with lens.

is placed below the sample at a distance similar to its focal length (25 mm) to act as a condenser. The lens is attached to the stage by a custom 3D-printed piece (Figure 6.1d). The addition of this lens improves imaging significantly, as shown in Figure 6.1e, where the addition of the lens results in a much smoother image with no distortions from material outside the focal plane. A schematic of the lateral view of the microscope system with the lens added is shown in Figure 6.1c.

### Temperature control

To heat and cool our samples while applying a magnetic field we use a custom sample holder made of copper that includes a heating element and a temperature probe (Figure 6.1d right). To guarantee the distance of the sample from the spherical lens an aluminum piece is added as a spacer. The stage acts as a Peltier stage and its temperature is controlled by the cryogenic temperature

controller 24C (Cryo·con). Due to its design we can only heat the element in a controlled way. Cooling is limited by room-temperature cooling. A custom 3D printed piece is also added to the stage to accommodate the spherical length at the appropriate distance.

## 6.2 Defect-free tori

### 6.2.1 Wall formation

We initially apply a magnetic field to defect-free tori with a double-twisted initial configuration. We increase the magnetic field in discrete steps of 0.01T, from 0 to 0.5T. The waiting time between steps is set to 10 seconds, which is enough to ensure that the torus achieves the equilibrium configuration at each magnetic field strength. This is tested by repeating the experiment increasing the waiting time and confirming there is no difference in the images taken.



We first observe the texture evolution under crossed polarizers. The initial zero-field configuration is consistent with the double-twisted one and consists on a dark cross formed by four dark brushes separated 90° from each other and separated by bright regions (see also Figure 4.6). As we increase the magnetic field not much change is observed until $B \approx 0.02$T. From this point on, the bright regions, initially at 90° from each other, start getting thinner and begin to move. The bright regions on the right/left side of the torus get closer to $\Phi = 0/180°$, respectively, as shown in Figure 6.2a. For $B > 0.3$T, both stripes become so close that they are optically indistinguishable. However, independently of the strength of the field there always are some bright features that never disappear, indicating that the torus is not able to fully align with the external magnetic field.

This texture is reminiscent of the one expected for splay-bend alignment inversion walls under crossed polarizers, when the polarizer is perpendicular to the magnetic field. In this case, far from the wall, the director field is parallel to the B field, and thus perpendicular to the incident light polarization. The polarization, thus, does not change and is blocked by the analyzer, resulting in a black texture. As we get closer to the wall, the orientation of the director starts changing leading to a bright strip up to when the director becomes parallel to the polarizer at the wall. At the wall center, the director is parallel to the polarizer, resulting in the presence of a dark stripe. As we move away from the wall in the other direction we recover the symmetric case. The characteristic texture consists on two bright stripes separated by a dark stripe at the wall, which is what we experimentally observe.

The observed phenomenology is also reproduced for parallel analyzer and polarizer. In this case, however, the pattern is inverted. The dark areas become

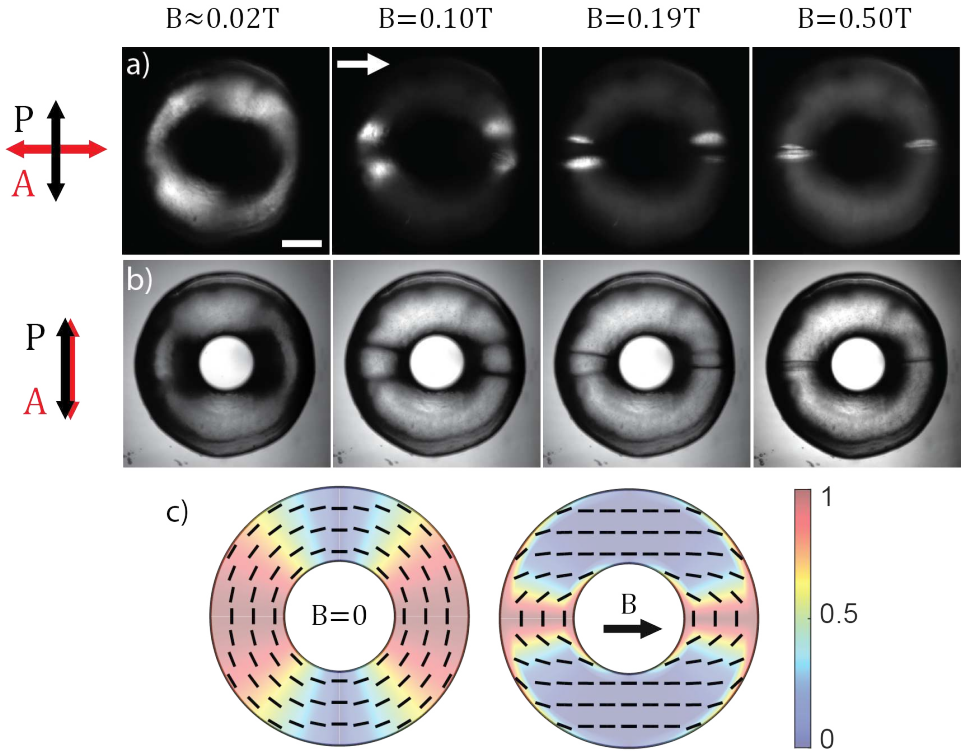



**Figure 6.2:** a) Experimental images of the crossed polarizer texture change with magnetic field in the white arrow direction. The polarizer is perpendicular to the magnetic field. The initial magnetic field is not zero due to the residual magnetic field of the iron cone pieces. Scale bar is $200\mu m$. b) Experimental images of the same torus with the polarizer and analyzer parallel to each other and perpendicular to the magnetic field. The intensity for B=0.5T images has been adjusted for visualization purposes. c) Schematics of the configuration in the 2D approximation for zero field (left) and with magnetic field (right) with the boundary conditions preserved. Color bar represents the director component in the vertical direction. Blue regions are aligned with the magnetic field (horizontal), while red ones are perpendicular (vertical).

bright and vice-versa. Nevertheless, the dark stripes become sharper, allowing a better visualization of how the stripes get thinner and closer as the magnetic field increases (Figure 6.2b).

To understand this texture change, we can start by neglecting double twist and assuming the initial configuration is axial (see figure 4.7a). In this case, the director field is concentric and tangential to the horizontal plane everywhere. We can further simplify the system by taking a two-dimensional approach and

assuming that what happens in the equatorial plane represents the change in the torus. Furthermore, we can assume that the director field is tangential to the horizontal plane at all times. This is a reasonable assumption for high fields since the director will be almost parallel to the magnetic field almost everywhere.

From this approach, if we start from the concentric configuration (Figure 6.2c left), we can see that the director field at $\Phi = 90°$ and $\Phi = 270°$ is already parallel to the magnetic field, as depicted in blue color. As the magnetic field is increased, the director field will want to align more and more with it and the blue regions will grow. Nevertheless, we can also see that as we go around the torus the director field rotates by $2\pi$, and thus, the director has a winding number of +1. This indicates that if we virtually extended the director field into the inner circle region, a +1 defect needs to appear. Topological constrains in 2D also tell us that the winding number needs to be preserved under continuous transformations.



As $B$ increases, the total $2\pi$ rotation of the director field starts getting concentrated into two alignment inversion walls, with the director field rotating $\pi$ at each of them. We then get two alignment inversion walls of the splay-bend type, located at $\Phi = 0$ and 180°, as shown in Figure 6.2c right. The width of the alignment inversion wall is given by the balance between the elastic torque, that grows as the wall gets thinner, and the magnetic torque, that grows with the magnetic field. This means that as the $B$ increases, the width of the wall gets smaller, as observed experimentally.

This simple model explains the experimental observations in terms of the appearance of two splay-bend alignment inversion walls when a magnetic field is applied to a defect-free torus. In the experiments, however, the director field lives in 3D space and can point in any direction. If we do not consider the boundary conditions it is easy to picture a way for the director field to become homogeneous: just escape in the vertical direction and then rotate altogether to become parallel to the magnetic field. Although this pathway is possible, it has a very high energetic barrier associated with it, since for high fields the energetic cost for the director field to become vertical and thus perpendicular to the magnetic field is very high.

As a result, the magnetic field presence forces the director field to become essentially 2D, except, perhaps, at the inversion walls, since deviations from the aligned configuration are highly energetically penalized. If, in contrast, we consider that the boundary conditions can not be broken, the director field needs to be tangential to the surface of the torus. In this case, a continuous transition to the homogeneous state might not be possible, making the appearance of inversion walls necessary.

### 6.2.2 Boundary conditions

Since the two scenarios above are plausible, provided the anchoring conditions can be broken, we now estimate the effect the magnetic field has on them.

First, as discussed in section 2.2.6.1, we can compute the transition layer thickness $\xi_m$ [27]. When assuming infinite anchoring strength, the transition layer thickness gives an order of magnitude of the distance from the surface where the director field starts aligning with the magnetic field. In other words, $\xi_m$ is the distance where the anchoring conditions stop having an effect for a given magnetic field. In our case, our tori have a radius of about $150\mu m$ and from the experimental images, a deviation from the zero field configuration is observed at field strengths $B \approx 0.05T$. For our system:

$$\xi_m = \frac{1}{B}\sqrt{\frac{\mu_0 K}{\chi_a}} \sim \frac{2.5\,[\mu m \cdot T]}{B} \tag{6.1}$$

where we have used the parameters for 5CB, $\chi_a \sim 10^{-6}$ [166], and $K \sim 5{\cdot}10^{-12}N$ [167], and $\mu_0 = 4\pi{\cdot}10^{-7}N/A^2$ is the vacuum permeability. For $B = 0.05$T, $\xi_m \sim 50\mu m$. This is comparable but smaller than the torus radius, indicating that a distance $\xi_m$ inside the torus, the director field starts aligning with B, as observed experimentally. This suggests that, most likely, the anchoring conditions are not broken significantly and have an effect on the configuration.

Secondly, if we assume a finite anchoring strength in the Rapini-Papoular approximation $W_a$, we can calculate a critical magnetic field $B_{crit}$ for the anchoring to be broken and the director at the surface to start deviating significantly from the tangential plane. This critical field is given by:

$$B_{crit} \sim W_a\sqrt{\frac{\mu_0}{K\chi_a}} \approx 5 \cdot 10^5 \left[\frac{T \cdot m}{N}\right] \cdot W_a \tag{6.2}$$

For reference, the typical anchoring strength values measured for PVA in solid substrates ranges between $10^{-5} - 10^{-4}N/m$ [168]. In that case, the critical magnetic field ranges between $5 - 50T$, which is at least an order of magnitude higher than the magnetic field that induces the largest change in texture ($0.1 - 0.3T$). Even if the anchoring strength was lower, but still of the reasonable order of magnitude of $10^{-6}N/m$ [169], the critical magnetic field would be $0.5T$ and the effect of the anchoring will still be important during the realignment of the director field. For this reason, we can safely assume that the anchoring conditions are not broken during the director field realignment in the presence of B.

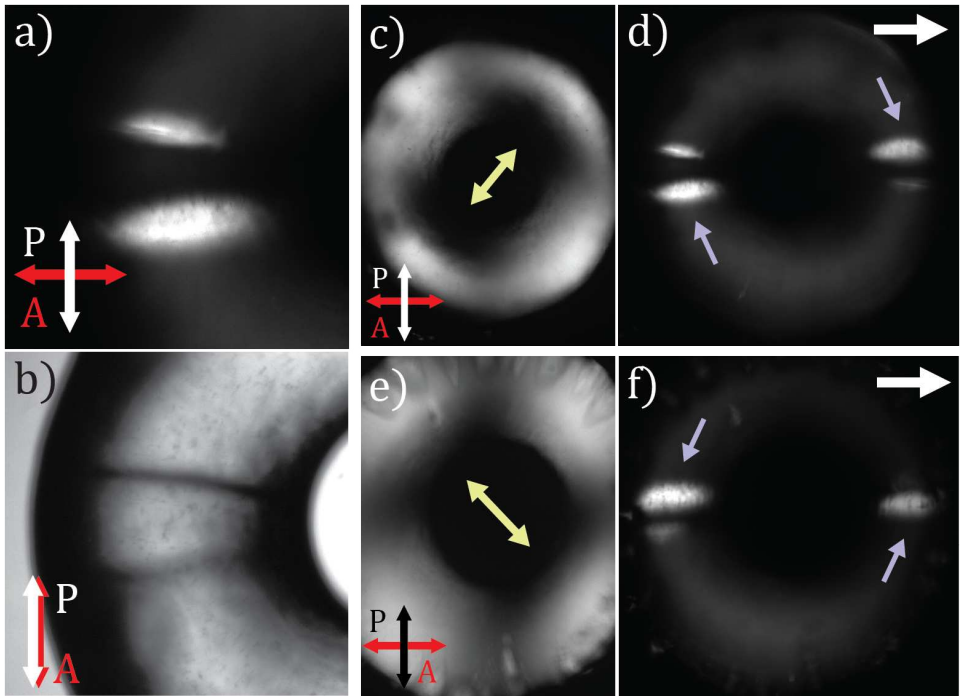



**Figure 6.3:** a)-b) Close up of wall texture between crossed polarizers and parallel polarizers. c) Microscope image for a torus with one chirality. Yellowish double arrows indicate the darker diagonal indicative of the chirality direction. d) Crossed polarizer images of the same torus in the presence of a magnetic field of 0.19T. Purple arrows indicate the location of the brightest bands. e) Microscope image for a torus with the opposite chirality of the one in c). f) Crossed polarizer images of the same torus in the presence of a magnetic field of 0.14T.

### 6.2.3 The role of the double twist

So far, our discussion has considered the simple case where the inversion walls are symmetric due to the up-down mirror symmetry of the assumed axial configuration. Taking a closer look into the bright bands under crossed polarizers, as well as to the dark bands under parallel polarizers, we see that the bands at each side are not symmetric. Under crossed polarizers, one of the bright bands is thicker than the other band (Figure 6.3a). Under parallel polarizers, one of the dark bands is sharper and thinner than the other band (Figure 6.3b). Moreover, if the thick band is the top/bottom one on the left side, the thick band on the right side is the bottom/top, respectively (Figure 6.3d,f). This is consistent with the azimuthal rotational symmetry of the initial configuration, based on which the bands on the right should match the ones of the left but rotated by

$\pi$.

This symmetry breaking of the texture, in fact, is indicative of chirality. Also recall that the chiral symmetry in the torus is broken from the beginning by the double-twisted configuration. This means that the symmetry breaking of the texture may come from the initial double twist, which was neglected in our simple explanation of the walls. To test this idea, we generate more nematic tori until we obtain some with opposite chirality[1]. The chirality of the configuration is checked by placing the torus between crossed polarizers and rotating the analyzer until the darkest regions appear. The rotation sense that gives the darkest regions for the smaller analyzer rotation angle determines the chirality of the torus. For thick tori, the chirality can also be seen under crossed polarizers by checking the two dark areas that appear near the inner ring in diagonal, as indicated by the orange double arrows in Figure 6.3c,e. Which diagonal they are in is indicative of the chirality.



If the double twist was the origin of the asymmetric texture, then, the initial chirality should determine the magnetic field texture chirality, and the thick and narrow band positions would only depend on the initial chirality. We can see from the experiments that all the tori with the same chirality produce the same texture asymmetry when the magnetic field is applied and that tori with the opposite chirality give the opposite texture asymmetry. This is shown for two tori of different chirality in Figure 6.3d,f, proving that the asymmetry from the texture comes from the initial double twist of the torus. The configuration of the inversion walls formed is then, indeed, asymmetric.

### 6.2.4 Wall thickness as a function of magnetic field

One of the characteristics of the alignment inversion walls described by Helfrich [48] is how their width, $w$, changes as a function of the magnetic field. Defining the wall width as the distance between the regions where the director forms an angle of $\pm 45°$ with the magnetic field, Helfrich showed $w \sim 1/B$ (see Section 2.3.3). In our experiments, in fact, we see that the inversion walls generated decrease in width as the magnetic field increases, since the bright/dark bands seen between crossed/parallel polarizers get closer with increasing magnetic field. To test whether the configuration observed is compatible with alignment inversion walls, we now study how the width varies with the magnetic field.

In the case of a splay-bend wall, when looking at the wall between crossed polarizers with the polarizers either parallel or perpendicular to the magnetic field direction, the brightest regions should be the ones where the director forms

[1] Although we could think that the chances of getting one chirality or the other are the same, it turns out that the generation system is biased and gives mainly one type of chirality. The other chirality was obtained by changing the pulled capillary.

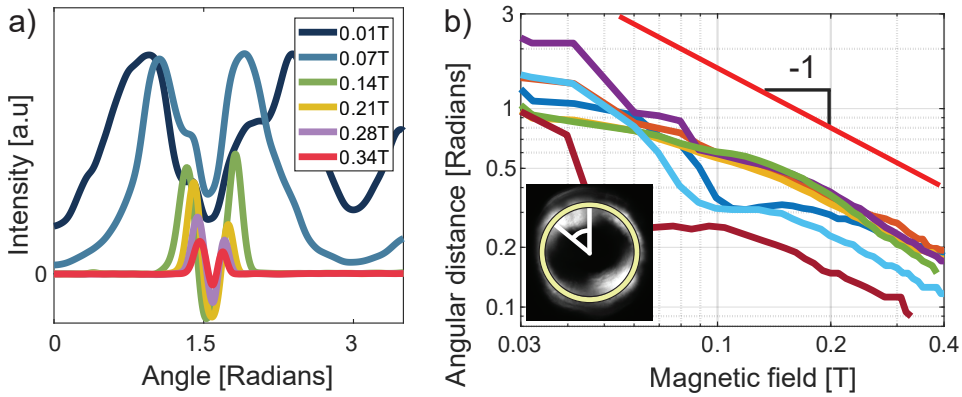



**Figure 6.4:** a) Processed line intensity profile for half of a torus and different magnetic fields. b) Log-log plot of angular width of the wall as a function of the magnetic field for 7 different experiments. All different tori have aspect ratio $\xi \approx 2$. The red segment serves as a guide to the eye for the theoretically predicted slope of -1. Inset corresponds to an example of the circle chosen for the line profile in a torus.

6

an angle of $\pm 45°$ with the polarizer[1]. This means that the wall width can be approximated by the distance between the intensity peaks associated to the band structure. Since the nematic liquid crystal is confined to a toroidal droplet, it is reasonable to inquire whether the relevant distance for the wall is the linear distance between the bands or if we must consider the angular distance.

The toroidal confinement of the liquid crystal also implies that the system is finite and thus, that talking about walls is reasonable when the wall width is small compared to the torus size $2R$. As the magnetic field increases the bands localize and start getting closer to each other. The separation of the bands when this happens is around $\pi/6$. For separation angles equal or smaller than this, we can approximate $\sin\alpha \approx \alpha$ so that both the angular and linear distances will give the same result. In our analysis we will use the angular distance.

To obtain the wall width as a function of the magnetic field, we analyze the experimental images by taking the intensity line profile around a circular contour on the torus, as shown in the inset of Figure 6.4b. We reduce the noise for each point of the contour by getting the intensity mean in an area around it of about 30x30 pixels. The background intensity, which is the intensity profile for the maximum magnetic field where the walls are barely visible, is subtracted to ease the peak analysis. This reduces the background, making the peaks more apparent. We finally smooth the curve with a Gaussian window to reduce

[1]This argument and all the other related to crossed-polarizer images in the rest of the section are also valid for the case of parallel polarizers.

**Table 6.1:** Slopes obtained from the analysis of wall width for different torus

| Sample | $\xi$ | Polarizer and analyzer | Slope |
|---|---|---|---|
| 4 | 2.1 | Crossed | $-0.72$ |
| 8 | 1.8 | Crossed | $-0.83$ |
| 8 | 1.8 | Parallel | $-0.95$ |
| 10 | 1.9 | Crossed | $-1.16$ |
| 11 | 2.0 | Crossed | $-1.37$ |
| 19 | 1.6 | Crossed | $-0.97$ |
| 21 | 1.5 | Crossed | $-0.88$ |



any further noise. The parameters of each step are chosen manually for each analyzed so that the intensity peaks are as clear as possible. We then take the wall structure with the clearer peaks, and plot the associated intensity profiles for different magnetic fields. This is shown in Figure 6.4a.

From this plot we see that the zero and low field profiles exhibit additional features relative to those expected for well defined walls, but that for magnetic fields larger than 0.1T, the profile is that expected with two clear peaks. As the magnetic field is increased the peak height is reduced and the peaks get closer. Also, we can clearly observe the asymmetry discussed in the previous section in the height difference between the peaks. It is interesting to note that the intensity goes negative in the regions between the peaks. This is because the subtracted intensity profile at high magnetic field has an intensity peak at the center. This can shift the actual peak position when the peaks get close enough so they overlap with the high field peak region. Nevertheless, this starts happening for fields larger than 0.3T, and the effect is in any case small.

To get the angular width we find the peaks at each side of the minimum and compute their distance. This is done for seven different experiments in different tori. We then plot the angular distance $w$ as a function of the magnetic field as shown in Figure 6.4. We see that the observed $w - B$ dependence is consistent with the $1/B$ dependence expected for Helfrich walls, specially for $B > 0.15$T. Linear fits of the data in this region, indeed result in exponents between -0.7 and -1.4, with some of them close to -1 (see Table 6.1).

Our results are then consistent with the theoretical expectation value of -1 for inversion walls. The variability in the exponent could be due to the limited quality of the images in the simple microscope setup, where, for example, drops or other objects in the optical pathway can distort the position and intensity of bright spots and patterns. In addition, the boundary conditions for $\hat{\mathbf{n}}$ at the toroidal surface, as well as the nematic confinement could also affect the equilibrium width as a function of the magnetic field.

## 6.3 Tori with defect pairs

After studying the effects of a magnetic field in planar nematic tori without defects, we heat and cool our samples to obtain configurations with defect pairs, and study the effect that magnetic fields have on them.

### 6.3.1 Interpreting defect pairs as splay-bend walls

Before discussing the experimental results, it is interesting to note that defect pairs can be understood as thick splay-bend walls. This becomes apparent when, in the planar approximation described before, we move across the defect pair and measure how much the director rotates relative to the azimuthal direction. We can easily see that $\hat{\mathbf{n}}$ rotates by $\pi$. When the defects are in the canonical position, the rotation sense is opposite to that of the azimuthal unit vector (see Figure 6.5a). The comparison with a splay-bend wall is even clearer when we observe the equatorial plane and use the rectangular coordinates used for deriving the ansatz in section 4.4.2.1, with the horizontal coordinate representing the azimuthal angle. As shown in Figure 4.15b, the director field corresponds to a splay-bend wall with the magnetic field perpendicular to the wall.

When looking at the configuration in the equatorial plane with the defects in the canonical position, the total angle the director rotates when crossing the defect pair structure is smaller than $\pi$ as shown in Figure 6.5a. In the figure, the angle $\alpha$ associated to this rotation corresponds to the angle that the director rotates when moving between the indicated white lines. The two white lines mark the region where the director field starts deviating from the axial configuration so that $\alpha$ measures the total angle the director rotates as the wall is crossed. It is clear from the figure that this angle for the canonical defect pair is indeed smaller than $\pi$.

For the case that the defect pair is in the inverse configuration (negative/-positive defect located in the inner/outer ring), the director rotation as we cross the wall corresponds to the conjugate of the angle rotation in the canonical case, $2\pi - \alpha$, and is thus larger than $\pi$ (Figure 6.5b). The fact that the director field has to rotate less in the canonical configuration implies that the deformation in this configuration for the same wall thickness is smaller, and thus that its bulk energy is lower than that for the defect pair in the inverse configuration. This would explain why, for tori, the canonical configuration is the one mainly observed in experiments, since this positioning of the defects minimizes the bulk energy. The intermediate configurations with the defect pair out of the equatorial plane would have an intermediate energy, since, for example, when both defects are on the top and bottom of the circular cross-section, the director rotates out of the plane an angle $\pi$ (Figure 6.5c).

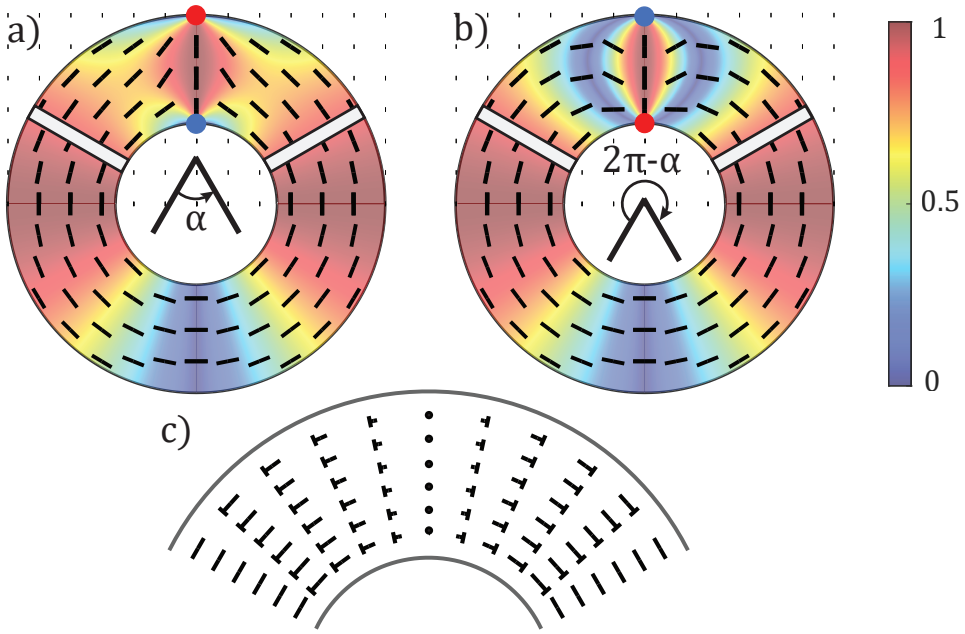



**Figure 6.5:** a) Schematic of the configuration in the equatorial plane of a canonical defect pair in the planar approximation. The two white lines indicates the region where the director field configuration deviates from the axial one. The angle in the middle is the overall angle the director field rotates as we go from the left white line to the right one. b) Same as a) for the inverse defect pair. The color bar indicates the projection of the director in the vertical direction. c) Schematic of the case with the defects at the top bottom. The director field escapes in the perpendicular direction at the wall.

Alternatively, this also can be understood by using the fact that for the canonical defect pair, as we cross the wall, the director rotates in the opposite sense it would naturally bend in the axial configuration due to the bending of a beam. Since the $\pi$ rotation at the wall is with respect to the azimuthal direction, the overall rotation angle is obtained by adding the wall rotation to the azimuthal rotation. In this case, as they rotate in opposite senses, there is a compensation leading to a smaller overall rotation angle. For the inverse defect pair case, both rotations do not compensate each other but are instead added to each other, leading to a larger overall rotation angle.

Finally, if we have canonical defect pairs in our tori, the $\pi$ rotation with respect to the azimuthal direction in the opposite direction means that each defect pair reduces the total winding number by 1/2. A torus with one defect pair, then, can be considered as having a winding number 1/2 after azimuthally

going around the torus. A torus with two defect pairs, would then have a winding number of 0, which is the same as that of the uniform aligned configuration.

### 6.3.2 Defect pairs close to wall generating regions

When an external magnetic field is applied to a torus with a single canonical defect pair, the resulting texture depends on the initial location of the defect pair. The first and most simple case is when the defect pair is close to wall generating regions, that is, regions where walls would form in the defect free case. These regions are located at $\Phi = 0$ and $\pi$.

Tori with one defect pair are obtained by heating and cooling the tori until we get a configuration with only one defect pair. The defect pair presence is verified between crossed polarizers in a standard microscope by rotating the sample 45° and observing the texture change, as shown in Figure 6.6a. The texture under crossed polarizers consist on a thin dark brush when the polarizer is parallel or perpendicular to the defect pair orientation and a bright area surrounded by two dark brushes going from one defect ot the other when the polarizer forms an angle of $\approx 45°$ with the defect pair. We then place the cuvette containing the torus in the magnetic field setup, such that the defect pair is located close to the wall generating regions in the defect free case, and observe texture change between crossed polarizers. When the magnetic field is increased, the region with the defect pair (left side in Figure 6.6b) gets completely dark, indicating that the director field is able to align with the external field. The other wall generating region (right side in Figure 6.6b) generates a wall, similar to those present in the defect free case. This is further confirmed for tori with two defect pairs, one at each wall generating region. In this case, as we increase the magnetic field, the torus becomes completely dark under crossed polarizers (Figure 6.6c), indicating that it has been able to completely align with the external magnetic field without generating any wall[1]. It is important to note that after the magnetic field is removed, the number of defect pairs is preserved. The magnetic field we apply does not annihilate the already present defect pairs.

The different behavior observed in the presence of defect pairs, also manifests when plotting the line intensity as we go around half of the torus through the region containing the defect pair. While for the half of the torus without the defect pair there are always intensity peaks at any magnetic field (Figure 6.6d top), for the half of the torus with the defect pair the intensity profile converges to a background intensity (Figure 6.6d bottom). This background intensity is attained at a magnetic field of around 0.1T, indicating that for larger fields the director configuration does not change significantly and is aligned with the

[1]The winding number is 0 in this case, homotopic to the aligned configuration. This is why the director can align without forming walls.

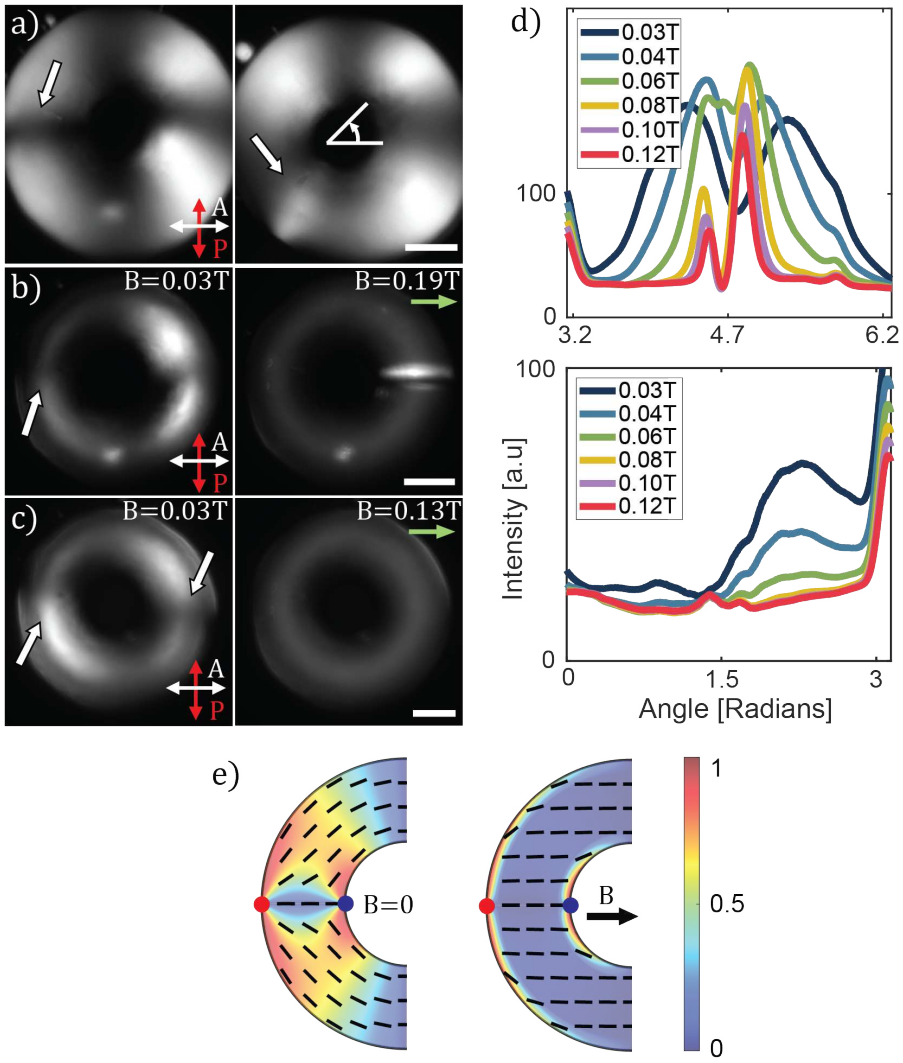



**Figure 6.6:** a) Crossed polarizer microscope images. Right image corresponds to the sample rotated $\sim 45°$. White arrow points to the defect pair. b) Effect of an external magnetic field on the texture of the torus in a). Green arrow indicates direction of magnetic field. c) Effect of an external magnetic field on a torus with two defect pairs located in wall generating regions. Scale bar is $200\mu m$. d) Line intensity profile for the torus in b) as a function of the magnetic field. The top/bottom plot corresponds to the right/left side of the torus respectively. e) Schematic of defect pair configuration in zero field (left) and high magnetic field (right). Color bar indicates the vertical projection of the director.

magnetic field.

We can easily explain this by looking at the zero field configuration of a defect pair in the planar approximation, as shown in Figure 6.6e left. As we move from the top to the bottom through the defect pair the total rotation of the director is 0. This is because the natural $\pi$ rotation of the axial configuration is compensated by the $-\pi$ rotation associated to the structure of the defect pair with relative to the azimuthal direction. This means that the conditions for a wall in the presence of the magnetic field are not met and we can imagine a continuous transformation towards the uniform configuration as shown in Figure 6.6e right. In this case, the boundary conditions have been preserved by adding a boundary layer interpolating between the uniform and the defect pair configuration (see Appendix G for more details).



Another way of interpreting the continuous transformation to the uniform state is by thinking in terms of walls such that the splay-bend wall that would appear in the defect-free configuration annihilates with a splay-bend wall of opposite rotation associated to the defect pair. Indeed, if we imagine two splay-bend walls of opposite rotation signs, the total rotation as we go through them is 0, and as a result, they are able to can annihilate. In contrast, two splay-bend walls with the same rotation sense would not be able to annihilate[1].

### 6.3.3 Defect pairs far from wall generating regions

If the defect pair is initially located far enough from the wall generating regions in defect-free tori, for example at $\Phi \sim 90°$ or $270°$, the director field reorganization in the presence of a magnetic field is different from the previous case.

When observed under crossed polarizers, we find that as the magnetic field is increased, one wall additional to those observed in the defect-free case appear; this is located in the region where the defect pair is located (see Figure 6.7a). This wall is also characterized by two thin bright bands separated by a dark band. As we increase the magnetic field the bands get thinner and closer to each other.

This texture change of the defect pair is consistent with our interpretation of the pair as an inversion wall. In this case, the magnetic field concentrates the $\pi$ rotation of the director close to the defect pair, while the other $2\pi$ rotation of the axial configuration is concentrated in the same two regions as in the defect free case. Since alignment inversion walls are localized distortions of the director field, once they are formed and they become localized enough, at high enough magnetic fields, the director field between the walls is aligned with $B$ and the

[1] This is true for a 2D director field. If the director is able to point in any direction in 3D, two splay-bend walls with the same rotation sense can be continuously transformed into the homogeneous configuration.

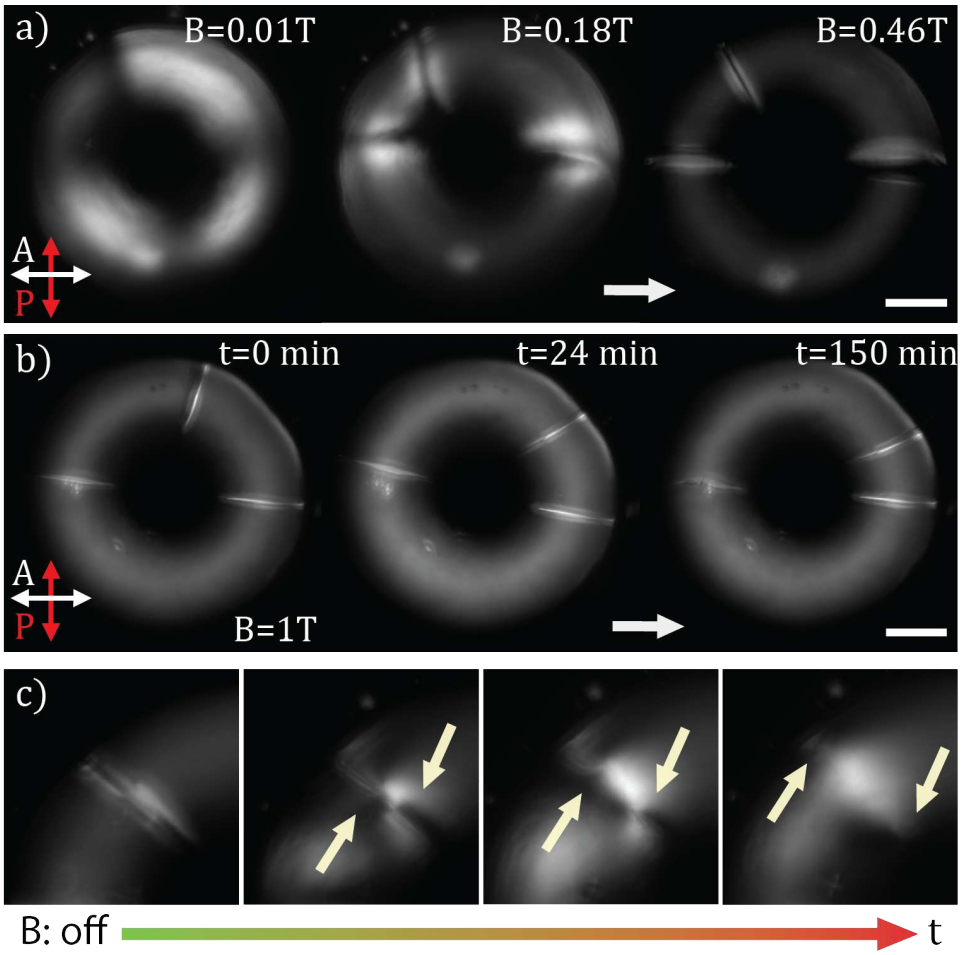



**Figure 6.7:** a) Wall generation as the magnetic field is increased in crossed polarizers. b) movement of defect pair wall at a constant magnetic field of 1T. White arrow indicates the direction of magnetic field. Scale bar is 200$\mu m$. c) Texture evolution of defect pair wall under crossed polarizers when the magnetic field is turned off. Arrows indicate point defects.

interaction between walls is negligible. If the defect pair is initially located far enough from the wall forming regions in defect-free tori, the walls are able to form independently.

The inversion wall originated from the defect pair presents some interesting characteristics when studied in more detail.

### Defect pair movement under constant magnetic field

In the presence of a constant $B = 1\text{T}$, we find that, in a time span of several hours, the wall generated in the defect pair region starts to move towards the closest wall at $\Phi = 0°$, as shown in Figure 6.7b. The motion of this wall implies the motion of the topological defects and the reorganization of the director field. This means that the energy of the system is reduced as the wall moves. At some point, when the two walls have become close enough, the motion stalls. After that point, even if we wait for 12 hours or more, no significant change in texture nor wall annihilation occurs, and the system seems to be in equilibrium.

Naively, one could think that since the defect free wall is a splay-bend wall with the opposite sense of rotation compared to the defect pair splay-bend wall, they would annihilate leading to a homogeneous texture with the defect pair located at $\Phi = 0°$. This would lead to the dark texture observed when the defect pair is initially located in that region. Interestingly, this is not what happens. As a result there must be some energy barrier preventing wall annihilation, indicating the wall configuration might be more complex than initially anticipated.



### Point defects reorganization

If we switch the magnetic field off after the wall associated to the defect pair has formed, but is far from $\Phi = 0°$ or $\Phi = 180°$, and observe its relaxation, we find that the point defects rearrange themselves. Right after setting $B = 0\text{T}$, we observe two point features that move towards the inner and outer rings of the torus to result in the usual canonical defect pair texture. It thus seems reasonable to think that the point features correspond to the point defects of the defect pair. This process is shown in Figure 6.7c, where the arrows point to the point defects.

If we assume that point defects stay at the surface the whole time, the defects would have moved to the top/bottom position of the circular cross-section of the torus for $B = 0\text{T}$. This in turn could imply a change in the wall configuration. In this case, the director field in the defect pair cross-section points in the vertical direction and the wall becomes different from the simple splay-bend wall.

The wall associated to the defect pair then, seems to have different equilibrium configurations depending on whether the magnetic field is applied or not. This change in equilibrium configuration is different from the wall thinning of usual walls with increasing $B$, possibly indicating a change in the nature of the wall allowed by the mobility of the point defects at the toroidal surface.

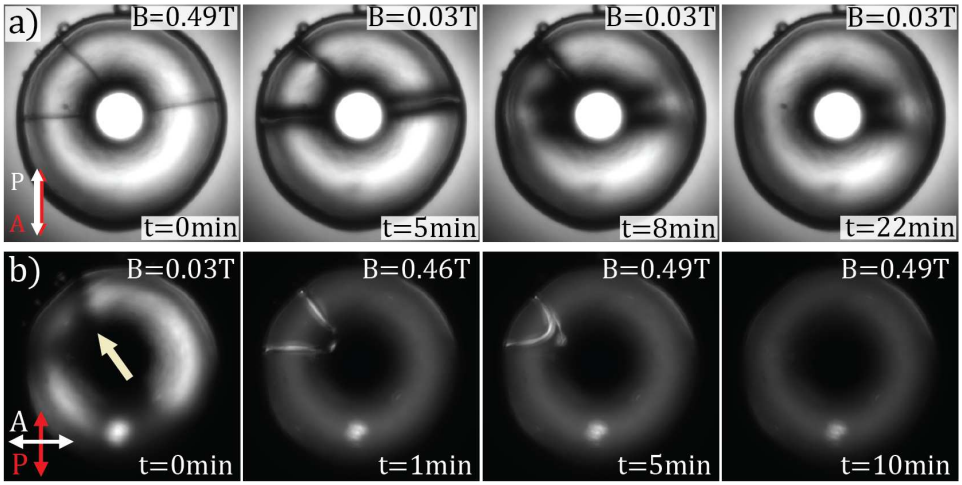



**Figure 6.8:** a) Time sequence images between parallel polarizers of wall annihilation when the magnetic field is turned off. Wall annihilation takes place in the left side of the torus leading to the aligned configuration. b) Time sequence images between crossed polarizers of wall annihilation when the magnetic field is turned on. Wall annihilation occurs in the left side. The right side becomes dark since there is another defect pair that led to the aligned configuration right away.



### Wall annihilation

Finally, if we turn off the high magnetic field when the defect pair is sufficiently close to $\Phi = 0°$ or $\Phi = 180°$, we find that both inversion walls annihilate (Figure 6.8a). This results in a fast relocation of the point defects towards the closest wall at $\Phi = 0°$ or 180°. The final configuration has the defect pair perfectly located in that region. We can understand this annihilation from the point of view of walls. When the magnetic field is turned off the walls start widening until they overlap start interacting elastically. The elastic force then induces wall annihilation, ultimately acting as a force on the point defects that positions them in their final location. This provides a strategy to move defect pairs to desired locations by the application and removal of a magnetic field for long enough time.

We can also observe wall annihilation as the magnetic field is applied if the defect pair and defect-free wall are not very far apart; see Figure 6.8b. In this case, the defect pair is close enough to $\Phi = 0°$ or 180° to completely align, but far enough for the process to take some time; the walls form and the annihilate.

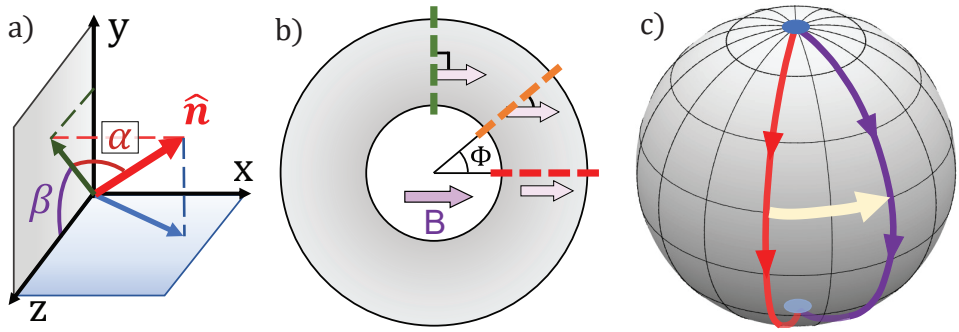



**Figure 6.9:** a) Schematic of coordinates and angles used for describing the director field of a wall. b) Schematic of the different wall positions and the angle it forms with the external magnetic field. c) Schematic of the order parameter space for the director. Lines indicate the path the director takes as the wall is crossed.



### 6.3.4 Inversion wall simulations

From the experimental observations of the previous section it seems like when the magnetic field is applied and the wall associated to the defect pair is far from the $\Phi = 0°$ or 180° region, it first reorganizes into a different configuration with the defects at the top and bottom, to then move towards the closest $\Phi = 0°$ or 180° wall, indicating the energy is lowered as the wall moves. To understand these observations, we perform some simple simulations of different types of walls. The results provide an intuitive explanation of the wall behavior and its stability against coalescence with the $\Phi = 0°$ or 180° splay-bend wall.

#### 6.3.4.1 Assumptions and simplifications

We consider infinite walls perpendicular to the x direction, parallel to the y-z plane. The director field only depends on the x coordinate, thus, only changes as we move perpendicular to the wall. In this way, we only need to define the director field in the x axis, taking a 1D approach, with computed quantities per unit area of the wall. The director is allowed to point everywhere in space and its orientation is given by two angles, the angle it forms with the y-z plane, $\alpha$, and the angle the projection of the director in the y-z plane makes with the z-axis, $\beta$. Both angles with the coordinate axis are shown schematically in Figure 6.9a. The director field is them expressed as:

$$\hat{\mathbf{n}}(x) = (\sin\alpha, \cos\alpha \sin\beta, \cos\alpha \cos\beta) \tag{6.3}$$

with $\alpha = \alpha(x)$ and $\beta = \beta(x)$. We also consider that the wall is confined to a finite length $L$, with extremes located at $x = 0$ and $x = L$, and that the

orientation of $\hat{\mathbf{n}}$ is fixed at both extremes and parallel to the external magnetic field. In vectorial form, this implies that $\hat{\mathbf{n}}(L) = -\hat{\mathbf{n}}(0)$ with the imposed $\pi$ rotation ensuring the director field describes an inversion wall.

Since in the experiments, the wall is parallel to the cross-section of the torus, the angle the magnetic field makes with the wall depends on its angular position $\Phi$, as shown in Figure 6.9b. Since the director wants to align with the external field, the director field of the wall produced by the external magnetic field is parallel to it far from the wall. In our simulations, the wall is set parallel to the y-z plane, so the defect pair wall located at $\Phi$ is simulated by imposing the director field at both ends to form an angle $\Phi$ with respect to the wall plane. This is enforced on the left end by setting the boundary condition: $\alpha(0) = \Phi$ and $\beta(0) = 0$. The other end is set to the opposite orientation.

Finally, to obtain the equilibrium configuration we will compute the energy as a sum of the Frank-Oseen elastic energy, assuming different elastic constants for splay, bend and twist, and the magnetic interaction energy. The saddle-splay constant $K_{24}$ in the Frank-Oseen energy can be neglected, since the boundary conditions are fixed and there are no defects in the nematic volume.



#### 6.3.4.2 Inversion wall types

Once a wall is formed and the boundary conditions are fixed by the external field, the $\pi$ rotation of the director as we cross the wall is topologically protected, and the wall can not disappear by continuous deformations. This implies that as long as the $\pi$ rotation is preserved, the director can take any continuous configuration in between. The configuration the wall prefers is then set by the free energy energy minimization, which in this case accounts for both the elastic and magnetic contributions.

In order to study the minimum energy configuration we first define the types of walls we can observe. Attending to the main type of elastic deformation of the director field and whether the external magnetic field is parallel or perpendicular to the wall, Helfrich studied three types of simple walls [48]. According to the relative orientation of the magnetic field with the wall, we can classify the walls into the following categories:

**Case I: Magnetic field parallel to the wall**

Since we assumed that the wall formed is parallel to the cross-section, this case corresponds to when the wall is positioned at $\Phi = 0°$ as shown in Figure 6.9b. In this case, Helfrich distinguishes between two types of walls.

The first type is the splay-bend wall. In this case the director lies in the plane formed by the magnetic field and the direction perpendicular to the wall. This wall is the one depicted in Figure 6.2c for describing the walls form at $\Phi = 0°$

and 180° in the absence of defect pairs.The name splay-bend is given since these are the two elastic distortions involved. In fact, if we look at the direction the director field tips as we move away from the boundary, we can see that the tipping direction is along the direction perpendicular to the wall, and thus the corresponding deformation is splay. At the center of the wall, nevertheless, the director points perpendicular to the wall, tipping in the direction parallel to the magnetic field as we move apart from the wall, implying a bend deformation. An example of this type of wall is shown in Figure 6.10a. To depict the wall, we plot the director field variation as the wall is crossed along the x direction. The projections of the director are plotted in the x-y and x-z plane for ease of visualization. The corresponding vector in our mathematical description is shown as red arrows to highlight the $\pi$ rotation. This wall is initialized in our simulation by fixing the angles at the end points to: $\alpha(0) = \beta(0) = \beta(L) = 0$ and $\alpha(L) = \pi$.



The second type is the twist wall (see Figure 6.10b). In this case, the director lies tangential to the wall plane and rotates as we cross the wall. Since the director field tips in a direction perpendicular to the x-axis as we move along that direction, the relevant distortion is pure single twist, hence the name of the wall. This wall is initialized in our simulation by fixing the angles at the end points to: $\alpha(0) = \beta(0) = \alpha(L) = 0$ and $\beta(L) = \pi$.

It is interesting to note that these two walls are topologically equivalent, this is, they can be transformed continuously into each other. This is easily visualized if we plot the director rotation as the wall is crossed in the order parameter space as shown in Figure 6.9c. The order parameter space is represented by a sphere with its antipodal points identified and is mathematically named the real projective space $\mathbb{RP}^2$. The director field evolution as the wall is crossed is represented by a line on this sphere that starts at the point corresponding to a boundary and ends up in the antipodal point. Any continuous deformation of the director field is then represented by a continuous deformation of the curve in the projective space with its end points fixed[1]. If the red curve in Figure 6.9c represents the splay-bend wall, we can continuously deform it by rotating around the ending points, as shown by the yellow line, ending up in a different configuration represented by the purple curve. If the rotation is of $\pi/2$, the splay-bend wall turns into a twist one, showing that a continuous transformation between the two is possible. Moreover, half a turn will lead to another splay-bend wall with the opposite rotation sense and three quarters of a turn to a twist wall with opposite rotation sense as the previously mentioned

[1]This explains why a wall with a $2\pi$ rotation is not topologically protected. Since in the projective space this corresponds to a loop that ends up in the same point as it started, this loop can shrink continuously to a point since you "can not lasso a ball". This implies that any two consecutive $\pi$ walls can annihilate.

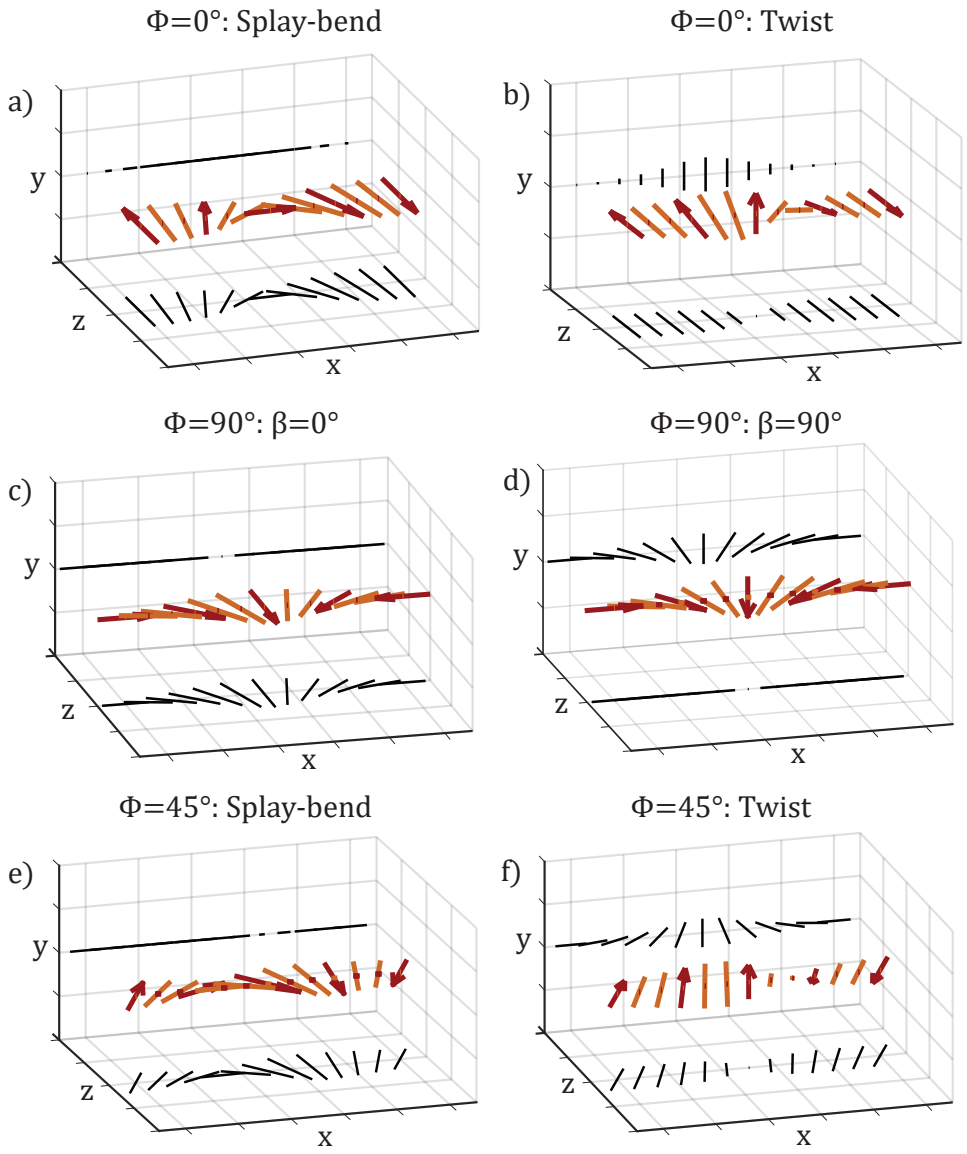



**Figure 6.10:** Schematics of the relaxed configurations obtained through our simulations for different types of walls. The external field is set to 0.15T in the simulations and the length of the wall to $100\mu m$. a) Splay-bend wall for $\Phi = 0°$. b) Twist wall for $\Phi = 0°$. c) Splay-bend wall for $\Phi = 90°$ and $\beta = 0°$. d) Splay-bend wall for $\Phi = 90°$ and $\beta = 90°$. e) Splay-bend wall for $\Phi = 45°$. f) Twist wall for $\Phi = 45°$.

one.

Although splay-bend and twist walls are topologically equivalent, our formalism distinguishes between both of them. Since we use the angles $\alpha$ and $\beta$ as defined in Figure 6.9a, the $\pi$ rotation can be obtained by fixing any of the two to $\pm\pi$ at $x = L$[1]. The angle chosen for the $\pi$ rotation determines the type of wall while its sign determines the sense of rotation. This separation between types of walls that can continuously be transformed into each other is a consequence of the fact that $\alpha = \pi$ fixes the orientation of $\hat{\mathbf{n}}$ regardless of the value of $\beta$.

**Case II: Magnetic field perpendicular to the wall**

This case corresponds to when the wall is located at $\Phi = 90°$. For this case, Helfrich defines only the splay-bend wall. This wall is similar to the splay-bend one described in the previous section except that the bend deformation is located at the edges while the splay deformation is concentrated at the wall center. This wall is depicted in Figure 6.10c and corresponds to the one associated with the defect pair structure. We initialize it in our simulation by fixing the angles at the end points to: $\alpha(0) = \pi/2$ and $\alpha(L) = 3\pi/2$. In this case, the angle $\beta$ at the ends is irrelevant, since the direction of $\hat{\mathbf{n}}$ is fixed by the value of $\alpha$ independently of the value of $\beta$.

If we repeat the same procedure as in the previous case of rotating the wall in the order parameter space, the result is just a rotation of the director field around the x-axis, which does not change the wall type or deformation, as shown in Figure 6.10d. This is because this rotation of the director field is equivalent to rotating the system around the x-axis and a rotation of the whole system does not change its energy or deformation, it just changes the plane the director field lies in. Indeed, this is also reflected in the freedom we have for choosing $\beta$ in the initialization. Additionally, including twist only increases the energy of the system as doing this does not relieve any other deformation. For this reason, twist walls are not defined when the magnetic field is perpendicular to the wall.

**Case III: Magnetic field forms a different angle with the wall**

So far, the three cases described by Helfrich only account for two particular positions of the wall. For a general wall position $\Phi$ we can extend the previous analysis. The angle the magnetic field forms with the wall, and thus, the angle the director field at the ends forms with the wall is $\Phi$, which has to be reflected

[1] This need to chose between the two angles can be removed by using the usual spherical coordinates around the director field direction, so the wall is completely determined by a $\pi$ change of the polar angle, while the azimuthal angle indicates the nature of the wall. Nevertheless, the formalism used allows producing walls with a certain type of deformation which we can then compare energetically.

in the boundary conditions for $\alpha$ and $\beta$.

We start by defining a splay-bend wall by imposing that the angle $\alpha$ is the one that rotates. This gives a wall with the director field tangent to the plane formed by the magnetic field and the x-direction as shown in Figure 6.10e. This wall does not need any twist deformation and hence we will call it splay-bend wall. We initialize it by fixing $\alpha(0) = \Phi$, $\beta(0) = \beta(L) = 0$ and $\alpha(L) = \Phi + \pi$. These conditions agree with the initializing condition for the previous splay-bend walls in the limiting cases $\Phi = 0$ and $\Phi = \pi/2$.

We then define a twist wall in the same way as we did for Case I above. In this case, we change the angle $\beta$ only, to find the director is not the same at both ends. To solve this issue we also need to impose a change in the $\alpha$ angle. This indicates that the deformation of this twist wall is not purely twist but necessarily has some splay-bend deformation. This type of wall is shown in Figure 6.10f. We can initialize it by fixing $\alpha(0) = \Phi$, $\beta(0) = 0$, $\alpha(L) = -\Phi$, and $\beta(L) = \pi$. In the limiting case when $\Phi = 0°$, this wall corresponds to the pure twist wall of Case I, while in the case $\Phi = 90°$ the twist is lost and we recover the splay-bend wall of Case II. This twist wall is a mixture of both walls and varies as the angle $\Phi$ changes.

As in Case I, both the splay-bend and twist walls are topologically equivalent, so a continuous transformation between them exists.

#### 6.3.4.3 Numerical simulations of walls

With the results of the previous section, we can initialize both types of walls for each position $\Phi$ by using a linear interpolation between the boundary conditions for both angles $\alpha$ and $\beta$:

$$\begin{cases} \alpha(x) = \alpha(0) + \dfrac{\alpha(L) - \alpha(0)}{L}\, x \\ \beta(x) = \beta(0) + \dfrac{\beta(L) - \beta(0)}{L}\, x \end{cases} \tag{6.4}$$

where the boundary conditions $\alpha(0)$, $\alpha(L)$, $\beta(0)$ and $\beta(L)$ for each type of wall are given in the previous section.

To obtain the equilibrium configuration of a wall at a given magnetic field we start with the initial non-equilibrium configuration and compute the molecular field [27, 43]. This molecular field can be interpreted as the torque acting on the director field at each point. Actually, this torque can be computed as minus the functional derivative of the free energy with respect the director field. From this approach, the molecular field at a point $x_i$ indicates the rate of change of the free energy density when the director at $x_i$ rotates. The minus sign is added so that the torque tends to reduce the energy of the system.

For our walls, we can compute the total energy as the sum of the elastic and magnetic energy. The elastic energy per unit area of wall is given by:

$$\begin{aligned}\frac{F_d}{A} &= \frac{1}{2}\int_0^L K_1(\nabla\cdot\hat{\mathbf{n}})^2 + K_2(\hat{\mathbf{n}}\cdot\nabla\times\hat{\mathbf{n}})^2 + K_3\left|\hat{\mathbf{n}}\times\nabla\times\hat{\mathbf{n}}\right|^2 dx \\ &= \frac{1}{2}\int_0^L K_1(\alpha')^2\cdot\cos^2\alpha + K_2(\beta')^2\cdot\cos^4\alpha + \\ &\quad + K_3\left[(\alpha')^2\cdot\sin^2\alpha + (\beta')^2\cdot\sin(\alpha)^2\cos^2\alpha\right] dx\end{aligned} \tag{6.5}$$

where $\hat{\mathbf{n}}(x)$ is given by 6.3 and the primes indicate derivatives with respect to $x$. The $K_i$ are the liquid crystal elastic constants. The magnetic field free energy in SI units depends on the position of the wall $\Phi$ and is given by [27, 43]:

$$\begin{gathered}\vec{\mathbf{B}} = (B\sin(\Phi), 0, B\cos(\Phi)) \\ \frac{F_m}{A} = -\frac{\chi_a}{2\mu_0}\int_0^L (\vec{\mathbf{B}}\cdot\hat{\mathbf{n}})^2 dx = -\frac{\chi_a B^2}{2\mu_0}\int_0^L \big[\sin^2\Phi\sin^2\alpha + \\ \cos^2\Phi\cos^2\alpha\cos^2\beta + \frac{1}{2}\sin 2\Phi\sin 2\alpha\cos\beta\big] dx\end{gathered} \tag{6.6}$$

where $\vec{\mathbf{B}}$ is the magnetic field with $B$ its magnitude, $\chi_a$ the magnetic anisotropy of the liquid crystal and $\mu_0$ the vacuum permeability. The total free energy, which is a functional of the angles describing the orientation of the liquid crystal $\alpha(x)$ and $\beta(x)$, is given by the sum of the two energies:

$$\frac{F_{tot}}{A} = \int_0^L \left[f_d(\alpha,\alpha',\beta,\beta') + f_m(\alpha,\beta)\right] dx \equiv \int_0^L \mathcal{L}(\alpha,\alpha',\beta,\beta')dx \tag{6.7}$$

The torques that act on each angle can be obtained as minus the first variation of $\mathcal{L}$ with respect to each function, as done to obtain the Euler-Lagrange equations. This first variation corresponds to the functional derivative with respect to the functions $\alpha(x)$ and $\beta(x)$. To obtain the torque with respect a function $g$ of a single variable we use the formula [44, 133]:

$$T_g = -\frac{\partial\mathcal{L}}{\partial g} + \frac{d}{dx}\left(\frac{\partial\mathcal{L}}{\partial g'}\right) \tag{6.8}$$

Using this equation, the torques acting on $\alpha$ and $\beta$ are:

$$
\begin{aligned}
T_\alpha = &-\frac{\chi_a B^2}{2\mu_0}\sin 2\alpha\cos^2\beta + \frac{1}{2}(K_3 - K_1)(\alpha')^2\sin 2\alpha + \\
&+ K_2(\beta')^2\cos^2\alpha\sin 2\alpha - \frac{1}{2}K_3(\beta')^2\sin 2\alpha\cos 2\alpha + \\
&+ K_1\alpha''\cos^2\alpha + K_3\alpha''\sin^2\alpha \\
T_\beta = &-\frac{\chi_a B^2}{2\mu_0}\sin 2\beta\cos^2\alpha + \beta''[K_2\cos^4\alpha + K_3\sin^2\alpha\cos^2\alpha] + \\
&+ \alpha'\beta'[K_3\sin 2\alpha\cos 2\alpha - 2K_2\cos^2\alpha\sin 2\alpha]
\end{aligned}
\tag{6.9}
$$

Once we have the torque expressions for both angles, we can let the system evolve in time assuming each point has negligible inertia and that there is a friction term slowing the rotation of the director, which acts as a dissipation term that stabilizes the system in the energy minimum:

$$
\begin{aligned}
\gamma_\alpha\frac{d\alpha}{dt} &= T_\alpha \\
\gamma_\beta\frac{d\beta}{dt} &= T_\beta
\end{aligned}
\tag{6.10}
$$

where $\gamma_i$ corresponds to the rotational viscosity for angle $i = \{\alpha, \beta\}$ and $t$ represents time. The system will evolve towards a local free energy minimum configuration where the torque at each point is zero. When this is reached, the configuration fulfills the Euler-Lagrange equations that minimizes the free energy functional, corresponding to the equilibrium configuration. The solution to this system of ordinary differential equations (ODE) for a given initial configuration should converge in time to the equilibrium configuration of minimum energy. We set the initial configuration for a certain wall type and location $\Phi$ according to 6.4 and then solve the differential equation until it converges to the equilibrium configuration for that wall and location. From this configuration we can compute the final free energy of the wall.

We numerically solve the system of ODEs by the finite differences method [170, 171]. We discretize our system both in space and time. In space we first re-scale the x axis using the mapping $u = x/L$ such that the ends of the wall are located at $u = 0$ and $u = 1$. The only effect of this change of variables on the differential equation 6.10 is the re-scaling of the elastic constants: $a_i = K_i/L^2$, with $a_i$ the effective elastic constants. We discretize the $u$ coordinate into $n$ points. To compute first and second spatial derivatives at point $u_i$ we use the central difference:

$$g'(u) \approx \frac{f(u_{i+1}) - f(u_{i-1})}{u_{i+1} - u_{i-1}}$$
$$g''(u) \approx \frac{f(u_{i+1}) + f(u_{i-1}) - 2f(u_i)}{(u_{i+1} - u_i)^2} \tag{6.11}$$

The subindex indicates the chosen point, ordered from one end to the other. At the edges, the derivative is computed as the forward or backward difference. To maintain the wall character, the director field at the wall is not allowed to change. With the spatial differences we can compute the torque at each point. We can also compute the energy associated to each deformation through equations 6.5 and 6.6 by approximating the integral to a sum of values computed at each discrete point. To update the value of the angles at each point except at the boundaries ($u = 0, 1$), we use a first order Taylor approximation leading to:



$$\alpha(t_{i+1}, u_i) = \alpha(t_i, u_i) + \left.\frac{d\alpha}{dt}\right|_{t_i,u_i} \Delta t = \alpha(t_i, u_i) + T_\alpha \cdot \frac{\Delta t}{\gamma_\beta} \tag{6.12}$$

where $\Delta t$ is the time step chosen. Since we also have the freedom to choose $\gamma_\alpha$ effectively changing the time step size, we set $\Delta t = 1$ so the time step is determined only by $\gamma_\alpha$.

For our simulations we use the material parameters of 5CB: $K_1 = 6.5pN$, $K_2 = 3.5pN$, $K_3 = 9.8pN$ [167], $\chi_a \approx 10^{-6}$ [166] and set the wall maximum width to $L = 100\mu m$. The other parameters are set as following: Number of spatial points = 61, $\gamma_\alpha = \gamma_\beta = 100$ and number of timesteps = 80000. With these parameters, we explore the effect of the location of the wall $\Phi$ and the external magnetic field $B$ on the energy of the equilibrium configuration.

To test that our program produces the right results, we simulate a twist wall at $\Phi = 0$ and obtain the equilibrium profile $\beta x$ as a function of B. For the case $B = 0.5T$, we obtain that the energy of the configuration is reduced every iteration until it converges to a value as shown in Fig 6.11a; This would correspond to the equilibrium configuration . Moreover, if we plot the energetic contribution from each distortion as the wall evolves (Figure 6.11b), the magnetic energy is reduced indicating that the director is getting more aligned with $B$, while the twist elastic energy increases due to the wall width reduction. The splay and bend energies are constant and equal to 0 since they do not appear in this type of wall and only increase distortion and thus the energy.

We can further validate our simulations by fitting the obtained profile $\beta(x)$ to the analytic solution for an infinite twist wall of width $\eta_m$ [48] using a least squares approach:

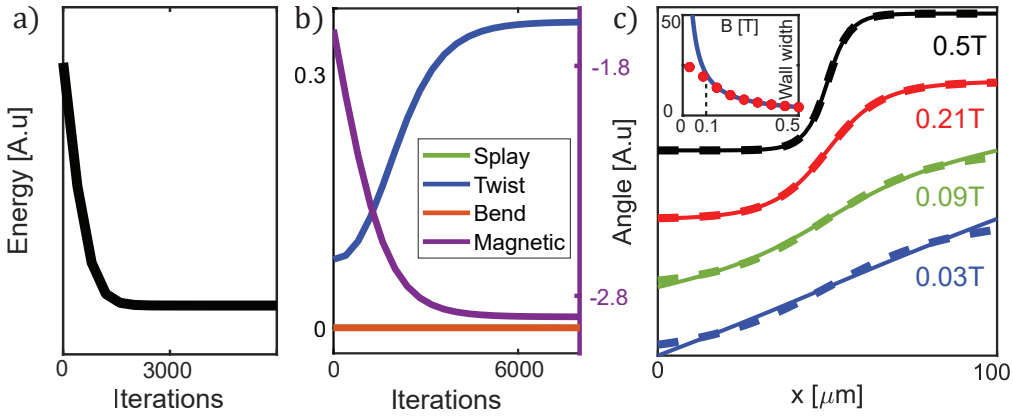



**Figure 6.11:** Simulation results for a twist wall at $\Phi = 0$ for different magnetic fields and $L = 100\mu m$. a) Energy evolution as a function of iterations for B=0.5T. b) Energy evolution for splay, bend, twist and magnetic energies for the previous simulation. c) Equilibrium configuration of the angle $\beta(x)$ for different magnetic fields. Solid lines are the simulation results while the dashed lines are the fit to the infinite wall expression 6.13. For each magnetic field the angle goes from 0 to $\pi$. The curves are shifted vertically for clarity. The inset shows the comparison between the fitted wall width (red circles) and the theoretical one for an infinite wall (blue solid line) as a function of the magnetic field.

$$\beta(x) = 2\arctan\left(e^{\frac{x}{\eta_m}}\right)$$
$$\eta_m = \frac{1}{B}\sqrt{\frac{K_2 \cdot \mu_0}{\chi_a}} \tag{6.13}$$

For high magnetic fields, when the wall width is much smaller than $L$ the fitting provides excellent agreement, as shown in Figure 6.11c, proving that our simulations give consistent results. This is also shown in the inset of Figure 6.11c where the wall width of the fitting at different magnetic fields (solid points) is plotted against the analytical expression in equation 6.13 (line). We can see that for magnetic fields $B > 0.1T$ the agreement is very good. Also, since the experimental results are obtained at magnetic fields higher than this threshold, fixing the length of the wall to $L$ does not affect the conclusions. For magnetic fields $B < 0.1$T, the simulated and analytical profiles start deviating. This is due to the fixed maximum length of the wall $L$ so the width at $B = 0$ is comparable to $L$ while theoretically it should be infinity.

#### 6.3.4.4 Motion and stability of the walls

With the simulated equilibrium configurations for both types of walls, splay-bend and twist, we can compare their energies for the same magnetic field when they are located at the same position $\Phi$. To see which is the one with the smallest energy, we compute the free energy difference $F_{sb} - F_{tw}$. If the energy difference is positive the twist wall has less energy and is more favorable, while if it is negative the favorable one is the splay-bend wall. The results show that this energy difference is always positive for every position $\Phi$ and magnetic field, as shown in Figure 6.12a. The difference gets to a maximum for $\Phi = 0$ while it is 0 for $\Phi = 90°$ and changes monotonically in between. The absolute energy difference also increases as $B$ increases.



In our simulations, in realty, the energy difference does not get exactly to 0 for $\Phi = 90°$ but becomes slightly negative. We attribute this to the fact that for the twist wall at this angle we impose that both angles $\alpha$ and $\beta$ change by $\pi$ between extremes, while only the angle $\alpha$ changes for the splay-bend wall. This, together with the spatial discretization of the wall, can result in a slightly larger free energy for the twist wall, resulting in a small negative energy difference $F_{sb} - F_{tw}$ at $\Phi = 90°$.

This result is expected since for 5CB the lowest elastic constant is the twist one, $K_2$, and thus, twist deformations cost less energy and will be preferred in front of splay and bend. The maximum energy difference is reached at $\Phi = 0$ where the twist wall has only twist deformation. When the location of the wall becomes $\Phi = 90°$, the twist wall converges into the splay-bend one and the energy difference between both types becomes zero.

This explains why the point defects move to the upward and downward position of the cross-section when the magnetic field is applied. The twist wall, which is energetically preferred, needs the director to point vertically at the center plane. This is achieved by moving the defects into the aforementioned position.

Now we can compute how the energy of the twist wall changes with the position of the wall. As shown in Figure 6.12b the energy decreases monotonically from $\Phi = 90°$ to $\Phi = 0°$ where it reaches the minimum. This can be intuitively understood by the fact that for $\Phi = 90°$ the twist wall becomes pure splay-bend and as it moves towards $\Phi = 0°$ the splay-bend deformation is reduced while the twist increases until the wall becomes pure twist reaching the minimum energy. The energy difference between the two extreme positions increases as the magnetic field is increased.

This explains why the defect pair wall moves towards $\Phi = 0$ at constant magnetic field. First, the wall is transformed into a twist wall and then moves towards $\Phi = 0$ reducing its total energy. As argued along this chapter, the canonical position of the point defects in the outer and inner ring reduces the

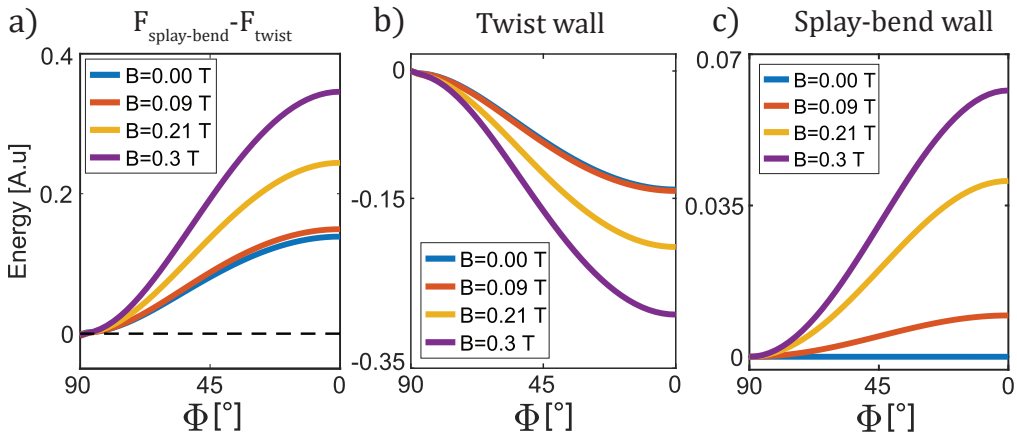



**Figure 6.12:** a) Energy difference between splay-bend and twist wall for different magnetic fields as a function of wall position $\Phi$. Dashed black line is the zero energy difference line. b) and c) Energy of twist and splay-bend wall respectively for different magnetic fields as a function of wall position $\Phi$.



total bulk energy so there should be some reluctance for them to move to the top/bottom position. This energy barrier can be overcome by increasing the magnetic field by two mechanisms. The first one is that the twist wall starts becoming more favorable with respect the splay-bend wall. Secondly, the wall width decreases and the effect of the curvature of the center beam, responsible for the canonical location of the defects, is reduced, since the $\pi$ rotation happens in a smaller region. This effectively reduces the energy barrier.

It is important to remark that this transition between walls is possible due to the motion of defect pairs that can align the director field at their cross-section along any direction tangential to it. The splay-bend walls generated in the defect-free case nevertheless do not have this defect freedom and the need to preserve anchoring conditions can play a relevant role in making the splay-bend wall more energetically favorable. Both the wall associated to the defect pair and the splay-bend wall do not annihilate since each of these walls have a different equilibrium configuration and can not annihilate without changing the twist wall into a splay-bend wall or vice versa. This provides a energetic barrier that effectively stabilizes the walls against coalescence. Once the magnetic field is turned off, the wall associated to the defect pair goes back to the splay-bend wall configuration and both walls widen, starting to interact elastically. This elastic interaction during the transition is able to move the defect pair into the wall generating regions.

Finally, it is also interesting to study the splay-bend wall energy. In this case, the energy actually increases monotonically as it moves from $\Phi = 90°$ to $\Phi = 0°$

for all magnetic fields, except at zero field, where the energy remains constant; see Figure 6.12c. The energy difference between both positions increases as the magnetic field increases. In this way, the splay-bend wall in the presence of a magnetic field would prefer to be located at $\Phi = 90°$[1]. This behavior can be simply understood by noticing that the main elastic deformation at the center of the wall is splay so that when located at $\Phi = 90°$, while it is bend at $\Phi = 90°$. For 5CB the splay elastic constant is smaller than the bend one ($K_1 < K_3$) so when the magnetic field is applied the elastic deformation is concentrated at the center of the wall, becoming the main elastic energetic cost and explaining the change in energy. This also implies that unless the nature of the wall is changed from splay-bend to twist, the wall would not want to move towards $\Phi = 0°$.



## 6.4 Heating and cooling under magnetic fields

In chapter 4, we find defect populated configurations in planar nematic tori when heated to the isotropic phase and cooled back to the nematic phase. So far, in this chapter, we have studied how defect-free or defect-populated with single defect pair configurations change with an external magnetic field. We now study the equilibrium configurations that appear when the magnetic field is applied during the isotropic-nematic transition. To this end, we use the temperature control stage to heat and cool in the presence of an external magnetic field our nematic tori.

### 6.4.1 Large magnetic fields

We first study the case when we apply a large magnetic field, $B = 1T$, during the phase transition. It is interesting to note that the crossed-polarizers texture of the transition looks different relative to the $B = 0$T case. We observe the nucleation and coalescence of domains, as in the zero field case, but while in this case we observe high birefringence of the domains, when the magnetic field is on, the domains look very dark and homogeneous. Increasing the brightness of the images allows seeing the domains and their homogeneous texture; see Figure 6.13a. The brightness of the images has been increased so domains are observed. An example of the real intensity in the final configuration can be seen in the inset of the rightmost image. The darkness and homogeneity of the domains

[1] To explain why the splay-bend walls in the defect-free case do not go towards $\Phi = 90°$ we can argue that the winding of the director as we go around the torus imposes the sense of rotation of the director. For a splay-bend wall at $\Phi = 90°$ the director rotates in the opposite sense, while it rotates in the same for a splay-bend wall located at $\Phi = 0°$. This implies that if the splay-bend wall was located at $\Phi = 90°$, there must be other deformations of the director field elsewhere in the torus to fulfill the winding number.

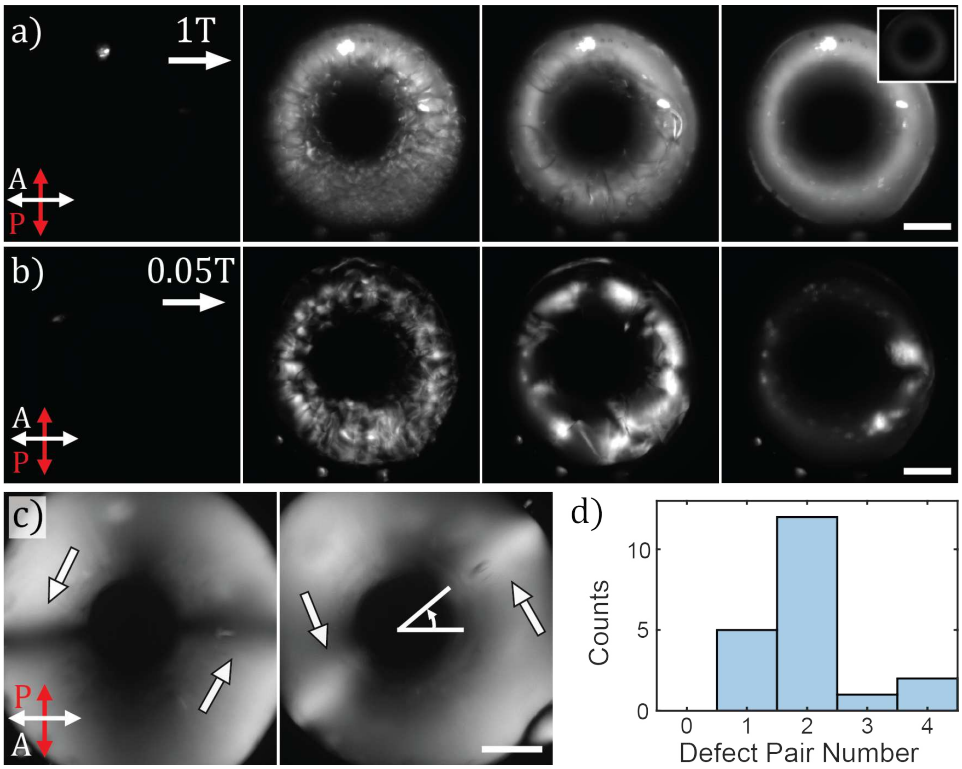



**Figure 6.13:** a) Crossed polarizer images of nucleation and relaxation of torus with a magnetic field of 1T as it cools (from left to right). Brightness of the images has been increased to be able to see the process. Inset shows an example of a non-treated image of a torus in the final configuration. b) Same as a) for a magnetic field of 0.05T. c) Microscope images of configuration with two defect pairs obtained consistently when cooling the torus in a 1T magnetic field. Scale bars are $200\mu m$. d) Histogram of the number of defect pairs in the equilibrium configuration when heating and cooling tori with a magnetic field of 0.05T.

suggest that they are pretty aligned with the magnetic field. The texture looks aligned during the whole process everywhere in the torus.

When the domains merge, we end up with a uniform dark configuration, indicating the director field is aligned. This texture resembles the one obtained when applying the external magnetic field to a torus with two defect pairs located at $\Phi = 0°$ and $\Phi = 180°$ (Figure 6.6c). When observing the texture in the microscope, it actually consists of two defect pairs located at at $\Phi = 0°$ and $\Phi = 180°$, as shown in Figure 6.13c.

While in the zero field case the number of defect structures generated was relatively random, in this case, the only configuration observed is the one with

two defect pairs. Applying a magnetic field during the cooling cycle allows somewhat selecting a certain configuration. We hypothesize that applying a suitable spatially varying magnetic field could result in other configurations with a controlled number and location of defect pairs.

### 6.4.2 Small magnetic fields

While heating and cooling our nematic tori in zero magnetic field results in structures with uncontrolled number of defect pairs, in the presence of high magnetic fields, we are able to select a specific configuration. For moderate magnetic fields we then expect an intermediate behavior between these two. To test this, we repeat the heating and cooling experiments with $B = 0.05$T, below the value where a significant distortion of the nematic configuration is produced by the magnetic field.



In this case, the nucleation process resembles the one in the defect free case, with textures showing birefringence and having a large contrast between dark and bright areas (see Figure 6.13b), as opposed to the situation in the presence of high magnetic fields. The texture evolves until the equilibrium configuration is reached. We heat and cool our tori in this magnetic field 20 times and observe that the number of defect pairs in the final configuration vary from experiment to experiment, although approximately around half the cases the configuration with two defect pairs located at at $\Phi = 0°$ and $\Phi = 180°$ is observed. This suggests that while the possibility of observing different defect-pair numbers is preserved, the magnetic field introduces a bias towards the two defect pair configuration, as shown in the histogram in Figure 6.13d.

## 6.5 Conclusions

Applying magnetic fields to planar nematic solid tori in the direction perpendicular to the symmetry axis results in a variety of stable alignment inversion walls. If the torus initially has the defect-free configuration, applying a magnetic field produces two splay-bend walls in opposite regions of the torus. If we start with a configuration with defect pairs, which can be interpreted as inversion walls themselves, the behavior depends on the initial position of the pair. If it is close to the wall generating regions in the defect-free case, the texture at that side of the torus becomes aligned with the magnetic field.If it is far from those regions, the splay-bend initial wall of the defect pair transforms into a twist wall and drifts towards the wall generating region in the defect-free case to reduce its energy by releasing splay-bend deformation at the expense of increasing the twist one. If a splay-bend wall is already located in the wall generating region in the defect-free case, the twist wall associated with the defect pair stalls and

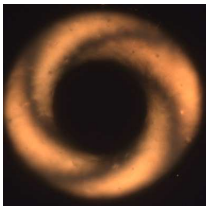
does not annihilate with the splay-bend one until the magnetic field is turned off.

This is confirmed by simulations that suggest that a twist wall reduces energy with respect to the splay-bend wall, additionally favoring location at the wall generating regions in the defect-free case. While the transformation into a twist wall might not be possible in general for our tori due to the boundary conditions, for the walls associated to defect pairs, the mobility of defects on the surface allows the reorientation of the director to form a twist wall. This is confirmed experimentally where the defects are observed to be on the top and bottom part of the cross-section when the field is on. When the field is removed, the defects move towards the inner/outer rings of the torus back to the canonical position.

From a different perspective, generating inversion walls in planar nematic tori is a simple and consistent process. The walls are generated in the presence of a magnetic field and are stable in time. This is different from prior work on inversion walls [172, 173, 174, 175, 176, 177, 178] which were reported for systems confined in one dimension between parallel plates, small spherical caps, or thin shells. In our case, the wall is confined to the cross-section of the torus, which is of the order of hundreds of microns in radius; this is an order of magnitude larger than the typical distance in flat nematic cells. In prior studied, inversion walls were found as either unstable configurations that disappear with time, metastable states generated by some combination of steps involving nematohydrodynamic instabilities, or walls separating different domains appearing after a Fréedericksz transition and that are more complex than simple Helfrich walls.

Finally, this work shows that we can control the position of defect pairs with constant magnetic fields and generate configurations with two defect pairs by heating and cooling the nematic tori in an external magnetic field. Both these effects observed experimentally indicate that by using a suitable spatially varying magnetic field during the heating and cooling cycle we can obtain final equilibrium configurations with controlled number and location of defect pairs. Additionally, external fields can be used to move defect pairs around the torus.

Chapter 7



# Homeotropic nematic solid tori



In chapters 4 and 6, we have studied nematic toroidal droplets with planar anchoring conditions. In this chapter, we turn our attention to the case of homeotropic (perpendicular) boundary conditions for the director field at the confining boundaries. We study the configuration of homeotropic tori as a function of the aspect ratio, and the surfactant concentration we use to control the anchoring strength. The effect of ethanol in the outer yield stress medium is also addressed. For high surfactant concentrations, the previously reported twisted escaped radial (TER) is observed. In this case, two different TER textures are observed and rationalized as an effect of the anchoring strength. For intermediate surfactant concentrations, configurations with stable disclination line loops appear. These disclination lines seem to be located either on the surface of the toroidal droplets or close to the surface. We characterize them topologically. Finally, for small surfactant concentration, the planar configuration is recovered.

## 7.1 Previous work in the group

Previous work in the group considered homeotropic tori and addressed the role of surfactant concentration and aspect ratio on the nematic organization. The outer yield stress material composition used in these experiments consisted of 30 wt% ethanol, 1.5 wt% polyacrylamide gels (Carbopol ETD 2020, Lubrizol),

3 wt% glycerol and ultra-pure water (MilliQ). Sodium dodecylsulfate (SDS) was the surfactant; it was used at different concentrations. The presence of ethanol implies that the generated tori can only be stored for one or two days before the nematic spontaneously transitions to the isotropic phase. Hence the textures described in prior work correspond to the short-time relaxed ones. Long time relaxation was not studied. The anchoring strength was controlled by changing the concentration of SDS from 2mM up to 10 mM[1].

The nematic textures were summarized in a surfactant concentration aspect ratio diagram, as shown in Figure 7.1a. Various textures, as indicated by different markers, were observed in segregated regions of the diagram. We can classify them as follows:

### Defect-free homeotropic configurations



For an SDS concentration of 10 mM, two different defect-free configurations were seen. For low aspect ratios and under crossed polarizers, the texture shows four black lines forming a spiral pattern (see Figure 7.1b). For this reason, from now on we refer to this texture as the "spiral" configuration. For larger aspect ratios, the texture observed is similar to the usual escaped radial configuration [61, 153, 180, 181, 182], with features concentrated in the center of the tube (see Figure 7.1c). From now on we refer to this texture as the "concentrated" configuration.

Studying the intensity profile in the radial direction shows that for both configurations, spiral and concentrated, the intensity peaks show an asymmetry and the intensity ratio between the peak intensity average and the local minimum in between, is smaller than 4, which corresponds to the value observed for the pure escaped configuration of 5CB confined in a capillary with homeotropic anchoring conditions [61]. An intensity ratio smaller than 4 is also in agreement with a twisted escaped radial configuration as seen in capillaries filled with a lyotropic chromonic liquid crystal [61]. This suggests that the toroidal confinement induces a twist in the escaped radial configuration [15, 16]. Experimentally, both configurations, spiral and concentrated, are consistent with the TER configuration. This was further confirmed by studying the intensity profile in a bent homeotropic capillary filled with 5CB. In this case, twist was not observed when the capillary is straight, but as soon as it is bent the twist appeared.

To explain the difference between the spiral configuration obtained for low aspect ratios and the concentrated one seen at high aspect ratios, it was assumed that there was a critical aspect ratio where the equilibrium configuration changes. While the concentrated configuration is consistent with the usual es-

[1]The critical micellar concentration (CMC) for this surfactant is $\sim 8mM$ [179]. As a result, we do not expect much difference at higher concentrations.

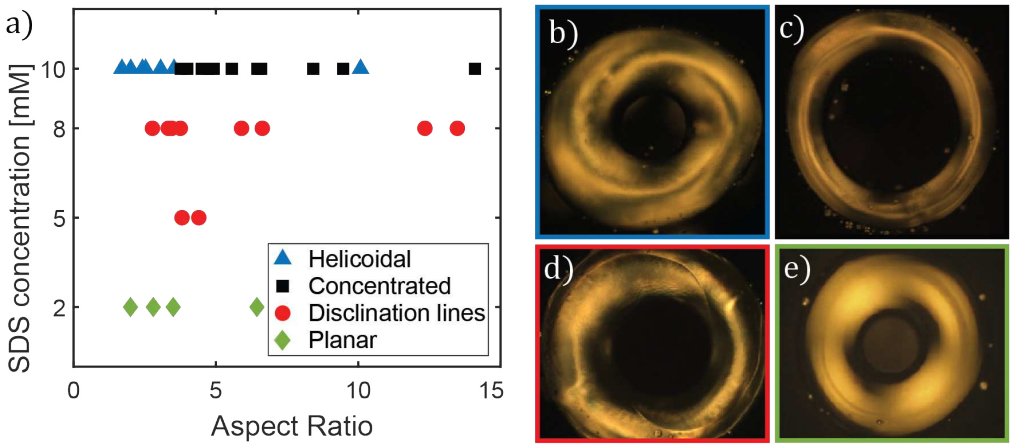



**Figure 7.1:** a) Phase diagram previously obtained in the group showing the different configurations obtained for homeotropic tori. b)-e) Crossed-polarizers images showing the different textures identified: Spiral (b), Concentrated (c), Configuration with disclination lines (d), Planar (e). Credit to Karthik Nayani for the data and images.



caped radial configuration, as shown using Jones Matrix simulations, to explain the spiral one, a escaped configuration was still assumed with the escape profile modified [113].

In cylindrical coordinates the director field for the escaped configuration is given by $\hat{\mathbf{n}} = \sin(\Omega(r))\hat{r} + \cos(\Omega(r))\hat{z}$, with $\Omega(r)$ the angle the director makes with the cylinder axis. This angle is assumed to depend only on r. In the one constant approximation, with boundary conditions $\Omega(0) = 0$ and $\Omega(a) = \pi/2$, the equilibrium solution is $\Omega(r) = 2\arctan(r/a)$ [182], resulting in a texture consistent with the concentrated configuration. To explain the spiral configuration a profile of the form $\Omega(r) = (r/a)^{\nu}$ was proposed. Jones matrix simulations give textures resembling the spiral one when $\nu \gg 1$ [113]. In this case, the director field rotation is concentrated close to the surface.

### Defect populated configurations

For SDS concentrations of 5mM and 8mM, configurations populated with disclination lines were obtained (see Figure 7.1d). The disclination lines form close loops that seem to be located on the surface of the torus, and that, as a result, can be classified as loops on a toroidal surface. This configuration is compatible with the planar polar configuration of homeotropic cylinders [63, 151].

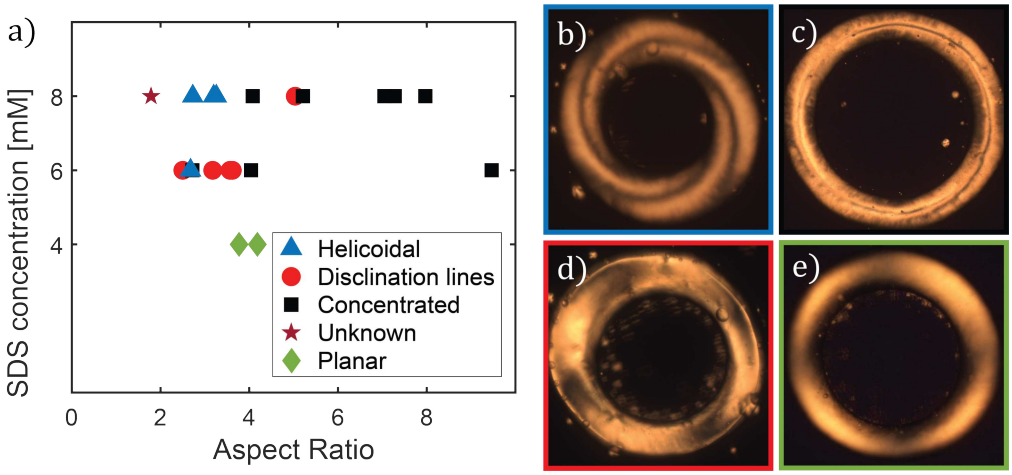



**Figure 7.2:** a) Reproduced phase diagram showing the four different configurations obtained for homeotropic tori. b)-e) Crossed-polarizers images showing the different textures identified: Spiral (b), Concentrated (c), Configuration with disclination lines (d), Planar (e).



### Defect-free planar configurations

For a low SDS concentration of 2mM, the anchoring is not homeotropic anymore and the configuration becomes the double-twisted one (see Figure 7.1e). This means that at small SDS concentration, either the homeotropic anchoring strength becomes zero [183] or it is low enough that the double-twisted planar configuration is the preferred one.

### Replicating these previous results in the group

We first reproduce the previously reported results by generating homeotropic tori in a yield stress material with the same composition as used before. As shown in Figure 7.2 we obtain the same configurations described previously. The only difference is the SDS concentration threshold. For 8mM SDS, both defect free homeotropic configurations are observed. Configurations with disclination lines are obtained for 6 mM SDS, and the planar configuration is recovered at SDS concentrations of 4mM.

## 7.2 Spiral and concentrated configurations

### 7.2.1 Spiral configuration as a transient state

In previous work in the group, the spiral and concentrated configurations were assumed to correspond to the equilibrium configuration at different aspect ratios, with the spiral appearing for low aspect ratios and the concentrated at high ones [113]. To test whether this is indeed true, we generate nematic tori with different aspect ratios and an outer SDS concentration of 8mM. We then wait until all defects annihilate and image the texture under crossed polarizers for classification.

We characterize our tori by two methods. First, we classify them qualitatively by its visual appearance into spiral or concentrated. Second and for a more quantitative assessment, we compute the relative peak width for a line that goes through the cross-section in a direction parallel or perpendicular to the polarizer, as shown in the inset of Figure 7.3b. We define the relative peak width as the ratio between the distance of the bright peaks in crossed polarizers and the tube diameter. The rational behind this measurement is based on the fact that the bright regions for the concentrated configuration are visually closer than for the spiral.

To compute the relative peak width, we measure the torus diameter by looking at the intensity profile in the bright field images and manually select the minima that correspond to the dark areas appearing due to refraction (Figure 7.3a). Then, we manually select the maxima of the crossed-polarizers images to obtain the peak distance (Figure 7.3a). The ratio between the peak distance and the torus diameter gives the relative peak width, which we express as a percentage. For each experimental image we compute the relative peak width, for all the intensity lines where the peaks can be clearly distinguished out of the four possible ones where the radial cut is either perpendicular or parallel to the polarizer. From these data points, we calculate the mean and the standard deviation of the measurements. The aspect ratio is measured from the bright field images of the tori using imageJ by fitting the inner and outer circles[1].

We plot the relative peak width as a function of the aspect ratio for all tori, as shown in Figure 7.3b. The data points have been colored as a function of their visual classification; red indicates spiral, black indicates concentrated. There are several aspects in this plot worth noting:

1. The relative peak width is a good quantitative indicator of the texture since all the points corresponding to the concentrated configurations have a width of around 20% while they have values of around 30-40% for the spiral configuration.

[1] From these measurements the aspect ratio is computed as $\xi = (R_{out} - R_{in})/(R_{out} + R_{in})$.

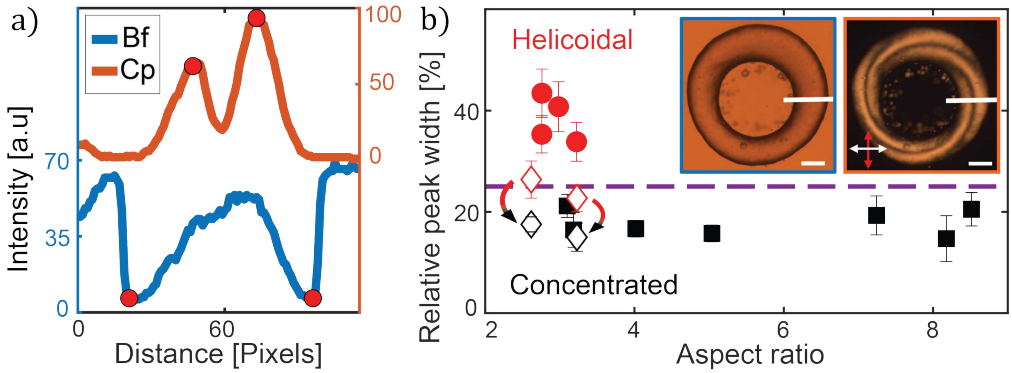



**Figure 7.3:** a) Example of intensity lines used for the computation of the relative peak width. The blue line corresponds to the intensity profile of the bright field image along the white segment in the inset of b). The orange line is the intensity profile in the same segment, also shown in the inset of b), for the crossed polarizer images. The manually selected points are marked with red dots. b) Relative computed width with the standard deviation calculated for different tori as a function of their aspect ratio. Color represents the visual texture. Rhombus represent tori where two images where taken at different times with the arrows indicating the evolution.



2. While the concentrated configuration can be observed for all aspect ratios, the spiral one only appears for low aspect rations. This means that for low aspect ratios both structures are observed, which implies that either one of them is the ground state, with the other one being a transient configuration, or both of them correspond to metastable states.

3. In a couple of cases, we took a second image of the torus a day after it was imaged. The configuration had transitioned from spiral to concentrated.

Interestingly, if we look at the time that has passed between making the tori and taking the picture, for all spiral cases, the images were taken a couple hours after making the torus, while the concentrated images were taken the following day. This fact and the change from spiral to concentrated configuration observed for a couple of tori suggest that the spiral configuration may not be the final equilibrium configuration but that instead, it corresponds to a transient state before the torus arrives at the final concentrated configuration, corresponding to the usual twisted escaped radial (TER).

The aspect ratio lack of spiral tori for large aspect ratios can be explained by the fact that for higher aspect ratio, the nematic volume is larger. It then takes longer for the liquid crystal to relax into the defect free configuration, and in this time, the concentrated configuration gets to be established. This is observed

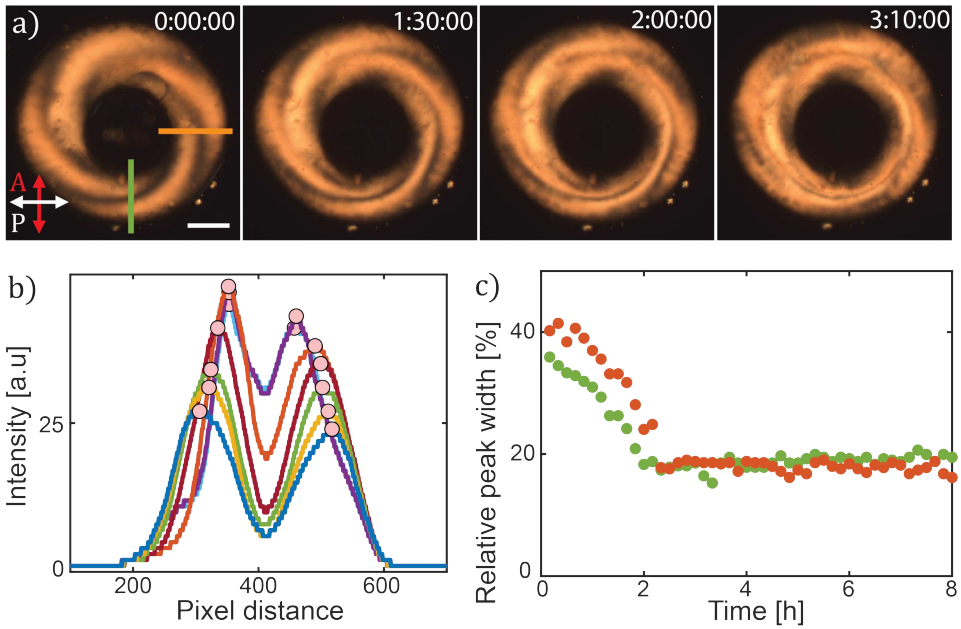



**Figure 7.4:** a) Time sequence of crossed polarizer images showing the transition from the spiral to the concentrated configuration. Scale bar is $200\mu m$ b) Line intensity profile for different times for the orange segment in a). The dots represent the computed maxima. c) Evolution of the relative peak with with time for the two segments shown in a). In a couple of hours the value stabilizes.

experimentally for some tori where, before all defects have annihilated, there are regions of the torus with the spiral texture. After complete defect annihilation though, the final configuration is the concentrated configuration.

To further test this idea, we generate a thick torus with low aspect ratio and monitor its evolution through time before it transitions to the isotropic phase due to ethanol diffusion from the outside yield stress material into the nematic tori. Figure 7.4a shows a series of snapshots of the torus where the transition from the spiral to the concentrated configuration is visually apparent. We also compute how the relative peak width changes as a function of time for the orange and green segments. To do that, we automate the peak detection program. The noise is eliminated by applying a Gaussian filter with standard deviation 3 pixels so the intensity profiles become smoother. An example of the peak detection for the intensity profiles at different times is shown in Figure 7.4b. With the peak distance and the tube diameter we can now compute the relative peak width for both line profiles as a function of time (see Figure 7.4c). In both cases, the width starts at a value of around 40%, consistent with the spiral configuration,

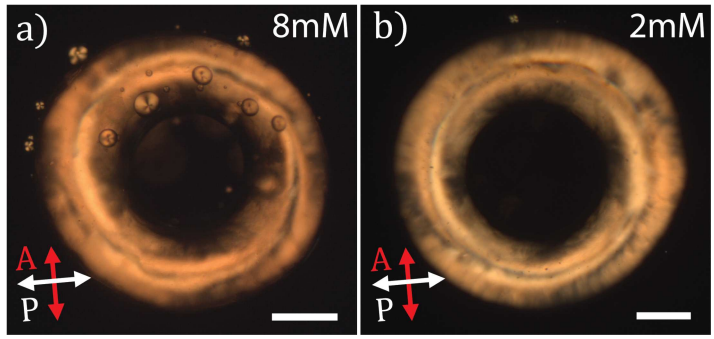



**Figure 7.5:** a) Crossed polarizer image of homeotropic tori in yield stress material without ethanol and 8mM SDS. b) Same as a) for 2mM SDS concentration. Scale bar is $200\mu m$.

and drops in a time span of a couple of hours to a constant value of around 20%. From that point on, the width remains constant for six hours, indicating that the concentrated configuration is the equilibrium configuration.

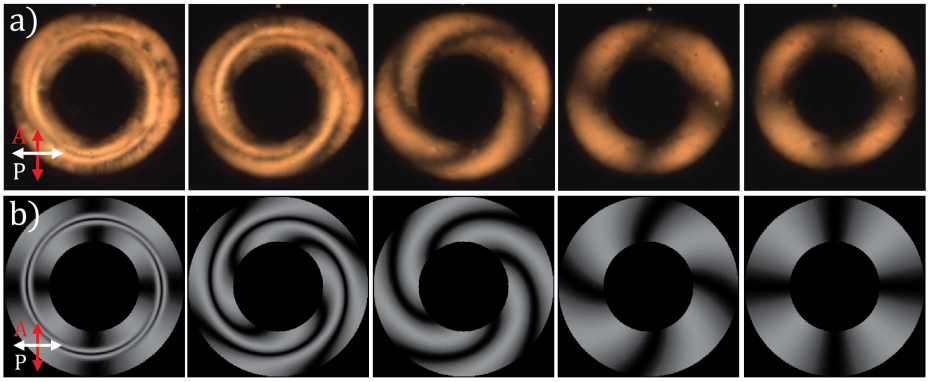
These experiments show that the spiral configuration does not correspond to an equilibrium configuration at low aspect ratios but to a transient one that evolves into the equilibrium concentrated configuration after $\sim$ 2 hours.

### 7.2.2 Yield stress material without ethanol: Concentrated-Spiral-Planar transition

All the previous experiments where carried out in tori stored in a yield stress material with ethanol. These tori could not be kept longer than one or two days due to the nematic transitioning to the isotropic phase. As done with the planar nematic tori to avoid the spontaneous nematic-isotropic transition and keep our samples for longer, we use a yield stress material without ethanol. To keep the yield stress at a similar value, the concentration of Carbopol is reduced to 1 wt%.

When we make toroidal droplets in this yield stress material we find that the previous phase diagram of Figure 7.2a does not apply anymore. In this case, no spiral configuration is ever observed after generating the tori and the concentrated configuration is always observed (see Figure 7.5a). Moreover, when reducing the SDS concentration, no configurations with stable disclination lines are ever observed. Even at 2mM SDS, where in the previous experiments the configuration observed was consistent with planar anchoring, do we see anything but the concentrated configuration, as shown in Figure 7.5b.

This means that the presence of ethanol changes the equilibrium and transient configurations observed for homeotropic tori. The usual twisted escaped




| | | | | | |
|---|---|---|---|---|---|
| $K_{24}=0$ | $W_a>5\cdot10^{-7}$ | $W_a\sim2.5\cdot10^{-7}$ | $W_a\sim1.6\cdot10^{-7}$ | $W_a\sim1.3\cdot10^{-7}$ | $W_a<10^{-7}$ N/m |
| $K_{24}=0.5K$ | $W_a>5\cdot10^{-7}$ | $W_a\sim2.0\cdot10^{-7}$ | $W_a\sim1.1\cdot10^{-7}$ | $W_a\sim0.8\cdot10^{-7}$ | $W_a<0.5\cdot10^{-7}$ |

**Figure 7.6:** a) Crossed polarizer images of the transition. b) Jones Matrix simulations of finite anchoring escape radial configurations in the one constant approximation matching the experimental images. The simulated torus has aspect ratio $\xi = 4$. We estimate the anchoring strength by using the tube radius $a \sim 150\mu m$ and elastic constant $K \sim 10pN$ .The anchoring strength estimated for each texture is shown below as a function of the value of the saddle splay constant $K_{24}$.



radial is the only configuration observed; his is in fact expected in view of the large tube radius of our droplets [152].

Nonetheless, when making tori in a yield stress material with 2mM SDS concentration and waiting for the next day, the torus spontaneously transitions to the planar configuration. When taking a video of the texture evolution over night, we observe how it first transitions from the concentrated texture to the spiral texture by expanding the concentrated features towards the edges of the torus, forming the spiral pattern of dark brushes, to then slowly unwind and result in the four dark regions at right angles characteristic of the planar configuration. The experimental images of the concentrated-spiral-planar transition is shown in Figure 7.6a.

The transition from homeotropic to planar is indeed expected when the anchoring strength becomes low enough and the homeotropic anchoring is not favored. This suggests that the anchoring strength is decreasing with time, maybe due to depletion of SDS from the surface. The fact that in between the concentrated and planar configurations, the spiral structure appears, indicates that the spiral configuration is the equilibrium configuration for finite and low enough anchoring strengths when the director stops been perpendicular to the surface. This also means that, when generating homeotropic tori in yield stress materials with ethanol, the initial anchoring strength is small and becomes stronger with

time. This could perhaps be attributed to the electrostactic screening from sodium ions, coming from the sodium hydroxide used to neutralize the yield stress material. The presence of these ions could slow down the adsorption rate of SDS on the surface. For the case without ethanol, less sodium hydroxide is needed to neutralize the solution, which could result in a faster adsorption of SDS on the toroidal surface. Apart from this, the presence of ethanol could alter the adsorption of SDS on the toroidal surface, thus affecting the anchoring strength [184].

Within this framework, the appearance of stable configurations with disclination lines is also understood, since the planar polar configuration is the stable one for either small enough cylinders or low enough anchoring strength [152, 185]. The disclination lines, then, are initially formed as the stable configuration for the initial low anchoring strengths and, as it increases, this configuration is trapped in a metastable state, where a high energy barrier would prevent the annihilation of the disclination lines required for it to relax to the twisted escaped radial configuration [186].



## 7.3 Escaped radial configuration with finite anchoring strength

To test whether finite anchoring is responsible for the spiral texture observed experimentally, we perform Jones Matrix simulations of the escaped radial configuration with finite anchoring strength. For simplicity, we initially neglect twist and the effects of the toroidal geometry and consider a cylinder with axial direction $\hat{z}$. Locally, for our torus $\hat{z} \equiv \hat{\phi}$. The system of coordinates chosen is represented in Figure 7.7a. We will also use the one constant approximation and take $K = K_3 = K_1$[1]. In this approximation, we can obtain simple analytical solutions that can be used for simulating the textures.

### 7.3.1 One elastic constant model

The director field describing the escaped radial configuration has no twist, and therefore, no component in the polar direction $\hat{\theta}$. It also has azimuthal symmetry and translational invariance so the director field does not depend on the coordinates $\theta$ and $\phi$. The director field can be then written in terms of a single function of one variable:

$$\hat{\mathbf{n}} = \sin(\Omega(r))\hat{r} + \cos(\Omega(r))\hat{\phi} \tag{7.1}$$

[1]The twist constant does not appear, since for the escaped radial configuration its energy is 0; the particular value of the constant does not affect the results.

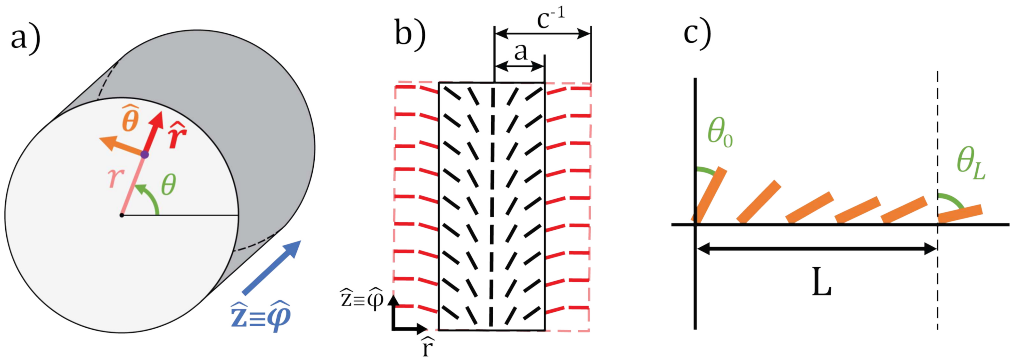



**Figure 7.7:** a) Cylindrical coordinates used in the analytical derivation. b) Schematic for the escaped radial configuration in a cylinder of radius a and finite anchoring strength. The configuration is the same as the escaped radial configuration for a cylinder of radius $c^{-1} > a$ with perfect homeotropic alignment cut to size $a$. c) Schematic of the system used for interpreting the extrapolation length. The preferred orientation at the surface is vertical in this case.



where $\Omega(r)$ represents the angle the director makes with the axial direction $\hat{\phi}$. In the one constant approximation and using polar coordinates, the elastic free energy density is given by:

$$\begin{aligned} f_e &= \frac{1}{2}K\left[(\nabla\cdot\hat{n})^2 + |\nabla\times\hat{n}|^2\right] \\ &= \frac{1}{2}K\left[\frac{\sin(\Omega)^2}{r^2} + \frac{2\sin(\Omega)\cos(\Omega)}{r}\frac{\partial\Omega}{\partial r} + \left(\frac{\partial\Omega}{\partial r}\right)^2\right] \end{aligned} \tag{7.2}$$

The total elastic energy per unit length is obtained by integrating the energy density in polar coordinates over the cross-section. After integration over the polar coordinate, we obtain the energy per unit length as a single integral for the radial coordinate:

$$F_e = \pi K\int_0^a \left[\frac{\sin(\Omega)^2}{r} + 2\sin(\Omega)\cos(\Omega)\frac{\partial\Omega}{\partial r} + r\left(\frac{\partial\Omega}{\partial r}\right)^2\right]dr \tag{7.3}$$

We can find $\Omega(r)$ from minimizing the energy. This is a variational problem for the energy functional. The corresponding Euler-Lagrange equation [44, 133] for the integrand $\mathcal{L}(r,\Omega,\Omega')$ becomes:

$$\frac{\partial\mathcal{L}}{\partial\Omega} - \frac{d}{dr}\frac{\partial\mathcal{L}}{\partial\Omega'} = 0 \tag{7.4}$$

$$r\frac{\partial^2\Omega}{\partial r^2}+\frac{\partial\Omega}{\partial r}-\frac{1}{2r}\sin 2\Omega=0 \tag{7.5}$$

where $\Omega'=\partial\Omega/\partial r$. The differential equation 7.5 can be solved in two steps. First we use the variable change $x=\ln r$ [182] and multiply equation 7.5 by $\partial\Omega/\partial x$. This gives a total derivative that can be directly integrated. The integration constant is obtained by imposing that the director points in the azimuthal direction at the center of the cross-section, $\Omega=0$ at $r=0$, and that this does not lead to a singularity. We are left with a first order differential equation that can be solved with standard methods resulting in the simple form:

$$\Omega(r)=2\arctan(c\cdot r) \tag{7.6}$$

where c is a constant. It is interesting to note that all solutions collapse into the same one when making the coordinate transformation $r'=c\cdot r$ which corresponds to an expansion or contraction in the radial direction. The collapsed solution $\Omega(r')=2\arctan(r')$ corresponds to a cylinder with its surface at $r'=1$ and perfect homeotropic anchoring, $\Omega(r'=1)=\pi/2$. The constant c controls the angle the director makes with the surface. If this angle is given by $\Omega(r=a)=\Omega_0$, the integration constant $c$ can be expressed as:

$$c=\frac{1}{a}\tan\left(\frac{\Omega_0}{2}\right) \tag{7.7}$$

Indeed, the constant c can be seen as an inverse length such that the configuration corresponds to the one of a cylinder of radius $c^{-1}$ with perfect anchoring conditions. If the radius of our cylinder, $a$, is smaller than this value, the director at the boundary would not be perpendicular. The boundary of our cylinder would be inside of a fictitious cylinder with perfect boundary conditions, radius $c^{-1}$, and it would have the same director field configuration inside (see Figure 7.7b).

From the solution for $\Omega(r)$ we can compute the total elastic energy per unit length as a function of c using equation 7.3:

$$F_e=4\pi K\left[1-\frac{1}{(1+c^2r^2)^2}\right] \tag{7.8}$$

We can now compute the surface anchoring strength. For that, we use the usual Rapini-Papoular form for the energy per unit area[1] (see Section 2.2.4):

$$f_a=-\frac{1}{2}W_a\cdot\sin^2\Omega_0 \tag{7.9}$$

[1]Note that we use the sine of the angle $\Omega_0$ instead of the cosine, since $\Omega_0$ is the complementary angle to the one the director forms with the preferred perpendicular orientation.

Integrating this expression over the circular contour we get the anchoring energy per unit length of cylinder:

$$F_a = -4\pi a W_a \frac{c^2 a^2}{(1 + c^2 r^2)^2} \tag{7.10}$$

We can obtain the equilibrium configuration for a certain anchoring strength $W_a$, by minimizing the total energy $F_e + F_a$ with respect to the parameter $c$. This, in turn, gives the angle the director forms with the surface through equation 7.7:

$$c = \frac{1}{a}\sqrt{1 - \frac{2K}{aW_a}} = \frac{1}{a}\sqrt{1 - \frac{2b}{a}} \tag{7.11}$$

where $b = K/W_a$ is the extrapolation length defined in section 2.2.6.2.

Another way of deriving this equation, often employed in mechanics, is to use the balance of torques. In our case, we would balance the torque produced by the anchoring, $T_a$, and the torque produced by the bulk nematic liquid crystal, $T_e$. The computation of the anchoring torque is simple, since it is directly minus the derivative of the anchoring energy density with respect to the orientation of the director at the surface:

$$T_a = -\frac{\partial f_a}{\partial \Omega_0} = 2W_a \frac{ca(1 - c^2 a^2)}{(1 + c^2 a^2)^2} \tag{7.12}$$

The torque produced by the bulk nematic liquid crystal can be computed by looking at the molecular field at the surface given by the left hand side of equation 7.4. As pointed out by de Gennes [27], this Euler-Lagrange equation can be understood as a balance of torques. In this case the first term would correspond to a volumetric torque (torque per unit volume) like the ones produced by external fields. The interesting term is the second one. Since it involves a spatial derivative, the quantity inside the spatial derivative can be understood as a torque acting on the surface of a differential volume; the derivative just gives the difference between the torques at each side of the differential volume.

Since the surface has no volume but has nematic liquid crystal on only one side, the term inside the spatial derivative actually corresponds to the torque at the surface[1]:

$$T_e = -\left.\frac{\partial f_e}{\partial \Omega'}\right|_{r=a} = K\left[\frac{2c}{1 + c^2 a^2} + \frac{2c(1 - c^2 a^2)}{(1 + c^2 a^2)^2}\right] \tag{7.13}$$

[1]Note that instead of using the Lagrangian $\mathcal{L}$, we have used the energy density. This is because the Lagrangian, when integrated, is multiplied by the Jacobian, which corrects the density to polar coordinates.

Equation 7.11 can be obtained by imposing that the sum of torques is zero:

$$T_a + T_e = 0 \tag{7.14}$$

#### 7.3.1.1 Including saddle-splay: $K_{24}$ as an effective anchoring strength

In the previous calculations we have used the one constant approximation and have neglected the saddle splay term. As discussed in section 5, this term is traditionally expressed as a total divergence and can often be converted to a surface integral. Since there are no singularities of the field inside the volume, the saddle-splay energy can in this case be interpreted as a surface term that adds up to the anchoring energy. The saddle-splay free energy density (see section 2.2.2) is given by:

$$f_{24} = -K_{24}\nabla \cdot [\hat{\mathbf{n}}\nabla \cdot \hat{\mathbf{n}} + \hat{\mathbf{n}} \times \nabla \times \hat{\mathbf{n}}] \tag{7.15}$$



Integrating, the total saddle-splay energy per unit length becomes:

$$F_{24} = -8\pi K_{24} \frac{c^2 a^2}{(1 + c^2 a^2)^2} \tag{7.16}$$

This energy has the same functional form as the anchoring energy, equation 7.10. Adding both terms together gives the total surface energy per unit length:

$$F_s = F_a + F_{24} = -4\pi \left( W_a + \frac{2K_{24}}{a} \right) \frac{c^2 a^2}{(1 + c^2 a^2)^2} \tag{7.17}$$

From this equation, we see that the effect of adding the saddle-splay is to effectively increase the anchoring strength, favoring homeotropic alignment. If we define the effective anchoring strength as $W_{eff} \equiv W_a + 2K_{24}/a$, all the previous calculations remain valid and the constant c becomes:

$$c = \frac{1}{a}\sqrt{1 - \frac{2K}{aW_{eff}}} = \frac{1}{a}\sqrt{1 - \frac{2b_{eff}}{a}} \tag{7.18}$$

where we have defined the effective extrapolation length $b_{eff} \equiv K/W_{eff}$.

Another consequence of having a non-zero and positive $K_{24}$ is that the effective anchoring strength can never become zero and will always be positive, favoring homeotropic alignment. This residual anchoring strength depends on the radius of our cylinder and becomes smaller for larger cylinder radius.

#### 7.3.1.2 Homeotropic-Planar transition at finite anchoring strength

If we take a closer look at equation 7.18, we can see that as the anchoring strength becomes infinite, $c \to 1/a$, and the director is perpendicular to the surface, with $\Omega(a) = \pi/2$. If the anchoring strength decreases, the value of c decreases and so does the angle the director forms with the surface. Surprisingly, the value of c, as indicated by previous authors [62, 153], becomes 0 for a finite value of anchoring strength. This means that for a non-zero low value of the anchoring strength the torus prefers to be planar, and a transition from homeotropic to planar alignment then takes place at finite anchoring strength. This critical value of the anchoring strength is given by:

$$W_{crit} = \frac{2(K - K_{24})}{a} \tag{7.19}$$

We then see that when the saddle-splay constant is larger than the other elastic constants, $K_{24} > K$, the homeotropic to planar transition does not take place for any positive value of $W_a$. For 5CB, $K_{24}$ is estimated to be similar to $K_2$ [9], and smaller than $K_1$ and $K_3$. As a result, we expect the homeotropic-planar transition to be possible.

The presence of a finite anchoring value where the anchoring becomes exactly zero can ultimately be attributed to the fact that the continuity of the field and its azimuthal symmetry force the director field at $r = 0$ to form a $\pi/2$ angle with respect to the preferred homeotropic orientation at the surface. The director field is exactly parallel to the surface at a finite distance from it, eventually favoring that this planar arrangement propagates to the toroidal volume.

This becomes clear when revisiting the simple configuration used to illustrate the meaning of the extrapolation length (see section 2.2.6.2). We define the 2D director field by using an angle $\theta$ measuring the deviation with respect the preferred orientation at the surface (Figure 7.7c). In this case, if we set the angle of the director a distance L from the surface to $\theta_L$, we can solve the Euler-Lagrange equations in the one constant approximation and minimizing the sum of the elastic and surface anchoring energies, to obtain an implicit equation for the angle at the surface $\theta_0$:

$$\frac{L}{b}\frac{sin(2\theta_0)}{2} = \theta_L - \theta_0 \tag{7.20}$$

If $\theta_L < \pi/2$, for any value of the extrapolation length $b$, the angle at the surface is always larger than 0 and only becomes exactly 0 when $b \to \infty$. In contrast, if $\theta_L = \pi/2$, $\theta_0 = \pi/2$ is always a possible solution and becomes the only solution when $L < b$, that is, for a finite value of the anchoring strength. The extrapolation length then gives a typical maximum distance where if we impose $\theta_L = \pi/2$, the anchoring conditions completely break down.

The case of the escaped radial configuration is similar to the one just discussed in that the director is exactly perpendicular to the anchoring direction at a finite distance from the surface. This can be understood as the origin of the homeotropic to planar transition at finite anchoring strengths.

Finally, to sum everything up, the escaped radial configuration of a cylinder in the one constant approximation and including the saddle-splay term is given by:

$$\Omega(r) = \begin{cases} 2\arctan\left(\sqrt{1-\dfrac{2K}{W_{eff}a}}\cdot\dfrac{r}{a}\right) & W_a > \dfrac{2(K-K_{24})}{a} \\ 0 & W_a \leq \dfrac{2(K-K_{24})}{a} \end{cases} \tag{7.21}$$

For a torus, this configuration, in toroidal coordinates, is given by introducing this angle function in equation 7.1.



#### 7.3.1.3 Jones Matrix simulations: Comparison with experiments

With equation 7.21 we perform Jones Matrix simulations to obtain the crossed-polarizer texture of the escaped radial torus as a function of the effective anchoring strength $W_{eff}$. In this case, unlike i section 4.4.2.2, we perform our simulations for the multi wavelength case, using the Matlab program previously developed in the group by Perry Ellis [113]. We generate crossed-polarizer textures for a torus with aspect ratio $\xi = 4$ using a weighted average over 200 evenly-spaced wavelengths between 400 nm and 700 nm. The weights are uniform, corresponding to the profile in the visible range of the xenon lamp in our microscope[1]. In all our simulations the grid is discretized with a voxel size of $0.03a$.

We make simulations for different anchoring strengths in the range where the angle at the surface $\Omega(r = a)$ changes significantly. This range corresponds to $W_{eff} \in [2K/a, 100K/a]$. Indeed, the actual configuration depends on the value of the dimensionless number $aW_{eff}/K$. The results of the simulations are shown in Figure 7.6b. Like in the experimental case, as the anchoring strength decreases, the initial concentrated configuration opens up into a spiral between the inner and outer rings. When further decreasing the anchoring strength the spiral unwinds until it stabilizes in the four dark spots characteristic of the planar configuration.

The simulated textures agree very nicely with the experimental images where the dark spirals form a very similar pattern. This supports the idea that the spi-

[1]The simulation results do not appreciably change when using the weights for a tungsten lamp, which are given by $weight(\lambda) = \sqrt{(\lambda - 375)/500}$ [113].

ral configuration appears as a result of the director field not being perpendicular to the surface due to finite anchoring strength. This texture was also simulated in prior work in the group [113] using the angle function ansatz $\Omega(r) = (r/a)^{\nu}$ with $\nu \gg 1$. The function chosen concentrates the angle distortion in the outer shell of the torus. When simulating this texture, the thin layer barely changes the polarization so the texture becomes dominated by the interior part. Removing the outer layer results in a escaped radial configuration with the director tilted with respect to the normal to the surface, as in our simulations. The thin layer associated to the rapid change in director field results in a grainy background. This explains why the ansatz used also recovers the spiral texture.

By matching the simulated textures with the experimental images, specially in terms of the spiral winding, and using the estimated values for the tube radius $a \sim 150\mu m$ and the one elastic constant $K \sim 10pN$[1], we can obtain an estimation of the effective anchoring strength for the different configurations. From this effective anchoring strength, we can obtain the actual anchoring strength by using the value of the saddle-splay elastic constant $K_{24}$ and the tube radius of the torus $a \sim 150\mu m$. In figure 7.6 the values of the estimated anchoring strength for each picture are shown for the cases $K_{24} = 0$ and $K_{24} \approx 0.5K$, where the last one corresponds to the value estimated for 5CB from the double twist of planar tori [9].

In our experiments the spiral configuration appears when the anchoring strength becomes of the order of $10^{-7}N/m$. For values larger than $5 \cdot 10^{-7}N/m$ the equilibrium configuration is the concentrated one and is not sensitive to the exact value of the anchoring strength. The transition from concentrated to planar occurs in the range $W_a \in [0.5 \cdot 10^{-7}, 5 \cdot 10^{-7}]N/m$. Below $5 \cdot 10^{-8}N/m$ the configuration becomes planar.

In these experiments where the anchoring strength seems to be decreasing, we observe the homeotropic-planar transition. This transition at a finite anchoring strength has been predicted theoretically but never thought to be experimentally accessible deep in the nematic phase [62, 153] and only observed close to the nematic-isotropic transition [187]. This was mainly due to the fact that the experiments where done with nanopores, where the anchoring strength is fixed, and this transition would take place at cylinder radius small enough such that the planar polar configuration becomes the equilibrium one rather than the escaped radial. In our tori, the use of a water based yield stress medium allows tuning the anchoring strength with the concentration of surfactant, which in turn, can dynamically change depending on the adsorption of the surfactant on the surface. The decrease in anchoring strength with time allowed observing this homeotropic-planar transition for a large tube radius of $\sim 150\mu m$.

[1]This value has been taken as a representative value for 5CB corresponding to the bend elastic modulus. An average between the splay and bend constant could as well be used.

Moreover, the sensitivity of the observed texture with the anchoring strength opens up the possibility of using this system to probe the anchoring strength of surfactants in solution as a function of their concentration. Note the configuration is only sensitive to values that are orders of magnitudes lower than the usual values reported. Since the configuration of the torus depends on the dimensionless number $aW_{ref}/K$, the range in anchoring strength where the configuration becomes spiral can be tuned by changing the size of the torus or the value of the elastic constant. Reducing the tube radius an order of magnitude allows probing the effect of the anchoring strength at an order of magnitude higher. Making such small tori is challenging though. Changing the elastic constant to probe higher anchoring strengths would require increasing the elastic constants, which might also not be straightforward. Nonetheless, this could be attempted by setting the temperature closer to the crystal-nematic transition.

### 7.3.2 Role of twist and different elastic constants



Although the previous results look preliminary, we know that the actual configuration of the director field in our homeotropic tori does not correspond to the ideal escaped radial configuration in the one elastic constant approximation. We know that the actual configuration corresponds to the twisted escaped radial configuration [61], and that the bend and splay elastic constants of 5CB are not the same [167]. We now study the effect of adding twist and including different elastic constants in the simulated textures as a function of the anchoring strength. We perform Jones Matrix simulations and compare the results with the untwisted, one-constant approximation, escaped radial textures shown in Figure 7.8a.

#### Adding twist

We can add twist to our escaped radial configuration by combining the escaped radial configuration with the two parameter ansatz used for describing the double twist of planar tori [9, 10]. The twist ansatz becomes:

$$\begin{cases} n_r = \sin(\Omega(r)) \\ n_\theta = \cos(\Omega(r)) \dfrac{w\frac{r}{a}}{1 - g\frac{r}{R}\cos(\theta)} \\ n_\phi = \cos(\Omega(r)) \sqrt{1 - \left(\dfrac{n_\theta}{\cos(\Omega(r))}\right)^2} \end{cases} \tag{7.22}$$

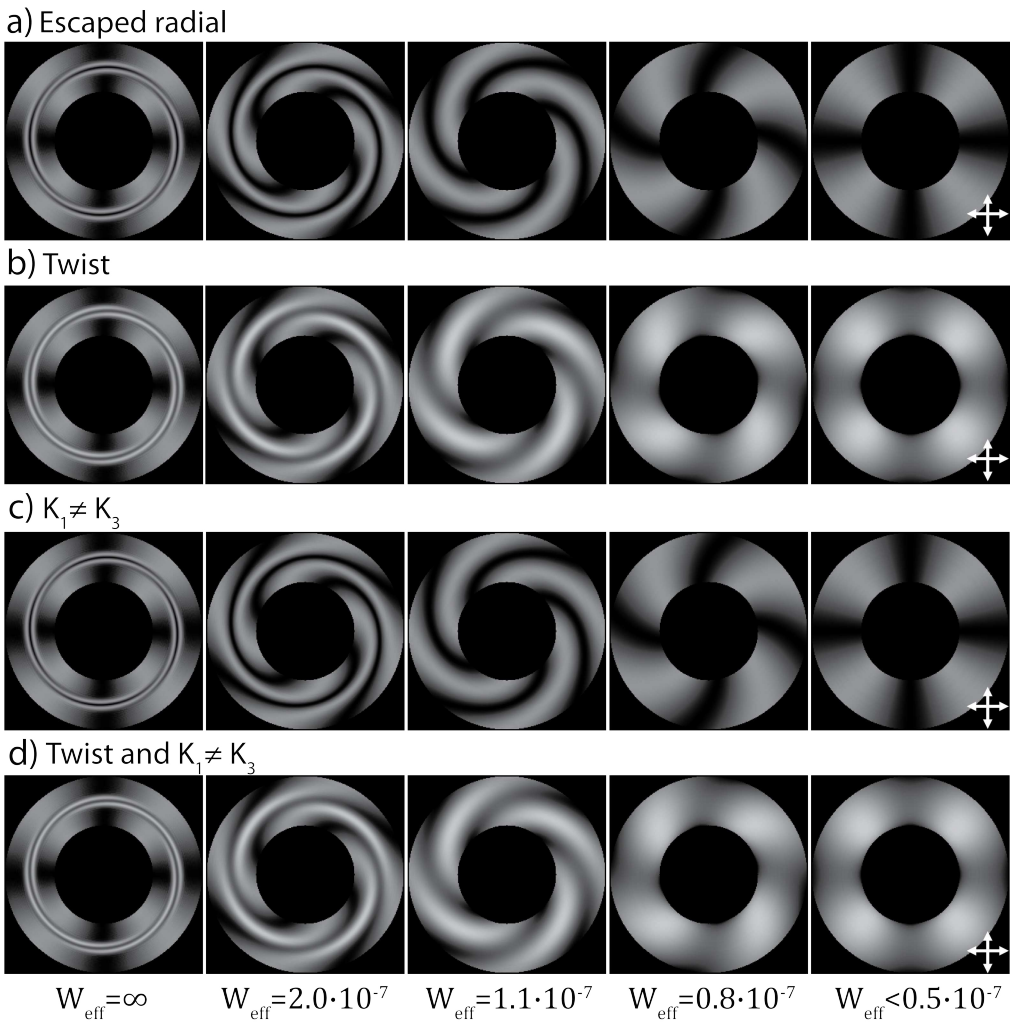



**Figure 7.8:** a) Jones matrix simulations in crossed polarizers for the simple escaped radial configuration and different effective anchoring strengths. b) Simulations for the twisted escaped radial ansatz of equation 7.22 using $w = 0.396$ and $g = 0.813$. c) Simulations for the no twist and different elastic constant case. The director field is given by the ansatz of equation 7.23 using the elastic constant ratio for 5CB $k = K_3/K_1 = 1.5$. d) Simulations for the combined case of twist and different elastic constants. The effective anchoring strength value is in N/m and is obtained using $K = 10pN$ as the value for the elastic constant.

We take $w = 0.396$ and $g = 0.813$, which are the minimum energy values for the double-twisted structure of a torus of similar aspect ratio [113] and twist an-

gle 47°. The resulting textures are shown in Figure 7.8b. When comparing them with the escaped radial case we see that the dark regions form the same exact spiral pattern; the only difference being the dark regions become lighter. This is consistent with the fact that the ratio between the intensity of the bright peaks and dark regions is smaller for the twisted escaped radial configuration [61]. This implies that for the spiral pattern the amount of twist can be quantified by the ratio of maximum to minimum intensity, as done previously [61].

Since the shape of the dark region does not change for the same anchoring strength, the untwisted escaped radial textures can be used to estimate the anchoring strength.

### Different elastic constants $K_1 \neq K_3$

The case for finite anchoring and different elastic constants has been already analytically solved [62, 153]. The equilibrium configuration is given by the following implicit equation:



$$\frac{r}{a} = \sqrt{\frac{\sigma+1}{\sigma-1}\frac{\Delta-1}{\Delta+1}}\exp\left(\sqrt{k-1}\arctan\frac{\sqrt{k-1}(\Delta-\sigma)}{\Delta\sigma+k-1}\right) \tag{7.23}$$

where $\sigma = (aW_a + K_{24})/K_1 - 1$ represents the effect of the anchoring strength, $k = K_3/K_1$, and $\Delta = \sqrt{1+k\tan(\Omega(r))^2}$. To simulate the textures we initially solve the implicit equation using the elastic constant ratio for 5CB, $k = 1.5$. The resulting textures are shown in Figure 7.8c. In this case, the textures are almost identical. Therefore, the one constant approximation is valid for estimating the anchoring strength.

In a more quantitative way, we can compare the angle profiles $\Omega(r)$ for the one constant approximation and for the case with different elastic constants; see Figure 7.9a. We can see that for perfect anchoring ($\sigma \to \infty$) the distortion is more concentrated in the inner region. This can be easily understood since for 5CB the highest elastic constant is that associated to bend, which is predominant at the outer shell. To minimize the total energy, the bend is reduced at the outer shell by reducing the distortion. This comes at the cost of increasing the splay distortion in the center. As the anchoring strength is reduced we can see that the profiles are not very different and become more and more alike as the anchoring strength decreases.

If we plot the director angle at the surface, $\Omega(a)$, for both approximations as a function of $\sigma$ we find that the angle mismatch becomes larger at intermediate anchoring strengths and that it tends to the same value in the very large and very low anchoring limits; see Figure 7.9b. The maximum mismatch is smaller than 0.1 radians, though, as indicated by the peak of the black line.

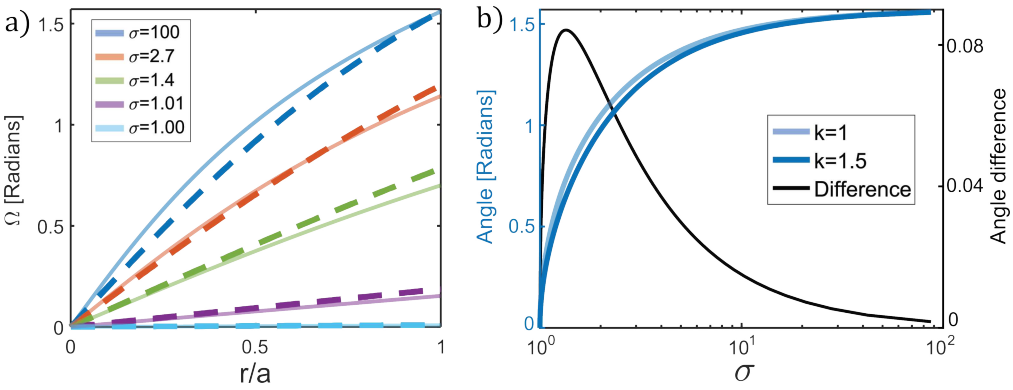



**Figure 7.9:** a) Angle profile comparison between the one constant approximation (dashed lines) and the solution of the different elastic constants (solid lines). Different colors represent different anchoring strengths, controlled by the adimensional parameter $\sigma$. b) Blue lines represent the angle of the director at the boundary ($\Omega(a)$) as a function of the adimensional parameter $\sigma = aW_{eff}/K_1 - 1$ controlling the anchoring strength . Black line corresponds to the difference between both cases.



We can also combine both twist and different elastic constants. We use the same parameters as before and obtain the textures shown in Figure 7.8d. These textures combine the features of twist, with the presence of lighter bands, and different elastic constants, with a slightly different texture at high anchoring strengths.

We would like to note that, despite the escaped radial configuration gives very nice agreement with experiments, the actual configuration of the torus might be even more complex. Indeed, it was theoretically shown that a displacement of the escaped center can indeed lower the energy of homeotropic tori [188], which could lead to a slight change in the texture as a function of the anchoring strength.

## 7.4 Configurations with disclination lines

When using as the outer medium the yield stress material with ethanol and SDS concentration of 6mM, we obtain stable configurations with disclination lines. The stability of these configurations has been confirmed during the lifetime of the tori, which is about a day or two due to the presence of ethanol. Longer term stability, thus, can not be assessed.

The presence of disclination lines is inferred from the bright-field images of the torus, where instead of the smooth image obtained for the defect-free case,

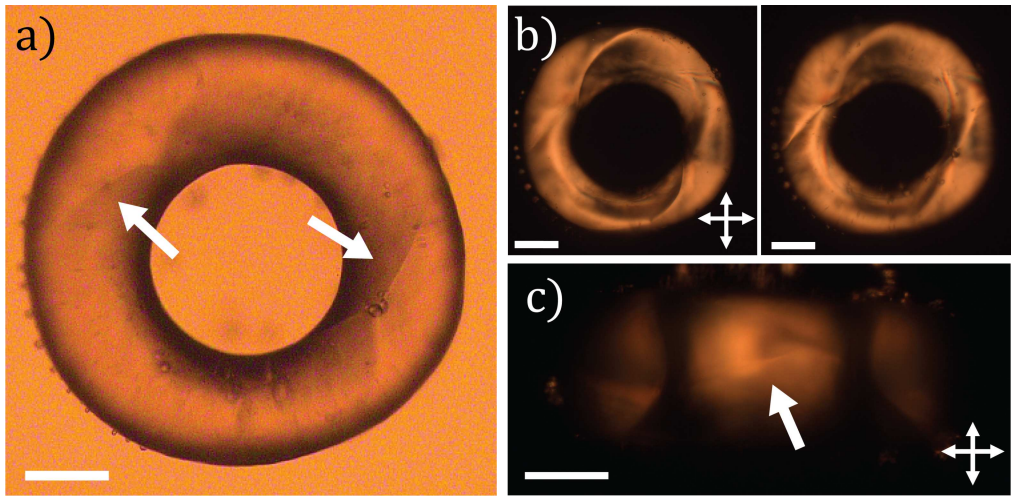



**Figure 7.10:** a) Bright field image of a torus with disclination lines. The arrow indicate the location of the thin dark lines corresponding to disclination lines. Image has been sharpened to enhance the disclination features b) Crossed polarizer image of the same torus changing the focal plane. The focused part of the disclination line changes. c) Crossed polarizer image of the side view of the torus where the disclination crossing it horizontally is indicated with the white arrow. Scale bars are $200\mu m$.



we observe the presence of thin black lines, similar to scars, which correspond to disclination lines; see Figure 7.10a. When observing the configuration in crossed polarizers, the disclination lines become more apparent. By changing the focal plane, as shown in Figure 7.10b, we can see that different parts of the disclination lines become in focus. This means that the disclination lines are not confined to a plane, which is also confirmed by the crossed polarizer side view of the torus; see Figure 7.10.

The configuration with disclination lines is different for each generated torus. The common feature between them is the presence of singular lines. Because of this, we will focus on studying the disclination lines rather than trying to unravel the exact configuration for each particular case. Before showing the experimental results, we first discuss some theoretical aspects that will be helpful in the interpretation of the experimental configurations.

### 7.4.1 Preliminary discussion

As discussed in section 2.4.2, configurations with disclination lines for homeotropic cylinders have been discussed long ago [62, 153, 185]. Translational invariance has traditionally been assumed so that the configuration can be described solely

by the cross-section director field. The homeotropic anchoring conditions force the projection of the director field in the cross-section to have a total topological charge of +1. This can be fulfilled by either having a +1 defect line at the center whose singularity can be removed by escaping in the third dimension to result in the escaped radial configuration, or by having two +1/2 disclination lines whose singularity can not be removed. In this last case, two different configurations have been proposed depending on whether the disclination lines are on the surface, resulting in the planar polar (PP) configuration (Figure 7.11a), or inside the cross-section, resulting in a configuration called planar polar with disclination lines (PPLD) (Figure 7.11b).

The theoretical phase diagram shows that the planar polar configuration becomes the stable one when the anchoring strength or the capillary diameter are small enough [62, 152, 185, 185]. This last case is backed up by experiments where the configuration of nematic liquid crystal confined to nanopores with homeotropic anchoring conditions was determined by neutron magnetic resonance (NMR). The results confirm that the planar polar configuration was the equilibrium configuration acquired by the nematic liquid crystal for small enough pore diameters [64, 153]. The PPLD configuration is metastable and only becomes stable in the presence of a sufficiently high external field and strong anchoring [185].



Since the singularity line for half-integer disclinations can not be continuously removed, disclination lines form either loops or have their ends located at the surface of the sample [46, 189]. In the configuration of our homeotropic tori we only observe loops; given that any line ending at two points on the surface can be contracted to a single point, reducing the singular core length and, therefore, the energy.

If we assume that in our tori with disclination lines we have the PP or a similar configuration with the defects on the surface, the disclination lines form loops on the surface of the torus. If, on the contrary, we assume the cross-sections with disclination lines have a similar configuration to the PPLD, the disclination lines run inside the torus. Since both lines nevertheless repel each other the disclination lines can be taken to form loops on an effective toroidal surface with an effectively PP configuration.

Loops on a toroidal surface can be classified topologically by two integers $(p, q)$ [190] which represent the number of turns $p$ the loop does around the tube and the number of turns $q$ it does around the axis of revolution as we traverse the loop once. Any pair of loops with the same two integers can be continuously transformed into each other by deforming them on the toroidal surface, with the special case of $(0, 0)$ loops being the only ones able to contract to a point [8]. Loops with opposite sign $p$ and $q$ correspond to loops of the same, $(p, q) \equiv (-p, -q)$. In contrast, the relative sign of $p$ and $q$, which can

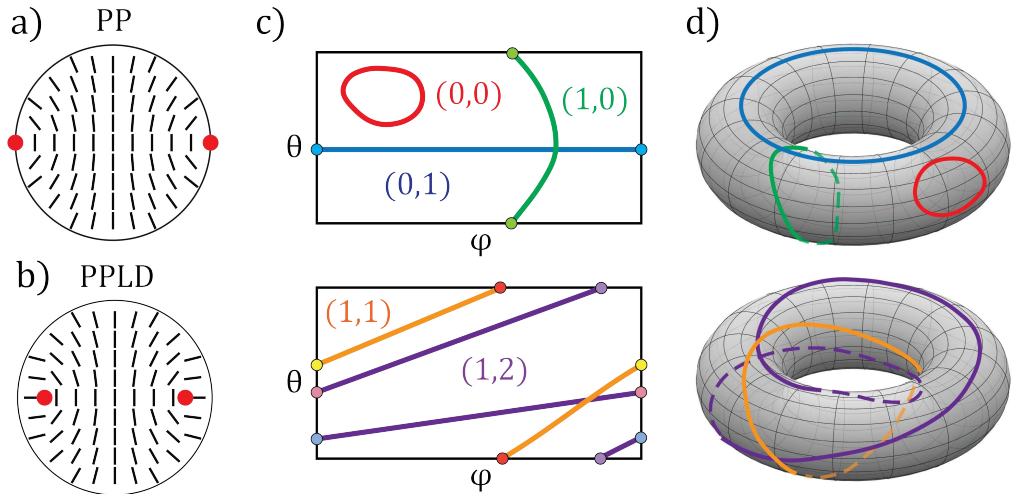



**Figure 7.11:** a) Planar polar configuration (PP) with the defects on the surface marked with red points. b) Planar polar with line disclinations configuration. Red points mark the defect position inside the cross-section. c) Representation in the rectangular frame with periodic boundary conditions of different types of loops on the surface of torus. Dots of the same color indicate identified points due to the periodicity of the toroidal surface. d) Representation on a toroidal surface of the loops shown in c). Colors are matched.



be computed as the sign of $pq$ determines the handedness of the loop. We can represent these loops on a rectangular region with periodic boundary conditions with its axis associated to the pair of coordinates $(\theta, \varphi)$.

Although all the $(p, q)$ loops are theoretically possible, in our tori, we do not expect to observe all of them. Loops with $q > 2$ are not expected since, as loops traverse a cross-section at least q times, this will imply having more than 2 defects on the cross-section which is energetically unfavorable. By the same argument, loops with $q = 1, 2$ should always go around the "hole" of the torus in a single sense when traversing the loop, since not fulfilling this would also imply having sections with more than two defects that can be continuously removed by stretching the disclination line. Finally, loops that self-intersect are not physically reasonable, since the intersection point has four branches that can split into two separate disclination lines, as for example happens during recombination processes [191]. This is for example the case of $(0, n)$ or $(n, 0)$ loops with $n > 1$[1]. The non-contractible loops we expect to observe on our tori

[1]This can be proved by splitting the loop into two segments where both of them make at least one turn around an axis of the torus and applying the intermediate value theorem to their difference in one coordinate.

are:

1. $(1, 0)$ loops. This loop goes around the tube once. The loop can go right the circular cross-section or not. In this last case, since the loop necessarily goes back in the $\varphi$ coordinate, it fulfills the topological condition of two $+1/2$ defects at the cross-sections where the loop is present.

2. $(0, 1)$ loops. This loop goes around the axis of revolution axis once. It should be accompanied by another loop of the same type to fulfill the topological requirements of the cross-section.

3. $(n, 1)$ loops with $|n| \geq 1$. This defect loop must be accompanied by another of the same kind to fulfill the topological conditions and avoid intersection between the two disclination lines.

4. $(n, 2)$ loops with $|n| \geq 1$. This loops automatically fulfill the anchoring conditions with a single disclination line that goes twice through every cross-section.



These type of loops are depicted in Figure 7.11c in $(\theta, \varphi)$ coordinates and in Figure 7.11d on a toroidal surface.

While the above discussion is valid for the PP configuration in all cases, for the PPLD configuration it is only true for $q \geq 1$ since in these cases there are two disclinations at all cross-sections which repel each other so that the disclination lines run in an effective toroidal surface. Loops with $q = 0$ are in all cases contractible to a point inside the toroidal volume and thus, they are not topologically protected; these loops can either self-annihilate or contract to a defect point.

### 7.4.2 Identifying disclination lines with epifluorescence microscopy

Identifying the vertical position of disclination loops from bright field and crossed-polarizers images could be difficult. In bright field the disclination lines are not very clear (Figure 7.10a), while under crossed polarizers, it is hard to tell from the resulting texture what the actual path of the disclination is (Figure 7.10b). To improve the image of the disclination lines, we dope our liquid crystal with a fluorescent molecule that accumulates at the disclination lines and image our tori using epifluorescence microscopy. This method has been previously used to study disclination lines in different configurations [192, 193, 194, 195].

Epifluorescence microscopy is a type of fluorescence microscopy where the sample is illuminated at a certain wavelength through the microscope objective. The light is absorbed by a fluorescent dye, which emits at a longer wavelength. This emitted signal goes through the objective and is captured by the camera.

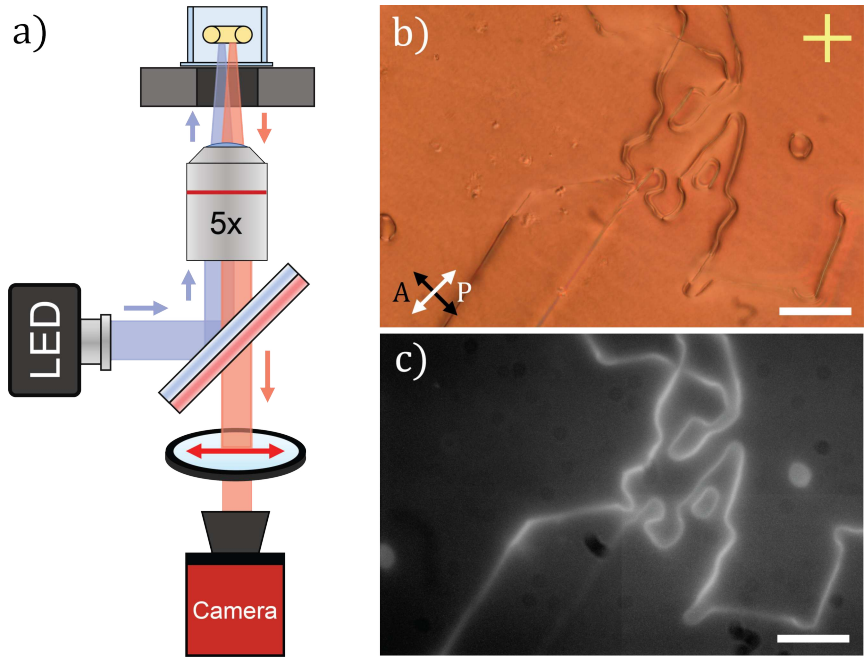



**Figure 7.12:** a) Simplified schematic of epifluorescence microscopy. The polarizer is optional. b) Crossed polarizer image of a twisted cell. The crossed polarizers form a 45° angle with respect the rubbing direction indicated by a yellow cross. c) Epifluorescence microscopy of the same cell as b) where the disclination appear as bright features. Scale bars are $100\mu m$.

The shift between the absorption and emission wavelengths allows separating the excitation and emission light paths using a dichroic mirror that is reflective to the excitation wavelength and transmittive to the emitted light. A schematic of the setup is shown in Figure 7.12a.

In our experiments, we use the multi-color LED source Colibri 7 of the Axio Observer microscope (Zeiss) as the excitation source. This source uses LEDs to emit at different wavelengths. We use the provided dichroic mirror which reflects all of the wavelengths emitted by the LED source and transmits the other wavelengths. We can also add a polarizer after the dichroic mirror.

As the fluorescent dye we use pyrromethene 597 (PMN). 5CB is doped with the fluorescent dye at a concentration of 0.01 wt%. The interesting properties of this dye makes it suitable for imaging disclination lines; it is less soluble in the 5CB nematic phase than in its isotropic phase [196, 197]. The dye then tends to concentrate in the non-nematic core of singularities. The fluorescence signal is, then, stronger at those regions, which appear brighter. Furthermore,

in the nematic phase, PMN 597 aligns with the director field [194]. Since it is an anisotropic molecule the dipole excitation depends on the polarization of the incident light. The molecule absorbs more light when the polarization of light is in the direction parallel to the molecule and, conversely, it emits polarized light in that direction. PMN 597 absorbs in the wavelengths between 450 and 575nm, with its absorption peak at around 525nm, and emits between 550 and 650, with its emission peak at around 575nm [198]. To excite the dye we use the blue led of our source, which emits at $(469 \pm 19)nm$. Although this is at the edge of the absorption band, and ideally we want to excite near the emission peak to improve efficiency, it is the only LED in our setup able to excite PMN 597.

To test our setup we make planar twisted cells [199, 200, 201, 202]. This type of cell is characterized by having parallel boundary conditions and preferred directions at the top and bottom plate that are perpendicular to each other. The director field is then forced to twist when going from the top to the bottom plate. Interestingly, since both rotation senses cost the same energy, it is common to have configurations consisting on domains with different twist directions separated by disclination lines.



To make our twisted cells we first clean two glass slides by sonication in a mixture of water and detergent for 10 min followed by sonication in DI water for 5 min. The slides are then washed and dried with nitrogen gas. To force the planar anchoring, we spin-coat the slides using a 3% PVA solution. The protocol for spin-coating consists on a first spin at 600 rpm for 12 seconds followed by a second spin at 1500 rpm for 60 seconds. Once we have our PVA thin layer on the glass we evaporate the water by pre-heating the slides at $80°C$ for 10 min and then heating them at $140°C$ for 90 minutes. To impose the preferential anchoring at the surface we gently rub the coated side with a cloth in the direction we want the anchoring. We finally assemble the cell by putting $25\mu m$ thick double sided tape as spacers and use UV glue to hold them together.

We fill our cell with the fluorescently doped 5CB and observe it in the microscope. Disclination lines can be seen as thin lines in bright field. Under crossed polarizers, with the polarizers at 45° with respect to the rubbing direction, the disclination lines are clearly visible in a bright background indicative of the twist (Figure 7.12b). If we observe our sample in epifluorescence, bright lines are observed in a dark background. This lines are the same ones observed under crossed polarizers (Figure 7.12c), confirming that the fluorescent dye accumulates in the disclination lines making the liens visible irrespective of the nematic texture.

Finally we make homeotropic tori with the fluorescently doped 5CB. While under crossed polarizers the disclination lines at different planes affect the birefringent texture, making it sometimes difficult to interpret the image and even

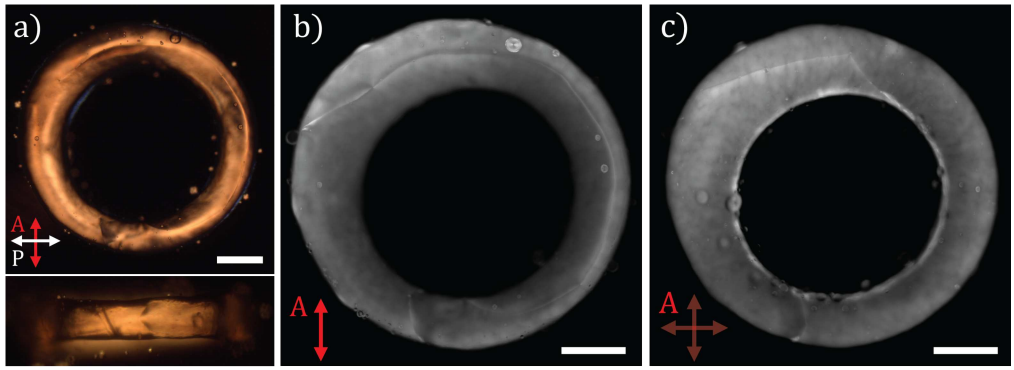



**Figure 7.13:** a) Crossed polarizer image of the texture of the homeotropic drop one day after made. Bottom image corresponds to side view where disclinations can be seen. b) Epifluorescence image of the same torus with the analyzer at 90°. The disclination lines observed corresponds to the one in the bottom surface. c) Epifluorescence image of the torus when the cuvette is set upside down. The image has been flipped to coincide in orientation with a) and b). For visualization purposes the image is a 50/50 mixture of the images with the analyzer at 90° and 0°. Scale bars are 500$\mu m$.



discern the lines (Figure 7.13a), with epifluorescence microscopy, we can clearly see the disclination lines as bright lines in a homogeneous background (Figure 7.13b). Using the analyzer makes it easier to discern the disclination lines due to the polarized emission. Depending on the orientation of the analyzer, different regions of the disclination lines look brighter or darker. The disclination lines that appear in epifluorescence microscopy correspond only to some of the ones observed under crossed polarizers. When placing the sample upside-down, we indeed observe other disclination lines (Figure 7.13c). Since our sample is quite thick, this could mean that epifluorescence only allows seeing disclination lines on the illuminated surface or close to it, with the disclination lines far from it not being visible. From the experimental images, there is an apparent continuity between disclination lines at both surfaces and no disclination line disappears in the middle of the torus; all of them are lost at the inner or outer rings. This could be interpreted as the disclination lines being on or close to the surface and going continuously through the inner/outer region.

These observations lead us to believe that the configuration of the cross-section with disclination lines is either planar polar with the disclinations on the surface or PPLD with the disclination lines very close to the surface, as only the would they be seen with epifluorescence microscopy.

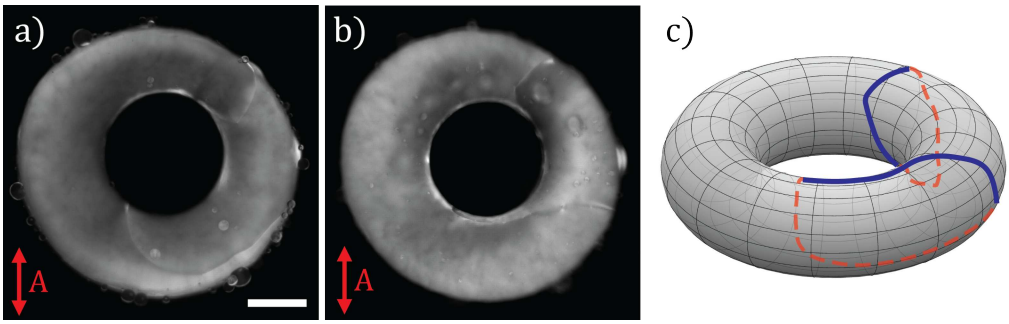



**Figure 7.14:** a) Epifluorescence image of bottom surface of a torus with the analyzer in the vertical position. b) Epifluorescence image of the top surface of the same torus placed upside down. Scale bar is 200$\mu m$ c) Reconstruction of the two $(1, 0)$ loops. Blue line corresponds to the part of the line on the visible side of the torus while the dashed red line correspond to the part of the line in the hidden part.



### 7.4.3 Loop characterization

With this technique we can start characterizing the disclination loops in our nematic tori. The most common type of loop we find is the $(1, 0)$ that just rotates around the tube once. An example of a torus with two of these loops is shown in Figure 7.14 together with the reconstruction on a toroidal surface. Although we could expect that these loops would minimize their length to reduce energy, we find that the loops are way longer than their minimum length. We also observe sharp turns of the disclination lines. This could indicate that there is pinning of the disclinations at some points in the surface that prevents them from reducing their length and resulting in the sharp turns observed.

This is reminiscent to what is observed for twisted nematic cells. In this case the disclination lines are expected to be in the bulk, but pinning of the disclination lines on the surface is sometimes observed. From these pinning points the disclination lines can go back to the bulk and minimize their length between pinning points [199, 202].

Another case that is sometimes observed is the case of a $(0, 0)$ loop. This is a trivial loop that could be contracted to a point. Depending on the topological character of the loop, this contraction can result in total annihilation of the disclination or in a point defect. In the case where this loop is observed, it was imaged a couple of hours only after the torus was made. It is possible that after some time the loop would have shrunken or annihilated. The experimental images with the reconstruction of the loop are shown in Figure 7.15.

Finally, we sometimes find a configuration with two $(0, 1)$ loops that go around the revolution axis of the torus. This case is relevant since that corre-

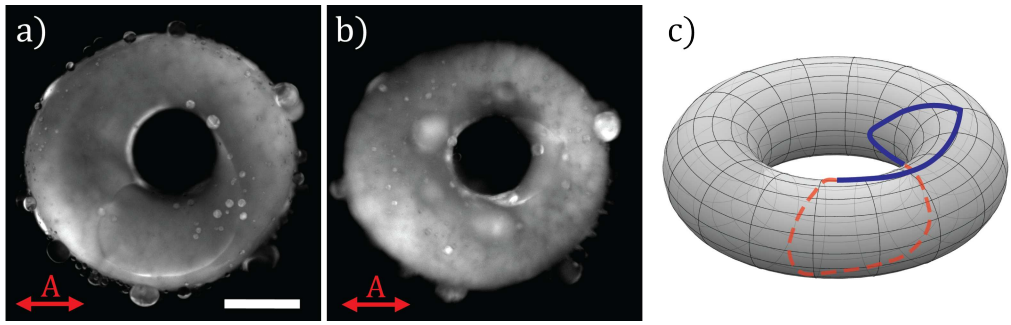



**Figure 7.15:** a) and b) Epifluorescence image of bottom and top surface of the torus with the analyzer in the horizontal position. Scale bar is $200\mu m$. c) Reconstruction of the $(0, 0)$ loop.



sponds to the classical PP or PPLD configuration, depending on whether the disclination is in the surface of the torus or not. This configuration has been even observed sometimes for tori in yield stress material without ethanol, where they remain stable for the lifetime of the torus (around a month). Both loops can be seen in crossed polarizers. While only one is observable from the top, as shown in Figure 7.16a, there are clearly two disconnected disclination lines at different focal planes when looked from the side (Figure 7.16b). These two lines are also observed, although very faintly due to the bubbles that decorate the disclination lines in epifluorescence, where one disclination loop is observed at the bottom surface (Figure 7.16c) and the other is observed at the top surface, close to the inner ring (Figure 7.16d).

The reconstruction of the two loops is shown in Figure 7.16e. If we look at one cross section, both disclination lines are located in almost diametrically opposite regions, consistent with the PP and PPLD configurations. Interestingly, one disclination is located near the inner ring, corresponding to the minimum length $(0, 1)$ loop possible in the torus. This is reasonable since the energy cost of a disclination line is proportional to its length.

Moreover, if we look carefully at the crossed polarizer top view, we observe interference colors in the region between disclinations (see inset of Figure 7.16a). These bright colors appear for thin enough samples or low birefringence as shown in the Michel-Levy chart. For the thickness of our tori, the birefringence has to be low enough for the bright colors to appear, which indicates that the director field is almost vertical in those areas. This is consistent with the expected director field configuration for the PP configuration with the disclination lines located where we experimentally find them, as shown in Figure 7.16f. In this schematic we see that the blue disclination is close to the minimum length possible while the red one, instead of been diametrically opposite is closer to

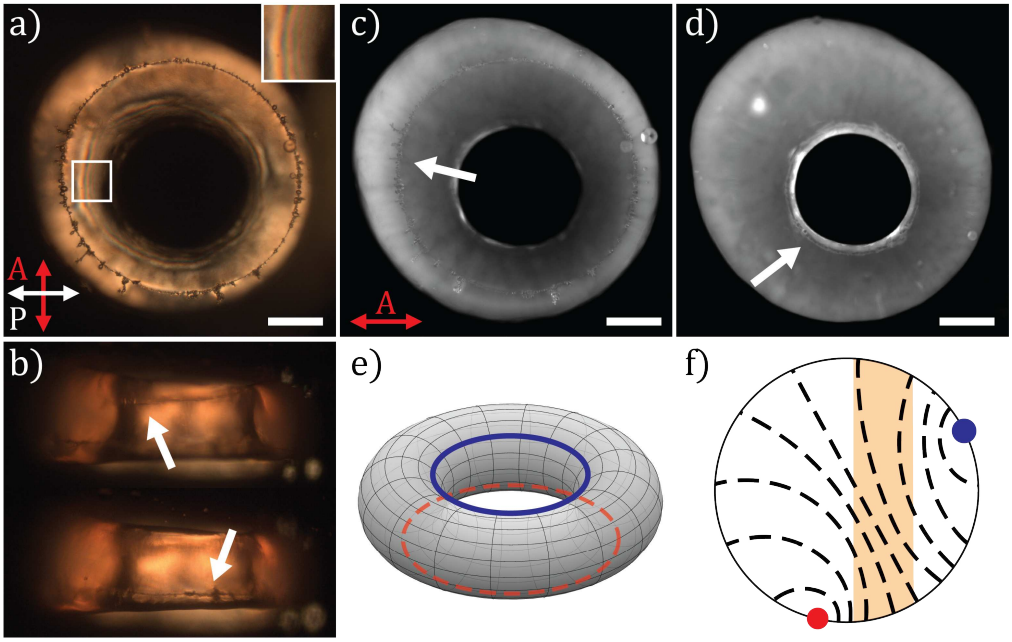



**Figure 7.16:** a) Top view image of the torus between crossed polarizers where one disclination line is clearly visible. Inset shows the magnified interference colors of the white square. b) Side view of torus in crossed polarizer with the focus in different planes. For each plane one disclination line is seen. c) and d) Epifluorescence images of the bottom and top surface respectively. White arrow indicates the position of the disclination line. e) Reconstruction of the disclination line loops on the toroidal surface. f) Schematic of the director field configuration of the cross-section. The orange region corresponds to where the director field is almost vertical and could explain the interference colors. Scale bars are $200\mu m$.

the inner ring in one of its sides. This might result from the fact that the total energy could be reduced if the loop reduces its length, at the expense of slightly increasing the elastic energy. Another explanation could rely on the possible pinning of the disclination line. The fact that we have observed other tori in the same configuration makes this last option less plausible.

The schematic in Figure 7.16f shows the director field tangential to the cross-section. Despite this simple configuration explains some of the experimentally observed features, we know it can not be the actual configuration. If this was the case, there should be a dark cross parallel to the polarizers, similar to the planar case that we do not see. This means that the configuration is not as simple as the one proposed and the director field may twist out of the cross-sectional plane.

We have found that for a yield stress material with ethanol and 6mM SDS

concentration we can generate homeotropic nematic droplets of large tube radius $\sim 150\mu m$ with long-lasting disclination loops. We have been able to characterize the loops in terms of their winding numbers $(p, q)$ using epifluorescence microscopy. Although we identified different types of loops and found, among the observed configurations, the planar polar configuration with two $(0, 1)$ disclination lines, more experiments should be carried out to fully understand the configuration of the disclination lines. It would be interesting to know whether they are located at the surface, in the bulk but close to the surface or a mix of the two situations and whether all the lines are stable for long times. It also remains to be explored whether other types loops can be generated and/or favored by changing the geometrical parameters of our tori, like for example, their aspect ratio.

## 7.5 Heating and cooling homeotropic tori



As done for planar tori, we can heat our homeotropic tori to the isotropic phase and cool them back to the nematic phase to see whether we get any interesting metastable configurations. We use our tori made in the yield stress material without ethanol, since they can be preserved for longer and their composition is closer to that used in the planar case. The starting equilibrium configuration for all SDS concentrations probed is the escaped radial one (see Section 7.2.2).

After heating and cooling our tori we observe a couple of point features in the bright field image (Figure 7.17a). When observing the configuration in crossed polarizers we can see that the configuration corresponds to the typical escaped radial with two point features separating two domains (Figure 7.17b). Moreover, these point features are inside the torus, as confirmed by the side view under crossed polarizers (Figure 7.17c). This is consistent with the presence of point defects separating two escaped radial domains with a different escape direction. If the escape direction of both domains points to the defect, the defect is a $+1$, while if they point away, it is a $-1$ defect; see the schematic in Figure 7.17d. This configuration, called the escaped radial with point defects (ERPD) (see section 2.4.2), has been known for a long time and has been observed in homeotropic capillaries [153, 203].

We can characterize the charge of the defects by rotating the crossed polarizers and quantify the rotation sense of the dark brushes. If they rotate in the same/opposite sense, the point defect has a $+1/-1$ topological charge. This is shown in Figure 7.17e,f, where we can see that the top defect is a $+1$ while the bottom one is a $-1$. Note that due to the bulk character of the nematic and that the defects are 3D, the texture is less clear than what one often sees when distinguishing $+1$ and $-1$ surface defects [204]. Due to the periodic boundary conditions and the zero total topological charge constrain imposed by the

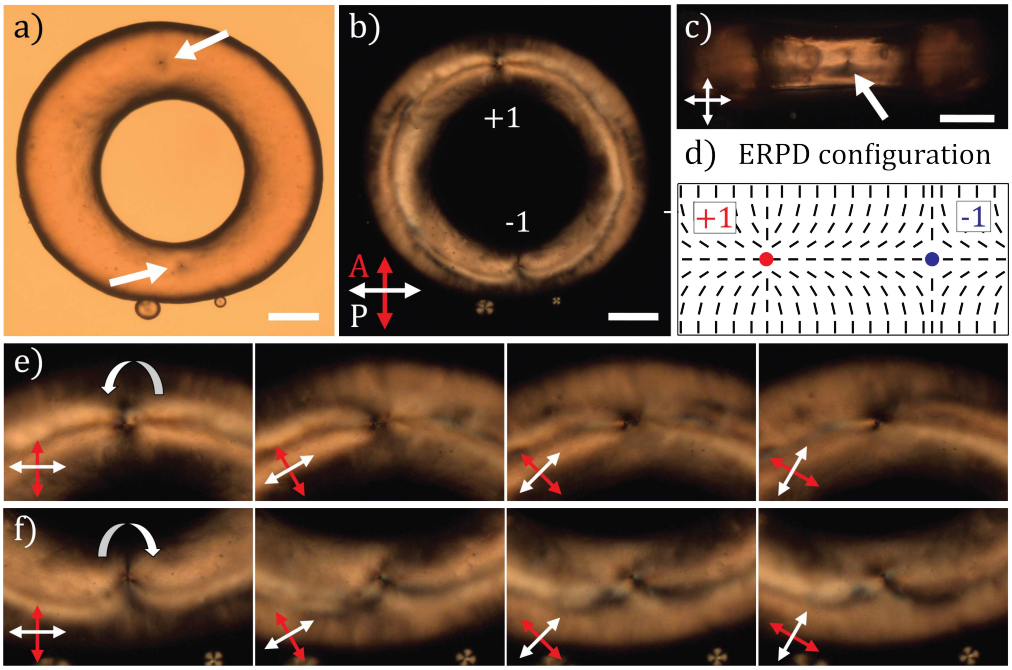



**Figure 7.17:** a) Bright field image of a torus after heating and cooling. Arrows point the two point-like features. b) Crossed polarizer image of the same torus. c) Crossed-polarizer side view of the torus. Arrow point the point-like feature. d) Schematic of the escaped radial with point defect configuration on a plane containing the cylinder axis. e) and f) Texture change with rotating crossed polarizers of the top and bottom point-feature respectively. Curved arrows indicate the sense of rotation of the brushes which is coincides with the rotation sense of the crossed polarizers for the top defect and is opposite for the bottom one. Scale bars are $200\mu m$.

Poincaré-Hopf index theorem, the number of these point defects has to be even. In our experiments we have only observed the case with two point defects. The ERPD configuration was also observed once after the torus was made without the need to heat and cool.

By making our homeotropic tori in a yield stress material with no ethanol and 2mM SDS concentration, we can generate the ERPD configuration by heating and cooling and then observe what happens with the point defects during the homeotropic-planar transition by tracking the evolution of the configuration with time. As shown in Figure 7.18a, as the anchoring conditions go from homeotropic to planar the point defects start moving towards the outer or inner ring depending on the topological charge. The positive defect goes to the outer

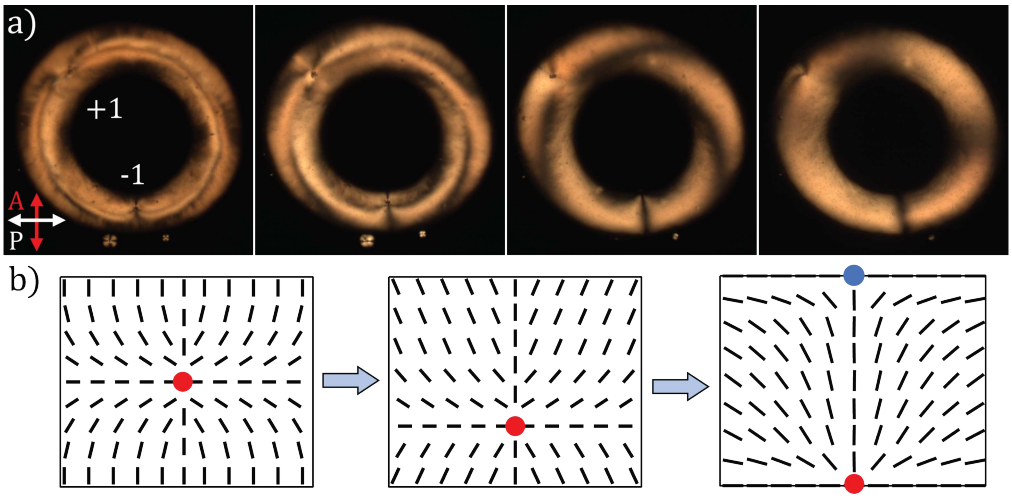



**Figure 7.18:** a) Snapshots of the homeotropic to planar transition of a torus with the ERPD configuration. The topological charge of the defect is indicated. The final configuration has two defect pairs. b) Schematic of the transition from point defect in the bulk to defect pair.



ring while the negative one moves toward the inner region. After the transition to the planar configuration has ended we can observe that we have two defect pairs, one per original point defect. In these defect pairs, one of the boojums of the pair comes from the point defect already present while the other is generated on the surface during the transition. A schematic of this process is shown in Figure 7.18b.

## 7.6 Droplet nucleation in homeotropic nematic tori

Lastly, for our homeotropic tori inside a yield stress material without ethanol, it is common to observe both in bright field and crossed polarizers, the formation in time of chain-like configurations. The amount of objects that form increases after a heating and cooling cycle. Furthermore, they are located in the liquid crystal, inside the toroidal volume, as proven by the top and side view bright field images of a torus with a large amount of these objects (Figure 7.19a and b). The aggregates, in fact, tend to locate themselves at the center of the cross-section. When using a higher magnification objective, we can see that the chains consist on droplets that tend to align with the nematic director, forming a structure reminiscent of the escaped radial configuration (Figure 7.19c and d).These objects also tend to be located at singular cores of point defects, as shown for the escaped radial configuration with point defects in Figure 7.17a, or

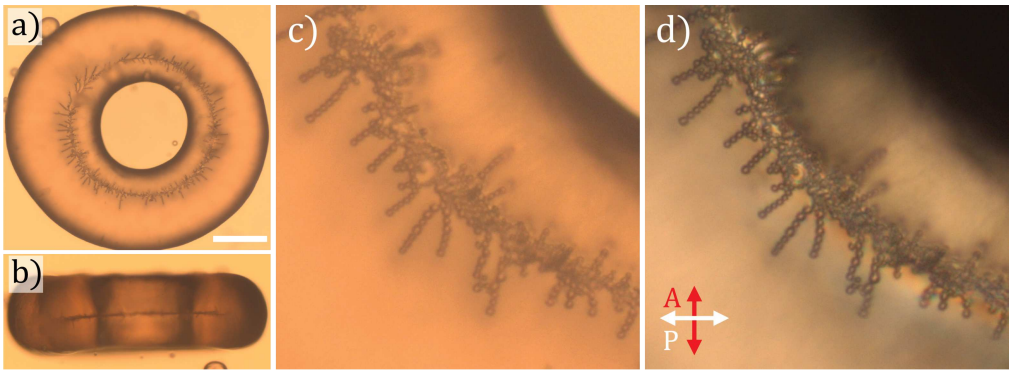



**Figure 7.19:** a) Bright field top view image of a homeotropic torus with chain like aggregates. Scale bar is 200$\mu m$. b) Bright field side view of the same torus. c) Close up bright field image on aggregate chains showing their droplet nature. d) Close up crossed-polarizer image of the aggregates.



at disclination lines, where they form a chain along the line as shown in Figure 7.16a.

This configuration is indeed very similar to the one recently reported in [109], where they study the phase separation in liquid crystal mixtures with ethanol. While cooling the mixture from the isotropic single phase, once the system has separated into a liquid crystal rich nematic phase and a solvent phase, if the temperature is further reduced, chains of solvent droplets appear in the liquid crystal. This is attributed to the solubility reduction of ethanol with temperature and subsequent nucleation of ethanol rich droplets. These droplets align into chains following the director field to reduce the elastic energy, as reported long ago for inverted emulsions and colloids in nematic liquid crystals [205, 206, 207, 208, 209]. Additionally, it has also been found that the solvent tends to nucleate at the point defect of homeotropic nematic droplets [210, 211]. This has also been observed in Arjun Yodh's group[1] for 5CB droplets in water with SDS where water droplets tend to nucleate at the point defect.

This explains the origin of our objects and their appearance when heating and cooling. When heating the tori, water solubility in the liquid crystal increases. When the temperature is reduced back again, the solubility drops, and water phase separates forming small droplets that aggregate into chain-like structures to minimize elastic energy. This happens in general when the concentration of water in the liquid crystal is larger than the equilibrium one, which can occur simply when the temperature reduces overnight, leading to water droplet nucleation. A possible reason of why this has not been noticed

[1] Discussed in private communications.

for tori in a yield stress material with ethanol is that the ethanol that diffuses into the liquid crystal might increase the solubility of water and prevent phase separation.

## 7.7 Conclusions

In this chapter, we have explored the different configurations of homeotropic tori in a yield stress medium with ethanol as a function of the surfactant concentration imposing the anchoring conditions and aspect ratio. For large surfactant concentrations (8mM) we observe defect-free configurations, which can be classified into two categories depending on the visual appearance under crossed polarizers: Spiral and concentrated. While the concentrated configuration corresponds to a twisted escaped configuration where the twist is induced by the curvature of the torus, the spiral configuration was previously attributed to be the equilibrium configuration at low aspect ratios and different from the concentrated one.



We have proven that this spiral configuration is indeed transient and relaxes into the concentrated one after long enough time. Moreover, in experiments using an outer yield stress material with ethanol, the spiral configuration has appeared as an intermediate configuration during the transition from the twisted escaped radial to the planar configuration, indicating that it could correspond to the twisted escaped radial configuration with finite anchoring strength. This is further confirmed by performing Jones matrix simulations of the theoretical texture for strong and weak anchoring, confirming this interpretation. This also implies that when making homeotropic toroidal droplets in an outer yield stress material with ethanol, the initial anchoring strength is small and increases over time.

When the concentration of surfactant is lower in the yield stress without ethanol (6 mM), configurations with disclination lines appear. These disclination lines seem to be close to the surface and form loops that can be topologically classified using epifluorescence microscopy. We have observed $(0, 0)$, $(1, 0)$ and $(0, 1)$ loops, where in the last case, there are two different loops resulting in a configuration similar to the planar polar. Knotted loops and disclination lines have been previously observed in toroidal cavities filled with liquid crystal with almost square cross-sections and homeotropic anchoring conditions [52]. In these experiments, the tube size is of the order $\sim 1\mu m$, small enough such that the planar configuration is the equilibrium one, but too small to be able to observe the disclinations with conventional microscopy. In our case we observe stable disclination loops during the lifetime of the sample ($\sim$1 day) in toroidal droplets with a tube size of the order $\sim 100\mu m$, which is typically too large for the observation of the planar polar configuration, at least in capillaries. We

attribute the appearance of these loops to the initial low anchoring strength that makes the planar polar configuration the ground state. As time passes, the anchoring strength increases and the system becomes trapped in a metastable state. Pinning of the disclination lines on the surface can also contribute to this stability.

Finally, if the surfactant concentration is low enough ($\leq$4mM), the homeotropic boundary conditions are lost and the planar double-twisted configuration is recovered.

Chapter 8

# Conclusions and further work

The main focus of this thesis is the study of the configurations acquired by the nematic liquid crystal 5CB when confined to a toroidal droplet with different boundary conditions and external fields. We focus on configurations populated with point defects, disclination lines and walls. We show how toroidal confinement, together with anchoring control and external fields can produce a plethora of configurations with different types of stable defects that can be studied in a simple way. In passing, we have also done work with hydrogels and a bit of drop formation.



## 8.1 Nematic liquid crystals confined to toroidal droplets

When we confine the nematic liquid crystal 5CB to a toroidal droplet with planar degenerate anchoring, the Poincaré-Hopf index theorem establishes that the total topological charge has to be zero. Prior work showed the defect-free ground state spontaneously breaks reflection symmetry by forming a double twisted configuration [9]. Note, however, that despite the total topological charge has to be zero, this does not imply that defect populated configurations can not exist.

In chapter 4 we study the stable defect populated configurations that appear after heating the toroidal droplets to the isotropic phase and cooling them back to the nematic phase. We show by polarized optical microscopy and simulations that these configurations are mainly made of $\pm 1$ defect pairs with the positive/negative defect located in the inner/outer ring of the same cross-section. Interestingly, the stability of these defect pairs does not come from the Gaussian curvature of the torus since they are also observed in cylinders. The energy barrier comes from the large bulk rearrangement needed for the defects to annihilate.

The only role of curvature comes from the location of the positive and nega-

tive defect which becomes random in the case of the cylinder. We attribute this location to the asymmetry between the inner and outer parts of the torus. This asymmetry results in an asymmetry in the bulk energy depending on the defect location that favors the observed configuration and that is lost in the cylinder. Another factor contributing to this is the interaction of defects with the underlying curvature such that point defects are attracted to regions of like-signed curvature.

We also discuss a different configuration with zero topological charge that is less frequently observed. It appears in bright field as an dark elongated "X". Although the exact configuration is unknown, we hypothesize that it might be a type of solitonic structure.

For the defect free double twisted configuration of planar tori, it can only be explained theoretically when the saddle-splay energy term is included. In prior work, this was interpreted in pure surface terms and related to the Gaussian curvature of the torus [10]. In chapter 5 we introduce the local normal decomposition of elastic distortions of the nematic director field into four fields. This results in a local interpretation of the saddle-splay term as biaxial splay. In this sense, the origin of the double twisted configuration is not the biaxial splay elasticity but the low double twist constant, $K_2 - K_{24}$, favoring double twist by lowering the bend distortion of the axial configuration. In fact, if, as previously estimated, $K_{24} \approx 1.02K_2$, the double twist constant would be slightly negative, indicating that double twist reduces the free energy.



However, since a state with only double twist deformation is not possible, the nematic phase is the ground state. This is proven by looking at the compatibility conditions for a nematic liquid crystal. These are equations that constraint the values of the deformation fields and their derivatives to ensure continuity of the director field. Using the normal mode decomposition, we derive the compatibility conditions using an infinitesimal approach where continuity of the director field is imposed when going through two different paths. Using this method we recover the recently derived compatibility equations [157, 158] in a visual and intuitive way. Moreover, this approach allows understanding how the curvature of the manifold enters the equation through the concept of parallel transport around a loop (holonomy).

In chapter 6, we experimentally study the configuration change of the planar nematic tori of chapter 4 when a magnetic field perpendicular to the revolution axis of the torus is applied. For the liquid crystal used, 5CB, the magnetic field tends to align the director field with it. We find that the configuration of planar tori in a magnetic field can be understood purely in terms of alignment inversion walls. For an initial defect-free configuration, we observe an alignment of the director field except for the formation of two walls in diametrically opposite regions of the torus aligned with the external field. This two walls, in fact,

concentrate the whole $2\pi$ rotation of the director as it goes around the torus into two localized regions of $\pi$ rotation each.

When there are defect pairs, we show how these can be interpreted as thick inversion walls with a rotation sense opposite to the rotation around the torus. We show how when they are located in the wall forming regions of the defect-free case they allow the perfect alignment of the director field since they reduce the total rotation of the director around the torus by $\pi$ each. The most interesting fact is when we have a single defect pair far from the wall forming region and apply a magnetic field. In this situation, not only the two walls of the defect free case, but an additional wall associated to the defect pair also forms. This wall, due to the mobility of the defects, transforms into a twist wall that reduces the energy, since the twist elastic constant of 5CB is the smallest one. When the magnetic field is removed the defects return to their original position.

This shows that inversion walls constitute the equilibrium state for a planar nematic tori when a magnetic field is applied, as opposed to the usual way of obtaining walls that relies on instabilities or symmetry breaking degeneracy. Moreover, we observe the transition between different types of wall, which, as far as we are aware has not been reported before.

Finally, in chapter 7 we study the case where the boundary conditions are homeotropic. Previous work in the group produced a phase diagram of the configuration observed as a function of the concentration of SDS, which is a proxy to the anchoring strength, and the aspect ratio of the torus. For high SDS concentrations (8 mM), two different configurations were observed, one with a helicoidal pattern of dark brushes and the usual escaped radial configuration. We show that the helicoidal pattern is transient and eventually transforms into the escaped radial configuration, which is the stable one.

Moreover, when using an external yield stress material without ethanol to preserve the samples for long times, the helicoidal configuration is not observed. When using a low concentration of SDS of 2mM and monitoring the torus evolution through time we observe a transition between the escaped radial to the double-twisted axial configuration where the helicoidal configuration appears as a transition state between the two. This suggests that the helicoidal configuration corresponds to finite anchoring and a director that is not perpendicular to the surface. We confirm this fact by comparing the experimental textures with Jones matrix simulations. The transition observed from the escape radial to the axial configuration was not thought to be observable since the planar polar configuration always has lower energy than the axial one. Moreover, comparing the Jones matrix simulations with the experimental images allows estimating the anchoring strength. This method could in principle be used to estimate the anchoring strength of different surfactants at a certain concentration range.

We conclude our study on homeotropic tori, by briefly studying the disclina-

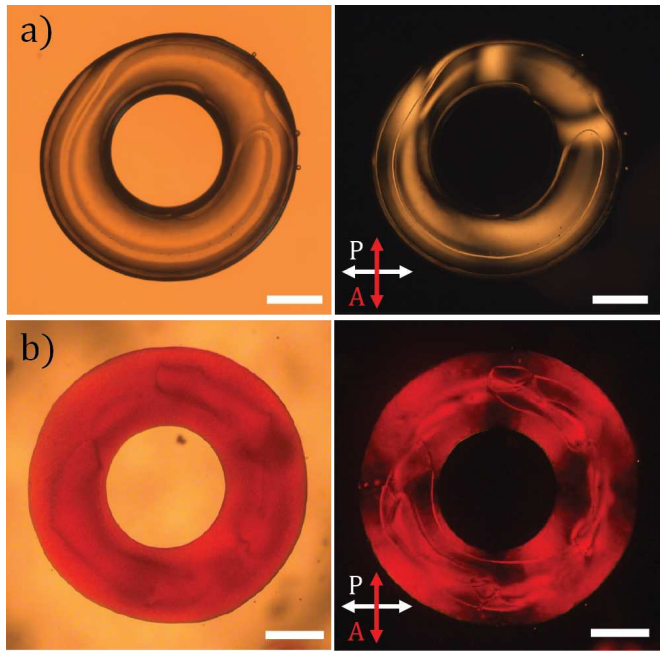



**Figure 8.1:** a) Bright field and crossed polarizer images of a cholesteric toroidal droplet. The cholesteric material is 5CB doped with 0.1% CB15 (4'-[(S)-2-Methylbutyl]biphenyl-4-carbonitrile) as a chiral dopant. b) Bright field and croseed polarizer images of a lyotropic chromonic toroidal droplet. The material used to make the torus is a $\sim$ 30% solution of Sunset Yellow (Disodium 6-hydroxy-5-[(4-sulfophenyl)azo]-2-naphthalenesulfonate) in water. Scale bars are $300\mu m$.



tion line populated configurations that appear at SDS concentrations of 4-6mM when the yield stress material has ethanol. Configurations with disclination lines are not predicted to be the stable ones for the size of our toroidal droplets and high anchoring strength. Nevertheless, the transition from the helicoidal to the escaped radial configuration suggests that the anchoring strength increases with time, so that at the beginning, the anchoring can be low enough for configurations with disclination lines to be stable. When the anchoring strength increases, the configuration becomes metastable due to the disclination loops not being contractible to a point or by the pinning of the disclination lines for the contractible case.

Summarizing, we have studied different ways for a nematic liquid crystal in toroidal confinement to arrange and deal with the frustration of its confinement. In our case, we observe stable defect populated configurations, equilibrium inversion walls when a magnetic field is applied, and configurational transitions when the anchoring strength changes.

There are also aspects of the work that require further research. These include understanding the "X pattern" configuration and its stability, understanding the origin of the asymmetry of the inversion walls that appear in the defect-free case and that seems related to the initial chirality of the double-twisted structure, and further understanding and studying the disclination line configurations in homeotropic tori.

The plethora of configurations and phenomena that can be observed in toroidal confinement for the simple nematic liquid crystal phase rises the question of what happens with other liquid crystal phases. This includes more ordered phases, like for example cholesteric liquid crystals, where the conmensurability of the pitch with the tube radius can further frustrate the liquid crystal preferred configuration. Indeed preliminary work with planar anchoring shows interesting features, with possible disclination lines (Figure 8.1a). Other interesting materials to confine into toroids are chromonic lyotropic liquid crystals, which have a very low single twist constant $K_2$ and thus, great preference for double twisting. Figure 8.1b shows some preliminary data, which is complicated by water diffusion out of the toroidal droplet into the outside oil-based yield stress material, densifying the mesogen concentration to result in the formation of the solid phase before the liquid crystal has fully relaxed.



## 8.2 Hydrogels

Our results with hydrogels are described in the different sections of chapter 3. We first show the created laboratory setup for generating chitosan gels through photopolymerization and study their water evaporation kinetics. We find that the evaporation curve for a single gel can be described by the Maxwell model where diffusion of water vapor is the limiting factor in the evaporation rate. When having an array of gels, water evaporation slows down and becomes slower as the gels get closer due to local vapor saturation effects. When the gels are too close, the water evaporation rate becomes constant, as for a layer of water. We finally compare the water evaporation rate of the chitosan gels to that of pure water finding that water evaporation is slower for the hydrogels. Further experiments show that this slow down is not a result of a decrease in the equilibrium water vapor saturation concentration. We attribute the slow down to a kinetic effect coming from an increase energy barrier for water molecules to escape the hydrogel. This causes the evaporation rate of the water molecules to become comparable to the water diffusion rate such that the water vapor concentration at the surface becomes smaller than the saturation one.

After studying the water evaporation rate of chitosan hydrogels we design a setup for a parallelized and continuous production of these gels that can scale up their production. Our injection tests show that not all capillaries inject

simultaneously for neither flow driven or pressure driven injection and rationalize our results in terms of the Laplace pressure of the pending drops that form. We also discuss some preliminary polymerization tests, where the setup is able to produce solid gels in a single injection mode. Our results suggest that the UV power should be increased for better results. Future work on chitosan hydrogels comprises fully testing the upscaled prototype for the production of chitosan hydrogels.

Lastly, we study a constant volume phase transition of thermorresponsive pNIPAM hydrogels when the temperature is increased suddenly above the phase transition temperature. For gels with circular cross-sections, the constant volume phase transition results in phase separation into a shrunken and a swollen region. Theoretical studies have shown that, to first order, the location of the shrunken region couples with the curvature and prefers to be in the region of negative curvature. Also, when there is no initial curvature, there is another term in the free energy that favors a spontaneous polarization, meaning that the shrunken region accumulates on one side of the cross-section. This polarization at the same time induces the deformation of the gel. This phenomenon has been called extreme thermodynamics. The coupling between curvature and polarization was experimentally demonstrated with toroidal gels [92], where the inner region of the torus is the one that shrinks inducing an instability that results in a Pringle-shape deformation. In our work we study cylindrical gels with no initial curvature and show how the shrunken region spontaneously chooses one side of the cylinder inducing the curvature of the gel. This is in agreement with the theoretical prediction resulting from the spontaneous polarization term in the free energy.



We also study the effect on the size and bath temperature on the type of deformation suffered by the gels and find that the spontaneous polarization only happens for thin enough gels. For thicker gels at temperatures below $80°C$ the gel bubbles but does not bend significantly, resulting in a corncob shape. Polarization is likely prevented by a higher instability mode that dominates the behavior of the gel. For large sizes and high temperature, an axial instability is observed where the gel barely changes size.

This work on extreme thermodynamics can be extended, and the theory further tested, by studying pNIPAM hydrogels of different shape. A natural continuation of our studies is to make experiments on "S"-shaped gels, where the region of negative curvature suddenly changes from one side of the cross-section to the other. By imposing continuity of the shrunken region, the theory predicts a spontaneous twist of the gel.

# References


[1] P. G. de Gennes, Rev. Mod. Phys. **64**, 645 (1992). (Cited on page 1.)

[2] G. L. Hunter and E. R. Weeks, Reports on Progress in Physics **75**, 066501 (2012). (Cited on page 1.)

[3] T. Kato, Y. Hirai, S. Nakaso, and M. Moriyama, Chem. Soc. Rev. **36**, 1857 (2007). (Cited on page 3.)

[4] B. Zhou, U. Gasser, and A. Fernandez-Nieves, Nature Communications **14**, 3827 (2023). (Cited on page 3.)

[5] G. H. Wannier, Phys. Rev. **79**, 357 (1950). (Cited on page 3.)

[6] Y. Han et al., Nature **456**, 898 (2008). (Cited on page 3.)

[7] V. N. Manoharan, Science **349**, 1253751 (2015). (Cited on page 3.)

[8] T. Needham, *Visual differential geometry and forms: A mathematical drama in Five acts*, Princeton University Press, 2021. (Cited on pages 3, 36, 169, 177, and 243.)

[9] E. Pairam et al., Proceedings of the National Academy of Sciences **110**, 9295–9300 (2013). (Cited on pages 4, 13, 39, 77, 112, 113, 115, 154, 163, 235, 237, 238, and 259.)

[10] V. Koning, B. C. van Zuiden, R. D. Kamien, and V. Vitelli, Soft Matter **10**, 4192 (2014). (Cited on pages 4, 13, 112, 154, 238, and 260.)

[11] M. Bowick, D. R. Nelson, and A. set, Phys. Rev. E **69**, 041102 (2004). (Cited on pages 4, 42, 129, and 170.)

[12] R. D. Kamien and J. V. Selinger, Journal of Physics: Condensed Matter **13**, R1 (2001). (Cited on page 4.)

[13] H. Y. Shunsuke Kobinata, Yuko Nakajima and S. Maeda, Molecular Crystals and Liquid Crystals **66**, 67 (1981). (Cited on page 10.)

[14] F. C. Frank, Discuss. Faraday Soc. **25**, 19 (1958). (Cited on pages 11 and 13.)

[15] K. Nayani et al., Nature Communications **6**, 8067 (2015). (Cited on pages 13, 154, 162, and 222.)

[16] J. Jeong et al., Proceedings of the National Academy of Sciences **112**, E1837 (2015). (Cited on pages 13, 40, and 222.)

[17] Z. S. Davidson et al., Phys. Rev. E **91**, 050501 (2015). (Cited on pages 13, 154, and 162.)

[18] G. Barbero and C. Oldano, Molecular Crystals and Liquid Crystals Incorporating Nonlinear Optics **168**, 1 (1989). (Cited on page 13.)

[19] S. Stallinga, J. A. M. M. van Haaren, and J. M. A. van den Eerenbeemd, Phys. Rev. E **53**, 1701 (1996). (Cited on page 13.)

[20] C. W. Oseen, Trans. Faraday Soc. **29**, 883 (1933). (Cited on page 13.)

[21] L. Longa, D. Monselesan, and H.-R. Trebin, Liquid Crystals **2**, 769 (1987). (Cited on page 13.)

[22] N. J. Mottram and C. J. P. Newton, Introduction to q-tensor theory, 2014. (Cited on page 13.)

[23] J. Nambisan, *Active defects in flat and curved spaces*, PhD thesis, Georgia Institute of Technology, 2022. (Cited on page 13.)

[24] C. A. Smith, Circuit World **34**, 35 (2008). (Cited on page 14.)

[25] S. Kobayashi, T. Miyama, H. Akiyama, A. Ikemura, and M. Kitamura, Proc. Jpn. Acad. Ser. B Phys. Biol. Sci. **98**, 493 (2022). (Cited on page 14.)

[26] A. Zangwill, *Modern electrodynamics*, Cambridge University Press, 2012. (Cited on page 15.)

[27] P. G. d. Gennes and J. Prost, *The physics of Liquid Crystals*, Oxford University Press, 1995. (Cited on pages 15, 19, 21, 26, 30, 31, 191, 209, 210, and 233.)

[28] O. L. C. Group, Molecular Crystals and Liquid Crystals **12**, 251 (1971). (Cited on page 17.)

[29] E. B. Priestley, P. J. Wojtowicz, and P. Sheng, *Introduction to liquid crystals*, Springer International Publishing, 1976. (Cited on page 17.)

[30] B. Jerome, Reports on Progress in Physics **54**, 391 (1991). (Cited on page 17.)

[31] M. G. J. Gannon and T. E. Faber, Philosophical Magazine A **37**, 117 (1978). (Cited on page 17.)

[32] C. Rosenblatt and D. Ronis, Phys. Rev. A **23**, 305 (1981). (Cited on page 17.)

[33] A. RAPINI and M. PAPOULAR, J. Phys. Colloques **30** (1969). (Cited on page 17.)

[34] A. Sugimura and O.-Y. Zhong-can, Phys. Rev. E **51**, 784 (1995). (Cited on page 17.)

[35] W. Zhao, C.-X. Wu, and M. Iwamoto, Phys. Rev. E **62**, R1481 (2000). (Cited on page 18.)

[36] Y. Cui, R. S. Zola, Y.-C. Yang, and D.-K. Yang, Journal of Applied Physics **111**, 063520 (2012). (Cited on page 18.)

[37] J.-H. Kim, M. Yoneya, and H. Yokoyama, Nature **420**, 159 (2002). (Cited on page 18.)

[38] X. Li et al., Soft Matter **14**, 7569 (2018). (Cited on page 18.)

[39] A. Fernández-Nieves, D. R. Link, M. Márquez, and D. A. Weitz, Phys. Rev. Lett. **98**, 087801 (2007). (Cited on pages 18, 38, and 107.)

[40] A. de la Cotte et al., Phys. Rev. E **105**, 044702 (2022). (Cited on pages 18 and 39.)

[41] T. Lopez-Leon and A. Fernandez-Nieves, Phys. Rev. E **79**, 021707 (2009). (Cited on page 19.)

[42] N. H. Pemika Hirankittiwong, Jirote Thongta and N. Chattham, Molecular Crystals and Liquid Crystals **0**, 1 (2024). (Cited on page 19.)

[43] I. W. Stewart, *The static and dynamic continuum theory of liquid crystals: A mathematical introduction*, CRC Press, 2019. (Cited on pages 19, 20, 209, and 210.)

[44] I. M. Gelfand and S. V. Fomin, *Calculus of variations*, Dover Publications, 2012. (Cited on pages 19, 210, and 231.)

[45] G. P. Alexander, B. G.-g. Chen, E. A. Matsumoto, and R. D. Kamien, Rev. Mod. Phys. **84**, 497 (2012). (Cited on pages 26 and 28.)

[46] N. D. Mermin, Rev. Mod. Phys. **51**, 591 (1979). (Cited on pages 27, 28, and 243.)

[47] J. Pollard, G. Posnjak, S. Čopar, I. Muševič, and G. P. Alexander, Phys. Rev. X **9**, 021004 (2019). (Cited on page 28.)

[48] W. Helfrich, Phys. Rev. Lett. **21**, 1518 (1968). (Cited on pages 33, 193, 205, and 212.)

[49] H. Hopf, Mathematische Annalen **96**, 225 (1927). (Cited on page 36.)

[50] R. D. Kamien, Rev. Mod. Phys. **74**, 953 (2002). (Cited on page 36.)

[51] D. Crowley and M. Grant, Journal of Geometry and Physics **117**, 187 (2017). (Cited on page 36.)

[52] M. Tasinkevych, M. G. Campbell, and I. I. Smalyukh, Proceedings of the National Academy of Sciences **111**, 16268 (2014). (Cited on pages 37, 39, and 256.)

[53] L. Čomić and P. Magillo, Graphical Models **112**, 101093 (2020). (Cited on page 37.)

[54] A. S. Utada et al., Science **308**, 537 (2005). (Cited on page 37.)

[55] S.-H. Kim, J. W. Kim, J.-C. Cho, and D. A. Weitz, Lab Chip **11**, 3162 (2011). (Cited on page 37.)

[56] T. Lopez-Leon, V. Koning, K. B. S. Devaiah, V. Vitelli, and A. Fernandez-Nieves, Nature Physics **7**, 391 (2011). (Cited on page 38.)

[57] A. Fernández-Nieves et al., Phys. Rev. Lett. **99**, 157801 (2007). (Cited on pages 38 and 105.)

[58] M. Kleman and O. D. Lavrentovich, Philosophical Magazine **86**, 4117 (2006). (Cited on page 38.)

[59] S. Ettinger et al., Phys. Rev. E **108**, 024704 (2023). (Cited on page 39.)

[60] M. G. Campbell, M. Tasinkevych, and I. I. Smalyukh, Phys. Rev. Lett. **112**, 197801 (2014). (Cited on pages 39 and 131.)

[61] P. W. Ellis et al., Phys. Rev. Lett. **121**, 247803 (2018). (Cited on pages 39, 77, 222, 238, and 240.)

[62] S. V. Burylov, Journal of Experimental and Theoretical Physics **85**, 873 (1997). (Cited on pages 39, 41, 235, 237, 240, 242, and 243.)

[63] I. Vilfan, M. Vilfan, and S. Žumer, Phys. Rev. A **43**, 6875 (1991). (Cited on pages 39, 41, and 223.)

[64] D. W. Allender, G. P. Crawford, and J. W. Doane, Phys. Rev. Lett. **67**, 1442 (1991). (Cited on pages 41 and 243.)

[65] E. Pairam and A. Fernández-Nieves, Phys. Rev. Lett. **102**, 234501 (2009). (Cited on pages 41, 44, 45, and 46.)

[66] A. A. Fragkopoulos, E. Pairam, E. Berger, P. N. Segre, and A. Fernández-Nieves, Proceedings of the National Academy of Sciences **114**, 2871 (2017). (Cited on pages 41 and 46.)

[67] P. W. Ellis et al., Nature Physics **14**, 85 (2018). (Cited on pages 42 and 129.)

[68] A. S. Utada, A. Fernandez-Nieves, H. A. Stone, and D. A. Weitz, Phys. Rev. Lett. **99**, 094502 (2007). (Cited on page 44.)

[69] A. A. Fragkopoulos, P. W. Ellis, and A. Fernandez-Nieves, European Journal of Physics **36**, 055023 (2015). (Cited on page 44.)

[70] E. Pairam, *Toroidal droplets: instabilities, stabilizing and nematic order*, PhD thesis, Georgia Institute of Technology, 2014. (Cited on pages 45, 112, and 113.)

[71] E. Pairam, H. Le, and A. Fernández-Nieves, Phys. Rev. E **90**, 021002 (2014). (Cited on pages 46 and 76.)

[72] M. S. Dimitriyev, Y.-W. Chang, P. M. Goldbart, and A. Fernández-Nieves, Nano Futures **3**, 042001 (2019). (Cited on pages 47, 53, 56, 82, 84, and 162.)

[73] P. J. Flory, *Principles of polymer chemistry*, Cornell university press, 1953. (Cited on pages 47 and 52.)

[74] P. J. Flory and J. Rehner, John, The Journal of Chemical Physics **11**, 521 (1943). (Cited on page 52.)

[75] S. Panyukov and Y. Rabin, Physics Reports **269**, 1 (1996). (Cited on page 52.)

[76] A. Scotti, M. Pelaez-Fernandez, U. Gasser, and A. Fernandez-Nieves, Phys. Rev. E **103**, 012609 (2021). (Cited on page 52.)

[77] R. Borrega, M. Cloitre, I. Betremieux, B. Ernst, and L. Leibler, Europhysics Letters **47**, 729 (1999). (Cited on page 52.)

[78] T. Ise, K. Nagaoka, M. Osa, and T. Yoshizaki, Polymer Journal **43**, 164 (2011). (Cited on page 54.)

[79] C. Boutris, E. Chatzi, and C. Kiparissides, Polymer **38**, 2567 (1997). (Cited on page 54.)

[80] K. Dusek, *Responsive gels: Volume transitions II*, Springer-Verlag: Springer e-books, 1993. (Cited on page 54.)

[81] K. Dusek, *Responsive gels: Volume transitions I*, Springer Berlin Heidelberg, 1993. (Cited on page 54.)

[82] P. J. Flory, Discuss. Faraday Soc. **49**, 7 (1970). (Cited on page 54.)

[83] A. Fernandez-Barbero, A. Fernandez-Nieves, I. Grillo, and E. Lopez-Cabarcos, Phys. Rev. E **66**, 051803 (2002). (Cited on page 54.)

[84] B. Erman and P. J. Flory, Macromolecules **19**, 2342 (1986). (Cited on page 54.)

[85] S. Hirotsu, Phase Transitions: A Multinational Journal **47**, 183 (1994). (Cited on page 55.)

[86] A. Suzuki and T. Ishii, The Journal of chemical physics **110**, 2289 (1999). (Cited on page 55.)

[87] T. Tanaka and D. J. Fillmore, The Journal of Chemical Physics **70**, 1214 (1979). (Cited on pages 55, 297, and 299.)

[88] I. J. Suárez, A. Fernández-Nieves, and M. Márquez, The Journal of Physical Chemistry B **110**, 25729 (2006). (Cited on pages 55 and 297.)

[89] E. Sato Matsuo and T. Tanaka, The Journal of Chemical Physics **89**, 1695 (1988). (Cited on pages 55 and 89.)

[90] E. S. Matsuo and T. Tanaka, Nature **358**, 482 (1992). (Cited on pages 56, 91, and 94.)

[91] M. Dimitriyev, *Function through form in soft matter: The influence of bounded geometries in heated gels and fluctuating proteins*, PhD thesis, Georgia Institute of Technology, 2017. (Cited on page 56.)

[92] Y.-W. Chang et al., Phys. Rev. E **98**, 020501 (2018). (Cited on pages 56, 83, 84, and 264.)

[93] R. Abdelghafar, A. Abdelfattah, and H. Mostafa, Scientific Reports **14**, 7655 (2024). (Cited on page 56.)

[94] L. Wang et al., ACS Applied Polymer Materials **5**, 9063 (2023). (Cited on pages 56 and 69.)

[95] I. Younes, S. Sellimi, M. Rinaudo, K. Jellouli, and M. Nasri, International Journal of Food Microbiology **185**, 57 (2014). (Cited on page 56.)

[96] A. Verlee, S. Mincke, and C. V. Stevens, Carbohydrate Polymers **164**, 268 (2017). (Cited on page 56.)

[97] N. Bhattarai, J. Gunn, and M. Zhang, Advanced Drug Delivery Reviews **62**, 83 (2010), Chitosan-Based Formulations of Drugs, Imaging Agents and Biotherapeutics. (Cited on page 57.)

[98] S. Takeshita, S. Zhao, W. J. Malfait, and M. M. Koebel, Angewandte Chemie International Edition **60**, 9828 (2021). (Cited on page 57.)

[99] O. M. Kolawole, W. M. Lau, and V. V. Khutoryanskiy, International Journal of Pharmaceutics **550**, 123 (2018). (Cited on page 57.)

[100] B. Li et al., Acta Biomaterialia **22**, 59 (2015). (Cited on page 57.)

[101] J. C. Maxwell, *The Scientific Papers of James Clerk Maxwell*, Cambridge Library Collection - Physical Sciences, Cambridge University Press, 2011. (Cited on page 63.)

[102] V. Vlasov, International Journal of Heat and Mass Transfer **178**, 121597 (2021). (Cited on page 63.)

[103] O. Carrier et al., Journal of Fluid Mechanics **798**, 774–786 (2016). (Cited on page 63.)

[104] B. Sobac and D. Brutin, Langmuir **27**, 14999 (2011). (Cited on pages 65 and 67.)

[105] R. Picknett and R. Bexon, Journal of Colloid and Interface Science **61**, 336 (1977). (Cited on page 65.)

[106] H. Hu and R. G. Larson, The Journal of Physical Chemistry B **106**, 1334 (2002). (Cited on page 65.)

[107] W. Massman, Atmospheric Environment **32**, 1111 (1998). (Cited on page 67.)

[108] S. Institution, W. Libbey, and G. E. Curtis, *Smithsonian Meteorological Tables*, Andesite Press, 2017. (Cited on page 67.)

[109] C. G. Reyes, J. Baller, T. Araki, and J. P. F. Lagerwall, Soft Matter **15**, 6044 (2019). (Cited on pages 78 and 255.)

[110] T. Bhattacharjee et al., Science Advances **1**, e1500655 (2015). (Cited on pages 79 and 294.)

[111] K. J. LeBlanc et al., ACS Biomaterials Science & Engineering **2**, 1796 (2016). (Cited on pages 79 and 80.)

[112] C. S. O'Bryan et al., MRS Bulletin **42**, 571–577 (2017). (Cited on page 79.)

[113] P. W. Ellis, *Nematic materials in curved spaces*, PhD thesis, Georgia Institute of Technology, 2018. (Cited on pages 81, 163, 223, 225, 236, 237, and 239.)

[114] S. M. Marquez, A. Fernandez-Nieves, T. E. Angelini, and Y.-W. Chang, 3d printing using phase changing materials as support, 2016. (Cited on page 86.)

[115] A. Boudaoud and S. Chaïeb, Phys. Rev. E **68**, 021801 (2003). (Cited on page 94.)

[116] D. Kliger and J. Lewis, *Polarized Light in Optics and Spectroscopy*, Elsevier Science, 2012. (Cited on page 98.)

[117] P. Yeh and C. Gu, *Optics of Liquid Crystal Displays*, Wiley Publishing, 2nd edition, 2009. (Cited on pages 98, 101, 110, and 126.)

[118] Microcourses, Microscope alignment for optimal image quality: Koehler illumination. https://www.youtube.com/watch?v=zrz9_ov6fak&t=853s. (Cited on page 103.)

[119] Wikimedia commons. https://en.wikipedia.org/wiki/liquid_crystal. (Cited on page 105.)

[120] W. Nesse, *Introduction to Optical Mineralogy*, Oxford University Press, 1991. (Cited on page 106.)

[121] C. Gribble, *Optical Mineralogy: Principles And Practice*, Taylor & Francis, 2003. (Cited on page 106.)

[122] R. Hoffman and M. W. Davidson, Michel-levy birefringence chart. https://evidentscientific.com/en/microscope-resource/knowledge-hub/techniques/polarized/michel. (Cited on page 107.)

[123] R. Oldenbourg, Nature **381**, 811 (1996). (Cited on page 107.)

[124] M. Shribak and R. Oldenbourg, Appl. Opt. **42**, 3009 (2003). (Cited on page 107.)

[125] B. Martínez-Prat, O. Arteaga, F. Sagués, and J. Ignés-Mullol, HardwareX **16**, e00480 (2023). (Cited on page 107.)

[126] C. Mauguin, Bulletin de Minéralogie **34**, 71 (1911). (Cited on page 110.)

[127] H. Almohammadi, S. A. Khadem, M. Bagnani, A. D. Rey, and R. Mezzenga, Nature Communications **13**, 2778 (2022). (Cited on page 117.)

[128] P. W. Oakes, J. Viamontes, and J. X. Tang, Phys. Rev. E **75**, 061902 (2007). (Cited on page 117.)

[129] M. J. Bowick, L. Chandar, E. A. Schiff, and A. M. Srivastava, Science **263**, 943 (1994). (Cited on page 118.)

[130] J. Rojo-González et al., Phys. Rev. Res. **6**, L012065 (2024). (Cited on pages 120, 127, 128, 132, 133, 134, 137, 139, and 140.)

[131] M. Ambrožič and S. Žumer, Phys. Rev. E **54**, 5187 (1996). (Cited on page 122.)

[132] R. J. Ondris-Crawford, G. P. Crawford, S. Zumer, and J. W. Doane, Phys. Rev. Lett. **70**, 194 (1993). (Cited on page 122.)

[133] M. L. Boas, *Mathematical methods in the physical sciences*, Wiley, 2015. (Cited on pages 124, 210, and 231.)

[134] Q. Liu, B. Senyuk, M. Tasinkevych, and I. I. Smalyukh, Proceedings of the National Academy of Sciences **110**, 9231 (2013). (Cited on page 126.)

[135] P. W. Ellis, E. Pairam, and A. Fernández-Nieves, Journal of Physics D: Applied Physics **52**, 213001 (2019). (Cited on page 126.)

[136] L. N. Carenza, G. Gonnella, A. Lamura, G. Negro, and A. Tiribocchi, The European Physical Journal E **42**, 81 (2019). (Cited on page 128.)

[137] C. R. Wand and M. A. Bates, Phys. Rev. E **100**, 052702 (2019). (Cited on page 129.)

[138] I. C. Gârlea et al., Nature Communications **7**, 12112 (2016). (Cited on page 131.)

[139] A. H. Lewis, D. G. A. L. Aarts, P. D. Howell, and A. Majumdar, Studies in Applied Mathematics **138**, 438 (2017). (Cited on page 131.)

[140] H. Miyazako and T. Sakajo, Proceedings of the Royal Society A: Mathematical, Physical and Engineering Sciences **480** (2024). (Cited on page 131.)

[141] P. M. Chaikin and T. C. Lubensky, *Principles of Condensed Matter Physics*, Cambridge University Press, Cambridge, 1995. (Cited on page 132.)

[142] G. K. Kanji, *100 statistical tests*, SAGE, Sage Publications, 2012. (Cited on page 137.)

[143] E. L. Kaplan and P. Meier, Journal of the American Statistical Association **53**, 457 (1958). (Cited on page 138.)

[144] M. Greenwood, *A Report on the Natural Duration of Cancer.*, London: H.M.S.O., 1926. (Cited on page 138.)

[145] J. Eun, J. Pollard, S.-J. Kim, T. Machon, and J. Jeong, Proceedings of the National Academy of Sciences **118**, e2102926118 (2021). (Cited on pages 148, 149, and 150.)

[146] I. I. Smalyukh, Reports on Progress in Physics **83**, 106601 (2020). (Cited on page 149.)

[147] J.-S. Wu and I. I. Smalyukh, Liquid Crystals Reviews **10**, 34 (2022). (Cited on page 149.)

[148] M. Kleman and O. D. Lavrentovich, *Soft matter physics: An introduction*, Springer, 2011. (Cited on page 153.)

[149] D. S. Miller and N. L. Abbott, Soft Matter **9**, 374 (2013). (Cited on page 155.)

[150] S. Žumer and S. Kralj, Liquid Crystals **12**, 613 (1992). (Cited on page 155.)

[151] S. Kralj and S. Zumer, Liquid Crystals **15**, 521 (1993). (Cited on pages 155 and 223.)

[152] S. Kralj and S. Žumer, Phys. Rev. E **51**, 366 (1995). (Cited on pages 155, 229, 230, and 243.)

[153] G. P. Crawford, D. W. Allender, and J. W. Doane, Phys. Rev. A **45**, 8693 (1992). (Cited on pages 155, 163, 222, 235, 237, 240, 242, 243, and 252.)

[154] V. H. Schmidt, Phys. Rev. Lett. **64**, 535 (1990). (Cited on pages 155 and 156.)

[155] J. V. Selinger, Liquid Crystals Reviews **6**, 129 (2018). (Cited on pages 155, 158, 159, 161, 162, and 163.)

[156] L. C. B. da Silva and E. Efrati, New Journal of Physics **23**, 063016 (2021). (Cited on pages 155, 163, and 177.)

[157] L. C. B. da Silva, T. Bar, and E. Efrati, Journal of Elasticity **153**, 755 (2023). (Cited on pages 155, 163, and 260.)

[158] I. Niv and E. Efrati, Soft Matter **14**, 424 (2018). (Cited on pages 155, 163, 168, 169, and 260.)

[159] S. Meiboom, J. P. Sethna, P. W. Anderson, and W. F. Brinkman, Phys. Rev. Lett. **46**, 1216 (1981). (Cited on page 163.)

[160] J.-F. Sadoc, R. Mosseri, and J. V. Selinger, New Journal of Physics **22**, 093036 (2020). (Cited on page 163.)

[161] J. Pollard and G. P. Alexander, New Journal of Physics **23**, 063006 (2021). (Cited on page 163.)

[162] E. G. Virga, Phys. Rev. E **100**, 052701 (2019). (Cited on pages 163 and 180.)

[163] J. Marsden and A. Tromba, *Vector Calculus*, Number pp. 1-93 in Vector Calculus, W. H. Freeman, 2003. (Cited on page 164.)

[164] S. Lang, *Green's Theorem*, pages 269–290, Springer New York, New York, NY, 1987. (Cited on page 164.)

[165] J. K. V. V. P. Panov and G. H. Mehl, Liquid Crystals **44**, 147 (2017). (Cited on page 180.)

[166] D. Demus, J. W. Goodby, G. W. Gray, H. W. Spiess, and V. Vill, *Handbook of Liquid Crystals*, Wiley-VCH, 1998. (Cited on pages 191 and 212.)

[167] W. Iglesias, N. L. Abbott, E. K. Mann, and A. Jákli, ACS Applied Materials & Interfaces **4**, 6884 (2012). (Cited on pages 191, 212, and 238.)

[168] Y. Cui, R. S. Zola, Y.-C. Yang, and D.-K. Yang, Journal of Applied Physics **111**, 063520 (2012). (Cited on page 191.)

[169] D. Rivière, Y. Lévy, and E. Guyon, Journal de Physique Lettres **40**, 215–218 (1979). (Cited on page 191.)

[170] R. J. LeVeque, *Finite difference methods for ordinary and partial differential equations: Steady-state and time-dependent problems*, Society for Industrial and Applied Mathematics, 2007. (Cited on page 211.)

[171] M. N. Ozısık, H. R. B. Orlande, M. J. Colacco, and R. M. Cotta, *Finite difference methods in heat transfer*, CRC Press, 2017. (Cited on page 211.)

[172] A. Stieb, G. Baur, and G. Meier, Le Journal de Physique Colloques **36** (1975). (Cited on page 219.)

[173] J. Nehring and A. Saupe, J. Chem. Soc., Faraday Trans. 2 **68**, 1 (1972). (Cited on page 219.)

[174] Y. Ishii et al., Soft Matter **16**, 8169 (2020). (Cited on page 219.)

[175] L. Leger, Solid State Communications **10**, 697 (1972). (Cited on page 219.)

[176] W. De Jeu, C. Gerritsma, and T. Lathouwers, Chemical Physics Letters **14**, 503 (1972). (Cited on page 219.)

[177] P. Salamon, Z. Karaszi, V. Kenderesi, A. Buka, and A. Jákli, Phys. Rev. Res. **2**, 023261 (2020). (Cited on page 219.)

[178] A. V. J. M. Gilli, S. Thiberge and F. Fried, Liquid Crystals **23**, 619 (1997). (Cited on page 219.)

[179] P. Mukerjee and K. Mysels, Critical micelle concentrations of aqueous surfactant systems:, 1971. (Cited on page 222.)

[180] A. Scharkowski, G. P. Crawford, S. Zumer, and J. W. Doane, Journal of Applied Physics **73**, 7280 (1993). (Cited on page 222.)

[181] C. Williams, P. Pierański, and P. E. Cladis, Phys. Rev. Lett. **29**, 90 (1972). (Cited on page 222.)

[182] R. B. Meyer, Philosophical Magazine **27**, 405 (1973). (Cited on pages 222, 223, and 232.)

[183] N. A. Lockwood and N. L. Abbott, Current Opinion in Colloid and Interface Science **10**, 111 (2005). (Cited on page 224.)

[184] A. I. Kovtun, S. L. Khil'ko, S. A. Zholob, and V. I. Rybachenko, Colloid Journal **72**, 389 (2010). (Cited on page 230.)

[185] Z. Bradač, S. Kralj, and S. Žumer, Phys. Rev. E **58**, 7447 (1998). (Cited on pages 230, 242, and 243.)

[186] Y. Han, Y. Hu, P. Zhang, and L. Zhang, Journal of Computational Physics **396**, 1 (2019). (Cited on page 230.)

[187] G. P. Crawford, R. Ondris-Crawford, S. Žumer, and J. W. Doane, Phys. Rev. Lett. **70**, 1838 (1993). (Cited on page 237.)

[188] J. P. McInerney, P. W. Ellis, D. Z. Rocklin, A. Fernandez-Nieves, and E. A. Matsumoto, Soft Matter **15**, 1210 (2019). (Cited on page 241.)

[189] A. Modin et al., Proceedings of the National Academy of Sciences **120**, e2300833120 (2023). (Cited on page 243.)

[190] J.-P. Luminet and B. F. Roukema, *Topology of the Universe: Theory and Observation*, pages 117–156, Springer Netherlands, Dordrecht, 1999. (Cited on page 243.)

[191] J. Jiang et al., Proceedings of the National Academy of Sciences **119**, e2122226119 (2022). (Cited on page 244.)

[192] Y. Zushi and K. A. Takeuchi, Proceedings of the National Academy of Sciences **119**, e2207349119 (2022). (Cited on page 245.)

[193] M. Wang, Y. Li, and H. Yokoyama, Nature Communications **8**, 388 (2017). (Cited on page 245.)

[194] T. Ohzono et al., Scientific Reports **7**, 16814 (2017). (Cited on pages 245 and 247.)

[195] I. Smalyukh, S. Shiyanovskii, and O. Lavrentovich, Chemical Physics Letters **336**, 88 (2001). (Cited on page 245.)

[196] T. Ohzono, K. Katoh, and J.-i. Fukuda, Scientific Reports **6**, 36477 (2016). (Cited on page 246.)

[197] J. ichi Fukuda, Do small molecules assemble at topological defects of a liquid crystal?, in *Emerging Liquid Crystal Technologies XII*, edited by L.-C. Chien, volume 10125, page 101250C, International Society for Optics and Photonics, SPIE, 2017. (Cited on page 246.)

[198] I. Nys, J. Beeckman, and K. Neyts, Journal of the Optical Society of America B **31** (2014). (Cited on page 247.)

[199] Geurst, J.A., Spruijt, A.M.J., and Gerritsma, C.J., J. Phys. France **36**, 653 (1975). (Cited on pages 247 and 249.)

[200] A. Spruijt, Solid State Communications **13**, 1919 (1973). (Cited on page 247.)

[201] A. Miyaji, M. Yamaguchi, A. Toda, H. Mada, and S. Kobayashi, IEEE Transactions on Electron Devices **24**, 811 (1977). (Cited on page 247.)

[202] E. P. Raynes and X. Jia, Liquid Crystals **44**, 1960 (2017). (Cited on pages 247 and 249.)

[203] M. Svetec, Z. Bradac, S. Kralj, and S. [Zbreve]umer, Molecular Crystals and Liquid Crystals - MOL CRYST LIQUID CRYST **413**, 43 (2004). (Cited on page 252.)

[204] A. Fernández-Nieves et al., Advanced Materials **17**, 680 (2005). (Cited on page 252.)

[205] P. Poulin and D. A. Weitz, Phys. Rev. E **57**, 626 (1998). (Cited on page 255.)

[206] P. Poulin, H. Stark, T. C. Lubensky, and D. A. Weitz, Science **275**, 1770 (1997). (Cited on page 255.)

[207] P. Poulin, Current Opinion in Colloid and Interface Science **4**, 66 (1999). (Cited on page 255.)

[208] I. Musevic and M. Skarabot, Soft Matter **4**, 195 (2008). (Cited on page 255.)

[209] M. Škarabot et al., Phys. Rev. E **76**, 051406 (2007). (Cited on page 255.)

[210] M. Patel, S. Shimizu, M. A. Bates, A. Fernandez-Nieves, and S. Guldin, Soft Matter **19**, 1017 (2023). (Cited on page 255.)

[211] J. Rault, Solid State Communications **9**, 1965 (1971). (Cited on page 255.)

[212] H. Beaty and J. Kirtley, *Electric Motor Handbook*, McGraw-Hill handbooks, McGraw-Hill Education, 1998. (Cited on page 279.)

[213] A. Oesterle, Micropipette techniques for electrophysiology, https://www.sutter.com/micropipette/cookbook.html. (Cited on page 281.)

# Appendix A

# Toroidal droplet generation setup

The laboratory setup to make small toroidal droplets consists on two main parts. A rotating stage of controllable speed where the cuvette with the outer material is placed, and an injection setup to inject the torus material through a tip. The position of this tip can be controlled with a micromanipulator.

## A.1 Rotating stage



An image of the experimental setup is shown in Figure A.1a. The rotating stage consists of a metal circular plate, held by optical table posts, with a hole in its center where the rotor of a ceiling fan motor has been attached with its corresponding bearings so that it can freely rotate. The stator of the motor is fixed to the circular plate at the same height of the rotor. The motor is controlled with a variable frequency driver connected to the motor through a switch box.

The motor of the setup is a shaded-pole single phase induction (asynchronous) motor with 6 poles (induction coils; see Figure A.1b,c). An induction motor works by generating a rotating magnetic field through the coils of the stator [212]. The rotor is made out of a conductor material and has a squirrel cage shape such that a rotating magnetic field induces electric currents on it. These electric currents produce a magnetic field that interacts with the rotating magnetic field producing a torque and thus a rotation of the rotor. For a three phase induction motor, the rotating magnetic field is easily obtained thanks to the lag between the phases by connecting each pole to a different phase. For a single phase induction motor, the single phase excitation is only able to produce an oscillating but not a rotating magnetic field. This prevents the initiation of the rotation of the motor. An oscillating magnetic field can be understood as

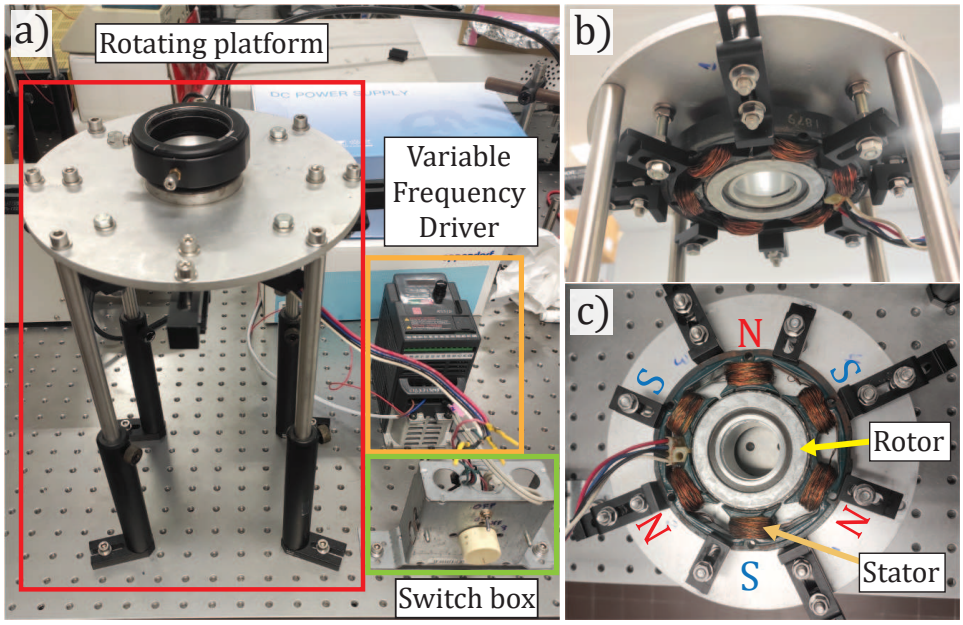



**Figure A.1:** a) Image of the laboratory rotating stage setup. It consists on a rotating platform (red square) a variable frequency driver (orange box) and a switch (green box). b) Image of the ceiling fan motor attached in the rotating platform. c) Top view of the ceiling fan motor. The polarity of each winding is indicated by the letters $N$ and $S$. There are six windings corresponding to six poles. The rotor and stator parts of the motor are correspondingly labeled.



a superposition of two rotating magnetic fields of equal strength and opposite directions. To break the symmetry, an auxiliary winding at one side of the main windings, called shaded pole, is added giving a chirality to the system and favoring one of the rotation fields versus the other. This provides the initial torque to start the rotation of the rotor.

Once the rotation has started, the rotor will want to follow the rotation speed of the rotating magnetic field. The rotation frequency of the rotating magnetic field, called synchronous frequency ($f_s$) can be computed from the electrical frequency ($f_e$) and number of poles ($p$) as:

$$f_s = \frac{2f_e}{p} \tag{A.1}$$

It is worth noting that if the rotor rotates at the same speed as the rotating magnetic field, from the reference frame of the rotor, there is no change of the magnetic field it feels with time. This results in no electric current induced, and thus, no torque balancing the friction. As a result, the rotor speed needs to

be lower than the synchronous frequency, so there is a torque that can balance friction. This is the reason that the motor is called asynchronous, the rotor speed is less than the synchronous speed. The difference between the synchronous and actual speed of the rotor is called slip.

To control the speed of the rotating stage we need to control the electrical input frequency. To do so, we use a variable frequency driver RS L510-201-SH1F-PLR (Figure A.1a). This variable frequency driver takes as an input the 220V 50Hz single phase signal from the socket and gives as an output a three-phase voltage at the desired frequency. Since our motor is single phase, we just use one of the outputs to drive it. A variable frequency driver works by initially rectifying the AC input into a constant voltage signal[1] and then using this DC signal to reconstruct a sinusoidal output of the desired frequency through pulse width modulation. As discussed earlier, for our setup, the rotation frequency of the rotating stage will be slightly lower than $f_e/3$.

Finally, there is a switch box connecting the motor and the variable frequency drive. The switch is able to change between the different inputs of the motor which connects to different lengths of the windings. The longer the length, the higher the magnetic field and thus the torque. This is used as a mean of controlling speed, since less torque will balance less friction which occurs at lower rotation speeds. In our experiments we only use the highest torque input such that the rotation frequency is as close as the synchronous frequency. The switch box is used just as an on/off switch.

## A.2 Injection setup



The liquid crystal is injected with a syringe pump (Chemyx Fusion 200-X) connected to a tip. For making small tori of radius $R \sim 500\mu m$ and tube radius $a \sim 150\mu m$ we use a $500\mu L$ glass air tight syringe (Hamilton). A G20 needle is attached to the syringe and connected to the injection tip through a PE-90 tubing (Instech). For making small tori, we use as the injection tip a pulled glass capillary with outer diameter $150\mu m$. The injection tip is connected to a micromanipulator through an alligator clip which is used to move and position the tip. An image of the injection setup is shown in Figure A.2a. The typical parameters used for generating our small toroidal droplets are: Volume=$0.3\mu L$, Flow rate=$20\mu L/min$, Input frequency=21Hz.

To make the pulled tip we start with round glass capillaries of 1mm outer diameter and 0.56mm inner diameter (Figure A.2b). We use a pipette puller (P-1000 Sutter Instruments) to pull the capillaries to a micrometer size tip (Figure A.2c). They are pulled using program D from the cookbook [213] to get very thin

[1] This can be done by using a full bridge rectifier followed by a low pass filter.

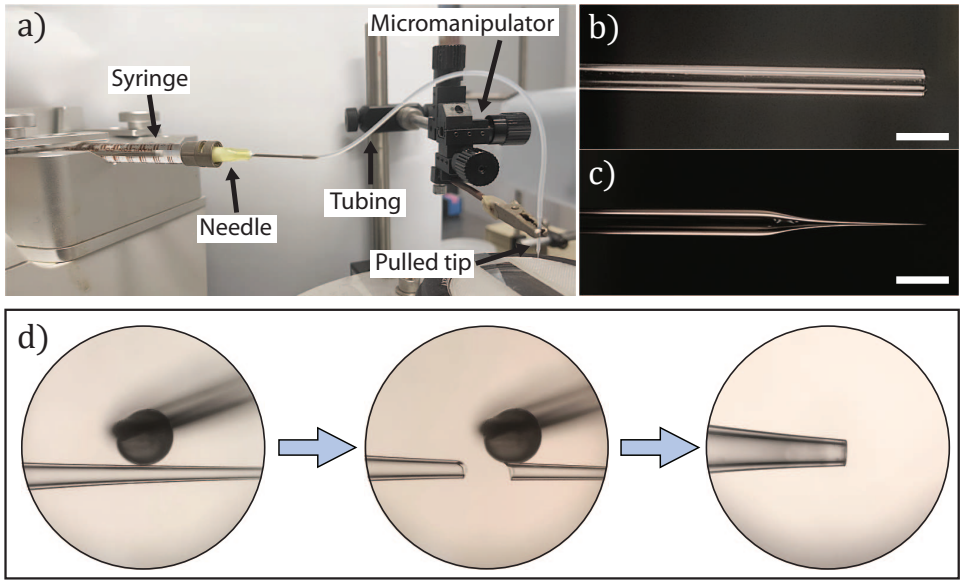



**Figure A.2:** a) Image of the injector setup in the laboratory with the components labeled. b) Image of a round glass borosilicate glass capillary of outer diameter 1mm and inner diameter 0.56mm. c) Pulled capillary with program D of the pipette puller. Scale bars are 2mm. d) Images of the process for cutting the tip to the desired size with the microforge. Left image show the glass bead in contact with the capillary. Middle image show the tip after cut. Right image show the final tip after sanding and fire polishing it to an outer diameter size of $\approx 150\mu m$.



and long tips since, which distort the yield stress material less than with other shaped tips, leading to better toroidal droplets. This program is characterized by the parameters: Heat=Ramp+10, Pull=75, Vel=75, Time/Del=200t or 90d, Pressure=400, where ramp is the glass transition value of the capillaries used[1].

Once the capillary is pulled, we cut it to the desired size using a microforge (MF2 Narishige). This is done by putting a small glass ball into contact with the capillary at the desired cutting point. When it is in contact, we slowly heat the glass ball until it starts melting with the capillary. At that point, we release the heating pedal, which results in a sudden movement that breaks the capillary. Some snapshots of the process are shown in Figure A.2d. For a large size of $\sim 100\mu m$, the cut is usually not straight[2].

To improve the shape of the tip we use 2500 grit sand paper to "polish" the tip to its final size. To do this without breaking the capillary, a strip of sand

[1]For each batch of capillaries this value can be measured with the pipette puller.

[2]The microforge works better for smaller sizes where the cut can be clean and straight. The ability of the experimentalist also plays a role.

paper is cut and slightly wet with water. The strip is placed with one edge on the table and the rest hanging on the air forming a ledge. The capillary is gently scratched against the ledge, while keeping the capillary perpendicular to it. The flexibility of the ledge allows us to sand the capillary applying a very small and controlled pressure such that it does not break. Once sanded to size, the glass dust is removed by rinsing the outside of the capillary with ethanol and injecting ethanol from the tip to remove the inner dust. Finally, to remove the small cracks that might have developed during the sanding process, the capillary is fire polished. The glass bead is heated and placed close to the tip such that it is locally heated up to a point where the cracks spontaneously heal.

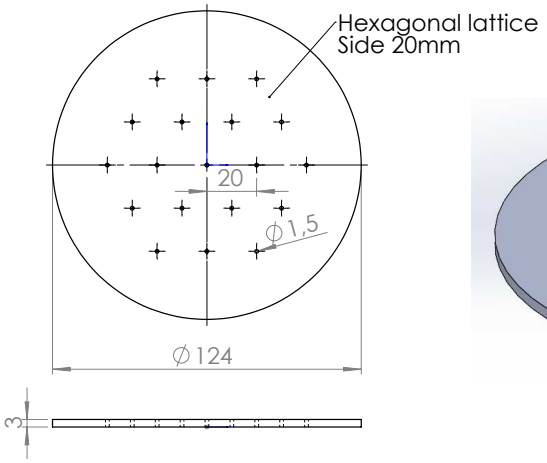
A

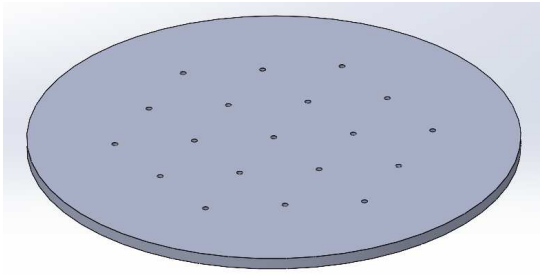
# Appendix B

# Upscaled gel generation setup: Drawings

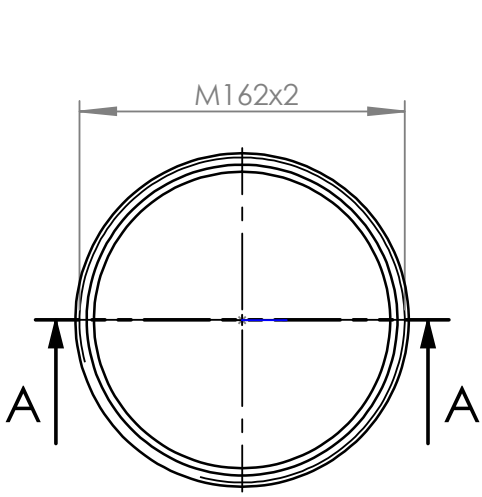
In this appendix we show the drawings of the designed pieces for the upscaled setup for the continuous generation of spherical hydrogels. The drawings show the main dimensions of the pieces together with a 3D view of the designed piece. The designed pieces are the top lid, connector, bottom cone with its cap, and pieces O.1, I.1 and I.2 with the capillary disk as named in 3.11. From these pieces only the top lid, connector and top O.1 pieces are made in the workshop with polyvinyl chloride (PVC). Every other piece is 3D printed.

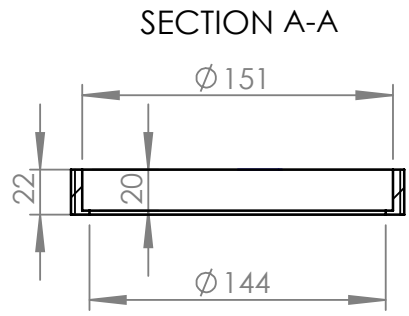
## Injector holder

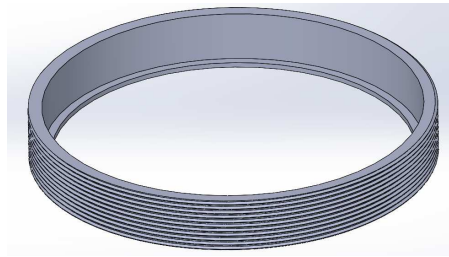


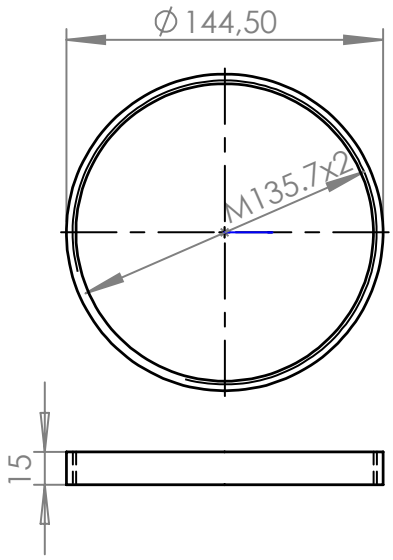
## Piece O.1



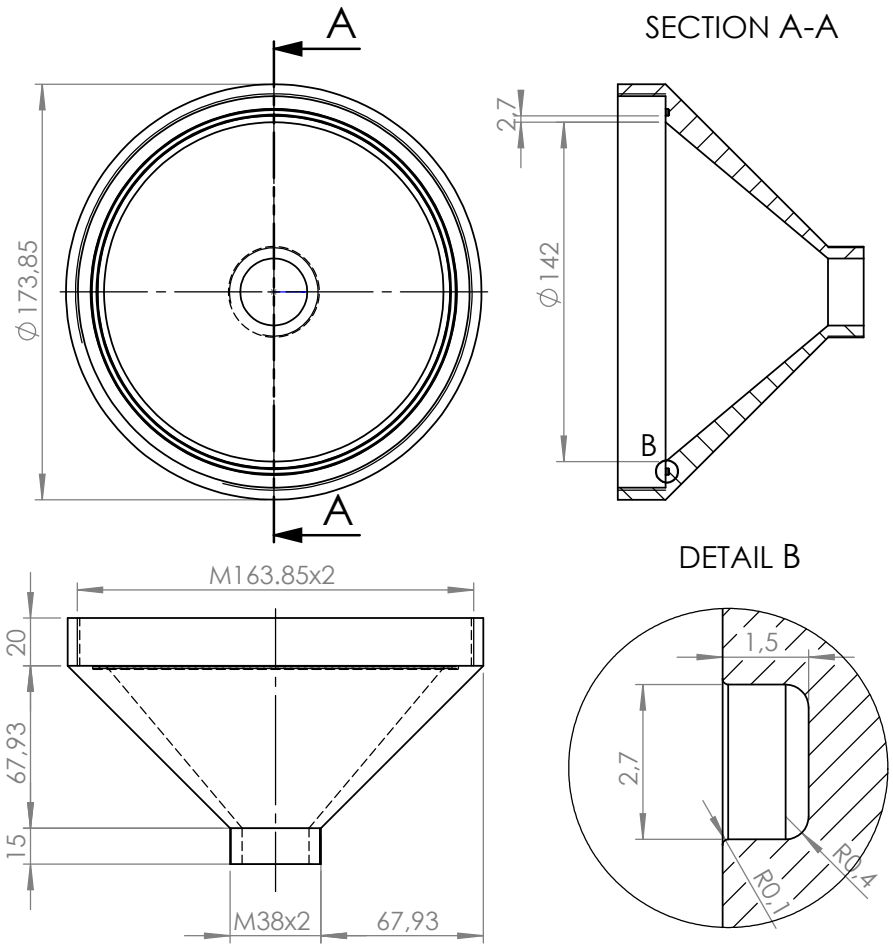



## Piece I.1



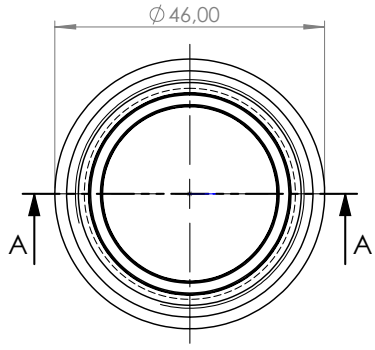



# Bottom cone

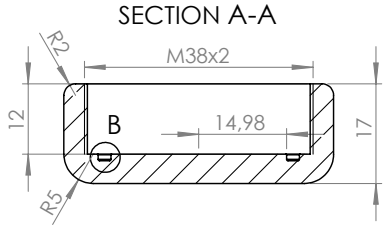

A
A
SECTION A-A
2,7
ϕ142
ϕ173,85
B
DETAIL B
M163.85x2
20
67,93
15
M38x2
67,93
1,5
2,7
R0,4
R0,1

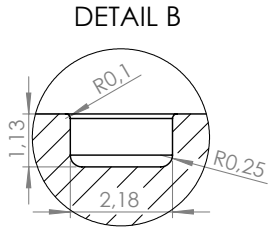


## Bottom cap

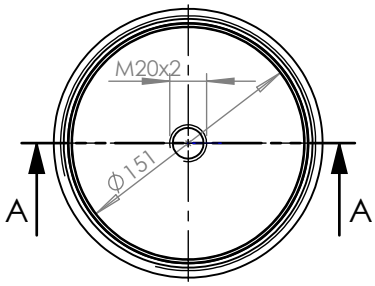


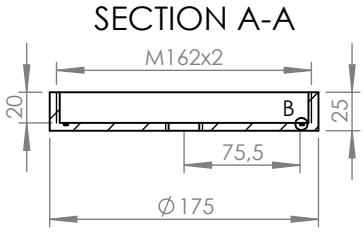


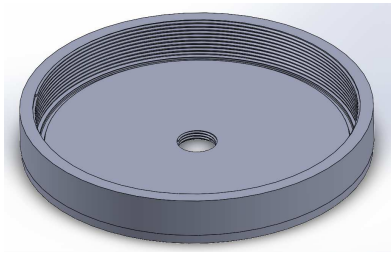



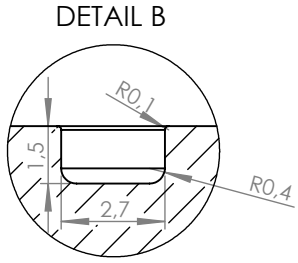




## Top lid

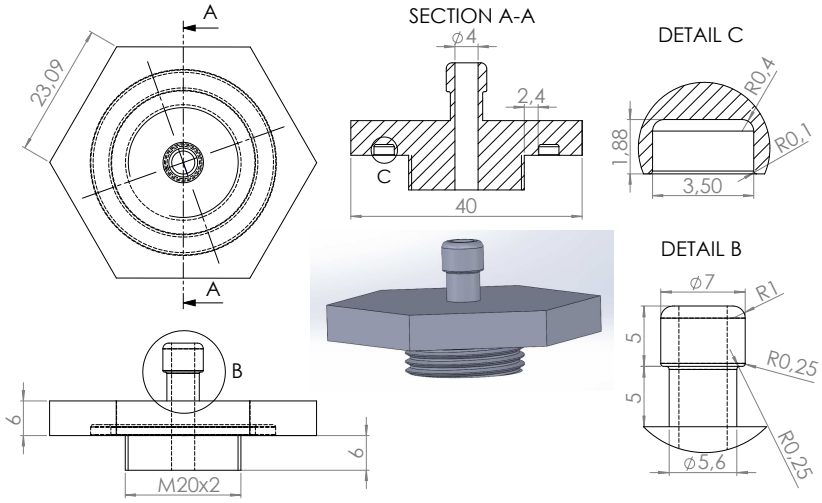




## Connector




## Piece I.2

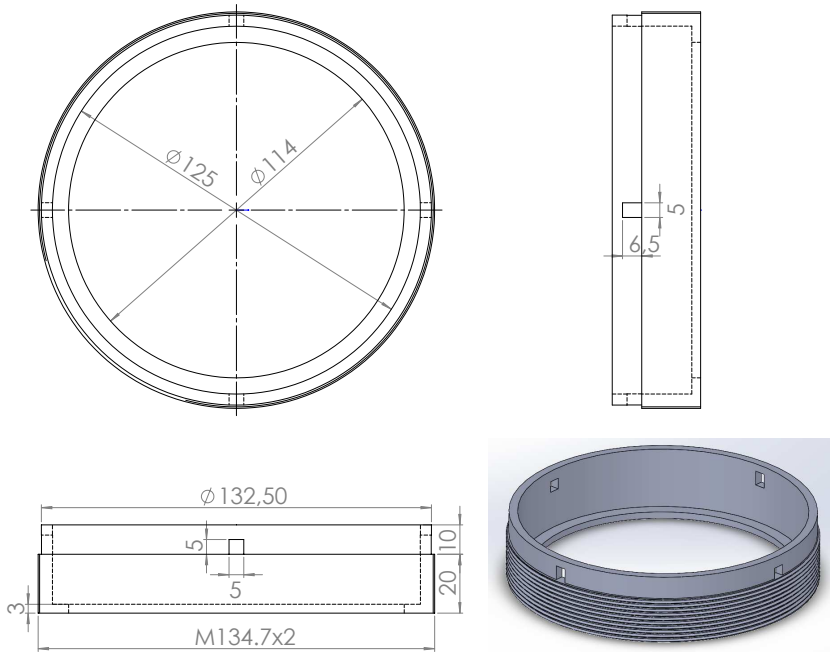




**Figure B.1:** 3D printed I.2 piece with the cross that helps threading it.

There are some details on the design of the pieces worth discussing:

- The injection holder consists on a disk with holes that is glued to piece I2. In the design presented, the holes form a hexagonal lattice of 20mm spacing. The diameter of the holes was set such that when 3D printed, the metal capillaries fit tightly and are held by friction alone.
- The threads are all designed with a pitch of 2mm. The male and female threads are designed accordingly so there is one of each for each connecting pair.
- Pieces O.1 and I.1 are glued and fixed to the PMMA UV transparent tube using water resistant glue.
- The pieces bottom cone, bottom cap, top lid and connector have a groove for an O-ring that improves sealing; see for example detail B of bottom cap. They are designed for 150x2mm, 32x1.5mm, 150x2mm and 24.5x2.5mm O-rings respectively.
- For the connector, the part shown in detail B is designed for connection with the peristaltic pump tubing such that friction keeps it together. Air tightness is a concern in this part.
- Piece I.2 has some square holes. These are made to be able to fit some sticks forming a cross to allow threading the piece in place; see Figure B.1.
- 3D printed pieces are water tight. Nevertheless, due to the porous nature of filament layers, they are not air tight For this reason, the top pieces are made in PVC such that air can not flow through them in time and the oil column remains in place.

## Appendix C

# Stable toroidal droplet generation: Troubleshooting

This appendix aims to be a troubleshooting guide for those attempting to make small stable toroidal droplets. This guide does not intend to be rigorous and is based on our experience on making stable toroidal droplets and the problems that appeared during our research. In order to assess the origin of the problems it is important to start with a setup and parameters that we know has worked in the past.

One example is the one used for making planar nematic toroidal droplets. In this case, for making droplets with radius $R \sim 500\mu m$ and tube radius $a \sim 150\mu m$, we use an external Carbopol yield stress material with no ethanol. The composition includes 1wt% Carbopol, 2wt% Glycerol and 1wt% PVA. The injection parameters used for making these droplets are: Volume=$0.3\mu L$, Flow rate=$20\mu L/min$ and Frequency=21Hz. Fixing the position of the injection tip to the desired radius $R$ is a matter of trial and error. For every trial, the radius of the injected material is checked in the microscope and the position of the needle adjusted accordingly. This method could be improved by adequately marking the center of rotation of the rotor and use a camera to observe the cuvette in the rotating stage from below such that the distance of the tip from the center can be measured and adjusted without the trial and error method.

The procedure to make toroidal droplets consists on the following steps:

1. Clean gently the tip by rubbing it with absorbent paper soaked in a 50/50% ethanol/water mixture.

2. Make sure the pump injects properly by pumping on an absorbent paper. If the paper is in contact with the tip, we can use that to check whether the injection works properly, which occurs when the injection stops as the pump stops injecting.

3. Clean again the tip, tape the cuvette filled with the yield stress material with its surface flattened on the rotor of the rotating stage and place the tip inside a few millimeters from the free surface.

4. Before starting the rotation, check that the tip will not crash with the walls by gently rotating the setup manually.

5. Start the rotation and wait for around 10 seconds to make sure we are in the steady state.

6. Start injection and take the tip out around one second after the pump finishes injecting. This timing between the pump stopping injection and the retrieval of the needle can become relevant for getting good toroidal droplets, as will be discussed later. How much to wait for retrieving the needle is something best learned by practice.

If after trying these parameters and following these steps, stable toroidal droplets are not obtained, there are several possible causes of the problem depending on the casuistry:

1. **No material is being injected:**

   - Leaks in the injection circuit:

     This can be a result of the needle not being properly attached to the glass syringe or the tubing connection with the glass capillary becoming loose. This last case can be a result of the glass edge being sharp and cutting the polyethylene tubing making the connection loose grip. It can be solved by sanding or fire polishing the connecting part of the glass capillary to eliminate sharp edges. Once this is done, make sure the tubing is properly fit by gently pulling back and checking whether it stays firmly attached.

   - Tip is clogged:

     Since we do not filter the injection solution, any dust larger than the tip size can produce clogging, preventing injection. Although this is not usual since the tip diameter is larger than the typical size of large dust, $\approx 50\mu m$, it is still a possibility. This can be checked in situ by taking one of the ocular of the microscope and use it the other way around as a magnifying glass. If it is not clear whether it is clogged or not, it can be further checked by detaching the tip from the tubing and checking it in the microscope. The problem is solved by cleaning the tip by injecting ethanol from the tip.

- Liquid crystal becomes solid:

  It is worth noting that the nematic-crystal transition temperature for 5CB is $\approx 18°C$, which is close to room temperature. If the liquid crystal cools too much, it might solidify at the tip, causing clogging problems. This can be easily solved by changing the temperature of the room and heating the injection tip and tubing with a hair-dryer until it becomes transparent (isotropic phase), indicating it has melted.

- There is solidified yield stress material on the tip:

  If the tip has not been cleaned from the previous trial, the yield stress material that sticks to the tip might dry out becoming solid and clogging the tip. This is easily solved by gently rubbing it with absorbent paper soaked in a 50/50% ethanol/water mixture.

- Pump settings are wrong:

  Check the pump settings. Sometimes it might be set to retraction mode instead of injection.

2. **There is no stable torus but only nematic droplets distributed along a toroidal shape:**

   In this case there are two possibilities. We can have a few large droplets or a lot of small droplets. Depending on the case, the cause of the problem might be different. For both cases one possibility is:

   - Tip is partially clogged or injection is delayed:

     This can be checked by injecting on a absorbent paper as it slides against the tip such that we can see whether the injection stops when the pump stops or whether it is delayed. If it is delayed, this can be a result of the system being partially clogged; in this case, the pressure builds and deforms the plastic tubing, so that after the pump stops, the relaxation back to its original shape maintains the injection beyond the set point. If it is the tip that clogged, injecting ethanol from the tip might be enough to solve the problem.

When we have small droplets, the possible causes are:

- Rotation speed is too fast or injection rate too low:

  If the rotation speed is too fast or the injection rate too low, the generated jet will be very thin and break very fast before a whole turn is completed.

- Yield stress is too high:

  Experience has shown that when the yield stress is too high, small droplets are very prone to appear. This might be due to the difficulty of fluidizing the yield stress material.

- Time between the end of pump injection and taking out tip is too long:

  If we wait for too long to take out the tip after the pump has finished injecting, the generated torus eventually breaks into small droplets.

When we have large droplets, the possible causes are:

- Rotation speed is too slow:

  In this case, we might be in the dripping regime rather than the jetting regime and large droplets are formed as the tip injects.

- Time between the end of pump injection and taking out tip is too short:

  If we take out the tip too soon, not all the liquid crystal might have been injected and we might have a too thin torus that will break if surface tension is able to deform the yield stress material.

- Yield stress is too low:

  In this case, the generated torus breaks due to Rayleigh-Plateau instability resulting in large droplets. If the yield stress material has been stored for too long, its properties might change. Using a fresh material or higher yield stress allows for testing if that is the problem.



Sometimes the cause of not getting toroidal droplets is not clear and none of the previous insights solves the problem. In that case, changing the injection tip for a new one and reassembling again the injection setup can help.

Once we are able to make stable toroidal droplets we can start optimizing the parameters to get as circular cross-sections as possible. Due to the yield stress of the outer medium, cross-sections tend to be elongated [110]. The best way to get rounded cross-sections is by matching the surface tension stress with

the yield stress of the outer material ($\gamma/a \approx \tau_y$) such that the circular shape is driven by surface tension, but surface tension does not produce the breakup of the toroidal droplet. This is done by trial and error varying the amount of Carbopol in the yield stress material. If we want to make tori with different tube radius $a$, the injection parameters should be tuned and optimized. The optimal parameters for making toroidal droplets also change when changing the system we want to study. For example, the surfactant and its concentration in the yield stress material affects the surface tension, as does the torus material, which changes the optimal yield stress.

C

# Appendix D

# Extreme thermodynamics: Preliminary studies

In this appendix, we describe preliminary studies on spherical and toroidal gels that ensure our fabricated gels give consistent results with previous studies on pNIPAM gels. We first check that our UV polymerization settings result in spherical pNIPAM gels that have a diffusion coefficient $D$ in the same order of magnitude as previous reports. We then study the influence of the heating rate for the transition from the swollen to the shrunken state to be considered quasistatic. Finally, we show data confirming that the aspect ratio of our torus remains constant in the quasistatic shrinking experiment.

## D.1 Diffusion coefficient of spherical pNIPAM gels

We make our spherical gels using the procedure described in section 3.7.2. The polymerization time is optimized such that the resulting gels are solid and transparent in water. In our studies, we use gels that have been polymerized for 60 and 90 seconds. We use these gels to asses whether there is a difference in the swelling and shrinking kinetics. A difference in their kinetics would indicate a difference in elastic properties and/or their internal structure, suggesting that the polymerization process is not over for the shortest polymerization time.

To study the kinetic properties of our gels, we study their size evolution when the temperature is suddenly increased below the transition temperature. The size change with time of the gel can be computed analytically using the elastic theory of hydrogels, assuming an initial radial deformation with no normal stress at the surface [87, 88]. The result is:

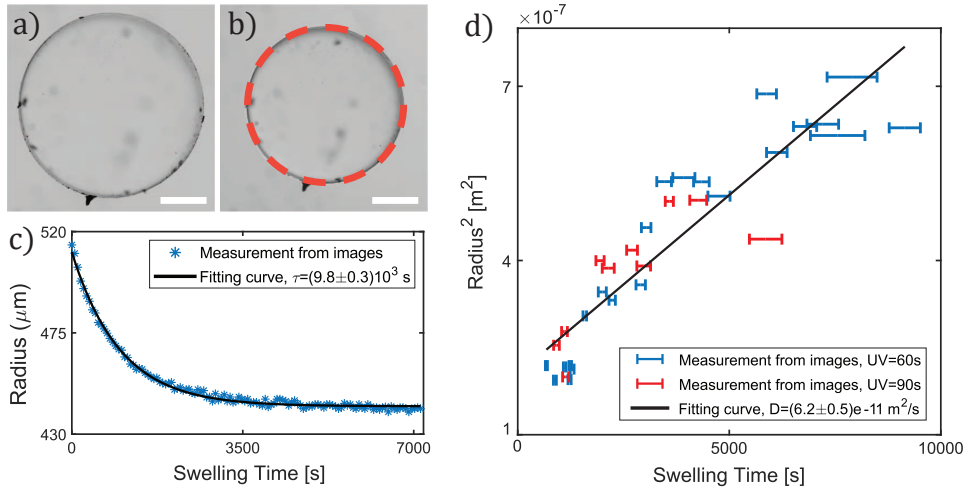



**Figure D.1:** a) Microscope image of initial state of the gel. b) Final state of the gel after heating stage to $30°C$. The dashed line is an example of an ellipse used to measure the radius of the gel. Scale bars are $250\mu m$. c) Example of a deswelling curve with its corresponding fit. d) Plot of the squared final radius as a function of the swelling time $\tau$. Data in blue and red correspond to a polymerization time of $60s$ and $90s$ respectively. The linear fitting provides the value of the diffusion coefficient $D$. The error bars correspond to the uncertainty of the fit in c).

$$r(t) = r_f - \frac{6}{\pi^2}(r_f - r_o)\sum_{n=1}^{\infty}\frac{e^{-n^2\frac{t}{\tau}}}{n^2} \tag{D.1}$$

where $r_f$ and $r_o$ are the initial and final radii of the gel and

$$\tau = \frac{r_f^2}{D} \tag{D.2}$$

is the characteristic swelling time. The radius evolution is expressed with a sum of decaying exponentials of characteristic decay time $\tau/n^2$. The deswelling time will be determined by the slowest exponential, which correspond to the case $n = 1$ mode. This characteristic swelling time is proportional to the square of the final size of the gels, and is inversely proportional to the gel diffusion constant, $D = (K + 4\mu/3)/f$ which is a function of the elastic moduli of the gel and the friction coefficient $f$ between the network and the solvent.

To experimentally obtain the diffusion coefficient of our gels, we make gels with initial diameter between 1 and 2 mm, and measure their size change when suddenly heating them to $\approx 30°$C. This allows obtaining the swelling time for

each final size by fitting equation D.1 to the experimental curve. With the swelling time and the final radius, we can obtain D from fitting the data with equation D.2.

We place the gels in a water cuvette on a heating stage and observe them in the microscope (Figure D.1a). We heat the gels by increasing the temperature of the stage to 30°C at a rate of 20°C/min, and record the shrinking of the gels. We obtain the radius evolution of the gels by manually fitting the gel contour to an ellipse with Image J, and computing the average between the major and minor semi-axis of the ellipse, which is taken as a representative radius (Figure D.1b). The difference between the major and minor axis is always small, indicating the gels are essentially spherical.

An example of a deswelling curve is shown in Figure D.1c, with its corresponding fit to equation D.1 truncated to the first three terms. The fitting is very good. Finally, we plot the final squared radius as a function of the swelling time for both polymerization times (Figure D.1d).There is no noticeable difference suggesting that polymerization is already finished after 60 seconds, which is the time we use from this point on to make pNIPAM gels. By making a linear regression of the data we obtain a diffusion coefficient of $D = (6.2 \pm 0.5) \cdot 10^{-11} m^2/s$. This value is consistent with the one previously reported for the swelling of pNIPAM macrogels with similar crosslinking concentration, $D = 3.2 \cdot 10^{-11} m^2/s$ [87].

## D.2 Quasistatic heating of spherical pNIPAM gels

If our pNIPAM gels are heated slow enough, they will continuously deswell while maintaining equilibrium. The process is also reversible, and thus, when the gels are cooled down, they swell back to their original size. If the gels are heated too fast, they will fall out of equilibrium, resulting in interesting phenomena for temperatures above the transition one.

As explained in the previous section, the time constant associated to the deswelling kinetics depends on gel size, and so does the maximum heating rate for quasistatic heating. We study gels of $\sim$ 1-1.5$mm$ diameter. As shown in Figure D.1d, the deswelling time scale for this gel size is in the order of hours. We first try heating one of our spherical gels at a rate of 4°C/h. As shown in Figure D.2a, as the transition temperature is crossed, the gel phase separates into a swollen (transparent) and a shrunken (dark) regions. After lowering the temperature and reswelling, we can clearly see a wrinkle pattern on the the region that was shrunk. We believe these wrinkles correspond to internal breakup of the gel network due to the large stress that it suffered at the boundaries between shrunken and swollen regions.

If we now reduce the heating rate by an order of magnitude, and heat the

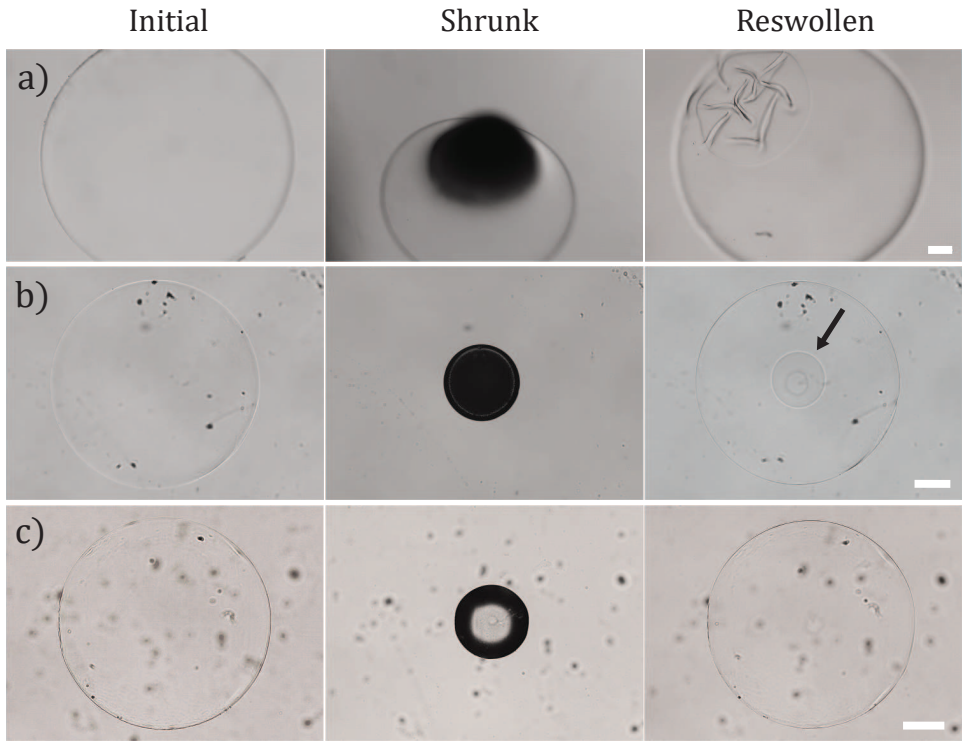



**Figure D.2:** Images of the initial, shrunk and reswollen states of a pNIPAM spherical gel heated at different rates. a) 4°C/h. b) 0.2°C/h. Arrow indicates circular feature that appears after reswelling. c) 0.2°C/day. Scale bars ar 200$\mu m$.

gels at a rate of 0.2°C/h, once the temperature goes above the phase transition temperature, phase separation is not observed and the gel shrinks to a spherical shape and becomes completely dark (Figure D.2b). As the gel swells back, however, a small circle in the top region of the gel is observed. To make experiments at these low heating rates, the heating stage is initially heated to 34°C and kept at that temperature for 10 hours to ensure the gel shrinks to its equilibrium size. At that point the temperature is increased at a rate of 0.2°C/h up to well above the transition temperature.

Finally, we perform tests at an even lower heating rate of 0.2°C/day. Since our stage does not allow continuously heating at a rate below 0.2°C/h, we make 0.1°C steps where the temperature is increased at 0.2°C/h rate and kept unchanged for 12 hours before the next step. The results of heating and cooling the gel are shown in Figure D.2c. The heating seems quasistatic since the gel preserves its spherical shape in the shrunken state. As opposed to the 0.2°C/h heating case, in this case, the central part of the gel still looks transparent

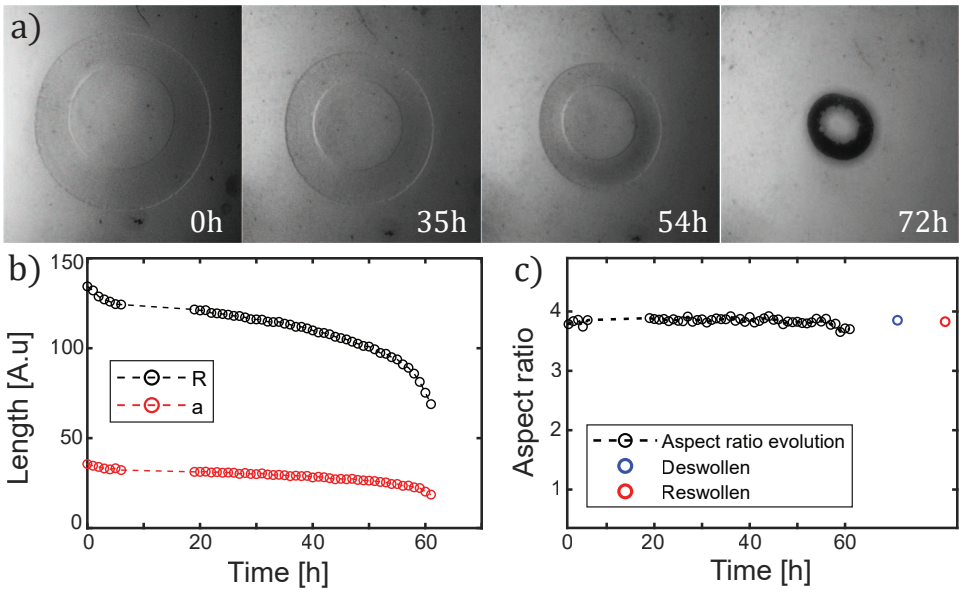



**Figure D.3:** a) Images of the shrinking process. b) Evolution of the radius $R$ and tube radius $a$ of the torus as a function of time. c) Evolution of the aspect ration of the torus with time. Blue dot corresponds to the long time deswollen state at temperatures above the transition temperature. The red dot is the aspect ratio of the reswollen torus after cooling it back to room temperature.

in the shrunken state. In fact, it fluctuates between being transparent and dark. Although we are not sure about the reason behind this, one possibility is that inhomogeneities or fluctuations in the polymer concentration result in fluctuations in the refractive index that favor scattering leading to a dark aspect. When the system is homogeneous, light can pass through it and the center of the gel becomes transparent. When cooling, the gel swells back to its original shape without any mark that could indicate fracture or irreversible deformation of the gel. This shows that the heating rate for millimeter sized gels for it to be considered quasistatic should be slower than 0.1°C/h.

## D.3 Quasistatic heating of toroidal pNIPAM gel

In the experiments with toroidal pNIPAM gels described in section 3.7.3 and shown in Figure 3.17, a toroidal pNIPAM gel is first quasistatically heated above the transition temperature and cooled back to its original state, to later heat it again very fast to result in the Pringle shape deformation observed.

In the quasistatic heating regime, a homogeneous gel should shrink affinely

and thus, the toroidal gel should preserve its aspect ratio $R/a$. From the experimental images of the shrinking torus at a 0.1°C/h rate (Figure D.3a), we can compute the radius $R$, and tube radius $a$ of the torus by manually fitting the inner and outer ring to an ellipse and computing the mean semi-axis values, which we take as the representative value. From this, we compute the radius and tube radius, $R = (R_{in} + R_{out})/2$ and $a = (R_{out} - R_{in})/2$.

As shown in Figure D.3b, both $R$ and $a$ decrease with time, consistent with the shrinking behavior. The aspect ratio, however, remains basically constant, except maybe in the latter stages of the transition, where it very slightly decreases; see Figure D.3c. After cooling down to room temperature, the aspect ratio becomes unchanged. This shows that our gels are homogeneous and that crosslinking is uniform throughout the gels.

## Appendix E

# Extreme thermodynamics: Additional data

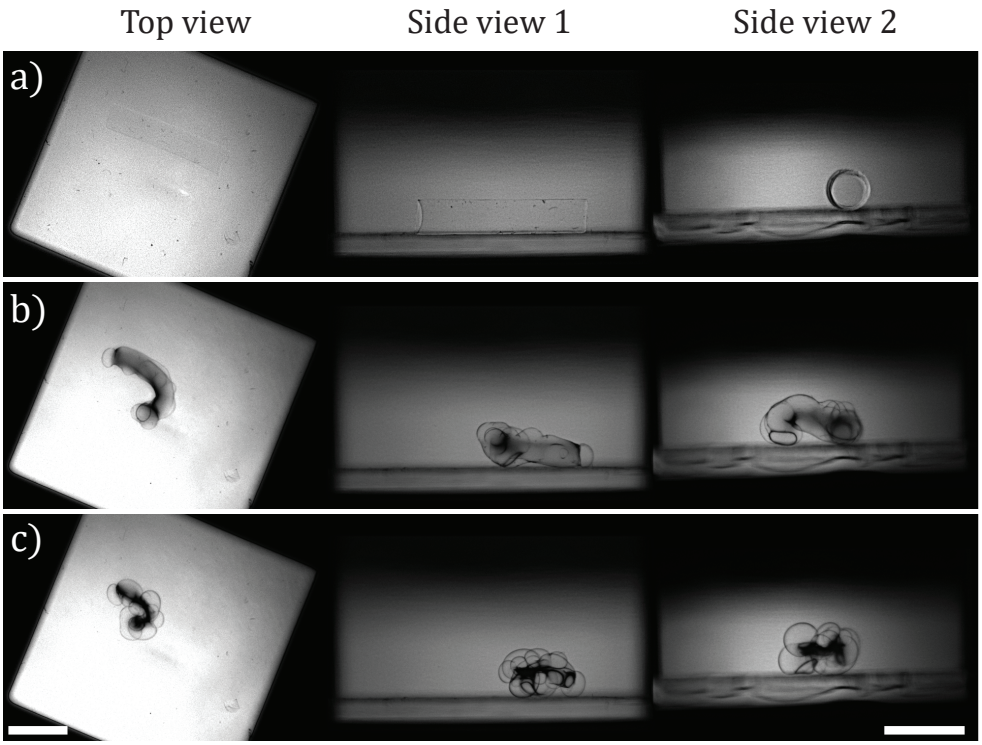



**Figure E.1:** a)-c) Time series of the deformation of a pNIPAM cylinder made in a mold when suddenly heated above the transition temperature. Scale bars are 5mm.

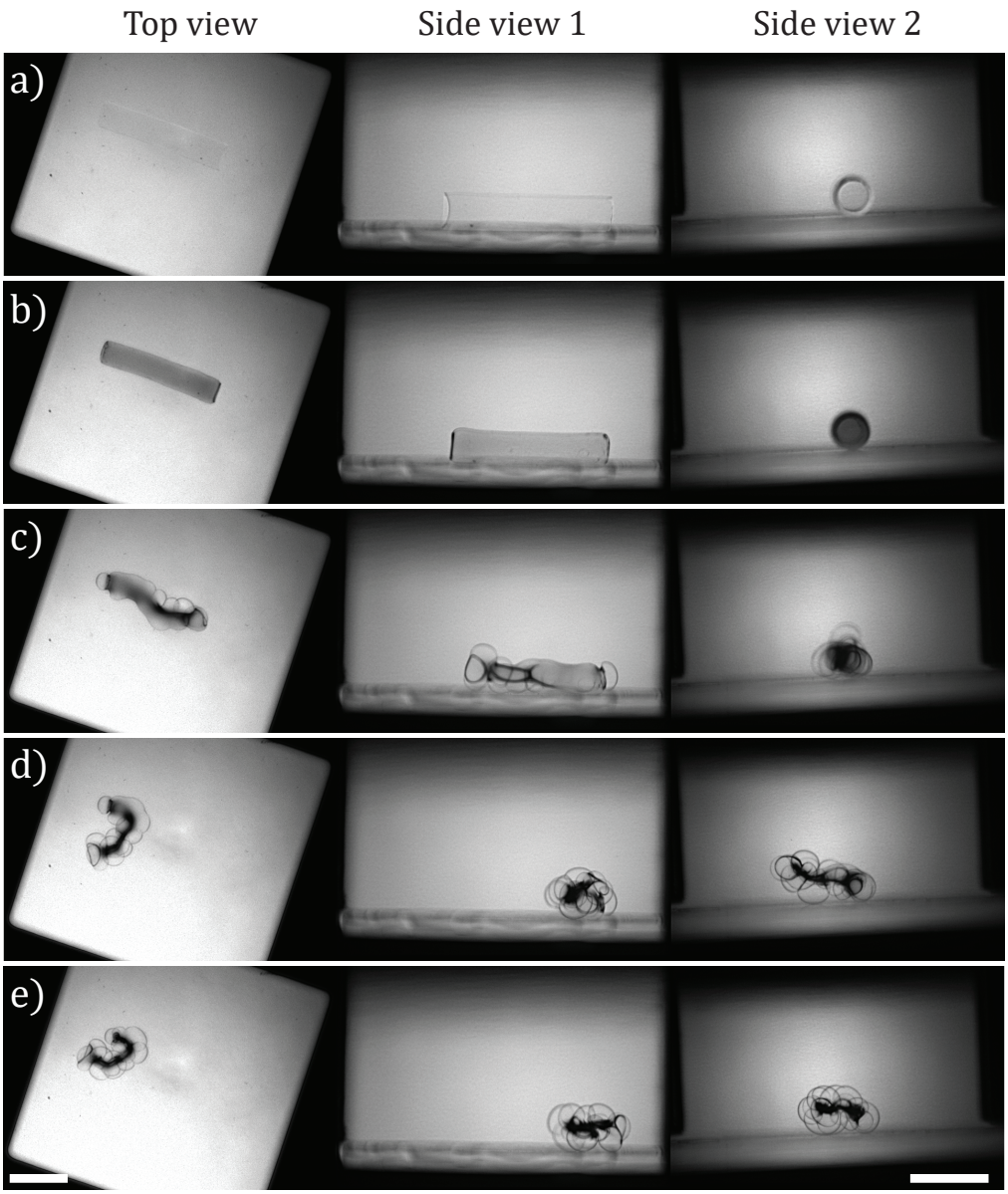



**Figure E.2:** a)-e) Time series of the deformation of a pNIPAM cylinder made in a mold when suddenly heated above the transition temperature. Scale bars are 5mm.

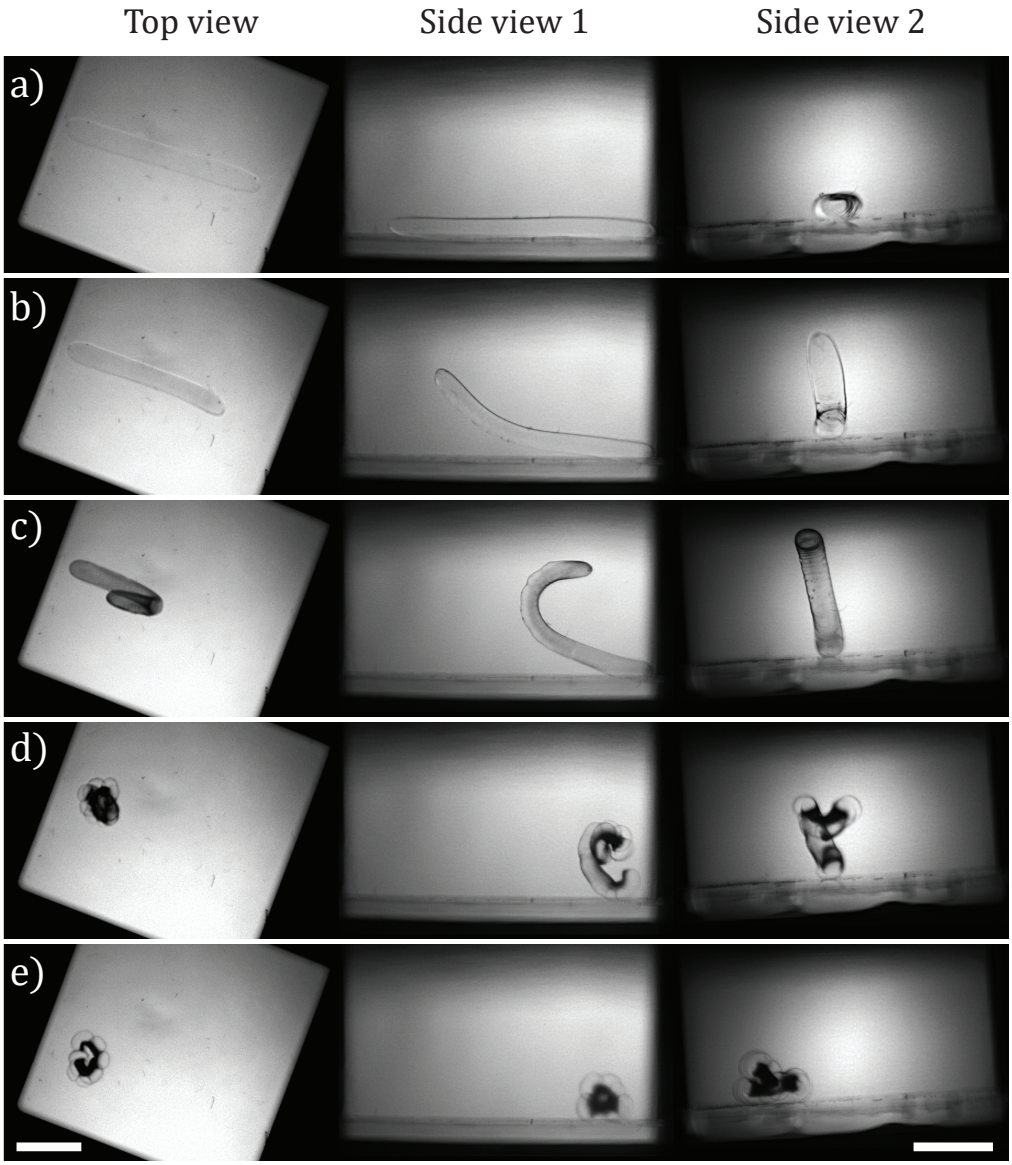



**Figure E.3:** a)-e) Time series of the deformation of a 3D printed pNIPAM cylinder when suddenly heated above the transition temperature. Scale bars are 5mm.

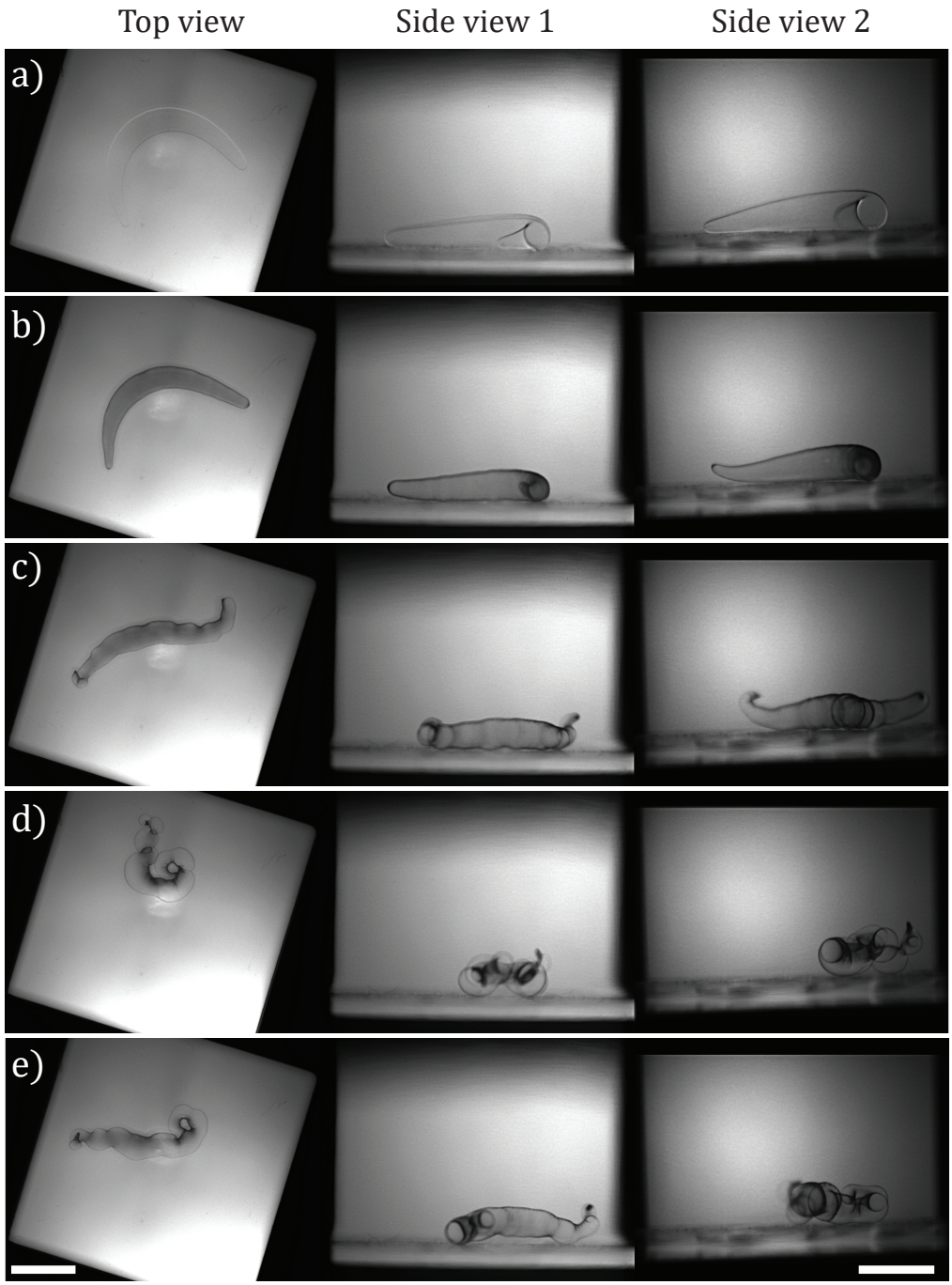



**Figure E.4:** a)-e) Time series of the deformation of a 3D printed pNIPAM arc when suddenly heated above the transition temperature. Scale bars are 5mm.

# Appendix F

# Compatibility equations for a 3D nematic

In this appendix we present the derivation of the four compatibility conditions not derived in chapter 5. These four compatibility equations come from making the infinitesimal path construction for the other two orthogonal planes, the $\hat{\mathbf{x}}_1$-$\hat{\mathbf{x}}_2$ and the $\hat{\mathbf{x}}_1$-$\hat{\mathbf{x}}_3$ planes. From each plane we get two compatibility equations.

## Plane $\hat{\mathbf{x}}_1$-$\hat{\mathbf{x}}_2$

We start by taking two infinitesimal paths in the $\hat{\mathbf{x}}_1$-$\hat{\mathbf{x}}_2$ plane both starting at point $P$ and ending at point $Q$. The first path corresponds to first moving along the $\hat{\mathbf{x}}_1$ direction an amount $\Delta x_1$ to point $A$ and then, moving an amount $\Delta x_2$ in the $\hat{\mathbf{x}}_2$ direction, to end at point $Q$. For the second path, we follow the reverse order and move first along the $\hat{\mathbf{x}}_2$ direction an amount $\Delta x_2$ to point $B$ and then, an amount $\Delta x_1$ in the $\hat{\mathbf{x}}_1$ direction to end at point $Q$.

We start with the first path. We can first estimate, to first order, the value of the director field at $A$ using equation 5.48, noting that $\hat{\mathbf{v}} = \hat{\mathbf{n}}$:

$$\hat{\mathbf{n}}(A) \approx \hat{\mathbf{n}}(P) + \Delta x_1 \nabla_{\hat{\mathbf{n}}} \hat{\mathbf{n}} = \hat{\mathbf{x}}_1 + \left(-b_2 \hat{\mathbf{x}}_2 - b_3 \hat{\mathbf{x}}_3\right) \Delta x_1 \tag{F.1}$$

In the infinitesimal limit, this corresponds to a director rotation of angle $\theta_A \approx \sqrt{b_2^2 + b_3^2} \Delta x_1$ towards the direction given by $-b_2 \hat{\mathbf{x}}_2 - b_3 \hat{\mathbf{x}}_3$. We compute the position of the new main axis $\hat{\mathbf{n}}_2$ and $\hat{\mathbf{n}}_3$ by a first rotation of angle $\theta_A$ around the direction given by the unit vector $\left[b_3 \hat{\mathbf{x}}_2 - b_2 \hat{\mathbf{x}}_3\right] / \sqrt{b_2^2 + b_3^2}$ and a second rotation around the director $\hat{\mathbf{n}}(A)$ of angle $\Delta x_1 \partial\omega / \partial x_1$. These rotations can be expressed, to first order, by the matrices:

$$R_1 = \begin{pmatrix} 1 & b_2\Delta x_1 & b_3\Delta x_1 \\ -b_2\Delta x_1 & 1 & 0 \\ -b_3\Delta x_1 & 0 & 1 \end{pmatrix} \tag{F.2}$$

$$R_2 = \begin{pmatrix} 1 & 0 & 0 \\ 0 & 1 & -\dfrac{\partial\omega}{\partial x_1}\Delta x_1 \\ 0 & \dfrac{\partial\omega}{\partial x_1}\Delta x_1 & 1 \end{pmatrix} \tag{F.3}$$

Multiplying the vectors $\hat{\mathbf{x}}_2$ and $\hat{\mathbf{x}}_3$ by $R_2 \cdot R_1$ gives the main axis direction at $A$:

$$\begin{cases} \hat{\mathbf{n}}_2(A) & \approx \hat{\mathbf{x}}_2 + b_2\Delta x_1\hat{\mathbf{x}}_1 + \dfrac{\partial\omega}{\partial x_1}\Delta x_1\hat{\mathbf{x}}_3 \\ \hat{\mathbf{n}}_3(A) & \approx \hat{\mathbf{x}}_3 + b_3\Delta x_1\hat{\mathbf{x}}_1 - \dfrac{\partial\omega}{\partial x_1}\Delta x_1\hat{\mathbf{x}}_2 \end{cases} \tag{F.4}$$

The value of the director field at $Q$ can then be approximated, to first order, as the value at $A$ plus the directional derivative in the $\hat{\mathbf{x}}_2$ direction multiplied by the length $\Delta x_2$. We can compute this using equation 5.48, taking into account that $v_1$, $v_2$ and $v_3$ are the projections of the moving direction ($\hat{\mathbf{x}}_2$ in this case) onto the deformation main directions $\hat{\mathbf{n}}(A)$, $\hat{\mathbf{n}}_2(A)$ and $\hat{\mathbf{n}}_3(A)$, respectively. Up to second order this results in:

$$\begin{aligned} \hat{\mathbf{n}}(Q) \approx & \hat{\mathbf{n}}(A) + \nabla_{\hat{\mathbf{x}}_2}\hat{\mathbf{n}}(A)\cdot\Delta x_2 = \hat{\mathbf{n}}(A) + b_2\ \mathbf{B}_A\Delta x_1\Delta x_2 \\ & + \left[\left(\frac{1}{2}S_A + \Delta_A\right)\Delta x_2 + \frac{1}{2}T_A\frac{\partial\omega}{\partial x_1}\Delta x_1\Delta x_2\right]\hat{\mathbf{n}}_2(A) \\ & + \left[-\left(\frac{1}{2}S_A - \Delta_A\right)\frac{\partial\omega}{\partial x_1}\Delta x_1\Delta x_2 + \frac{1}{2}T_A\Delta x_2\right]\hat{\mathbf{n}}_3(A) \end{aligned} \tag{F.5}$$

where the subindex indicates the point of evaluation of the deformation fields. When there is no subindex, the deformation field is evaluated at $P$. Expanding around $P$ and retaining up to second order, we get the final expression:

$$\begin{aligned} \hat{\mathbf{n}}(Q) \approx \hat{\mathbf{x}}_1 - (b_2\hat{\mathbf{x}}_2 + b_3\hat{\mathbf{x}}_3)\,\Delta x_1 + & \left[\left(\frac{S}{2} + \Delta\right)\hat{\mathbf{x}}_2 + \frac{T}{2}\hat{\mathbf{x}}_3\right]\Delta x_2 \\ + \Bigg[\left(b_2\left(\frac{1}{2}S + \Delta\right) + \frac{1}{2}Tb_3\right)\hat{\mathbf{x}}_1 & + \left(b_2^2 + \frac{1}{2}\frac{\partial S}{\partial x_1} + \frac{\partial\Delta}{\partial x_1}\right)\hat{\mathbf{x}}_2 \\ + \left(b_2b_3 + 2\Delta\frac{\partial\omega}{\partial x_1} + \frac{1}{2}\frac{\partial T}{\partial x_1}\right)\hat{\mathbf{x}}_3\Bigg]\Delta x_1\Delta x_2 & \end{aligned} \tag{F.6}$$

We now compute the variation of $\hat{\mathbf{n}}$ along the second path. The value of $\hat{\mathbf{n}}(B)$, $\hat{\mathbf{n}}_2(B)$ and $\hat{\mathbf{n}}_3(B)$ when moving along the direction $\hat{\mathbf{x}}_2$ was already computed in chapter 5:

$$\begin{cases} \hat{\mathbf{n}}(B) & \approx \hat{\mathbf{x}}_1 + \left[\left(\frac{1}{2}S + \Delta\right)\hat{\mathbf{x}}_2 + \frac{1}{2}T\hat{\mathbf{x}}_3\right]\Delta x_2 \\ \hat{\mathbf{n}}_2(B) & \approx \hat{\mathbf{x}}_2 + \left[-\left(\frac{1}{2}S + \Delta\right)\hat{\mathbf{x}}_1 + \frac{\partial\omega}{\partial x_2}\hat{\mathbf{x}}_3\right]\Delta x_2 \\ \hat{\mathbf{n}}_3(B) & \approx \hat{\mathbf{x}}_3 + \left[-\frac{1}{2}T\hat{\mathbf{x}}_1 - \frac{\partial\omega}{\partial x_2}\hat{\mathbf{x}}_2\right]\Delta x_2 \end{cases} \tag{F.7}$$

As before, we can approximate the value of $\hat{\mathbf{n}}(Q)$ by computing the directional gradient at point $B$ along $\hat{\mathbf{v}} = \hat{\mathbf{x}}_1$. This results in:

$$\begin{aligned} \hat{\mathbf{n}}(Q) \approx \hat{\mathbf{n}}(B) + \nabla_{\hat{\mathbf{x}}_1}\hat{\mathbf{n}}(B)\cdot\Delta x_1 = \hat{\mathbf{n}}(B) - \mathbf{B}_B\Delta x_1 \\ + \left[-\left(\frac{1}{2}S + \Delta\right)\left(\frac{1}{2}S_B + \Delta_B\right)\Delta x_1\Delta x_2 + \frac{T}{4}T_B\Delta x_1\Delta x_2\right]\hat{\mathbf{n}}_2(B) \\ + \left[-T\left(\frac{1}{2}S_B - \Delta_B\right)\Delta x_1\Delta x_2 - \frac{1}{2}T_B\left(\frac{1}{2}S + \Delta\right)\Delta x_1\Delta x_2\right]\hat{\mathbf{n}}_3(B) \end{aligned} \tag{F.8}$$

which after expanding results in:

$$\begin{aligned} \hat{\mathbf{n}}(Q) \approx \hat{\mathbf{x}}_1 - (b_2\hat{\mathbf{x}}_2 + b_3\hat{\mathbf{x}}_3)\Delta x_1 + \left[\left(\frac{S}{2} + \Delta\right)\hat{\mathbf{x}}_2 + \frac{T}{2}\hat{\mathbf{x}}_3\right]\Delta x_2 \\ + \left[\left(b_2\left(\frac{1}{2}S + \Delta\right) + \frac{1}{2}Tb_3\right)\hat{\mathbf{x}}_1 + \left(-b_2\frac{\partial\omega}{\partial x_2} - \frac{\partial b_3}{\partial x_2} - \frac{1}{2}TS\right)\hat{\mathbf{x}}_3\right. \\ \left. + \left(-\frac{\partial b_2}{\partial x_2} - \left(\frac{1}{2}S + \Delta\right)^2 + \frac{1}{4}T^2 + b_3\frac{\partial\omega}{\partial x_2}\right)\hat{\mathbf{x}}_2\right]\Delta x_1\Delta x_2 \end{aligned} \tag{F.9}$$

By imposing the equality of equations F.6 and F.9, we get two compatibility conditions:

$$b_2b_3 + \frac{1}{2}TS + 2\Delta\frac{\partial\omega}{\partial x_1} + \frac{1}{2}\frac{\partial T}{\partial x_1} + \frac{\partial b_3}{\partial x_2} + b_2\frac{\partial\omega}{\partial x_2} = 0 \tag{F.10a}$$

$$b_2^2 + \left(\frac{1}{2}S + \Delta\right)^2 - \frac{1}{4}T^2 + \frac{\partial b_2}{\partial x_2} + \frac{\partial(S/2+\Delta)}{\partial x_1} - b_3\frac{\partial\omega}{\partial x_2} = 0 \tag{F.10b}$$

## Plane $\hat{\mathbf{x}}_1$-$\hat{\mathbf{x}}_3$

We finish by computing the last two equations from the infinitesimal paths in the plane $\hat{\mathbf{x}}_1$-$\hat{\mathbf{x}}_3$. We take the first path as the one moving first along the $\hat{\mathbf{x}}_1$ direction an amount $\Delta x_1$ to point $A$ and then, moving an amount $\Delta x_3$ in the $\hat{\mathbf{x}}_3$ direction, to end at point $Q$. For the second path, we follow the reverse order and move first along the $\hat{\mathbf{x}}_3$ direction an amount $\Delta x_3$ to point $B$ and then, moving an amount $\Delta x_1$ in the $\hat{\mathbf{x}}_1$ direction to end at point $Q$.

From the previous section, we have already calculated the value of the director field and main deformation directions at point $A$:

$$\begin{cases} \hat{\mathbf{n}}(A) & \approx \hat{\mathbf{x}}_1 - b_2\Delta x_1\hat{\mathbf{x}}_2 - b_3\Delta x_1\hat{\mathbf{x}}_3 \\ \hat{\mathbf{n}}_2(A) & \approx \hat{\mathbf{x}}_2 + b_2\Delta x_1\hat{\mathbf{x}}_1 + \dfrac{\partial\omega}{\partial x_1}\Delta x_1\hat{\mathbf{x}}_3 \\ \hat{\mathbf{n}}_3(A) & \approx \hat{\mathbf{x}}_3 + b_3\Delta x_1\hat{\mathbf{x}}_1 - \dfrac{\partial\omega}{\partial x_1}\Delta x_1\hat{\mathbf{x}}_2 \end{cases} \tag{F.11}$$

We approximate the value of $\hat{\mathbf{n}}(Q)$ by using the directional gradient at point $A$ along $\hat{\mathbf{v}} = \hat{\mathbf{x}}_3$. This results in:

$$\begin{aligned} \hat{\mathbf{n}}(Q) \approx & \hat{\mathbf{n}}(A) + \nabla_{\hat{\mathbf{x}}_3}\hat{\mathbf{n}}(A)\cdot\Delta x_3 = \hat{\mathbf{n}}(A) + b_3\ \mathbf{B}_A\Delta x_1\Delta x_3 \\ & + \left[\frac{\partial\omega}{\partial x_1}\left(\frac{1}{2}S_A + \Delta_A\right)\Delta x_1\Delta x_3 - \frac{1}{2}T_A\Delta x_3\right]\hat{\mathbf{n}}_2(A) \\ & + \left[\left(\frac{1}{2}S_A - \Delta_A\right)\Delta x_3 + \frac{1}{2}\frac{\partial\omega}{\partial x_1}T_A\Delta x_1\Delta x_3\right]\hat{\mathbf{n}}_3(A) \end{aligned} \tag{F.12}$$

Expanding up to second order results in the final expression:

$$\begin{aligned} \hat{\mathbf{n}}(Q) \approx \hat{\mathbf{x}}_1 - (b_2\hat{\mathbf{x}}_2 + b_3\hat{\mathbf{x}}_3)\,\Delta x_1 + & \left[\left(\frac{S}{2} - \Delta\right)\hat{\mathbf{x}}_3 - \frac{T}{2}\hat{\mathbf{x}}_2\right]\Delta x_3 \\ + \left[\left(b_3\left(\frac{1}{2}S - \Delta\right) - \frac{1}{2}Tb_2\right)\hat{\mathbf{x}}_1 + \left(b_2b_3 + 2\Delta\frac{\partial\omega}{\partial x_1} - \frac{1}{2}\frac{\partial T}{\partial x_1}\right)\hat{\mathbf{x}}_2\right. & \\ \left. + \left(b_3^2 + \frac{1}{2}\frac{\partial S}{\partial x_1} - \frac{\partial\Delta}{\partial x_1}\right)\hat{\mathbf{x}}_3\right]\Delta x_1\Delta x_3 & \end{aligned} \tag{F.13}$$

For the second path, the director field value and main deformation directions at $B$ have already been computed in chapter 5:

$$\begin{cases} \hat{\mathbf{n}}(B) & \approx \hat{\mathbf{x}}_1 - \frac{1}{2}T\Delta x_3\hat{\mathbf{x}}_2\left(\frac{1}{2}S-\Delta\right)\Delta x_3\hat{\mathbf{x}}_3 \\ \hat{\mathbf{n}}_2(B) & \approx \hat{\mathbf{x}}_2 + \frac{1}{2}T\Delta x_3\hat{\mathbf{x}}_1 + \frac{\partial\omega}{\partial x_3}\Delta x_3\hat{\mathbf{x}}_3 \\ \hat{\mathbf{n}}_3(B) & \approx \hat{\mathbf{x}}_3 - \left(\frac{1}{2}S-\Delta\right)\Delta x_3\hat{\mathbf{x}}_1 - \frac{\partial\omega}{\partial x_3}\Delta x_3\hat{\mathbf{x}}_2 \end{cases} \tag{F.14}$$

We again approximate the value of $\hat{\mathbf{n}}(Q)$ by using the directional gradient at point $B$ along $\hat{\mathbf{v}} = \hat{\mathbf{x}}_1$. This results in:

$$\begin{aligned} \hat{\mathbf{n}}(Q) \approx & \hat{\mathbf{n}}(B) + \nabla_{\hat{\mathbf{x}}_1}\hat{\mathbf{n}}(B)\cdot\Delta x_1 = \hat{\mathbf{n}}(A) + \ \mathbf{B}_B\Delta x_1 \\ & + \left[\frac{1}{2}T\left(\frac{1}{2}S_B+\Delta_B\right)\Delta x_1\Delta x_3 + \frac{1}{2}T_B\left(\frac{1}{2}S-\Delta\right)\Delta x_1\Delta x_3\right]\hat{\mathbf{n}}_2(B) \\ & + \left[-\left(\frac{1}{2}S-\Delta\right)\left(\frac{1}{2}S_B-\Delta_B\right)\Delta x_1\Delta x_3 + \frac{1}{4}TT_B\Delta x_1\Delta x_3\right]\hat{\mathbf{n}}_3(A) \end{aligned} \tag{F.15}$$

Expanding up to second order results in the final expression:

$$\begin{aligned} \hat{\mathbf{n}}(Q) \approx & \ \hat{\mathbf{x}}_1 - (b_2\hat{\mathbf{x}}_2 + b_3\hat{\mathbf{x}}_3)\Delta x_1 + \left[\left(\frac{S}{2}-\Delta\right)\hat{\mathbf{x}}_3 - \frac{T}{2}\hat{\mathbf{x}}_2\right]\Delta x_3 \\ & + \left[\left(b_3\left(\frac{1}{2}S-\Delta\right) - \frac{1}{2}Tb_2\right)\hat{\mathbf{x}}_1 + \left(-\frac{\partial b_2}{\partial x_3} + b_3\frac{\partial\omega}{\partial x_3} + \frac{1}{2}TS\right)\hat{\mathbf{x}}_2\right. \\ & \left. + \left(-\frac{\partial b_3}{\partial x_3} - b_2\frac{\partial\omega}{\partial x_3} - \left(\frac{S}{2}-\Delta\right)^2 + \frac{1}{4}T^2\right)\hat{\mathbf{x}}_3\right]\Delta x_1\Delta x_3 \end{aligned} \tag{F.16}$$

Equating F.13 and F.16 gives the final two compatibility equations:

$$b_2b_3 - \frac{1}{2}TS + 2\Delta\frac{\partial\omega}{\partial x_1} - \frac{1}{2}\frac{\partial T}{\partial x_1} + \frac{\partial b_2}{\partial x_3} - b_3\frac{\partial\omega}{\partial x_3} = 0 \tag{F.17a}$$

$$b_3^3 + \left(\frac{1}{2}S-\Delta\right)^2 - \frac{1}{4}T^2 + \frac{\partial b_3}{\partial x_3} + \frac{\partial(S/2-\Delta)}{\partial x_1} + b_2\frac{\partial\omega}{\partial x_3} = 0 \tag{F.17b}$$

# Appendix G

# Continuous director evolution in magnetic fields: Ansatzes

In this appendix, we present the ansatzes for the continuous director field evolution used in Chapter 6 for generating the schematics in Figures 6.2c and 6.6e. Due to the symmetry of the system, the director field needs to be computed only for the region corresponding to the azimuthal angle range $0 \leq \varphi \leq \pi/2$. The rest of the director field is obtained by applying appropriate symmetries.

## G.1 Defect free case

In this case, we start with the axial configuration which is given by:

$$\hat{\mathbf{n}}(r, \theta, \varphi) = \hat{\boldsymbol{\varphi}}(\varphi) \tag{G.1}$$

with $\hat{\boldsymbol{\varphi}}(\varphi)$ the azimuthal unit vector (Figure G.1a). If we assume the external magnetic field to point in the horizontal direction, $\pi/2 - \varphi$ then corresponds to the angle the director field makes with the magnetic field . The director field is already aligned with the field at $\varphi = \pi/2$, while perpendicular to it at $\varphi = 0$. To emulate the effect of the magnetic field we can make a change of variable such that the deviation from the aligned region is concentrated in the region around $\varphi = 0$:

$$\varphi' = \frac{\pi}{2}\left(1 - \left(1 - \frac{2}{\pi}\varphi\right)^{\alpha}\right) \tag{G.2}$$

In this expression the $\varphi$ variable range is first linearly transformed to range from 0 at $\varphi = \pi/2$ to 1 at $\varphi = 0$. This is non-linearly transformed by raising it to the power of $\alpha$ which serves as a proxy for the magnetic field. When $\alpha > 1$, the exponent concentrates the change of the angle to the region close

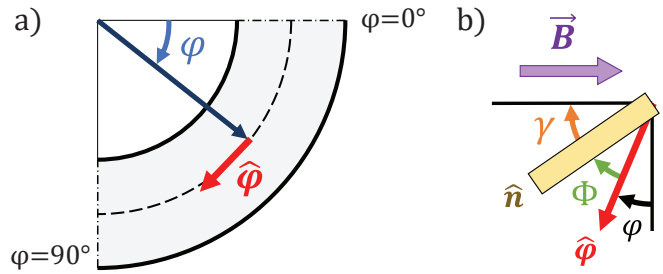



**Figure G.1:** a) Azimuthal coordinate in our torus. b) Schematic of the different angles used with respect the director, magnetic field and azimuthal orientation.

to 1. This is then linearly rescaled such that $\varphi'(0) = 0$ and $\varphi'(\pi/2) = \pi/2$. The net effect of this change of variable is to extend the region already aligned with the director field while concentrating the region where the director field changes. The parameter $\alpha$ serves as a proxy for the magnetic field since it accounts for how much the director field is distorted in a continuous way, with $\alpha = 1$ corresponding to the undistorted case and $\alpha > 1$ to the distorted one. The director field becomes:

$$\hat{\mathbf{n}}(r, \theta, \varphi) = \hat{\boldsymbol{\varphi}}(\varphi'(\varphi, \alpha)) \tag{G.3}$$

Note this ansatz does not fulfill the planar boundary conditions. To account for this, we linearly interpolate between the distorted and undistorted director fields along a boundary layer of thickness $\delta a$ such that the director field becomes the undistorted one at the surface and the distorted one at a distance $\delta a$ from the surface, with $a$ the tube radius. This results in the final expression:

$$\begin{cases} \varphi_d(\varphi, \alpha) = \varphi' = \dfrac{\pi}{2}\left(1 - \left(1 - \dfrac{2}{\pi}\varphi\right)^{\alpha}\right) & \dfrac{r}{a} < 1 - \delta \\ \varphi_d(\varphi, \alpha) = \varphi + (\varphi' - \varphi)\dfrac{a - r}{\delta a} & 1 - \delta \leq \dfrac{r}{a} \leq 1 \end{cases} \tag{G.4}$$

with a director field given by:

$$\hat{\mathbf{n}}(r, \theta, \varphi) = \hat{\boldsymbol{\varphi}}(\varphi_d(\varphi, \alpha)) \tag{G.5}$$

## G.2 Defect pair located at $\varphi = 0$

In this case, the key to the continuous transformation is to note that the director field is horizontal and aligned with the external director field both at $\varphi = 0$ and $\varphi = \pi/2$, becoming misaligned in the middle. If we plot the angle the director

makes with the magnetic field as a function of $\varphi$, the function corresponds to a hill between zeros. This hill can be continuously flattened by dividing the function by a parameter $\alpha$. If we take the defect pair ansatz, we can compute the angle the director makes with the magnetic field from the azimuthal angle $\Phi_0$ as:

$$\gamma = \frac{\pi}{2} - \Phi_0 - \varphi \tag{G.6}$$

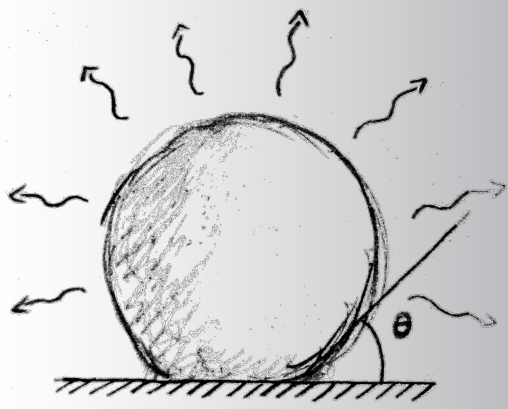
The effect of the magnetic field can be emulated by dividing this angle by $\alpha$:

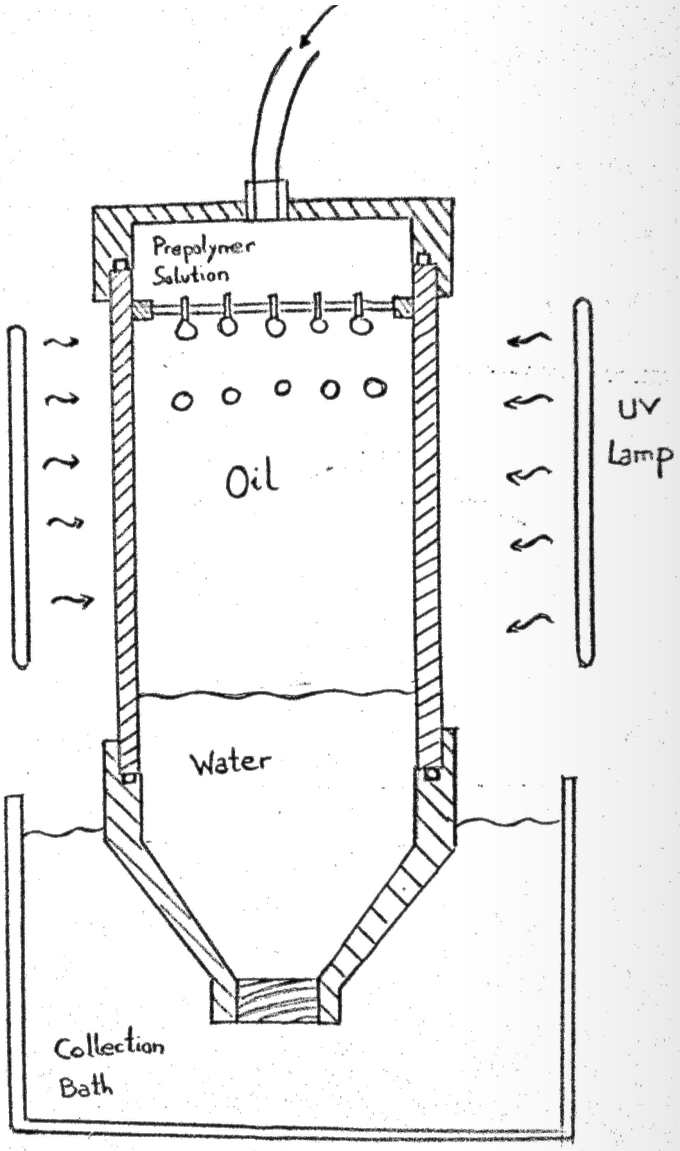
$$\gamma_d = \frac{\gamma}{\alpha} = \frac{\frac{\pi}{2} - \Phi_0 - \varphi}{\alpha} \tag{G.7}$$

The undistorted state is given by $\alpha = 1$, while the distorted state is given by $\alpha > 1$. Using equation G.6 we can recover the distorted azimuthal angle. Imposing the boundary conditions by an interpolation between the distorted and undistorted cases, as in the previous case, results in:

$$\begin{cases} \Phi_d(\varphi, \alpha) = \frac{\pi}{2} - \gamma_d - \varphi = \frac{\pi}{2} - \varphi - \frac{\frac{\pi}{2} - \Phi_0 - \varphi}{\alpha} & \frac{r}{a} < 1 - \delta \\ \Phi_d(\varphi, \alpha) = \frac{\pi}{2} - \gamma - \varphi - (\gamma_d - \gamma)\frac{a - r}{\delta a} & 1 - \delta \leq \frac{r}{a} \leq 1 \end{cases} \tag{G.8}$$

Using equation 4.14 and the expression for the polar angle $\Theta$ of the defect pair solution, we get the final ansatz.


θ


Prepolymer
Solution
Oil
Water
UV
Lamp
Collection
Bath